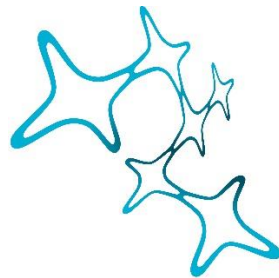# Dissertation

der Graduate School of Systemic Neurosciences

der Ludwig-Maximilians-Universität

München

Graduate School of
Systemic Neurosciences
LMU Munich

Functional anatomy of a visuomotor transformation in the optic tectum of zebrafish

Submitted by

Thomas Otmar Helmbrecht

30th May 2018

To Anne, my family and friends

Summary

Animals detect sensory cues in their environment and process this information in order to carry out adaptive behavioral responses. To generate target-directed movements, the brain transforms structured sensory inputs into coordinated motor commands. Some of these behaviors, such as escaping from a predator or approaching a prey, need to be fast and reproducible. The optic tectum of vertebrates (named "superior colliculus" in mammals) is the main target of visual information and is known to play a pivotal role in these kinds of visuomotor transformation. In my dissertation, I investigated the neuronal circuits that map visual cues to motor commands, with a focus on the axonal projections that connect the tectum to premotor areas of the tegmentum and hindbrain.

To address these questions, I developed and combined several techniques to link functional information and anatomy to behavior. The animal I chose for my studies is the zebrafish larva, which is amenable to transgenesis, optical imaging approaches, optogenetics and behavioral recordings in virtual reality arenas.

In a first study, I designed, generated and characterized BAC transgenic lines, which allow gene-specific labelling of neurons and intersectional genetics using Cre-mediated recombination. Importantly, I generated a pan-neuronal line that facilitates brain registrations in order to compare different expression patterns (Förster et al., 2017b).

In a second project, I contributed to the development of an approach that combines two-photon holographic optogenetic stimulation with whole brain calcium imaging, behavior tracking and morphological reconstruction. In this study, I designed the protocol to reveal the anatomical identity of optogenetically targeted individual neurons (dal Maschio et al., 2017).

In a third project, I took advantage of some of these methods, including whole-brain calcium imaging, optogenetics and brain registrations, to elucidate how the tectum is wired to make behavioral decisions and to steer behavior directionality. The results culminated in a third manuscript (Helmbrecht et al., submitted), which reported four main findings. First, I optogenetically demonstrated a retinotopic organization of the tectal motor map in zebrafish larvae. Second, I generated a tectal "projectome" with cellular resolution, by reconstructing and registering stochastically labeled tectal projection neurons. Third, by employing this anatomical atlas to interpret functional imaging data, I asked whether visual information leaves the tectum via

distinct projection neurons. This revealed that two distinct uncrossed tectobulbar pathways (ipsilateral tectobulbar tract, iTB) are involved in either avoidance (medial iTB, iTB-M) or approach (lateral iTB, iTB-L) behavior. Finally, I showed that the location of a prey-like object, and therefore the direction of orientation swims towards prey, is functionally encoded in iTB-L projection neurons.

In summary, I demonstrated in this thesis how refined genetic and optical methods can be used to study neuronal circuits with cellular and subcellular resolution. Importantly, apart from the biological findings on the visuomotor transformation, these newly developed tools can be broadly employed to link brain anatomy to circuit activity and behavior.

Acknowledgements

First and foremost, I would like to deeply thank Herwig. He is a great supervisor, giving me all the freedom during my PhD to explore the visual system of zebrafish from all directions I desired. He always guided me to ask the right questions, encouraged me to develop the necessary tools to answer them and always took an interest in my scientific or personal problems. In his lab, he concentrated great people to build up a fruitful and collaborative community of mutual support and scientific exchange.

Second, I want to thank my Thesis Advisory Committee. Harald Luksch and German Sumbre have been a great support during my PhD. Their feedback, criticisms and scientific discussions kept me scientifically on-track during the years. Importantly, I want to further thank Harald Luksch who inspired me to become a neurobiologist from the first day of attending his lectures throughout my Bachelor and Master thesis and until now. In addition, I want to thank Michael Gebhardt and Stefan Weigel, the supervisors during my early scientific stages and from whom I have learned so much. Here, I also want to thank Tod Thiele and Estuardo Robles, who taught me in the first years of my PhD everything, from setting up fish to optogenetics and anatomy.

Most certainly, I have to thank Marco dal Maschio. He was my second supervisor and became a very close friend, sharing the office with me for 5 years. He taught me almost everything I know about computational models, functional imaging, optogenetics or more generally modern neuroscience. His work, his intellect and diligence have always been an inspiration. Without his guidance, I would have been lost many times. I can only wish him good luck and all the best with his own new lab in Italy. Moreover, I want to thank my friend and colleague Joe Donovan, who "forced" me to learn Python and who taught me so much about coding, general computational approaches and engineering. Many other people and friends in the lab have contributed and accompanied me throughout my PhD life. I want to thank Dominique for his guidance in molecular biology, Miguel and Duncan for excellent scientific discussions, Robert for his patience while building the volumetric imaging system, Anki for coding help, and Enrico for being an awesome lab manager. Furthermore, I want to thank Eliane, Miguel, Dominique and Duncan for carefully reading my thesis, and all the current and former lab members for being awesome lab mates.

Finally, I want to thank all my friends not named so far and especially my family who always supported me throughout sometimes-difficult times. Most importantly, I want to thank Anne; without her, all these pages would be empty.

Contents

List of Figures

Introduction

Tectal control of behavior

An animal's ability to generate appropriate behavior in response to sensory stimuli requires that the categorization and localization of sensory information be converted into a pattern of activity in downstream premotor areas. Thus, two processes need to take place: first, a sensorimotor decision, where different stimuli must be mapped to different motor outputs, i.e. to approach or to escape from an object; second, the stimulus location must appropriately modulate that motor output to steer the directionality of movements. One main brain structure involved in this visuomotor transformation is the optic tectum, the homologue of the mammalian superior colliculus (SC). In the superficial layers of the tectum, visual inputs from retinal ganglion cells (RGCs) form a topographic representation of the visual surrounding in retinotopic coordinates – a visual map (Robles et al., 2014). On the other hand, deeper layers in the tectum form a motor map, which when activated generates combined head/tail and eye movements towards the corresponding position in the overlying visual map (Freedman et al., 1996; Herrero et al., 1998a; du Lac and Knudsen, 1990). In this way, retinotopic information received by the tectum is transformed into 'functionotopic' signals, which are relayed to premotor structures controlling motor programs (Hellmann et al., 2004).
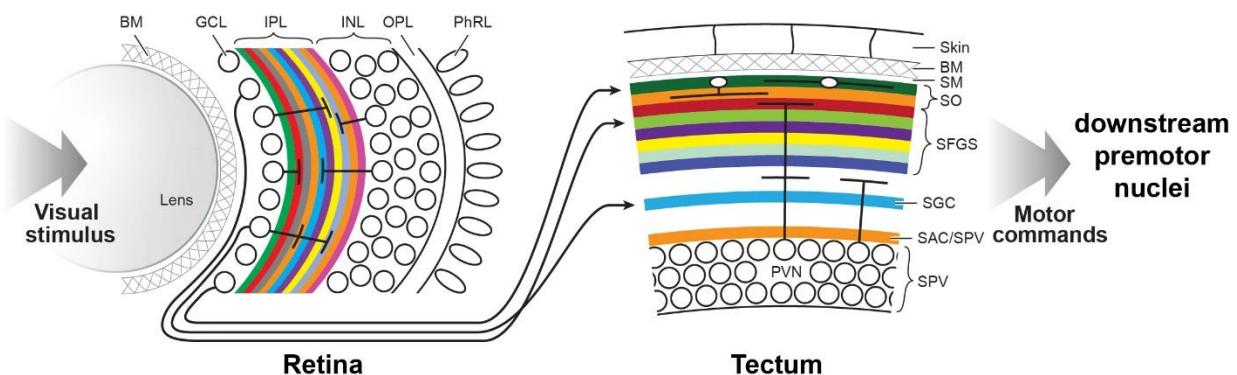
Figure 1: Tectal visuomotor transformation. Channeled information from the retina is projected to the tectum, where different layers are targeted. Tectal neurons reside mainly in the stratum periventriculare (SPV). These neurons arborize in different tectal layers to compute behavior relevant information in the visual map. Resulting from this processing a motor map is formed via axonal projections to downstream premotor areas. (Figure adapted from Baier, 2013)

Zebrafish larvae represent a vertebrate model organism well suited to investigate this stream of visual to motor processing. They are genetically and optically amenable, even more so in unpigmented larvae carrying mutations in the *mitfa* allele – nacre fish (Lister et al., 1999), which allows the use of light-based genetically encoded tools such as neuronal modulators (optogenetics), activity reporters (calcium imaging) and genetic axon tracing (Baier and Scott, 2009). Furthermore, they develop quickly and show a large repertoire of visually driven behaviors already at 5 days post fertilization (d.p.f), i.e. hunting prey (Bianco et al., 2011; Semmelhack et al., 2014), looming escape (Dunn et al., 2016a; Temizer et al., 2015), optomotor response (Neuhauss et al., 1999; Orger et al., 2000) and optokinetic reflex (Kubo et al., 2014; Schoonheim et al., 2010). In addition, their vertebrate brain is comparatively small (700x400x300 μm^3) with approximately 100,000 neurons, a size allowing whole brain functional and anatomical investigations (Ahrens et al., 2012; Robles et al., 2014; Sato et al., 2007).

Information flow from the retina

In vertebrates, visual information is carried to other brain regions exclusively by retinal ganglion cells (Karlstrom et al., 1996). The retina of zebrafish – as in other vertebrates – consists of different laminae (Figure 2 A) such as the outer and inner nuclear layer (ONL and INL, respectively), the outer and inner plexiform layer (OPL and IPL, respectively) and the ganglion cell layer (Sanes and Zipursky, 2010; Schmitt and Dowling, 1999). Different types of RGCs contact functionally diverse laminae in the inner plexiform layer (IPL) to project the features of the entire visual scene to targets of the 10 different arborization fields (AFs) including the tectum (AF10) (Burrill and Easter, 1994) (Figure 2 B). In fact, up to 82 different types of RGCs have been recently described, exhibiting various combinations of distinct dendritic and axonal morphological features (Robles et al., 2014) (Figure 2 B,C).

So what is the functional role of these different channels feeding visual information to the brain? Advancing the groundwork of Ewert and Ingle, who characterized visual features for behavior such as catching prey or escaping looming objects in toads (Ewert, 1970; Ingle, 1983), different arborization fields have recently been demonstrated to fulfill specific functions. RGCs projecting to AF7 and AF10 have been shown to be sensitive to visually displayed small dots or paramecia and to be necessary for prey capture (Semmelhack et al., 2014). On the other hand, AF6, AF8 and AF10 targeting RGCs have been shown to be involved in detecting looming and dimming stimuli inducing visual escapes (Temizer et al., 2015). In addition to being the main target of

RGCs, the tectum has been demonstrated to be required for both approach and escape responses (Barker and Baier, 2015; Gahtan et al., 2005).
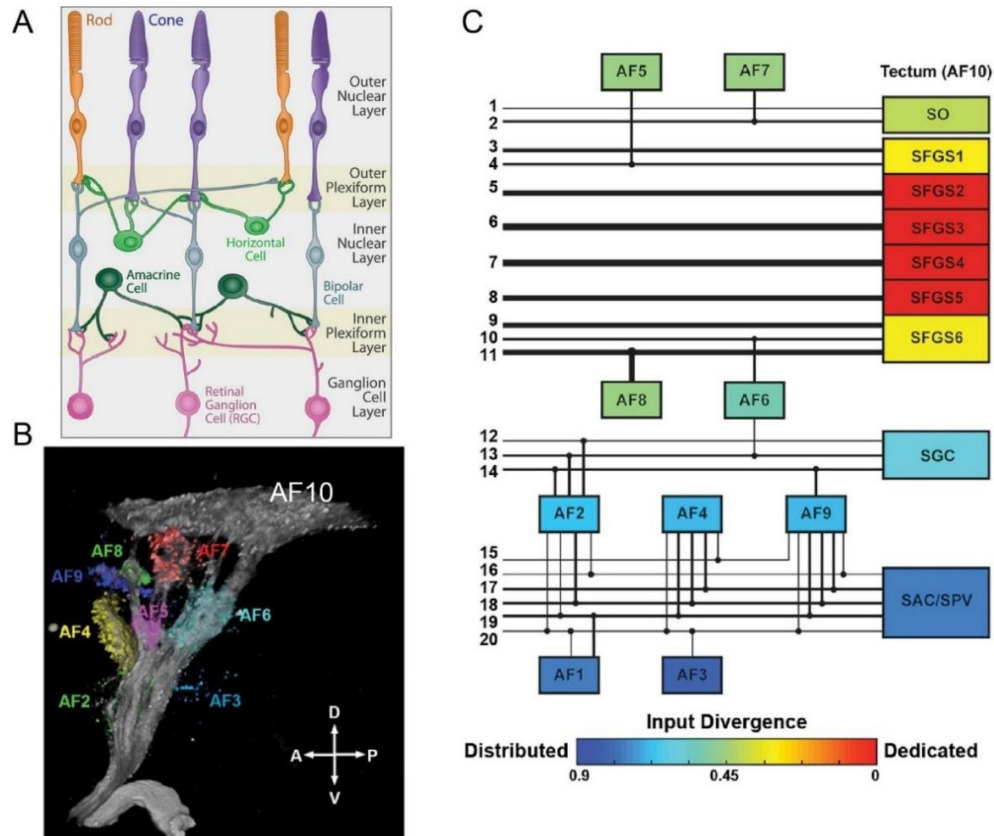
Figure 2: Projection targets of retinal ganglion cells. (**A**) Blueprint of the vertebrate retina (figure adapted form Sanes and Zipursky, 2010). (**B**) Arborization fields (AFs) formed by RGCs expressing mCherry (grey) and syp-GFP (colored) under the atoh7:Gal4 driver. The syp-GFP channel is used to annotate the AFs according to densities in synaptophysin expression. (**C**) Reconstructed wiring diagram of the 20 distinct projection patterns and their targets found by collecting and partly reconstructing 446 individual RGCs. (Figures B and C adapted from Robles et al., 2014)

Anatomical organization of the optic tectum

The tectum is a highly laminated structure, receiving RGC inputs in at least four superficial retinorecipient laminae in zebrafish (Robles et al., 2013) and birds (Mey and Thanos, 2000). These layers are named stratum opticum (SO), stratum fibrosum et griseum superficiale (SFGS), stratum griseum centrale (SGC) and stratum album centrale (SAC). In zebrafish these layers form at least 10 sublaminae – the SFGS layer can be further divided into 6 sublayers (SFGS 1-6) –

showing different responses to the visual scene (Nikolaou et al., 2012; Preuss et al., 2014; Temizer et al., 2015) and a topographical representation of visual space (retinotopy, Robles et al., 2013). For example, RGCs from the nasal retina, which receive light from the posterior visual field, project to the posterior tectum. Conversely, visual input from the anterior field of vision is projected onto the anterior tectum.
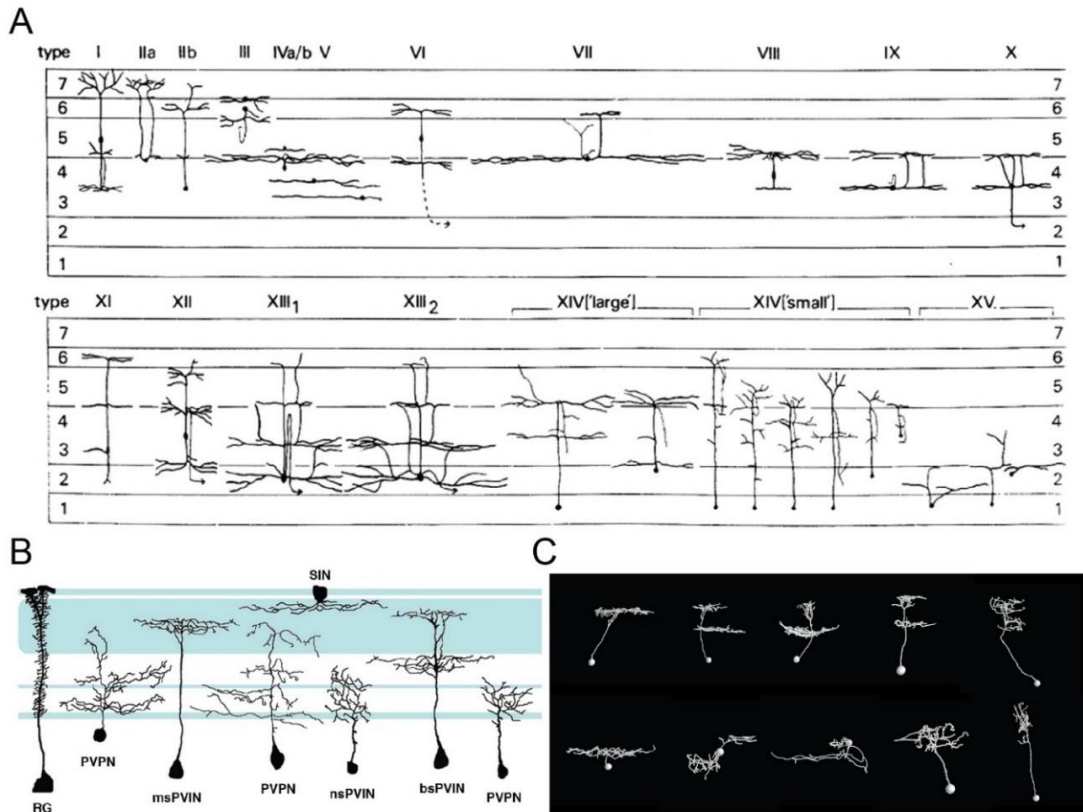
Figure 3: Tectal cell types. (**A**) Tectal cell types described in a Golgi study of the goldfish tectum (figure adapted form Meek and Schellart, 1978). (**B**) Neurons described in tectum of zebrafish larvae (figure adapted from Nevin et al., 2010). (**C**) Different types of tectal interneurons reconstructed using a stochastic single-cell labeling strategy (BGUG).

Tectal cell bodies mainly reside within the stratum periventriculare (SPV) with the exception of superficial interneurons (SINs) which reside in the tectal neuropil (Barker et al., 2017; Del Bene et al., 2010). Tectal neurons can be grouped into two main groups: interneurons (periventricular interneuron - PVIN) and projection neurons (periventricular projection neuron - PVPN)(Figure 3 B, Nevin et al., 2010). These two groups can be further subdivided regarding neurite stratifications in the neuropil and their extratectal projections. In this way, and considering differences in lumping or splitting of cell types, between 10 - 31 cell types have been described in birds (Luksch, 2003) and 15 types in a Golgi study in adult goldfish (Figure 3 A, Meek and Schellart, 1978). Of these

15 classes in the goldfish tectum, six efferent classes have been described which project to the contralateral tectum (class XV), the pretectum and contralateral tectum (class XIV), the tectobulbar tract (class XII and XIII) and unspecified targets (class VI and X) (Meek, 1983). In addition, but lacking cellular resolution, a variety of other targets have been suggested via tracer injections in several species (Kinoshita et al., 2006; Luque et al., 2008; Pérez-Pérez et al., 2003; Vanegas and Ito, 1983).

Motor functions of the tectum

The features of the tectal visuomotor transformation and the underlying motor functions have been studied across the whole animal kingdom, including birds (du Lac and Knudsen, 1990), mammals (Bergeron et al., 2003; DeSouza et al., 2011; Freedman et al., 1996), amphibians (Ingle, 1983) and fish (Herrero et al., 1998a). Using electrical microstimulation (Herrero et al., 1998a; Salas et al., 1997), different zones in the optic tectum of goldfish were defined, which encode a motor map for eye and tail movements (Figure 4 A). Among these, the anterior-medial zone of the tectum seems to be involved in prey capture, such as conversive eye movements to track putative prey. In contrast, the medial-posterior zone has been shown to be involved in orienting or escape-like behavior, such as contra- or ipsiversive tail and eye movements. Thus, in addition to the retinotopic visual map described, a 'motor map' is formed in the output layers of the tectum (Figure 4).
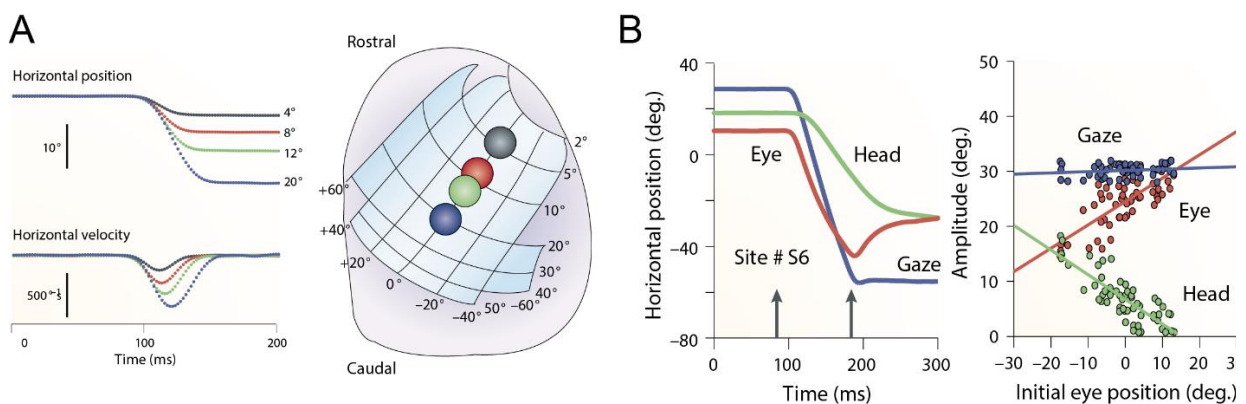
Figure 4: Tectal motor functions. (**A**) Encoding of eye-movements in the SC. The right panel depicts the space code of activity in the SC, which represents the different eye movements recorded in the left panel. (**B**) Recorded trajectories of eye and head movements after stimulating neurons in the deep layers of the SC. The right panel shows the influence of eye-position onto the behavioral outcome to keep the total gaze constant (figures adapted from Sparks, 2002)

The output signal of the tectum or the superior colliculus is thought to be a 'space code', where focal tectal activity represents the required head/tail and eye movements to reach a target (Klier et al., 2001; van Opstal et al., 1991; Sadeh et al., 2015; Sparks and Gandhi, 2003). Tectal projection neurons relay this space code to premotor nuclei in the mid- and hindbrain (descending tectofugal pathway). The targeted premotor centers are located in the reticular formation, which is segregated into the mesencephalic reticular formation (MRF) of the midbrain and the rhombencepahlic reticular formation (RRF) of the hindbrain (Herrero et al., 1998b). Residing reticulospinal neurons send their axons to motor neurons driving orienting movements of the tail (Saitoh et al., 2007).

Sensorimotor decision making

In addition to this motor coding the tectum is known to be involved in sensorimotor decisions (Barker and Baier, 2015; Felsen and Mainen, 2012), being capable of inducing approach maneuvers as well as escape responses (Herrero et al., 1998a; Shang et al., 2015). Depending on the valence of a stimulus, i.e. object size, speed, trajectory (looming), an animal has to decide whether to turn towards or to avoid the object (Figure 5 A). Behavioral studies explored the characteristics of stimuli and found small dots (1-5 degree, 60-90 deg/sec Bianco et al., 2011; Semmelhack et al., 2014) and black looming discs (> 30 deg/sec, Dunn et al., 2016; Temizer et al., 2015) as ideal stimuli to trigger either approach or escape behavior.

The zebrafish tectum has been demonstrated to be necessary for both, escape and approach behavior (Barker and Baier, 2015; Gahtan et al., 2005; Temizer et al., 2015) and different tectal descending pathways have been proposed to route this behavior selection. The crossed/contralateral tectobulbar tract for approaching behavior (i.e. turning towards prey) and the uncrossed/ipsilateral tectobulbar projection for aversive behavior (i.e. escape from predator) (Dean et al., 1989; Ellard and Goodale, 1988; Ingle, 1983; Sooksawate et al., 2013) (Figure 5 B). Although these pathways have been anatomically described in different animal models (Huerta and Harting, 1984a; Pérez-Pérez et al., 2003), a more detailed anatomical representation of tectal efferent pathways is still missing and their functional properties remain largely unknown (Figure 5 C).
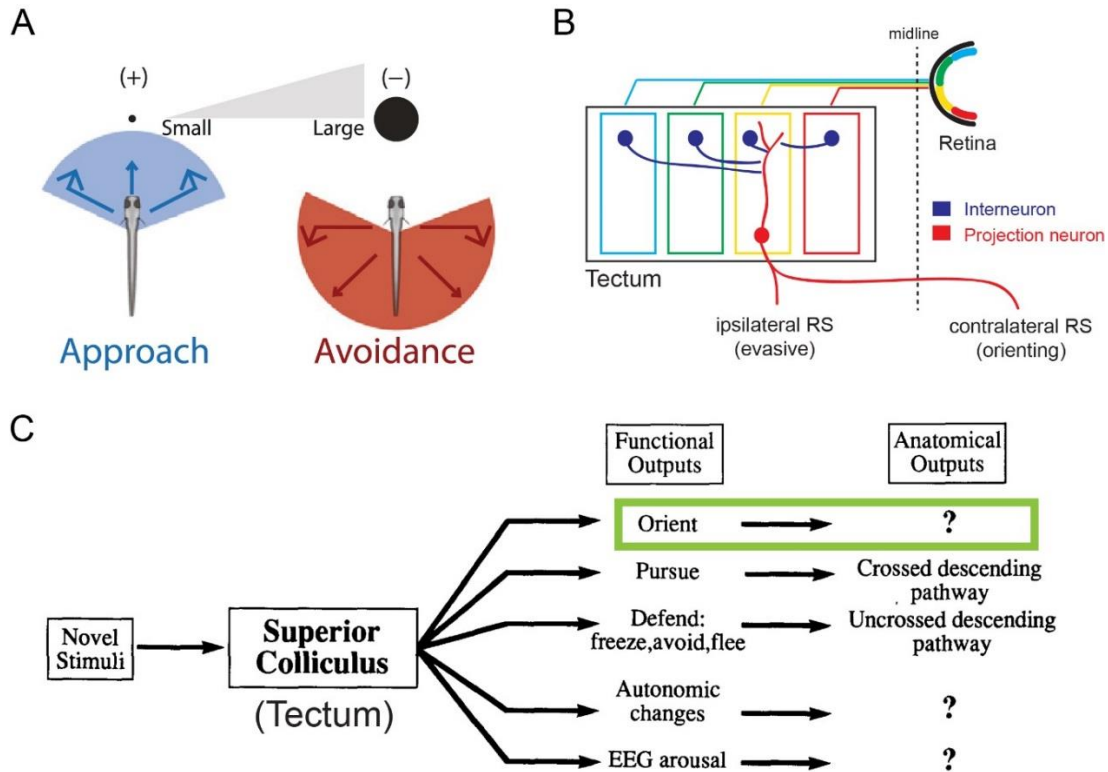
Figure 5: Behavioral decision making in the tectum. (**A**) Behavioral choice of approach or avoidance depending on the size of the visual object (figure adapted from Barker and Baier, 2015). (**B**) Model for sensorimotor decision makings in the tectum of lamprey. The uncrossed tectobulbar projection neurons mediate avoidance behavior, whereas crossed tectobulbar projection neurons steer orienting responses (figure adapted from Kardamakis et al., 2015). (**C**) Determined pathways in the superior colliculus of rats. The origin of orienting movements remains to be elucidated (green, figure adapted from Dean et al., 1989).

Genetic tools in zebrafish research

Generation of transgenic lines

The zebrafish genome is well studied and amenable to genetic manipulations, such as the Tol2-mediated Gal4-UAS method (Asakawa and Kawakami, 2009; Scott et al., 2007). The Gal4-UAS system has been widely used in *Drosophila* for targeted gene expression in specific tissues, and is an established technique in zebrafish (Scheer and Campos-Ortega, 1999). To drive transcription of target genes, the yeast transcriptional activator Gal4 binds to the upstream activating sequence (UAS). Thus, 'driver' lines with tissue specific expression of Gal4 can be crossed to 'effector' lines expressing target genes under control of the UAS promotor (Figure 6

A). However, many Gal4 lines used in the field were generated using gene or enhancer trapping, and the resulting expression patterns can be rather unspecific and the locus of insertion remains unknown for many lines. Recently, strategies such as CRISPR/Cas9 or BAC-recombination (Figure 6 B) are opening new doors (Albadri et al., 2017; Suster et al., 2011). These techniques allow labeling of specific neuronal subpopulations by either inserting Gal4 directly at the start-ATG of the genes of interest (CRISPR/Cas9) or via expression of Gal4 under the control of regulatory elements on a Bacterial Artificial Chromosome (BAC).

Optogenetic tools

Optogenetics and functional imaging are revolutionizing functional network analysis (Baier and Scott, 2009). Photoswitchable ion channels for excitation, including channelrhodopsin-2 (ChR2) and red shifted chimeric opsin variant (C1V1), as well as ion pumps for inhibition, including halorhodopsin (NpHR) or archaerhodopsin (ArchT 3.0) have been developed for optical manipulation of neuronal activity (for review see Mattis et al., 2011) (Figure 6 C). In addition, the use of genetically encoded calcium indicators (GECIs) is a well-established technique for imaging neuronal activity *in vivo.*

The most commonly used GECI is GCaMP (Figure 5 D), a fusion protein of GFP with calmodulin and a M13 fragment of the myosin light chain kinase (Nakai et al., 2001). Over the last decade this sensor was further genetically engineered to improve the kinetics, signal-to-noise ratio, affinity and dynamic range (Akerboom et al., 2012; Chen et al., 2013; Podor et al., 2015)*.*

Photoconvertible fluorescent reporters like Kaede (Ando et al., 2002), Dendra (Gurskaya et al., 2006) or photoactivatable GFP (paGFP, Patterson et al., 2002) have been developed and can be used to trace neuronal pathways. Using UV-light illumination, initially green fluorescing Kaede and Dendra proteins can be photoconverted to emit red fluorescence (Baier and Scott, 2009), whereas paGFP changes from a dark to a bright green state (Shcherbakova et al., 2014). Combining this labeling method with optogenetic stimulation allows localization of the stimulated region and, if targeted to a single cell, the reconstruction of local neurites (Dunn et al., 2016b; Förster et al., 2017a). In addition, our lab has generated a zebrafish line named BGUG (*Tg(brn3c:GAL4, UAS: gap43-GFP)s318t*; Scott et al., 2007), in which the expression of a membrane-bound GFP (mGFP) is strongly variegated. By crossing BGUG fish with any other Gal4 line, only a subset of neurons of the Gal4 pattern will express the mGFP. This 'genetic Golgi'

staining enables very detailed reconstruction of individual neurons and the creation of a cellular resolution brain atlas or wiring diagrams (Robles et al., 2014; Scott and Baier, 2009) (Figure 2 C, 3 C).
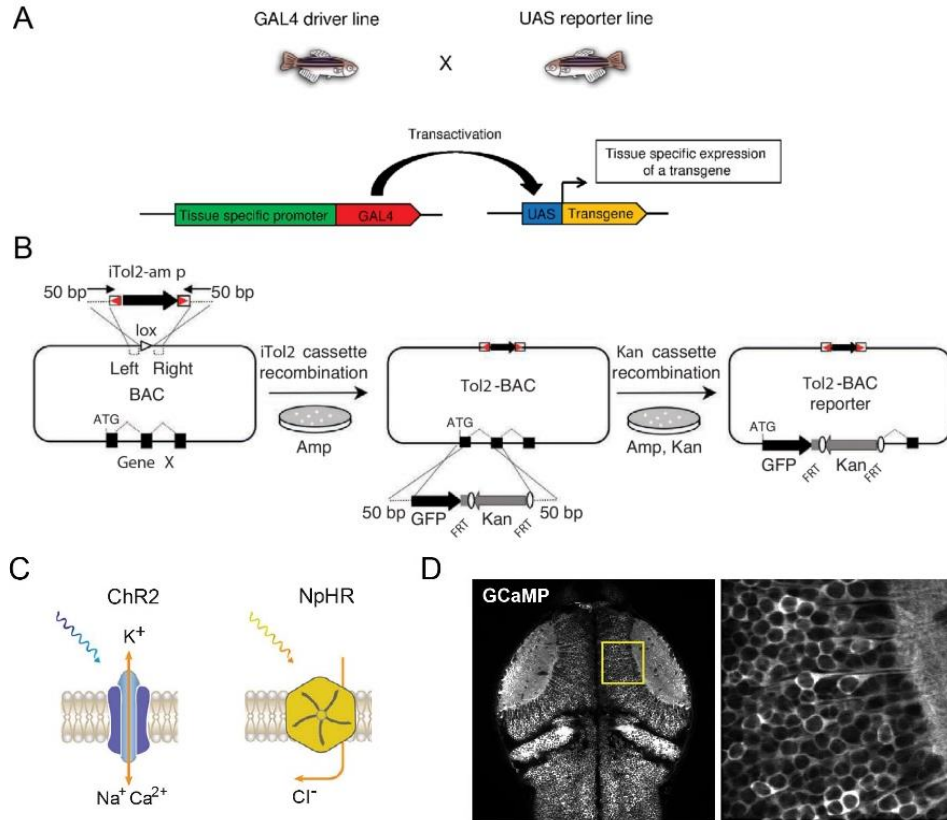
Figure 6: Genetic tools. (**A**) Application of the Gal4/UAS system in zebrafish (figure adapted from Sugano and Neuhauss, 2012). (**B**) Tol2-BAC recombination as a toolkit to generate gene-specific transgenic lines (figure adapted from Suster et al., 2011). (**C**) Optogenetic molecules such as ChR2 (activation) or NpHR (silencing) are widely used to modulate activity in cells (figure adapted from Rein and Deussing, 2012). (**D**) Genetically encoded calcium indicators (i.e. GCaMP) serve as an ideal tool to monitor neuronal activity in the transparent zebrafish (figure adapted from Renninger and Orger, 2013).

Methods to reveal circuit functions

Two-photon calcium imaging

In 1990, the invention of the two-photon microscope (Denk et al., 1990), opened the window of *in vivo* circuit explorations and the possibility to investigate brain activity dynamics at unprecedented

depths within the brain. The principle idea is to take advantage of non-linear absorption properties of fluorescent molecules excited in the IR range (700-1300nm) to achieve high-resolution images. This is implemented by the use of a femtosecond laser and combining this with fast point scanning (LSM – laser scanning microscopy) and PMT (photomultiplier tube) detection. The wavelength used to excite GCaMP for calcium imaging is most commonly around 920 nm (corresponding to one-photon peak absorption between 450 - 500 nm) (Akerboom et al., 2012). Due to the non-linear absorption, where a high spatio-temporal density of excitation photons occurs, only a very small volume is excited and the circuit activity can be reconstructed at high resolution point by point. Although laser point scanning and the kinematics of the calcium reporters are slow, this approach yields many advantages. First, and especially important for transparent zebrafish larvae, *in vivo* experiments can be carried out with minimal invasiveness and with wavelengths not visually detectable by the model organisms. Furthermore, hundreds of neurons can be recorded within one plane (Kubo et al., 2014; Portugues et al., 2014) and even whole brain imaging is feasible using remote focusing strategies (Botcherby et al., 2012; Dal Maschio et al., 2011; Grewe et al., 2011; Ji et al., 2016). Given these advantages, two-photon calcium imaging has become the most commonly used method for functional recordings in zebrafish.

Optogenetic stimulation and two-photon holography

The transparency of zebrafish makes them an extremely amenable model for the interrogation of neural circuits using light (Baier and Scott, 2009; Emiliani et al., 2015). Using optogenetic actuators (i.e. ChR2) or silencers (i.e. NpHR) enables investigations of functional connectivity (Förster et al., 2017a), network dynamics (Rickgauer et al., 2014) and behavioral control (Arrenberg et al., 2009; Kubo et al., 2014) at cellular resolution. Different ways to target the proteins with light have emerged during the last 10 years. First, one-photon optical fiber stimulation (Arrenberg, 2016) is useful to stimulate a larger ensemble of neurons (Figure 7 A). This method, using visible light, can be refined by employing optical fibers with different core diameters (most common: 10-200 µm, Thiele et al., 2014) or by expressing ChR2 in specific neuronal cell types (Shang et al., 2018, 2015). Second, two-photon optogenetics have been introduced to refine the axial resolution, to restrict the stimulation area and to stimulate single cells even in densely packed regions (Oron et al., 2012). Several approaches have been demonstrated, using spiral scanning of the laser over single neurons (Rickgauer and Tank, 2009)

or line-scanning approaches over defined regions of interest (Dunn et al., 2016b; Kawashima et al., 2016). In addition, scanless approaches using computer generated holography (CGH, Figure 7 C, D) have advanced the field of two-photon optogenetics (Dal Maschio, 2014; Dal Maschio et al., 2010, 2012; Vaziri and Emiliani, 2012). Two-photon holographic stimulation enables shaping the light wavefront according to the structure of the targeted cell bodies in 3D and to stimulate the entire membrane or the population of neurons simultaneously, thus maximizing the membrane current and temporal resolution. As a drawback, the light is not focused on one spot scanned over the cells and thus to keep the photocurrent high, the overall average power has to be increased when stimulating larger areas which causes the risk of heating and photodamage (Vaziri and Emiliani, 2012).
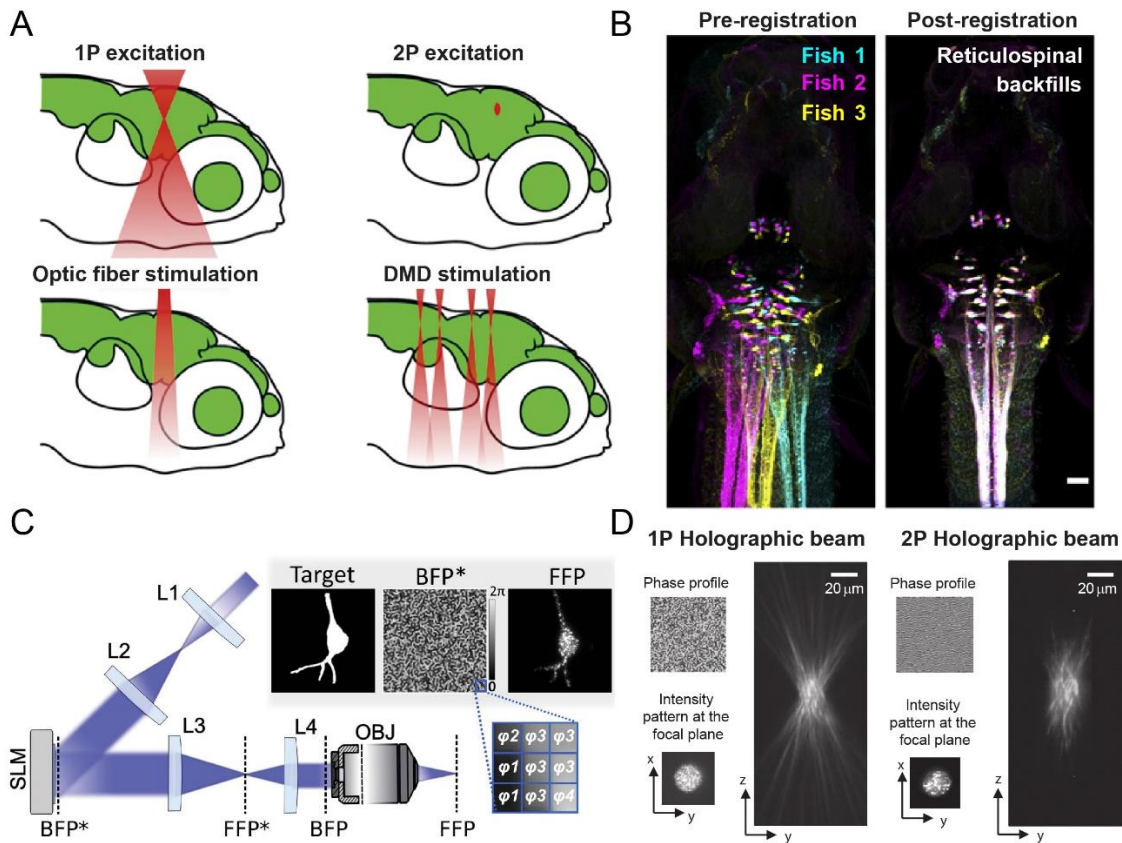
Figure 7: Advanced methods to tackle neuronal circuits. (**A**) Different methods to stimulate the zebrafish brain with light (figure adapted from Baier and Scott, 2009). (**B**) Brain registration used to merge different reticulospinal backfills into one coordinate system (figure adapted from Randlett et al., 2015). (**C**) Computer generated Holography (CGH) obtained via phase modulation by the use of a spatial light modulator (SLM) (Figure adapted from Ronzitti et al., 2017). (**D**) Axial resolution profiles using one-photon or two-photon CGH (figure adapted from Oron et al., 2012).

Brain image registration

A final and important tool used frequently in recent literature is brain image registration (Costa et al., 2016; Marquart et al., 2017; Randlett et al., 2015). Several algorithm have been developed to register one brain to another, such as CMTK (Rohlfing and Maurer, 2003), Elastix (Klein et al., 2010) and ANTs (Avants et al., 2011). These algorithms initially emerged to register medical images such as magnetic resonance imaging (MRI) or computer tomography (CT) scans, and use affine and warp transformations to register one volumetric image to another. Most commonly and for comparability, many distinct brain images are registered to one standard brain, which may be one representative brain image or an average of many different registered brains (Jefferis et al., 2007). After the registration, the transformations (affine and warp) can be applied to any secondary information channels of the brain image. These include expression patterns in a different color (Marquart et al., 2015; Panser et al., 2016), functionally analyzed pixel values (Dunn et al., 2016b; Portugues et al., 2014) or anatomical reconstructions (Figure 7 B), such as single cell tracings (Costa et al., 2016; Jefferis et al., 2007). Together, these registration approaches allow aligning functional and anatomical information across different animals in one common coordinate system.

Aims of my thesis

The advances in scientific technologies and computational power in the last 20 years allow researchers to investigate neuronal circuits on a new level. Novel genetic tools enable expressing cell-type specific proteins to record and manipulate neuronal activity and to reconstruct their morphology. Increased computational power and advanced methods allow not only to handle huge datasets like behavioral or whole brain functional recordings, but also to link them with circuit manipulations and anatomical reconstructions. During my PhD, I worked in different projects on strategies to combine these techniques in order to tie functional information and its anatomical substrate to behavior.

In a first study, I contributed to the generation of a zebrafish BAC transgenic lines resource, which targets genetically identified sets of neurons and provides a tool to refine expression patterns using Cre-recombination. I designed four BAC transgenic lines targeting promotor regions of

genes with tectum specific expression: *pcp4a*, *rorb*, *tmem200a*, *otx1b*, and one BAC-line targeting the gene *cabp7b* expressed specifically in the hindbrain reticular formation. In total, and as a lab effort, 58 BAC constructs were designed, injected and screened, which resulted in 22 stable transgenic lines (*otx1b* being one of them). The BAC lines expressed either Gal4VP16 alone, Gal4VP16 together with a red heart marker (bleeding-heart) or Cre with a blue heart marker (cold-heart). Furthermore, I created the line *elavl3:lyn-tagRFP*, with panneuronal tag-RFP expression. The expression of this line was used for brain registrations of the different expression patterns.

In the second study of this dissertation, I was involved in a project to better link optogenetic control of individual neurons with network functional activity and behavior. I was involved in the analysis of data and created a paGFP transgenic line. Furthermore, I designed a protocol for precise photoactivation and tracing of single neurons in the nucleus of the medial longitudinal fascicle (nMLF) using two-photon excitation. In this publication, we demonstrated an efficient combination of 3D two-photon holographic stimulation and volumetric calcium imaging, using ChR2 (920 nm) and GCaMP6s (1020 nm). Taking advantage of nuclear GCaMP expression, we successfully combined this approach with anatomical tracing of single functionally characterized paGFP labeled neurons. Furthermore, we employed dimensionality reduction and linear regression models to computationally identify the contribution of single nMLF neurons to network activity and behavior.

In the main study of my thesis, I aimed to characterize the role of the tectum in visuomotor transformations using optogenetics, functional imaging and single-cell reconstructions. Initially, using an optogenetic strategy we confirmed that the larval zebrafish tectum is sufficient to drive approach and escape responses. Moreover, we found that the direction of induced approach movements directly depends on the stimulation site in this motor map. As a next step, we wanted to know what downstream neuronal populations are involved in the generation of this behavior. Therefore, we combined optogenetics with whole brain calcium imaging and could show that the induced approach behavior recruits subsets of neurons in the caudal hindbrain. To elucidate how the tectum anatomically connects to these hindbrain premotor areas, we employed the BGUG system to stochastically label single tectal neurons. This allowed me to reconstruct the different wiring patterns of tectal projections, which could be registered to functional recordings. This fusion of anatomical and functional data revealed that looming/dimming and prey-like visual stimuli are differentially encoded in distinct uncrossed projections channels. Moreover, we could demonstrate that a topographical wiring conserves the space code for attractive stimuli in the lateral tectobulbar projection. Finally, we could optogenetically show that this uncrossed tract is

in turn sufficient to induce a graded behavioral outcome to reach a target in retinotopic space. Together, the results of my thesis suggest that sensorimotor decision making is implemented via discrete ipsilateral projection channels and that the lateral tectobulbar tract relays spatial information about a target to caudal hindbrain circuits driving the appropriate behavior.

The following chapters of my cumulative-style dissertation contain the manuscripts for these three studies. The first and second study have been published in Nature Scientific Reports (Genetic targeting and anatomical registration of neuronal populations in the zebrafish brain with a new set of BAC transgenic tools, Förster et al., 2017b) and Neuron (Linking Neurons to Network Function and Behavior by Two-Photon Holographic Optogenetics and Volumetric Imaging, dal Maschio et al., 2017). My main research project has been recently submitted and is currently under review (Topography of a visuomotor transformation, Helmbrecht et al.).

Publications

Paper I: Genetic targeting and anatomical registration of neuronal populations in the zebrafish brain with a new set of BAC transgenic tools

Dominique Förster, Irene Arnold-Ammer, Eva Laurell, Alison J. Barker, António M. Fernandes, Karin Finger-Baier, Alessandro Filosa, **Thomas O. Helmbrecht**, Yvonne Kölsch, Enrico Kühn, Estuardo Robles, Krasimir Slanchev, Tod R. Thiele, Herwig Baier & Fumi Kubo

Author contributions:

D.F., H.B. and F.K. conceived and designed the project. I.A.A. performed BAC recombineering. D.F., A.J.B., A.M.F., A.F., **T.O.H**., Y.K., E.R., T.R.T., H.B., F.K. selected candidate genes and designed BAC recombineering strategies. D.F., I.A.A., E.L., A.J.B., A.M.F., K.F.B., A.F., **T.O.H.**, Y.K., E.K., E.R., K.S., T.R.T., F.K. screened BAC transgenic founders. D.F., E.L. and A.M.F. performed antibody staining and confocal imaging. D.F. performed image registrations. **T.O.H.** generated HuC:lynTagRFP-T transgenic fish. D.F., H.B. and F.K. wrote the manuscript.

SCIENTIFIC REP⚙RTS

OPEN

Genetic targeting and anatomical registration of neuronal populations in the zebrafish brain with a new set of BAC transgenic tools

Dominique Förster [ID][1], Irene Arnold-Ammer[1], Eva Laurell[1], Alison J. Barker[1,2], António M. Fernandes[1], Karin Finger-Baier[1], Alessandro Filosa[1,2], Thomas O. Helmbrecht[1], Yvonne Kölsch[1], Enrico Kühn[1], Estuardo Robles[1,3], Krasimir Slanchev[1], Tod R. Thiele[1,4], Herwig Baier[1] & Fumi Kubo[1]

Genetic access to small, reproducible sets of neurons is key to an understanding of the functional wiring of the brain. Here we report the generation of a new Gal4- and Cre-driver resource for zebrafish neurobiology. Candidate genes, including cell type-specific transcription factors, neurotransmitter-synthesizing enzymes and neuropeptides, were selected according to their expression patterns in small and unique subsets of neurons from diverse brain regions. BAC recombineering, followed by Tol2 transgenesis, was used to generate driver lines that label neuronal populations in patterns that, to a large but variable extent, recapitulate the endogenous gene expression. We used image registration to characterize, compare, and digitally superimpose the labeling patterns from our newly generated transgenic lines. This analysis revealed highly restricted and mutually exclusive tissue distributions, with striking resolution of layered brain regions such as the tectum or the rhombencephalon. We further show that a combination of Gal4 and Cre transgenes allows intersectional expression of a fluorescent reporter in regions where the expression of the two drivers overlaps. Taken together, our study offers new tools for functional studies of specific neural circuits in zebrafish.

Deciphering the circuitry of the brain requires experimental strategies that allow monitoring and manipulating the function of individual neurons within larger, genetically defined populations. To this end, numerous genetically encoded sensors and actuators are available to neurobiologists[1,2], but their utility strongly depends on the precision by which these effectors can be genetically targeted to small subsets of cells. Binary expression systems, like the Gal4/UAS and the Cre/lox system, are to date the most popular tools to target gene expression to defined cell populations, while retaining flexibility of driver and effector combinations[3,4]. Further, engineering a combined Gal4-plus-Cre system in which a UAS-linked reporter is flanked by loxP sites followed by a second transgene on the same construct allows to restrict the expression of that second transgene to cells in which Gal4 and Cre expression patterns overlap. While this intersectional strategy was first implemented in zebrafish by Satou *et al.*[5], a related approach was pioneered for single-cell labeling by Sato *et al.*[6].

Several thousand transgenic zebrafish lines have been generated using short enhancer/promoter sequences from known genes or by unbiased enhancer trap screens[7–12]. As single enhancer sites typically do not regulate the complex spatial and temporal aspects of expression, these lines often do not faithfully recapitulate the expression pattern of the endogenous gene[13,14]. Recent advances in transgenesis techniques have made it possible to more reliably reproduce the endogenous expression of the gene of interest by using the larger gene regulatory

[1]Max Planck Institute of Neurobiology, Department Genes - Circuits - Behavior, Am Klopferspitz 18, D-82152, Martinsried, Germany. [2]Present address: Max-Delbrück Center for Molecular Medicine, Berlin, Germany. [3]Present address: Department of Biological Sciences, Purdue University, West Lafayette, USA. [4]Present address: Department of Biological Sciences, University of Toronto Scarborough, Toronto, Canada. Correspondence and requests for materials should be addressed to H.B. (email: hbaier@neuro.mpg.de) or F.K. (email: fumikubo@neuro.mpg.de)

17

regions (50–300 kb) contained in bacterial artificial chromosomes (BACs). State-of-the-art protocols for efficient application of BAC recombineering and transgenesis in zebrafish have been established[15, 16], paving the way for larger-scale approaches to generate reliable tools for targeted gene expression. Here we report the generation, characterization and comparison of 58 BAC-derived Gal4 and Cre constructs. This screen has led to the production of 22 new transgenic zebrafish lines, each of which allows genetic access to unique neuronal subpopulations.

Results and Discussion

Transgenesis by BAC recombineering yields 22 stable zebrafish lines.   To generate an array of transgenic lines that label diverse subsets of neuronal populations, we selected candidate genes primarily based on their published spatiotemporal expression patterns (Fig. 1a and Table 1). A large fraction of these genes had previously been shown by RNA *in situ* hybridization to be transcribed in small populations of retinal ganglion cells (RGCs) and/or tectal neurons. In addition, we were interested in neurons that share the transmitter GABA or acetylcholine across the brain and therefore included genes that encode for transmitter-synthesizing enzymes. A third category was genes encoding neuropeptides, since these are some of the most specific markers of defined cell types in the central nervous system[17, 18].

For each gene, we chose a BAC clone that contains both upstream and downstream sequences of the translation start site to include transcription regulatory elements on both sides of the coding sequence. BAC recombineering was performed according to the protocol of Bussmann and Schulte-Merker, which is a plasmid-based technique employing an arabinose-inducible homologous recombination[15]. The method was slightly modified by adding a stable fluorescent marker to the construct, which labels cardiac muscle cells for ease of screening and subsequent re-identification. The red-fluorescent marker "bleeding heart" (BH, *cmlc2:mCherry*) was linked to Gal4VP16 constructs, and "cold heart" (CH, *cmlc2:Cerulean*) was linked to Cre (Fig. 1b). In addition, a small subset of Gal4VP16 lines was generated without heart marker.

Recombineered BAC constructs were injected into fertilized eggs obtained from *UAS:Dendra-kras* transgenic fish or from wild-type fish. Potential F0 founders were selected at larval stages for their expression of the transgene and raised to fertility. Specifically, we selected F0 larvae that expressed Dendra (for Gal4VP16 and Gal4VP16-BH), the "bleeding heart" marker (for Gal4VP16-BH) or the "cold heart" marker (for Cre-CH). When the F0 fish had reached adulthood, they were crossed to wild type, *UAS:Dendra* or *UAS:intersec* (see below) and their F1 progeny were screened for inherited transgene expression in the expected pattern. Germline transformation and mosaicism rates were similar to other Tol2 based BAC transgenesis approaches previously reported[5, 15].

Out of 58 BAC constructs that were confirmed to drive expression of Gal4VP16, Gal4VP16-BH, or Cre-CH, we isolated 22 stable transgenic lines. The results are summarized in Tables 1 and 2. The success rate for obtaining stable transgenic lines was 42.9% (3/7 genes), 43.6% (17/39 genes) and 50% (6/12 genes) for Gal4VP16, Gal4VP16-BH and Cre-CH, respectively. For those stable transgenic lines, the percentage of germline transgenic founders out of all adult fish screened ("founder rate") ranged from 1.1% to 25% (average 6.3%). In general, the founder rates of different driver constructs derived from the same BAC (Gal4VP16 only, Gal4VP16-BH and Cre-CH) were found to be similar, with one exception being *grin2ab* (25% and 3.4% for the Gal4-BH and Cre-CH construct, respectively). Consistent with a previous report[15], we did not find a clear correlation between transgenesis efficiency and genomic insert length of the BACs (Fig. 1c).

Gal4VP16 and Cre drivers give access to defined neuronal subsets by largely recapitulating endogenous gene expression.   In accord with the RNA expression patterns of the chosen genes, the established Gal4 transgenic lines label different subsets of neurons in the brain (Fig. 1d and Supplementary Video 1–11). To determine to what extent the BAC-driven Gal4 patterns recapitulate endogenous gene expression, we compared expression of a UAS-linked reporter (*UAS:GFP* or *UAS:GCaMP6s*) to the distribution of the selected genes by antibody staining. The *Tg*(*chat:Gal4*) and *Tg*(*gad1b:Gal4*) lines labeled cells in several brain areas that were positive for choline acetyltransferase (ChAT) and GABA, respectively (Fig. 2a,b). Out of all ChAT- or GABA-positive cells, a little less than half visibly expressed the UAS-linked reporter in each line ($48 \pm 24\%$, n = 105 of 231 cells out of two larvae in *Tg*(*chat:Gal4*), and $42 \pm 15\%$, n = 150 of 355 cells out of four larvae in *Tg*(*gad1b:Gal4*)). In *Tg*(*galn:Gal4*) and *Tg*(*sst3:Gal4*) lines, antibody staining greatly overlapped with, or was identical to, the Gal4-driven reporter expression ($94 \pm 4\%$, n = 88 of 94 cells out of two larvae in *Tg*(*galn:Gal4*) line) (Fig. 2c,d). Differences in protein localizations in *Tg*(*galn:Gal4*) *and Tg*(*sst3:Gal4*) lines can be explained by the transport into axon terminals of the Galn and Sst proteins, both of which encode neuropeptide transmitters[19, 20] versus the cytosolic localization of GFP. It is also possible that some of the signal from the Galn and Sst antibodies is derived from extracellular localization of these secreted factors. These results with four transgenes, for which cross-reactive antibodies are available, suggest that the BAC transgenic Gal4 lines largely reproduce the endogenous gene expression pattern and thus provide genetic access to the labeled neuronal populations. Individual transgenic lines should be tested for recapitulation of endogenous gene expression patterns for each study at hand.

We also confirmed expression of our Cre constructs, either transiently or in stable transgenic lines, using a Cre reporter line named *UAS:intersec* (Fig. 3a). The *UAS:intersec* transgene is designed to drive the expression of the reporter gene in cells in which Gal4 and Cre overlap. This enables intersectional genetic approaches as reported previously[5, 21]. Taken together, the BAC transgenic driver lines established here allow experimental access to small neuronal populations, either in binary (Gal4/UAS) or ternary (Cre/Gal4/*UAS:intersec*) genetic configurations. We noted that Cre recombination is often incomplete in our transgenic animals (Fig. 3b–e), similarly to a previous observation reported for a different Cre transgenic line[22]. Specifically, even though the F0 founder fish produced offspring expressing transgenesis marker Cold Heart, Cre-mediated reporter expression was often incomplete in the Cold Heart-positive offspring. The reasons for the inefficient recombination event could be due to 1) variegated Cre expression at either transcription or translation level, 2) inefficient recombinase activity of expressed Cre protein, 3) variegated expression of the *UAS:intersec* reporter line, or a combination of all three effects.
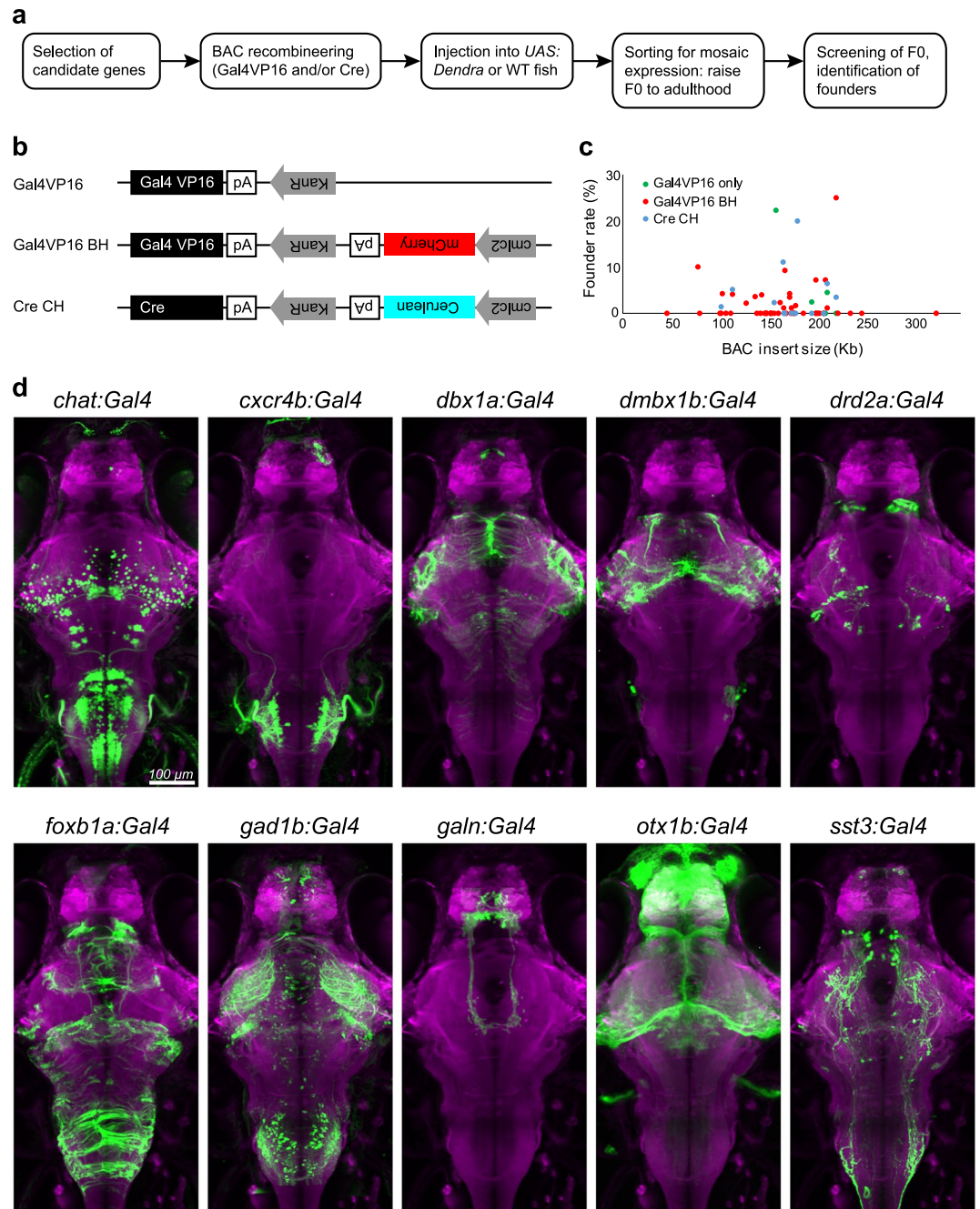
Figure 1. A candidate-based BAC screen identifies new genetic tools for targeting neuronal subpopulations. (**a**) Workflow to establish BAC transgenic fish lines. WT, wild-type. (**b**) Plasmid constructs used for BAC recombineering. *KanR*, kanamycine-resistant gene; *pA*, polyadenylation signal. (**c**) Relationship between the genomic insert length of all BAC constructs (7 *Gal4VP16* BACs, 39 *Gal4VP16-Bleeding Heart* BACs, and 12 *Cre-Cold Heart* BACs) and their founder rate (percentage of germline founders out of total adult fish screened). Note that the founder rate is not correlated with the genomic insert length (R-squared = 0.0007). (**d**) Dorsal view of 6 dpf old larval brains showing the live expression pattern of ten selected transgenic Gal4 lines (green; Dendra-kras, GCaMP6s or EGFP). Brains have been registered via co-expression of *HuC:lynTagRFP-T* (magenta). Scale bar, 100 μm.

Image registration and initial characterization of Gal4 patterns suggest new avenues into functional studies of neural circuits.

In order to determine the three-dimensional labeling pattern of our newly generated Gal4 lines, we scanned optical sections at high resolution with a confocal microscope and performed image registrations across age-matched specimens[23]. By registering expression patterns to a standard reference brain, it is possible to compare the distribution of labeled cells with those present in other lines. This data format can be integrated in a comprehensive brain atlas[21, 24]. We found that the *HuC:lynTagRFP-T* marker is

Gal4VP16 only							
Gene name	**Expression pattern**	**BAC clone #**	**BAC insert size (Kb)**	**# Fish screened**	**# Positive founders**	**Founder rate (%)**	**Allele number**
arl4ca	RGCs	DKEY-16H18	208	22	0	0	
cacnb3b	RGCs	DKEY-180E8	210	32	0	0	
chata	**OT, HB, spinal cord**	**DKEY-194K24**	**212**	**22**	**1**	**4.5**	**mpn202, 204×**
chodl	FB, tegmentum, OT, HB	CH211-209C15	200	22	0	0	
cxcr4b	**RGCs, FB, HB**	**DKEY-260L22**	**196**	**42**	**1**	**2.4**	**mpn206**
dmbx1b	**OT, HB**	**CH211-39M11**	**159**	**9**	**2**	**22.2**	**mpn207**
grin2ab	RGCs	DKEY-90H7	221	34	0	0	
Gal4VP16 Bleeding Heart (clmc2:mCherry)							
Gene name	**Expression pattern**	**BAC clone #**	**BAC insert size (Kb)**	**# Fish screened**	**# Positive founders**	**Founder rate (%)**	**Allele number**
adcyap1a	habenula, HB	CH73-310J3	107	28	0	0	
arl4ca	RGCs	DKEY-16H18	208	12	0	0	
bcl6a	cerebellum, OT, retina	DKEY-253J8	174	8	0	0	
cabp7b	OT, tegmentum, cerebellum	DKEY-87A16	161	108	0	0	
cacnb3b*	**RGCs**	**DKEY-180E8**	**210**	**14**	**1**	**7.1**	
cadm4	retina, FB, MB, HB	DKEY-178J22	204	71	0	0	
cart2*	**FB, HB, tegmentum**	**DKEY-114P5**	**175**	**91**	**1**	**1.1**	
chata*	**OT, HB, spinal cord**	**DKEY-194K24**	**212**	**85**	**1**	**1.2**	
chodl	FB, tegmentum, OT, HB	CH211-209C15	200	56	0	0	
coch	unknown	CH211-29J20	154	13	0	0	
dbx1a	**FB, MB, HB**	**CH211-271F10**	**128**	**45**	**1**	**2.2**	**mpn210**
drd1b	FB, hypothalamus, HB	CH211-148O10	147	63	0	0	
drd2a	FB, HB, OT, spinal cord	DKEY-50H16	325	41	0	0	
drd2a	**FB, HB, OT, spinal cord**	**CH73-335E14**	**103**	**24**	**1**	**4.2**	**mpn211**
foxb1a	**FB, HB, OT**	**CH211-2C17**	**144**	**50**	**2**	**4.0**	**mpn212**
foxb1b	OT, HB	CH211-92B21	177	59	0	0	
gad1b	**FB, HB, OT**	**CH211-24M22**	**168**	**54**	**5**	**9.3**	**mpn155, 200, 201**
gad2*	**FB, hypothalamus, pretectum**	**CH211-37E10**	**167**	**88**	**1**	**1.1**	
galn	**hypothalamus, preoptic area**	**CH211-103A19**	**78**	**10**	**1**	**10.0**	**mpn213**
grin2aa	retina	DKEY-255O2	202	29	0	0	
grin2ab*	**RGCs**	**DKEY-90H7**	**221**	**4**	**1**	**25.0**	
id2b	**retina, OT, HB**	**CH211-175H7**	**137**	**28**	**1**	**3.6**	**mpn215**
lhx2b	**FB, MB, HB, retina**	**CH211-159C13**	**173**	**57**	**2**	**3.5**	**mpn216**
lhx9	**FB, MB, HB**	**DKEY-121A9**	**200**	**56**	**4**	**7.1**	**mpn203, 205**
lrrtm4l2	MHB, HB, retina	CH73-359G19	102	45	0	0	
nos1	MB, spinal cord	CH73-385P12	112	34	0	0	
opn4b	retina, FB	DKEY-156P15	223	58	0	0	
otx1b	**FB, MB, OT**	**DKEY-209N21**	**173**	**48**	**2**	**4.2**	**mpn217**
pcp4a	FB, HB	CH211-231M12	149	57	0	0	
penka	FB, MB, HB, spinal cord	CH211-189N20	149	28	0	0	
rorb	retina, MB	DKEY-196E24	80	12	0	0	
sdk2b	unknown	DKEY-172F4	169	10	0	0	
slc6a4a	pretectum, raphe	DKEY-263M15	157	8	0	0	
slit1a	**retina, OT, HB**	**DKEY-118N13**	**114**	**74**	**3**	**4.1**	**mpn218**
sp5l	OT	DKEY-156F14	187	19	0	0	
sst3	**FB, MB**	**DKEY-265F18**	**163**	**44**	**1**	**2.3**	**mpn219**
tac1	FB, HB	CH211-51C11	143	28	0	0	
tbx20	**RGCs, tegmentum, HB**	**CH211-132C11**	**179**	**117**	**2**	**1.7**	**mpn220**
tmem200a	FB, OT, MB, RGCs	DKEY-252D12	139	20	0	0	

Table 1. List of Gal4VP16 and Gal4VP16-Bleeding Heart constructs and transgenic lines. Seven Gal4VP16 and 39 Gal4VP16-Bleeding Heart BAC constructs that were generated and validated to express Gal4VP16 after transient injection. Founder rate is defined as a percentage of germline founders out of total adult fish screened. Bold texts indicate the constructs from which Gal4VP16-expressing transgenic line(s) were isolated. FB, forebrain; MB, midbrain; HB, hindbrain; RGCs, retinal ganglion cells; OT, optic tectum; *lines discontinued; ×second line identified in an additional round of screening.

| Cre Cold Heart (clmc2:Cerulean)							
Gene name	Expression pattern	BAC clone #	BAC insert size (Kb)	# Fish screened	# Positive founders	Founder rate (%)	Allele number
arl4ca	RGCs	DKEY-16H18	208	75	0	0	
atoh7	**RGCs**	**DKEY-111E19**	**181**	**10**	**2**	**20.0**	**mpn221**
cart2	FB, HB, tegmentum	DKEY-114P5	175	12	0	0	
chata*	**OT, HB, spinal cord**	**DKEY-194K24**	**212**	**62**	**4**	**6.5**	
cxcr4b	RGCs, FB, HB	DKEY-260L22	196	80	0	0	
gad1b	FB, HB, OT	CH211-24M22	168	2	0	0	
gad2	FB, hypothalamus, pretectum	CH211-37E10	167	34	0	0	
grin2ab*	**RGCs**	**DKEY-90H7**	**221**	**58**	**2**	**3.4**	
isl2b*	**RGCs, cranial ganglia**	**DKEY-73M9**	**157**	**88**	**2**	**2.3**	
otx1b	FB, MB, OT	DKEY-209N21	173	N/A	N/A	N/A	
slit1a	**retina, OT, HB**	**DKEY-118N13**	**114**	**58**	**3**	**5.2**	**mpn222**
tbx20	RGCs, tegmentum, HB	CH211-132C11	179	4	0	0	
th	**FB, hypothalamus, HB**	**CH211-77O7**	**166**	**36**	**4**	**11.1**	**mpn223**

Table 2. List of *Cre-Cold Heart* constructs and transgenic lines. 12 *Cre-Cold Heart* BAC constructs have been generated and validated to express Cre after transient injection. Expression pattern is derived from previously reported expression data. Founder rate is defined as a percentage of germline founders out of total adult fish screened. Bold texts indicate the constructs from which CH-positive transgenic line(s) were isolated. FB, forebrain; MB, midbrain; HB, hindbrain; RGCs, retinal ganglion cells; OT, optic tectum; *lines discontinued. N/A, line has not been screened for founders. *otx1b:Cre* BAC was generated without the Cold Heart cassette.

excellently suited as a bridging template for across-line image registrations. This membrane-targeted red fluorescent reporter is expressed in almost all neurons and strongly labels the cell membrane-enriched neuropil areas, whose outlines in the fish brain are highly stereotyped. After crossing Gal4 carriers of selected lines, driving the expression of green-fluorescent UAS-linked reporters (*UAS:Dendra*, *UAS:GFP*, or *UAS:GCaMP6s*), to carriers of the *HuC:lynTagRFP-T* transgene, triple-transgenic larvae were identified and whole-brain images of red and green channels were obtained. These images were aligned with each other using the *HuC:lynTagRFP-T* pattern as a template, and the green reporter channels were superimposed using different colors to visualize the spatial relationships of the respective patterns (Fig. 4a and Supplementary Video 12).

This analysis demonstrates the utility of our new lines for functional investigations into neural circuitry. Three immediate applications come to mind. First, telencephalic inhibitory connections have to our knowledge not been studied in teleosts. Our new *gad1b:Gal4* line will be particularly useful for functional studies of GABAergic cells in the subpallium, where the labeling seems particularly strong (Fig. 4b). Second, while the zebrafish olfactory bulb has been extensively investigated, recently culminating in the complete electron-microscopic reconstruction of its synaptic connectome[25], considerably less is known about extrinsic modulation of olfactory processing. The new *chat:Gal4* line may give an entry point into this question, as it reveals the ventral pallial cholinergic innervation of the olfactory bulb (Fig. 4b). Lastly, neuropeptides have been shown to present highly specific markers of neurosecretory populations in preoptic and hypothalamic areas[17, 18]. Our new *sst3:Gal4* and *galn:Gal4* lines will allow recording and manipulation of these poorly understood modulatory systems.

Image registration reveals new aspects of the layered architecture of the larval brain. Our initial characterization also revealed interesting architectonic principles that invite future investigations. We identified Gal4 lines with clustered, but mutually exclusive expression in the rhombencephalon (Fig. 4c). Specifically, *chat:Gal4*, *gad1b:Gal4* and *cxcr4b:Gal4* exhibited non-overlapping expression in rostral to caudal stripes in horizontal sections (Fig. 4d,e), and dorsomedial to ventrolateral stripes in transverse sections, respectively (Fig. 4f). This observation is consistent with the previously reported striped organization of neurotransmitter and transcription factor expression in the hindbrain[26]. Our analysis now shows that this developmental patterning not only holds true for glutamatergic, GABAergic, and glycinergic groups of neurons, as reported by Kinkhabwala *et al.*[26], but also for cholinergic neurons. A multi-label image registration approach, such as the one used here, is uniquely suited to uncover principles of mesoscale spatial organization.

The tectum is an intensively studied, multisensory processing area in the vertebrate midbrain[27]. Its densely packed neuropil is subdivided into layers, originally defined by the stratification pattern of incoming RGC axons[28–30]. RGC axons project to the following layers (from superficial to deep): Stratum opticum (SO); stratum fibrosum et griseum superficiale (SFGS, with its six sublayers, SFGS1 through SFGS6); the retinorecipient stratum griseum centrale (SGC); and the boundary between stratum album centrale and stratum periventriculare (SAC/SPV). From among our collection of BAC lines, several showed expression in the tectal neuropil (Fig. 5a). Co-registration of the patterns of our newly generated lines with that of an RGC-specific Gal4 line (*isl2b:Gal4*)[31] allowed us to further explore the laminar architecture of the tectum beyond RGCs (Fig. 5a,b). A densitometric analysis revealed that *cxcr4b:Gal4* consistently but sparsely labeled SFGS3, SFGS4 and SAC/SPV (Fig. 5c). While the labeling of SFGS arises from *cxcr4b* + RGC axons, arborizations in the SAC/SPV layer originate from processes of deep midbrain
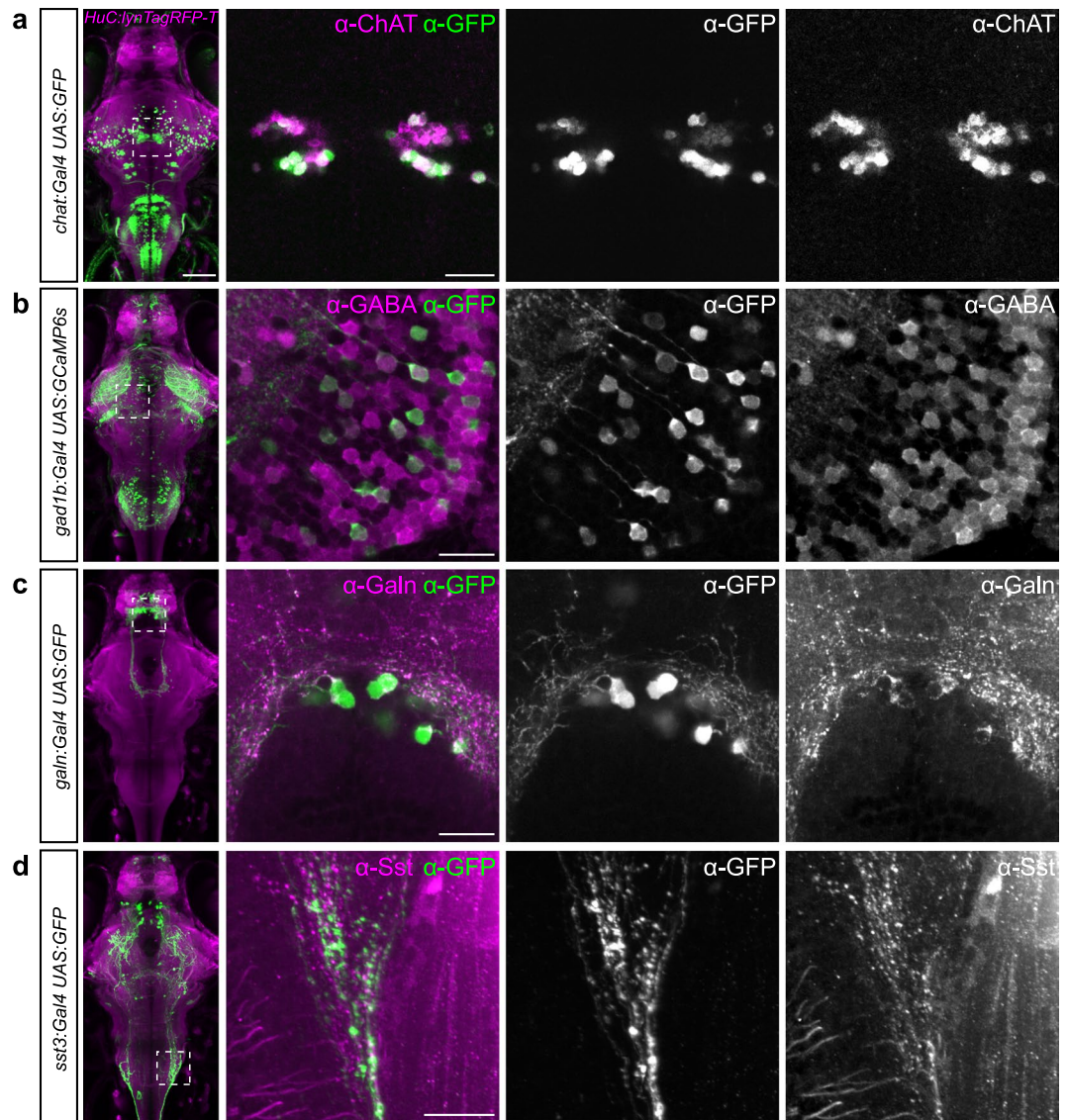
Figure 2. New transgenic lines largely recapitulate endogenous gene expression. (**a–d**) Antibody stainings of 6 dpf old larvae against GFP (green) and ChAT (**a**), GABA (**b**), Galanin (**c**) or Somatostatin (**d**), respectively (magenta). Genotypes are indicated on the left. Whole-brain images on the left show live expression pattern (lynTagRFP-T in magenta), outlining the location of the magnified regions on the right. Scale bar, 100 μm for overview, 20 μm for magnified images.

neurons (data not shown). Neuropil labelings in *chat:Gal4*, *dmbx1b:Gal4* and *gad1b:Gal4* do not derive from RGC axons, but from neurites of specific classes of periventricular tectal neurons and incoming axons from various other brain areas (Fig. 5d–f). The *chat:Gal4* pattern showed highest fluorescence intensities in the deep stratum griseum centrale (SGC) (Fig. 5d). Fluorescence signals in *gad1b:Gal4*, on the other hand, are strongest in the superficial layers (Fig. 5e), including superficial interneuron (SIN) cell bodies, which are GABAergic[32]. Neurites labeled by *dmbx1b:Gal4* arborize in SFGS and SGC sublayers that are superficial to the retinorecipient SGC (Fig. 5f). As a rule, neuropil stratifications in these three lines are not restricted to single layers, but differences in labeling intensities rather reflect graded preferences for layer positioning. In summary, we isolated an array of transgenic lines, which allow targeting of different components of the layer-specific circuitry in the zebrafish tectum.

Conclusions and outlook. Progress in the neurobiology of the zebrafish preparation has recently accelerated, driven by advances in imaging technology, behavioral analysis and computational methods[25, 33–39]. Optogenetics affords the ability to manipulate circuit components in the behaving animal[40–42]. We expect that our new set of BAC transgenic Gal4 and Cre lines will facilitate research that employs imaging or optogenetics in the zebrafish system and thus provide a valuable resource for the neuroscience community. In the future, breakthroughs are expected from the refinement of genetic tools that allow addressing specific subpopulations of neurons in the context of intact circuitry. Knock-in technology using CRISPR/Cas9 represents a promising approach to target endogenous loci with superior fidelity[43–46] and may in the future be scaled up for the systematic generation of transgenic lines.
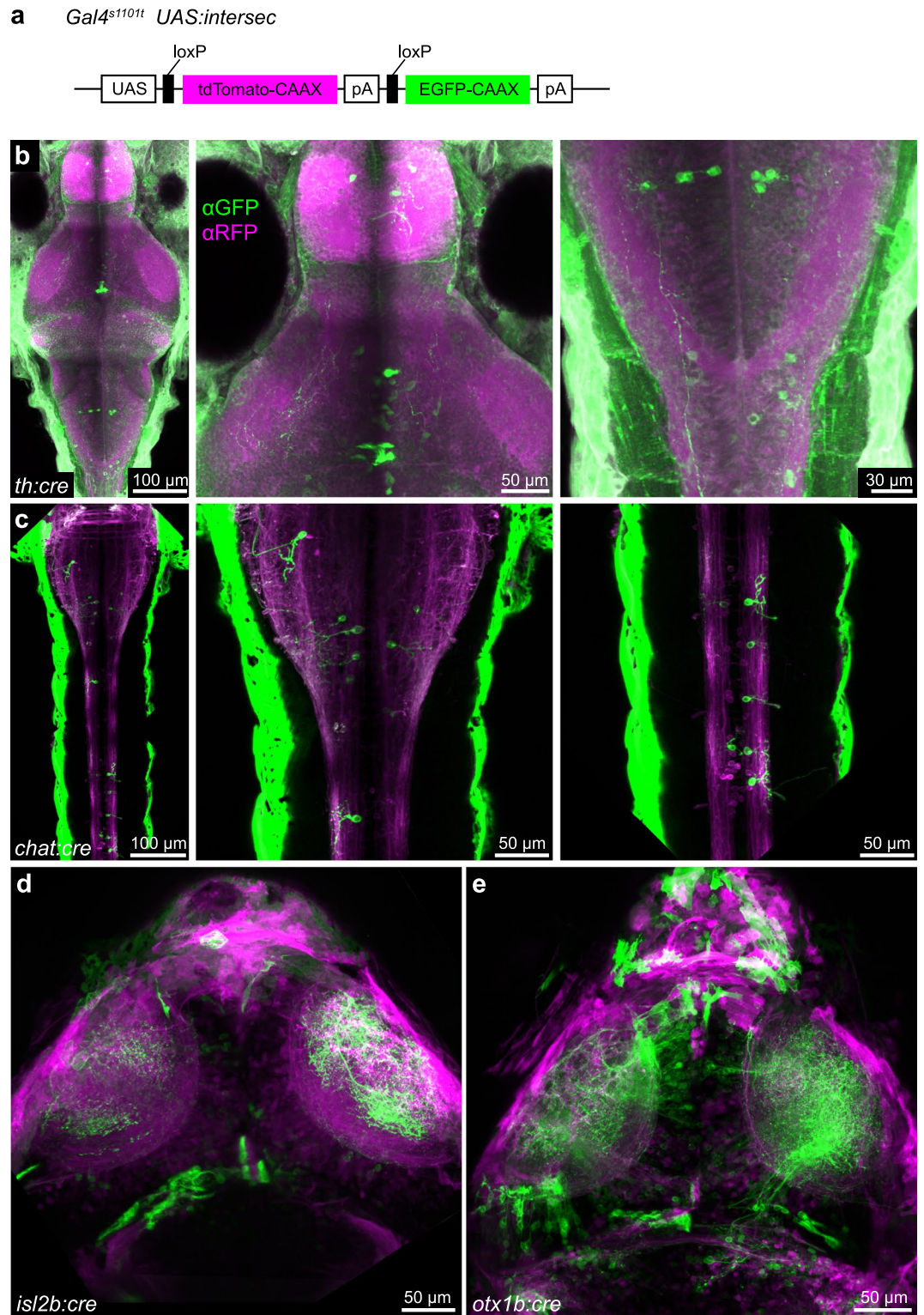
Figure 3. Cre-expressing BAC constructs allow intersectional genetics. (**a**) *UAS:intersec* construct for intersectional genetic approach. A pan-neuronal Gal4 line (*Gal4s1101t*) was used in this figure. (**b**) Antibody staining against GFP and RFP reveals highly variegated, transgenic expression of *th:cre* stable transgenic line. (**c–e**) Live imaging showing transient expression of *chat:cre* (**c**), *isl2b:cre* (**d**) and *otx1b:cre* (**e**).

Methods

Animal care and transgenic lines.   All animal procedures conformed to the institutional guidelines of the Max Planck Society and the local government (Regierung von Oberbayern). Experimental protocols were approved by Regierung von Oberbayern (55.2-1-54-2532-101-12 and 55.2-1-54-2532-31-2016). The
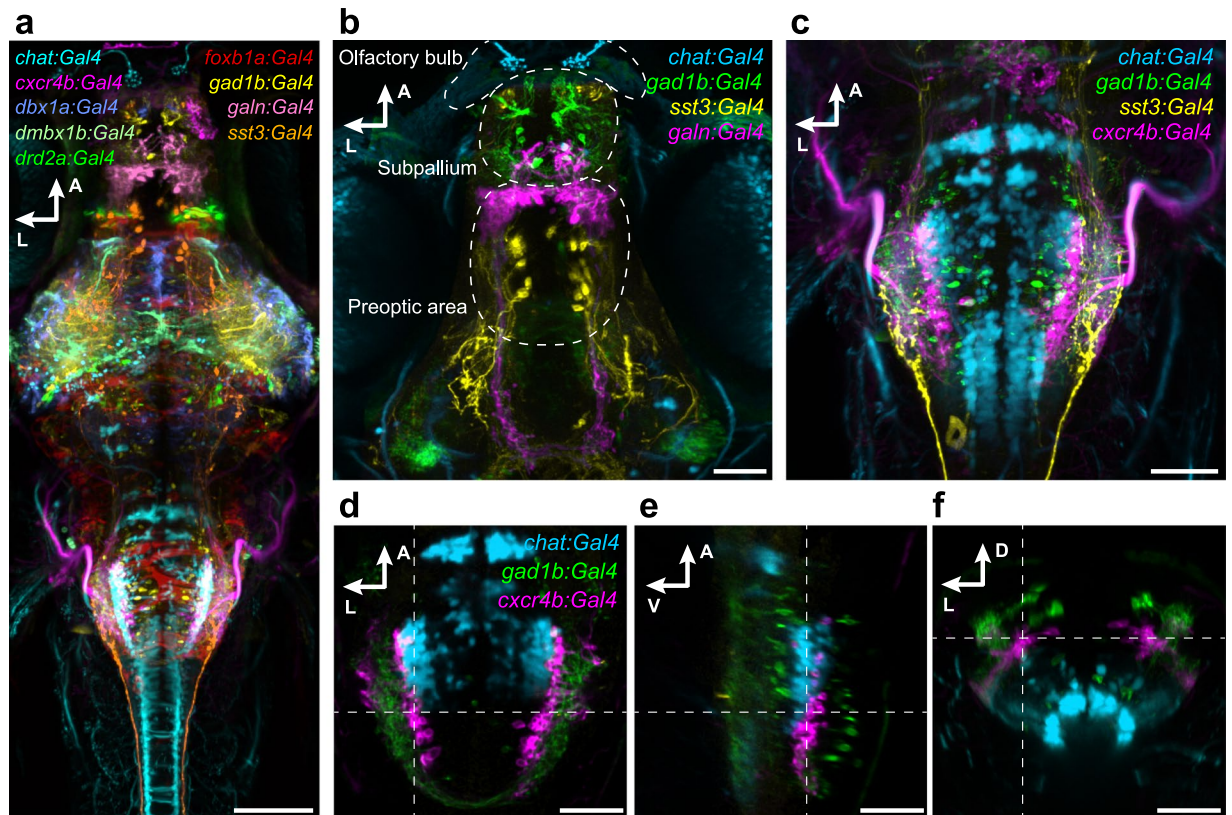
Figure 4. Registration of transgenic lines illustrates expression in distinct neuronal subpopulations. (**a**) Dorsal view on a reference brain showing the expression of selected, co-registered Gal4 lines. (**b,c**) Z-projection of confocal stacks showing the expression pattern of *chat:Gal4, gad1b:Gal4, sst3:Gal4 and galn:Gal4 or cxcr4b:Gal4*, respectively, in the deep fore-/midbrain (**b**), and in the hindbrain (**c**). (**d–f**) Single confocal slices of *chat:Gal4, gad1b:Gal4*, and *cxcr4b:Gal4* expression in the hindbrain, in dorsal (**d**), lateral (**e**) and cross-sectional view (**f**). Dashed lines indicate plane positions. Scale bar, 100 μm in (**a**) and 50 μm in (**b–f**).

previously described transgenic lines used in this study are as follows: *Tg(UAS:Dendra-kras)s1998t*; *Et(E1b:Gal4-VP16)s1101t*; *Tg(isl2b.3:Gal4-VP16)zc65*; *Tg(UAS:GCaMP6s)mpn101*; *Tg(5xUAS:EGFP)zf82*. These and all of the newly generated transgenic lines are available upon request.

Plasmids. To generate pCR8GW-Gal4VP16-FRT-Kan-FRT-Bleeding Heart and pCR8GW-Cre-FRT-Kan-FRT-Cold Heart plasmids, the Bleeding Heart (cmlc2:mCherry, also known as myl7:m-Cherry) and Cold Heart (cmlc2:Cerulean, also known as myl7:Cerulean) cassettes (obtained from Michael Nonet, Washington University, USA) were inserted into pCR8GW-Gal4VP16-FRT-Kan-FRT and pCR8GW-Cre-FRT-Kan-FRT[16], in the reverse orientation relative to Gal4VP16 or Cre coding sequence. To generate the Tol2 HuC:lynTagRFP-T plasmid, lynTagRFP-T (TagRFP-T tagged with lyn kinase membrane targeting sequence)[47] was PCR amplified and cloned downstream of the HuC promoter. For the intersectional reporter, the loxP-tdTomato-CAAX-loxP-EGFP-CAAX cassette was codon optimized and synthesized by Genscript (Piscataway, NJ), and subsequently cloned into a pTol2-14xUAS vector to obtain UAS:loxP-tdTomato_CAAX-loxP-EGFP_CAAX.

Selection of candidate genes and obtaining BAC clones. To identify corresponding BAC clones, we searched, using the Ensembl genome browser (www.ensembl.org/) or the UCSC genome browser (Zv6 assembly, https://genome.ucsc.edu/), for BAC clones that encompass both upstream and downstream of the first ATG site of the target gene. BAC clones were purchased from Source BioScience (www.lifesciences.sourcebioscience.com/) and BACPAC resources center, Children's Hospital Oakland (https://bacpacresources.org/).

BAC recombineering. BAC recombineering was performed as described previously[15, 16]. Briefly, in the first step, BAC clones were transformed with the *pRedET* plasmid (Gene Bridges), which enables the arabinose-inducible homologous recombination. In the second step, *Tol2* arms in opposing directions flanking an ampicillin resistance cassette were PCR amplified from *piTol2_amp* plasmid[16] and inserted into the BAC backbone. In the third and final step, either *Gal4VP16* only, *Gal4VP16-BH* or *Cre-CH* cassettes were PCR amplified and inserted into the BAC, such that the start-ATG site of the gene of interest was replaced by that of *Gal4VP16* or *Cre*. For *th:Cre-CH* line, the GFP coding sequence of the *th:GFP* BAC[48] was replaced with the
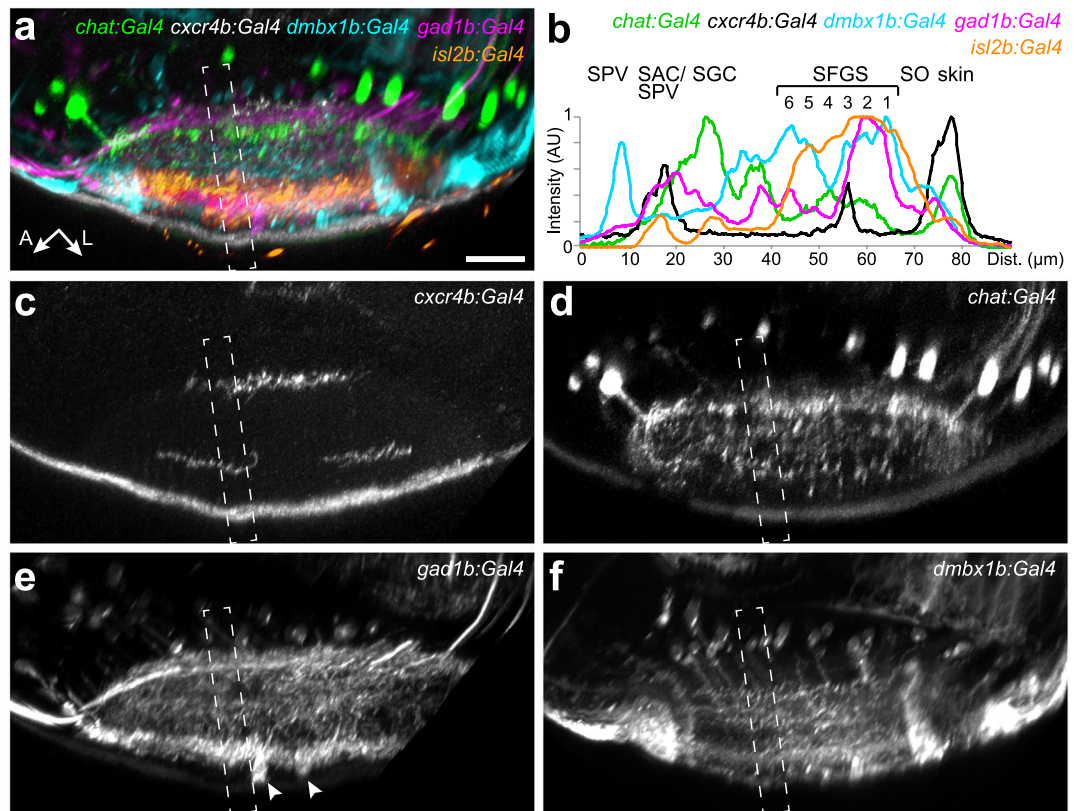
Figure 5. New transgenic lines label distinct sublaminae in the tectal neuropil. Lateral view of the tectal neuropil shows registered expression pattern of *chat:Gal4*, *cxcr4b:Gal4*, *dmbx1b:Gal4*, *gad1b:Gal4*, and *isl2b:Gal4*, as merged (**a**) or single channels (**c–f**). (**b**) Fluorescence intensity plots along the boxed regions in (**a–f**). Intensity peaks of *isl2b:Gal4* expression were used for layer determination. SIN cell bodies labeled by *gad1b:Gal4* are marked by arrowheads in (**e**). The peak for *dmbx1b:Gal4* in the SPV layer reflects labeled periventricular cell bodies.

Cre-CH cassette. After we confirmed successful insertions of the cassette by PCR, the final BAC DNA was purified using NucleoBond XTra BAC kit (Machery Nagel), and correct insertions were verified by sequencing.

Transgenesis. *Tg*(*HuC:lynTagRFP-T*)*mpn404*[49] and *Tg*(*UAS:intersec*)*mpn128* were created using the standard *Tol2* transposon system. BAC DNAs were injected at 100 ng/μl together with zebrafish codon–optimized *Tol2* transposase mRNA (50–100 ng/μl), synthesized from pCS-zT2TP plasmid[16]. *Gal4VP16* and *Gal4VP16-BH* BAC DNAs were injected into *Tg*(*UAS:Dendra-kras*)*s1998t* transgenic embryos. *Cre-CH* BAC DNAs were injected into wild-type TL embryos. After injection, embryos expressing Dendra, Bleeding Heart, or Cold Heart were screened and raised to sexual maturity. Injected fish were either incrossed or outcrossed with wild-type or *Tg*(*UAS:Dendra-kras*)*s1998t* transgenic adult fish to identify transgenic carriers. The germline mosaicism rate was defined as a percentage of transgenic offspring (F1) out of all offspring born from F0 founder fish. Outcrossing of F1 transgenic lines (and of following generations) revealed segregation of Gal4 expression at Mendelian ratios, suggesting that they carry a single insertion. In cases where multiple founders were identified, the founders which showed the most complete expression patterns in their F1 offspring were selected and maintained. We noted that the transgene expression of different larvae derived from the same transgenic founders was variable in some of our BAC transgenic lines, as is known for the Gal4/UAS system in general[50, 51]. Nevertheless, among larvae that were pre-screened for the high-level expression of the transgene, the expression patterns were largely consistent across different larvae (Supplementary Figure S1).

Immunohistochemistry. Immunostaining was performed according to ref. 24, with slight modifications. Fish were fixed in 4% paraformaldehyde (PFA) in PBS overnight. For the initial antigen retrieval, fish were heated to 63 °C for 15 minutes in 150 mM Tris-HCl. The time for staining with primary antibody was increased to at least 5 days and with secondary antibody to at least 2 days. Secondary antibodies were diluted in only PBT. After staining, samples were washed with PBT and postfixed for 30 minutes in 4% PFA, thereafter briefly washed in PBT and then soaked in 85% glycerol. ChAT antibody staining was performed according to ref. 52, with the proteinase K treatment prolonged to 120 min for 6 dpf larvae. For a list of antibodies used, see Supplementary Table S1.

Image acquisition. For live imaging, 6–7 dpf larvae were anesthetized in 0.016% tricaine and embedded in 2% low-melting-point agarose. Imaging was performed on a Zeiss LSM-780 or LSM-700 confocal microscope,

using 20×/1.0 NA water-dipping objectives. For imaging fixed samples, larvae were embedded in 85% glycerol, and imaging was performed using a 25×/0.8 NA multi-immersion objective. Whole-brain images were acquired by tiling the brain into three individual image stacks and subsequent stitching, using ZEN software (black edition, v8.0; Zeiss). Images were corrected for fluorescence attenuation in the z-dimension using the brightness correction function in the ZEN software.

Image registration. Registration was performed using the Computational Morphometry Toolkit (CMTK)[53]. Whole-brain images of living 6 dpf old zebrafish larvae were co-registered into one reference brain using expression of *HuC:lynTagRFP-T* as a template. For visualization of RGC innervation strata in the tectum, fish expressing *isl2b:Gal4 UAS:GCaMP6s* and *HuC:lynTagRFP-T* were co-registered into the reference brain.

References

1. Yizhar, O., Fenno, L. E., Davidson, T. J., Mogri, M. & Deisseroth, K. Optogenetics in neural systems. *Neuron* **71**, 9–34 (2011).
2. Looger, L. L. & Griesbeck, O. Genetically encoded neural activity indicators. *Curr. Opin. Neurobiol.* **22**, 18–23 (2012).
3. Brand, A. H. & Perrimon, N. Targeted gene expression as a means of altering cell fates and generating dominant phenotypes. *Development* **118**, 401–415 (1993).
4. Tsien, J. Z. *et al.* Subregion- and Cell Type–Restricted Gene Knockout in Mouse Brain. *CELL* **87**, 1317–1326 (1996).
5. Satou, C. *et al.* Transgenic tools to characterize neuronal properties of discrete populations of zebrafish neurons. *Development* **140**, 3927–3931 (2013).
6. Sato, T., Hamaoka, T., Aizawa, H., Hosoya, T. & Okamoto, H. Genetic Single-Cell Mosaic Analysis Implicates ephrinB2 Reverse Signaling in Projections from the Posterior Tectum to the Hindbrain in Zebrafish. *Journal of Neuroscience* **27**, 5271–5279 (2007).
7. Bergeron, S. A. *et al.* Brain selective transgene expression in zebrafish using an NRSE derived motif. *Front. Neural Circuits* **6**, 110 (2012).
8. Asakawa, K. *et al.* Genetic dissection of neural circuits by Tol2 transposon-mediated Gal4 gene and enhancer trapping in zebrafish. *Proceedings of the National Academy of Sciences* **105**, 1255–1260 (2008).
9. Scott, E. K. *et al.* Targeting neural circuitry in zebrafish using GAL4 enhancer trapping. *Nat Meth* **4**, 323–326 (2007).
10. Otsuna, H. *et al.* High-resolution analysis of central nervous system expression patterns in zebrafish Gal4 enhancer-trap lines. *Dev Dyn* **244**, 785–796 (2015).
11. Scott, E. K. & Baier, H. The cellular architecture of the larval zebrafish tectum, as revealed by gal4 enhancer trap lines. *Front. Neural Circuits* **3**, 13 (2009).
12. Halpern, M. E. *et al.* Gal4/UAS transgenic tools and their application to zebrafish. *Zebrafish* **5**, 97–110 (2008).
13. Levine, M. & Tjian, R. Transcription regulation and animal diversity. *Nature* **424**, 147–151 (2003).
14. Goto, T., Macdonald, P. & Maniatis, T. Early and late periodic patterns of even skipped expression are controlled by distinct regulatory elements that respond to different spatial cues. *CELL* **57**, 413–422 (1989).
15. Bussmann, J. & Schulte-Merker, S. Rapid BAC selection for tol2-mediated transgenesis in zebrafish. *Development* **138**, 4327–4332 (2011).
16. Suster, M. L., Abe, G., Schouw, A. & Kawakami, K. Transposon-mediated BAC transgenesis in zebrafish. *Nat Protoc* **6**, 1998–2021 (2011).
17. Herget, U. & Ryu, S. Coexpression analysis of nine neuropeptides in the neurosecretory preoptic area of larval zebrafish. *Front. Neuroanat* **9**, 5027 (2015).
18. Prober, D. A., Rihel, J., Onah, A. A., Sung, R. J. & Schier, A. F. Hypocretin/Orexin Overexpression Induces An Insomnia-Like Phenotype in Zebrafish. *Journal of Neuroscience* **26**, 13400–13410 (2006).
19. Podlasz, P. *et al.* Galanin gene expression and effects of its knock-down on the development of the nervous system in larval zebrafish. *Journal of Comparative Neurology* **520**, 3846–3862 (2012).
20. Devos, N. *et al.* Differential expression of two somatostatin genes during zebrafish embryonic development. *Mech Dev* **115**, 133–137 (2002).
21. Marquart, G. D. *et al.* A 3D Searchable Database of Transgenic Zebrafish Gal4 and Cre Lines for Functional Neuroanatomy Studies. *Front. Neural Circuits* **9**, 78 (2015).
22. Boniface, E. J., Lu, J., Victoroff, T., Zhu, M. & Chen, W. FlEx-based transgenic reporter lines for visualization of Cre and Flp activity in live zebrafish. *Genesis* **47**, 484–491 (2009).
23. Rohlfing, T. & Maurer, C. R. Nonrigid image registration in shared-memory multiprocessor environments with application to brains, breasts, and bees. *IEEE Trans Inf Technol Biomed* **7**, 16–25 (2003).
24. Randlett, O. *et al.* Whole-brain activity mapping onto a zebrafish brain atlas. *Nat Meth* **12**, 1039–1046 (2015).
25. Wanner, A. A., Genoud, C., Masudi, T., Siksou, L. & Friedrich, R. W. Dense EM-based reconstruction of the interglomerular projectome in the zebrafish olfactory bulb. *Nat Meth* **19**, 816–825 (2016).
26. Kinkhabwala, A. *et al.* A structural and functional ground plan for neurons in the hindbrain of zebrafish. *Proc Natl Acad Sci USA* **108**, 1164–1169 (2011).
27. Nevin, L. M., Robles, E., Baier, H. & Scott, E. K. Focusing on optic tectum circuitry through the lens of genetics. *BMC Biol.* **8**, 126 (2010).
28. Meek, J. Functional anatomy of the tectum mesencephali of the goldfish. An explorative analysis of the functional implications of the laminar structural organization of the tectum. *Brain Research Reviews* **6**, 247–297 (1983).
29. Xiao, T., Roeser, T., Staub, W. & Baier, H. A GFP-based genetic screen reveals mutations that disrupt the architecture of the zebrafish retinotectal projection. *Development* **132**, 2955–2967 (2005).
30. Robles, E., Smith, S. J. & Baier, H. Characterization of genetically targeted neuron types in the zebrafish optic tectum. *Front. Neural Circuits* **5**, 1 (2011).
31. Fujimoto, E., Gaynes, B., Brimley, C. J., Chien, C.-B. & Bonkowsky, J. L. Gal80 intersectional regulation of cell-type specific expression in vertebrates. *Dev Dyn* **240**, 2324–2334 (2011).
32. Del Bene, F. *et al.* Filtering of visual information in the tectum by an identified neural circuit. *Science* **330**, 669–673 (2010).
33. Ahrens, M. B. *et al.* Brain-wide neuronal dynamics during motor adaptation in zebrafish. *Nature* **485**, 471–477 (2012).
34. Kubo, F. *et al.* Functional Architecture of an Optic Flow-Responsive Area that Drives Horizontal Eye Movements in Zebrafish. *Neuron* **81**, 1344–1359 (2014).
35. Miri, A. *et al.* Spatial gradients and multidimensional dynamics in a neural integrator circuit. *Nat Neurosci* **14**, 1150–1159 (2011).
36. Baier, H. & Scott, E. K. Genetic and optical targeting of neural circuits and behavior–zebrafish in the spotlight. *Curr. Opin. Neurobiol.* **19**, 553–560 (2009).
37. Portugues, R., Feierstein, C. E., Engert, F. & Orger, M. B. Whole-brain activity maps reveal stereotyped, distributed networks for visuomotor behavior. *Neuron* **81**, 1328–1343 (2014).
38. Thiele, T. R., Donovan, J. C. & Baier, H. Descending control of swim posture by a midbrain nucleus in zebrafish. *Neuron* **83**, 679–691 (2014).
39. Orger, M. B. The Cellular Organization of Zebrafish Visuomotor Circuits. *Curr. Biol.* **26**, R377–85 (2016).

40. Arrenberg, A. B., Del Bene, F. & Baier, H. Optical control of zebrafish behavior with halorhodopsin. *Proceedings of the National Academy of Sciences* **106**, 17968–17973 (2009).

41. Wyart, C. *et al.* Optogenetic dissection of a behavioural module in the vertebrate spinal cord. *Nature* **461**, 407–410 (2009).

42. Douglass, A. D., Kraves, S., Deisseroth, K., Schier, A. F. & Engert, F. Escape Behavior Elicited by Single, Channelrhodopsin-2-Evoked Spikes in Zebrafish Somatosensory Neurons. *Current Biology* **18**, 1133–1137 (2008).

43. Auer, T. O., Duroure, K., De Cian, A., Concordet, J.-P. & Del Bene, F. Highly efficient CRISPR/Cas9-mediated knock-in in zebrafish by homology-independent DNA repair. *Genome Research* **24**, 142–153 (2014).

44. Hisano, Y. *et al.* Precise in-frame integration of exogenous DNA mediated by CRISPR/Cas9 system in zebrafish. *Sci Rep* **5**, 8841 (2015).

45. Kimura, Y., Hisano, Y., Kawahara, A. & Higashijima, S.-I. Efficient generation of knock-in transgenic zebrafish carrying reporter/driver genes by CRISPR/Cas9-mediated genome engineering. *Sci Rep* **4**, 6545 (2014).

46. Ota, S. *et al.* Functional visualization and disruption of targeted genes using CRISPR/Cas9-mediated eGFP reporter integration in zebrafish. *Sci Rep* **6**, 34991 (2016).

47. Yokogawa, T., Hannan, M. C. & Burgess, H. A. The Dorsal Raphe Modulates Sensory Responsiveness during Arousal in Zebrafish. *Journal of Neuroscience* **32**, 15205–15215 (2012).

48. Tay, T. L., Ronneberger, O., Ryu, S., Nitschke, R. & Driever, W. Comprehensive catecholaminergic projectome analysis reveals single-neuron integration of zebrafish ascending and descending dopaminergic systems. *Nat Comms* **2**, 171 (2011).

49. Dal Maschio, M., Donovan, J. C., Helmbrecht, T. O. & Baier, H. Linking Neurons to Network Function and Behavior by Two-Photon Holographic Optogenetics and Volumetric Imaging. *Neuron* **94**(4), 774–789.e5 (2017).

50. Goll, M. G., Anderson, R., Stainier, D. Y. R., Spradling, A. C. & Halpern, M. E. Transcriptional silencing and reactivation in transgenic zebrafish. *Genetics* **182**, 747–755 (2009).

51. Akitake, C. M., Macurak, M., Halpern, M. E. & Goll, M. G. Transgenerational analysis of transcriptional silencing in zebrafish. *Dev Biol* **352**, 191–201 (2011).

52. Rath, M., Nitschke, R., Filippi, A., Ronneberger, O. & Driever, W. Generation of high quality multi-view confocal 3D datasets of zebrafish larval brains suitable for analysis using Virtual Brain Explorer (ViBE-Z) software. Protocol Exchange https://www.nature.com/protocolexchange/protocols/2408#/procedure (2012).

53. Ostrovsky, A., Cachero, S. & Jefferis, G. Clonal analysis of olfaction in Drosophila: image registration. *Cold Spring Harbor Protocols* **2013**, 347–349 (2013).

Acknowledgements

Author Contributions

D.F., H.B. and F.K. conceived and designed the project. I.A.A. performed BAC recombineering. D.F., A.J.B., A.M.F., A.F., T.O.H., Y.K., E.R., T.R.T., H.B., F.K. selected candidate genes and designed BAC recombineering strategies. D.F., I.A.A., E.L., A.J.B., A.M.F., K.F.B., A.F., T.O.H., Y.K., E.K., E.R., K.S., T.R.T., F.K. screened BAC transgenic founders. D.F., E.L. and A.M.F. performed antibody staining and confocal imaging. D.F. performed image registrations. T.O.H. generated *HuC:lynTagRFP-T* transgenic fish. D.F., H.B. and F.K. wrote the manuscript.

Additional Information

Competing Interests: The authors declare that they have no competing interests.

Publisher's note: Springer Nature remains neutral with regard to jurisdictional claims in published maps and institutional affiliations.

Supplementary Information

Genetic targeting and anatomical registration of neuronal populations in the zebrafish brain with a new set of BAC transgenic tools

Dominique Förster[1], Irene Arnold-Ammer[1], Eva Laurell[1], Alison Barker[1,2], António Miguel Fernandes[1], Karin Finger-Baier[1], Alessandro Filosa[1,2], Thomas Helmbrecht[1], Yvonne Kölsch[1], Enrico Kühn[1], Estuardo Robles[1,3], Krasimir Slanchev[1], Tod Thiele[1,4], Herwig Baier[1]* and Fumi Kubo[1]*

[1] Max Planck Institute of Neurobiology, Department Genes - Circuits - Behavior, Am Klopferspitz 18, D-82152 Martinsried, Germany

[2] Present address: Max-Delbrück Center for Molecular Medicine, Berlin, Germany

[3] Present address: Department of Biological Sciences, Purdue University, U.S.A.

[4] Present address: Department of Biological Sciences, University of Toronto Scarborough, Canada

*Correspondence should be addressed to H. B. (hbaier@neuro.mpg.de) and F. K. (fumikubo@neuro.mpg.de)

Supplementary Figure S1
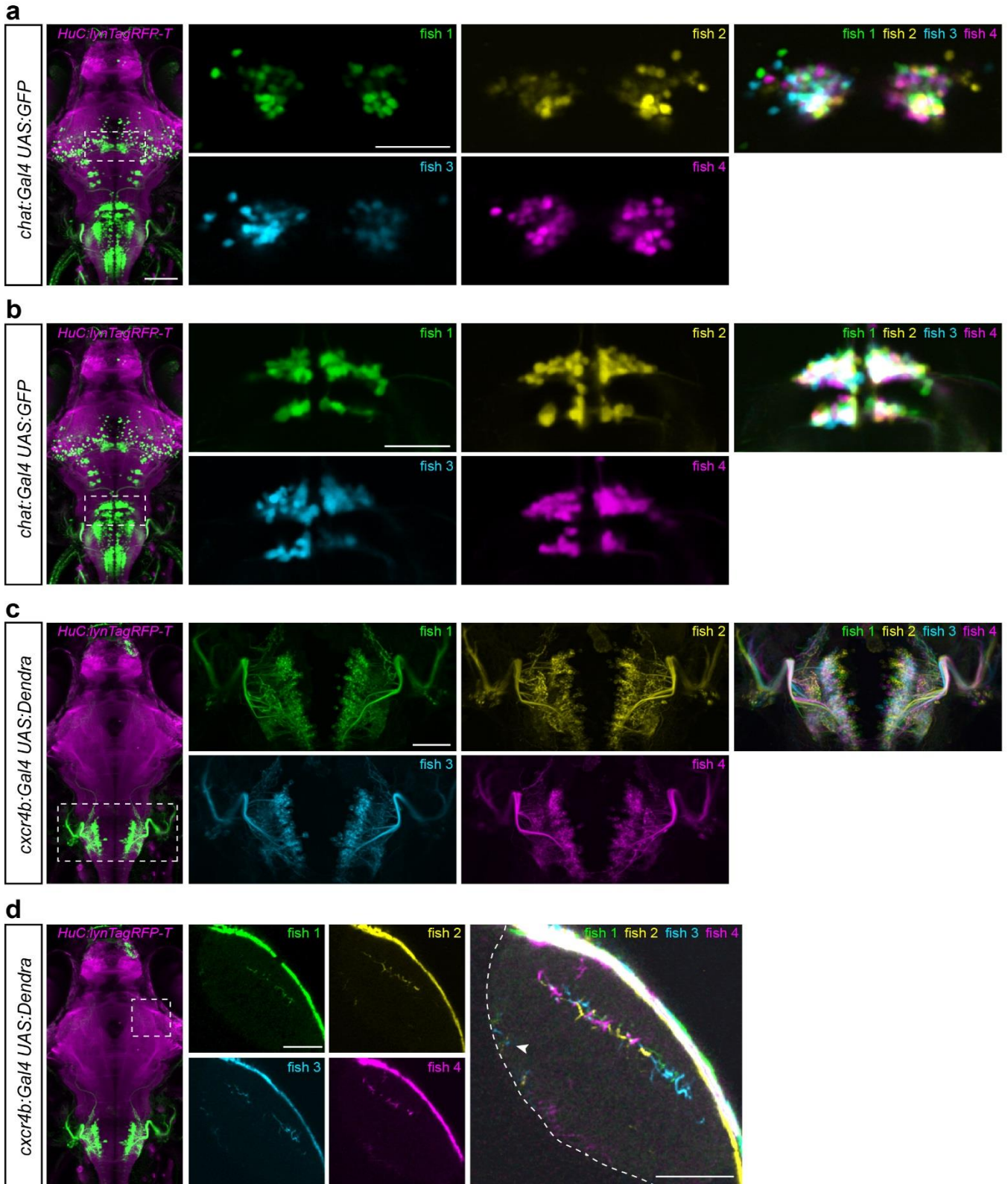
Supplementary Figure S1: Registration of different larvae of the same transgenic line illustrates variegated, but highly reproducible expression patterns. (a,b) Single confocal slices of *chat:Gal4* expression in extraocular motor nuclei (a) and hindbrain neurons (b). After sorting larvae for bright expression of the UAS reporter gene, four different larvae were imaged and co-registered using *HuC:lyn-TagRFPT* expression as a reference. **(c)** Z-projection of confocal stacks showing the expression pattern of *cxcr4b:Gal4* in the hindbrain. The overlay image reveals that consistent cell body position and axonal projections are largely consistent across four individual fish. **(d)** Single confocal slices of *cxcr4b:Gal4* expression in the tectum. An overexposed overlay is shown on the right. The labeled axons innervate the same layers (SFGS3 and SAC/SPV, arrow head) in the tectal neuropil in all four fish, although their precise location within the layers is variable between the four fish. Dashed line in the right panel indicates the border between the tectal neuropil and cell body layer. Scale bar, 100 µm (whole-brain images on the left) and 50 µm (close-ups).

Supplementary Table S1

Primary antibodies	Source	Concentration
Chick anti-GFP	Invitrogen A10262	1/250
Rabbit anti-Galanin	Merck Millipore AB5909	1/500
Rabbit anti-SST	ImmunoStar 20067	1/50
Rabbit anti-GABA	Sigma A2052	1/250
Mouse anti-HuC/D	Invitrogen A21271	1/250
Goat anti-ChAT	Merck Millipore AB144P	1/100

Secondary antibodies	Source	Concentration
Goat anti-chicken Alexa 488	Invitrogen	1/250
Goat anti-mouse Alexa 555	Invitrogen	1/250
Goat anti-rabbit Alexa 647	Invitrogen	1/250

Supplementary Table S1: List of antibodies used in this study.

Supplementary Video 1:

Confocal stack of *chat:Gal4* live expression pattern. See Figure 1 for details.

Supplementary Video 2:

Confocal stack of *cxcr4b:Gal4* live expression pattern. See Figure 1 for details.

Supplementary Video 3:

Confocal stack of *dbx1a:Gal4* live expression pattern. See Figure 1 for details.

Supplementary Video 4:

Confocal stack of *dmbx1b:Gal4* live expression pattern. See Figure 1 for details.

Supplementary Video 5:

Confocal stack of *drd2a:Gal4* live expression pattern. See Figure 1 for details.

Supplementary Video 6:

Confocal stack of *foxb1a:Gal4* live expression pattern. See Figure 1 for details.

Supplementary Video 7:

Confocal stack of *gad1b:Gal4* live expression pattern. See Figure 1 for details.

Supplementary Video 8:

Confocal stack of *galn:Gal4* live expression pattern. See Figure 1 for details.

Supplementary Video 9:

Confocal stack of *otx1b:Gal4* live expression pattern. See Figure 1 for details.

Supplementary Video 10:

Confocal stack of *sst3:Gal4* live expression pattern. See Figure 1 for details.

Supplementary Video 11:

3D volume representation of live expression in new Gal4 transgenic lines (green; Dendra-kras, GCaMP6s or EGFP). Brains have been registered via co-expression of *HuC:lynTagRFP-T* (magenta).

Supplementary Video 12:

3D volume representation of registered Gal4 expression patterns. Reporter channels of Supplementary Video 11 were superimposed with each other using different colors to visualize the spatial relationships of the respective patterns.

Paper II: Linking Neurons to Network Function and Behavior by Two-Photon Holographic Optogenetics and Volumetric Imaging

Marco dal Maschio, Joseph C. Donovan, **Thomas O. Helmbrecht**, Herwig Baier

Author contributions:

M.d.M., J.C.D., and H.B. conceived the project. M.d.M. developed the holographic configuration. J.C.D. developed the software for 3D-2P-CGH, user interface, behavior tracking, and their integration. M.d.M. conducted the experiments, J.C.D. characterized the CGH algorithm performance, and **T.O.H.** developed the protocol for paGFP and the tracing pipeline. M.d.M., J.C.D., and **T.O.H.** worked on the formal data analysis. M.d.M. wrote the original draft. M.d.M., J.C.D., **T.O.H.**, and H.B. reviewed and edited the final version. H.B. supervised the project.

Linking Neurons to Network Function and Behavior by Two-Photon Holographic Optogenetics and Volumetric Imaging

Highlights

- Simultaneous two-photon 3D imaging and 3D photostimulation

- Holographic optogenetics to explore behavior-related neuronal circuits

- Iterative approach plus analysis framework to generate/validate circuit models

- Morphological reconstruction of functionally identified neurons

Authors

Marco dal Maschio,
Joseph C. Donovan,
Thomas O. Helmbrecht, Herwig Baier

Correspondence

hbaier@neuro.mpg.de

In Brief

Dal Maschio et al. introduce a suite of methods for simultaneous 3D two-photon optogenetics and multiplane functional imaging. This approach, which also includes reconstruction of single neurons, enabled the identification of circuitry driving motor behavior in larval zebrafish.

CrossMark

CellPress

Linking Neurons to Network Function and Behavior by Two-Photon Holographic Optogenetics and Volumetric Imaging

Marco dal Maschio,[1,3] Joseph C. Donovan,[1,2,3] Thomas O. Helmbrecht,[1] and Herwig Baier[1,4,*]
[1]Department Genes – Circuits – Behavior, Max Planck Institute of Neurobiology, 82152 Martinsried, Germany
[2]Program in Neuroscience, University of California, San Francisco, San Francisco, CA 94143, USA
[3]These authors contributed equally
[4]Lead Contact
*Correspondence: hbaier@neuro.mpg.de
http://dx.doi.org/10.1016/j.neuron.2017.04.034

SUMMARY

We introduce a flexible method for high-resolution interrogation of circuit function, which combines simultaneous 3D two-photon stimulation of multiple targeted neurons, volumetric functional imaging, and quantitative behavioral tracking. This integrated approach was applied to dissect how an ensemble of premotor neurons in the larval zebrafish brain drives a basic motor program, the bending of the tail. We developed an iterative photostimulation strategy to identify minimal subsets of channelrhodopsin (ChR2)-expressing neurons that are sufficient to initiate tail movements. At the same time, the induced network activity was recorded by multiplane GCaMP6 imaging across the brain. From this dataset, we computationally identified activity patterns associated with distinct components of the elicited behavior and characterized the contributions of individual neurons. Using photoactivatable GFP (paGFP), we extended our protocol to visualize single functionally identified neurons and reconstruct their morphologies. Together, this toolkit enables linking behavior to circuit activity with unprecedented resolution.

INTRODUCTION

Disentangling the contributions of individual neurons to circuit function and behavior (Houweling and Brecht, 2008; Huber et al., 2008) remains a central goal for neuroscience (Kiehn, 2016). Technical advances have enabled functional imaging from large volumes of the brain (Ji et al., 2016), allowing external stimuli and behavior to be correlated with the activity of individual neurons (Ahrens et al., 2012; Dunn et al., 2016; Kubo et al., 2014; Miri et al., 2011; Portugues et al., 2014). This approach is useful for localizing neurons active during a particular task; however, correlative information alone is not sufficient to causally relate a neuron's firing to activity in other neurons (Chicharro and Ledberg, 2012; Weichwald et al., 2015) or to understand the mechanisms of sensorimotor transformations (Panzeri et al., 2017). In order to test and validate such relationships, functional recordings need to be combined with precise interventional paradigms and structural information of the involved circuits (Olsen and Wilson, 2008; Panzeri et al., 2017).

To this end, we established an optical approach that combines high-resolution optogenetic activation of neurons with functional population recordings over large brain regions. Building on state-of-the-art methods (Hernandez et al., 2016; Packer et al., 2015; Rickgauer et al., 2014; Szabo et al., 2014), our approach introduces the possibility to control 3D imaging and 3D photostimulation independently. This allowed us to link functional data to behavior recordings and apply a computational workflow based on dimensionality reduction and regression to extract the behavior-relevant features of the induced activity across the brain. As an additional enhancement, in our protocol, we introduced targeted photoactivatable GFP (paGFP) photoconversion to obtain a morphological reconstruction of individual functionally identified neurons.

In larval zebrafish, several circuits involved in robust and quantifiable behaviors have been identified (Dunn et al., 2016; Kubo et al., 2014; Naumann et al., 2016; Thiele et al., 2014). We focused on one such area, the nucleus of the medial longitudinal fascicle (nMLF), which is located in the tegmentum of the midbrain, ventral to the tectum. The nMLF was previously shown to play an active role in setting tail posture (Thiele et al., 2014), controlling swimming speed (Severi et al., 2014), and in the engagement of particular swim patterns (Dunn et al., 2016; Gahtan et al., 2005; Thiele et al., 2014). We applied our method to this circuit to identify and visualize neurons whose activation drives ipsilateral tail bends. Simultaneous GCaMP6s recordings from large brain volumes enabled us to assign functional scores to hundreds of individual neurons, within and outside of the nMLF, based on their contribution to network activity and behavior. In summary, we present a suite of optical tools and an analysis workflow for interactive and behavior-guided exploration of brain circuits.

RESULTS

Hardware Configuration for 2P-CGH

In order to activate targeted neurons with high resolution, we adopted a two-photon computer-generated holography

(2P-CGH) approach (Dal Maschio, 2014; Oron et al., 2012). This method uses a spatial light modulator (SLM) to engineer the phase distribution of a light wavefront and precisely shape complex illumination patterns in the sample volume (Figure 1A). The photostimulation path is coupled to a standard galvo-galvo 2P imaging system (Figures 1A, S1, and S2; Data S1), where an electrically tunable lens (ETL) is included to remotely refocus the imaging plane (Grewe et al., 2011; Smirnov et al., 2017; Stirman et al., 2016). The configuration includes a high-speed camera to record the tail movements of a head-restrained fish larva and a second camera for calibration (Figure 1A; see STAR Methods).

To generate precise 3D photostimulation patterns, we implemented a version of the iterative Gerchberg-Saxton algorithm (Haist et al., 1997; Figures S3A and S3B; in detail with pseudo-code in the STAR Methods), which we called multiplane adaptive Gerchberg-Saxton (maGS). This computational engine calculates the required phase correction and includes compensation for illumination uniformity (Figures S3C–S3F). Furthermore, the relative intensity across different regions in a 3D pattern can be independently controlled (Figures S3G–S3I). In addition to the computational engine, the software also provides a procedure for the 3D registration of the photostimulation and imaging paths. This calibration protocol, detailed in the STAR Methods, acquires images of reference points in the holographic and imaging coordinate systems and finds the optimal affine transformation to link them together. The registration typically achieves an alignment of 1 μm between the imaging and photostimulation beams (0.9 ± 0.3 μm; mean ± SD) within a 200 × 200 × 250 μm^3 volume addressable with high quality.

To photostimulate targeted cells, we selected an excitation profile with a diameter of 6 μm, based on the typical cell diameter of the neurons measured in the zebrafish midbrain region (6.9 ± 0.9 μm). Along the z axis, these excitation profiles, measured with a fluorescein layer, were characterized by a full width at half maximum (FWHM) of 7.8 ± 0.8 μm (Figure 1B). To evaluate the precision achieved for light patterning in a living brain in presence of scattering, we took advantage of paGFP photoactivation (Patterson and Lippincott-Schwartz, 2002). In fish with pan-neuronal expression of paGFP, we targeted simultaneously cells at seven corners of a 20 × 20 × 20 μm^3 brain volume. These neurons were successfully visualized after paGFP photoconversion, showing minimal off-target fluorescent signal in neighboring cells (FWHM$_z$ = 8.9 ± 0.9 μm; Figures 1C and S4).

Optimization of a Protocol for Simultaneous 2P Imaging and 2P Photostimulation

We designed a protocol to precisely photostimulate selected neurons while simultaneously imaging network activity. Ideally, the action spectra of actuator and sensor molecules should not overlap. Previous studies combined simultaneously 2P imaging of GCaMP variants near 920–930 nm with 2P photostimulation of red-shifted actuators, such as C1V1 (Carrillo-Reid et al., 2016; Packer et al., 2015; Rickgauer et al., 2014), excited at 1,020–1,064 nm, or ChR2 excited at 880 nm (Baker et al., 2016). However, many light-based actuators, including the red-shifted variants, can generate a significant current when excited around 920 nm (Ronzitti et al., 2016; Chaigneau et al., 2016; Pra-

kash et al., 2012). This photocurrent is proportional to the 2P cross-section of the molecule at the specific wavelength, the square of the light power density, and the opsin decay time constant (Chaigneau et al., 2016; Rickgauer and Tank, 2009). For these reasons, imaging GCaMP at 920 nm in the presence of light-gated actuators poses restrictions on the maximum power, pixel dwell time, and pixel resolution (Baker et al., 2016; Inagaki et al., 2014; Kim et al., 2015; Packer et al., 2015; Rickgauer et al., 2014). However, GCaMP sensors, while optimally excited near 920 nm, retain >0.4 of their peak ΔF/F performance at wavelengths >1,000 nm (Akerboom et al., 2012; Figure S5A) and can be used for functional recording at 1,000–1,020 nm (Dana et al., 2016; Inoue et al., 2015). Near 1,020 nm, while red-shifted actuators are close to the peak of activation, ChR2 is not efficiently excited and leads to small induced currents (Prakash et al., 2012). The relatively shorter tau-off of ChR2 compared to other opsins (Yizhar et al., 2011) could be advantageous for limiting the undesired opsin-induced current during imaging. We therefore devised a strategy with an excitation scheme based on imaging GCaMP6s at 1,020 nm, where the ChR2 photocurrent is small, and perform ChR2 activation at 920 nm (near its maximal cross-section). To further improve the imaging conditions, we used nuclear-localized GCaMP6s (Kim et al., 2014). This increases the signal to noise ratio (S/N) of the recordings due to the lack of neurite expression and the consequential reduction of background signal. Moreover, it enables calcium recording with a sparser spatial sampling, thus effectively decreasing the applied light dose and further reducing the risk of spurious activation.

To confirm that GCaMP imaging at 1,020 nm does not substantially alter or facilitate the neuronal firing from neurons expressing ChR2, we measured the spontaneous activity in neurons of transgenic zebrafish expressing GCaMP6s, with and without ChR2. For these experiments, we used a raster scanning scheme designed to increase the spike detection probability, with high S/N calcium recording at 15–25 Hz (S/N > 30; 0.3–0.5 μm/pixel and 2–4 μs dwell time; Figure S5B), thus also increasing photo-evoked currents compared to our standard imaging conditions. Across test laser power levels ranging from 12 to 37 mW, which significantly exceed the power used for our imaging experiments, the number of spontaneous transients was very similar for ChR2-positive and ChR2-negative cells (0.85 versus 0.63 events per minute, respectively; Figure S5C). Imaging at 920 nm, in contrast, led to more transients when ChR2 was co-expressed (1.9 versus 0.81 events per minute, respectively). With this scanning protocol, we cannot guarantee that we can detect single spikes (Dana et al., 2014, 2016) or completely rule out a modification of the subthreshold activity. However, imaging with lower power and with sparser spatial sampling minimizes spurious activation, as shown for excitation at 920 nm for both ChR2 (Baker et al., 2016) and Chronos (Ronzitti et al., 2016).

Finally, we investigated whether stimulation at 920 nm might adversely affect GCaMP6s imaging through indicator photobleaching, photoconversion, or phototoxicity. Following a photostimulation event, GCaMP6s fluorescence decreased with respect to the baseline by less than 4%, at stimulation power densities from 0.05 to 5 mW/μm^2 (Figure S5D). Furthermore,
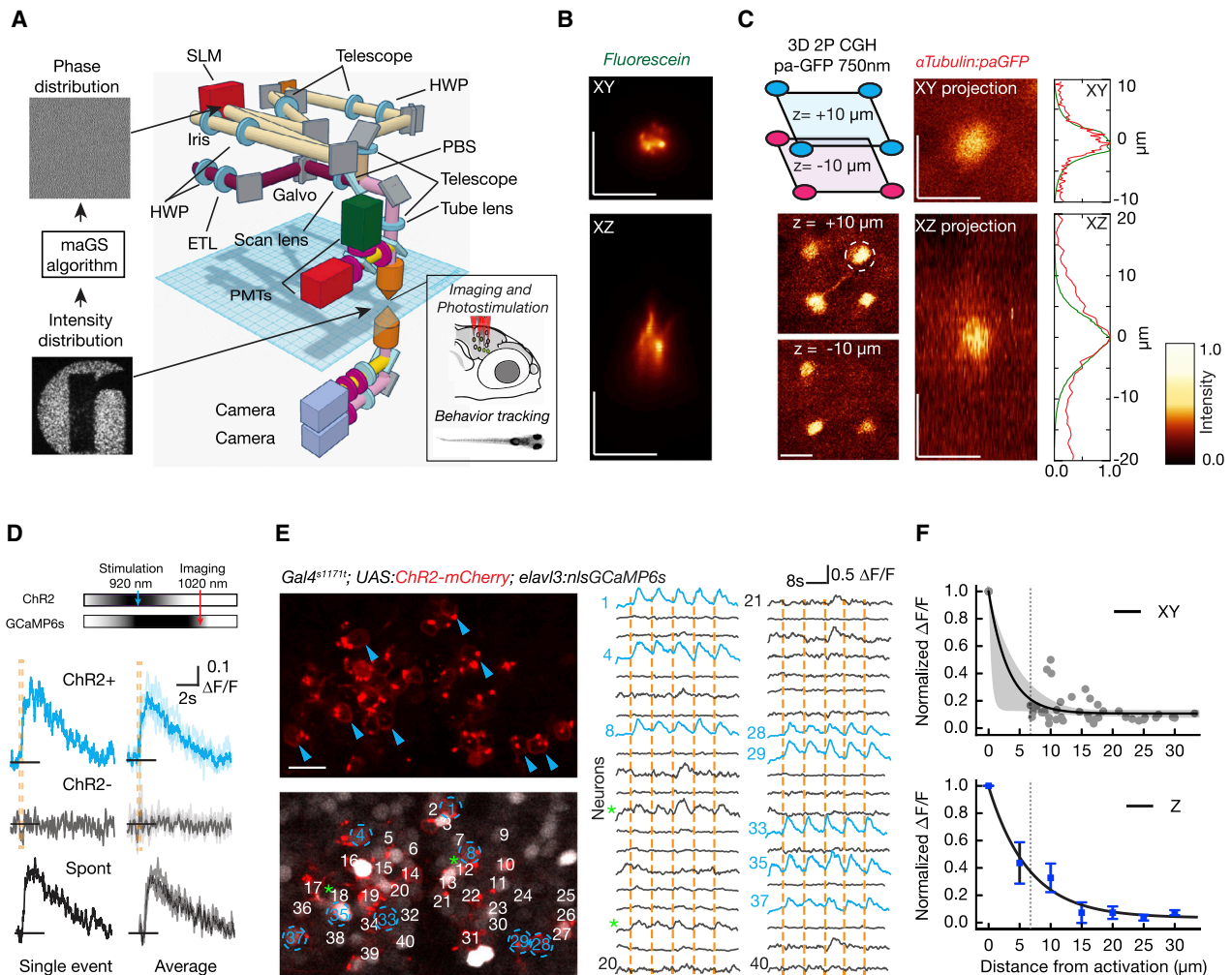
Figure 1. Parallel 2P Optogenetic Stimulation and Activity Readout

(A) Complex illumination patterns are obtained in the sample volume using computer-generated holography (CGH). A fast Fourier transform (FFT)-based algorithm (maGS) calculates the phase modulation that generates the desired pattern at the sample plane (logo of our institute). The photostimulation path (light brown) uses a spatial light modulator (SLM) (red) to apply phase corrections. The imaging path (magenta) includes an electrically tunable lens (ETL) for remote focusing. The two paths are combined with a polarizing beam splitter (PBS) (details in Figure S1 and STAR Methods).

(B) Measurement of the excitation profile obtained from a thin fluorescein layer illuminated with a circular spot 6 μm in diameter.

(C) Parallel 2P activation of paGFP in vivo using a 3D excitation pattern with a distribution of circular ROIs (6 μm in diameter). The photoactivation foci are generated in the optic tectum at a depth of about 100–120 μm in a zebrafish larva with pan-neuronal paGFP expression (*alpha-tubulin:paGFP*). Four spots are generated at +10 μm and three spots at −10 μm. Axial and lateral average projections of a photoactivation volume obtained in vivo with a target pattern 6 μm in diameter are shown. The paGFP profiles (FWHM: 5.79 ± 0.91 μm laterally and 8.9 ± 0.9 μm axially) were photoactivated at 750 nm with a power of 0.25 mW/μm^2 at the sample for 0.5 s. The right panel shows a comparison of the fluorescence profile measured for paGFP photoconversion (in red) and for a fluorescein layer (in green).

(D) Somatic GCaMP6s signals induced by 200 ms photostimulation at 920 nm while imaging at 1,020 nm. Cells expressing ChR2 and GCaMP6s show stimulation-induced calcium increases (blue traces) whereas cells expressing only GCaMP6s (gray traces) do not. Activation events in targeted neurons show similar response dynamics to spontaneous events (black traces; Figures S6A and S6B).

(E) Parallel neuronal stimulation in vivo. A small network of neurons is imaged during repeated simultaneous photostimulation of eight targeted neurons (in blue). Photostimulation events (200 ms) are indicated by orange vertical lines, and the traces for photostimulated neurons are in blue. Along with the targeted neurons, some cells show low-amplitude activity locked to the stimulation (green asterisk; see also Figures S6E and S6F).

(F) Effective photostimulation resolution. To measure lateral resolution, targeted cells were photostimulated while nearby neurons in the same imaging plane were recorded. Each gray dot represents a non-targeted cell, with ΔF/F normalized relative to the response in the targeted cell. An exponential decay fit is shown (black line) with 95% confidence interval (bootstrap; shown in gray). The thin dashed line shows the minimum distance between cells in this region of the brain. To measure axial (Z) resolution, the imaging plane was shifted axially from the target with the ETL. An example of the protocol is shown in Figures S6G and S6H. Induced ΔF/F is normalized relative to the photostimulated target cell. In blue, an exponential fit is shown, and error bars indicate the SEM. The scale bars represent 10 μm.

40

baseline fluorescence was similar before and after repeated photostimulations (2% ± 1.5%; five stimulations over 60 s), demonstrating the photostability of GCaMP6s. However, the stimulation light at 920 nm can cause detectable contamination in the recorded signal during photostimulation (Carrillo-Reid et al., 2016) with a non-linear relationship to stimulation intensity (Figure S5E). Therefore, we adopted a line-by-line subtraction procedure to filter out the stimulation artifact when contamination of the GCaMP signal was significant (see STAR Methods; Figure S5F).

Photostimulation with Near-Cellular Precision in the Zebrafish Brain

To test our protocol, we targeted neurons expressing ChR2 with 920 nm excitation while simultaneously imaging GCaMP6s at 1,020 nm (Figures 1D and 1E). When ChR2-positive neurons were stimulated, with typical power densities ranging from 0.1 to 0.5 mW/μm^2, we detected strong calcium transients in 90% of the cells tested (out of 70 cells across 11 fish). In particular, the average reliability during repeated stimulation trials was 78% ± 18% (positive responses over number of stimulation trials; Figure S6D). The temporal dynamics of each induced event were similar to spontaneous events (Figures 1D, S6A, and S6B), and their amplitudes were correlated with the expression level of ChR2 (Figure S6C). Stimulating neurons expressing GCaMP6s, and not ChR2, did not result in any detectable responses (0.03 ± 0.04 ΔF/F; 25 cells in four fish; Figure 1D).

To quantify the spatial resolution of our 2P-CGH photostimulation, we probed neurons sparsely expressing ChR2 and measured the GCaMP6s responses induced when changing the position of the stimulation spot (on target and 10 μm off target) or the number of off-target stimulation spots. Stimulation near the targeted soma did not induce comparable calcium responses to on-target stimulation, although there was a small increase in ΔF/F when increasing the number of spots surrounding the cell (eight cells; three fish; Figures S6E and S6F). In a different set of experiments, we photostimulated single, or few, cells in an area that was densely co-expressing ChR2 and GCaMP6s and recorded calcium signals within and around the activated region (details in STAR Methods). Large calcium transients were detected in the targeted cells in the vast majority of trials, and the induced ΔF/F rapidly decreased with increasing distance from the targeted cells (Figures 1E, 1F, S6G, and S6H). Outside a volume approximately 8 μm wide and 10 μm high, the detected responses had less than half the amplitude of those at the center of the target. Together, these experiments demonstrate that photostimulation can be restricted to a volume close to the typical dimensions of neuronal cell bodies in vivo.

## Simultaneous 2P-CGH Optogenetics and Multiplane Imaging

Next, to maximize the potential of the approach for circuit investigation, we coupled 3D optogenetic activation to fast volumetric functional imaging (Ji et al., 2016). An ETL was placed in the imaging path close to a plane conjugated to the back-focal plane of the objective (Figure S1). This enabled remote shifting of the imaging plane within a few milliseconds (6.1 ± 1.2 ms) over a

z range of 75 μm, independently of the photostimulation. Our acquisition protocol for investigating the nMLF circuit (Figure 2A) was optimized to record GCaMP6s signals in five different planes covering 80 × 160 × 32 μm^3 at four volumes per second. With this configuration, we showed that cells in different planes could be independently and selectively stimulated while recording neuronal activity from a larger population with minimal activation of non-targeted cells (Figures 2B–2D).

Using 2P-CGH Optogenetics to Identify Ensembles of Behaviorally Relevant Neurons

The nMLF is a midbrain nucleus that receives inputs from visual areas and projects axons to the spinal cord (Gahtan et al., 2005). In initial experiments, we confirmed an earlier report (Thiele et al., 2014) that broad unilateral ChR2 stimulation in the nMLF with a 50-μm optic fiber induces a tail deflection toward the activated side. Taking advantage of 2P-CGH, we initially mapped the circuit by using circular photostimulation patterns with slightly overlapping regions, 18 μm in diameter (0.2 mW/μm^2), which were located at different distances from the midline axis (Figure 3A). From the acquired behavioral data, we extracted the spatiotemporal kinematics of the tail with a computerized tracking routine (Semmelhack et al., 2014) to quantify tail bending events (Figure 3B) and to distinguish these events from other motor patterns. We found that activation of an nMLF region approximately 25 μm from the midline (position B of Figure 3A) resulted in the largest tail deflection angles (Figure 3C). The typical behavioral pattern during a 2-s stimulation consisted of a tail deflection (3.4 ± 2.2 deg/s), followed by a slower relaxation phase (1.7 ± 0.9 deg/s) at the end of the stimulation (Figure 3B, lower panel). Activation periods shorter than 2 s elicited progressively smaller bending amplitudes, with a minimal duration of 200 ms necessary to cause a detectable change in tail position (Figure 3D). The same stimulation protocol applied in control fish expressing only a fluorescent marker did not result in tail deflections (six ChR2+ and four ChR2− fish; Figure 3C).

When using high resolution and parallel light shaping for stimulation, the number of possible activation patterns becomes extremely large, even for small circuits composed of tens of neurons. To circumnavigate this "combinatorial explosion" problem, we developed an iterative procedure to isolate a minimal subset of neurons that are sufficient to drive a behavioral outcome. Starting from the coarse stimulation patterns detailed above, we focused on those that induced significant tail bending. We then probed subsets targeting one less neuron than the current set and selected the one subset inducing the greatest angle throughout bending events (Figure 3E). This procedure was repeated until no further neuron could be subtracted while still eliciting behavior. Using a regularized regression model for the tail angle, we then extracted, for each cell, the behavioral weight associated with its activation (Figures 3F and 3G). For the example shown, starting from the original set, this behavior-based selection procedure quickly converged on a critical subset of three neurons. This is an important preliminary step to isolate causative components. Identifying and stimulating only a minimal subset of behaviorally relevant neurons reduces the complexity of network perturbation and the risk of potential tissue heating (Hernandez et al., 2016).
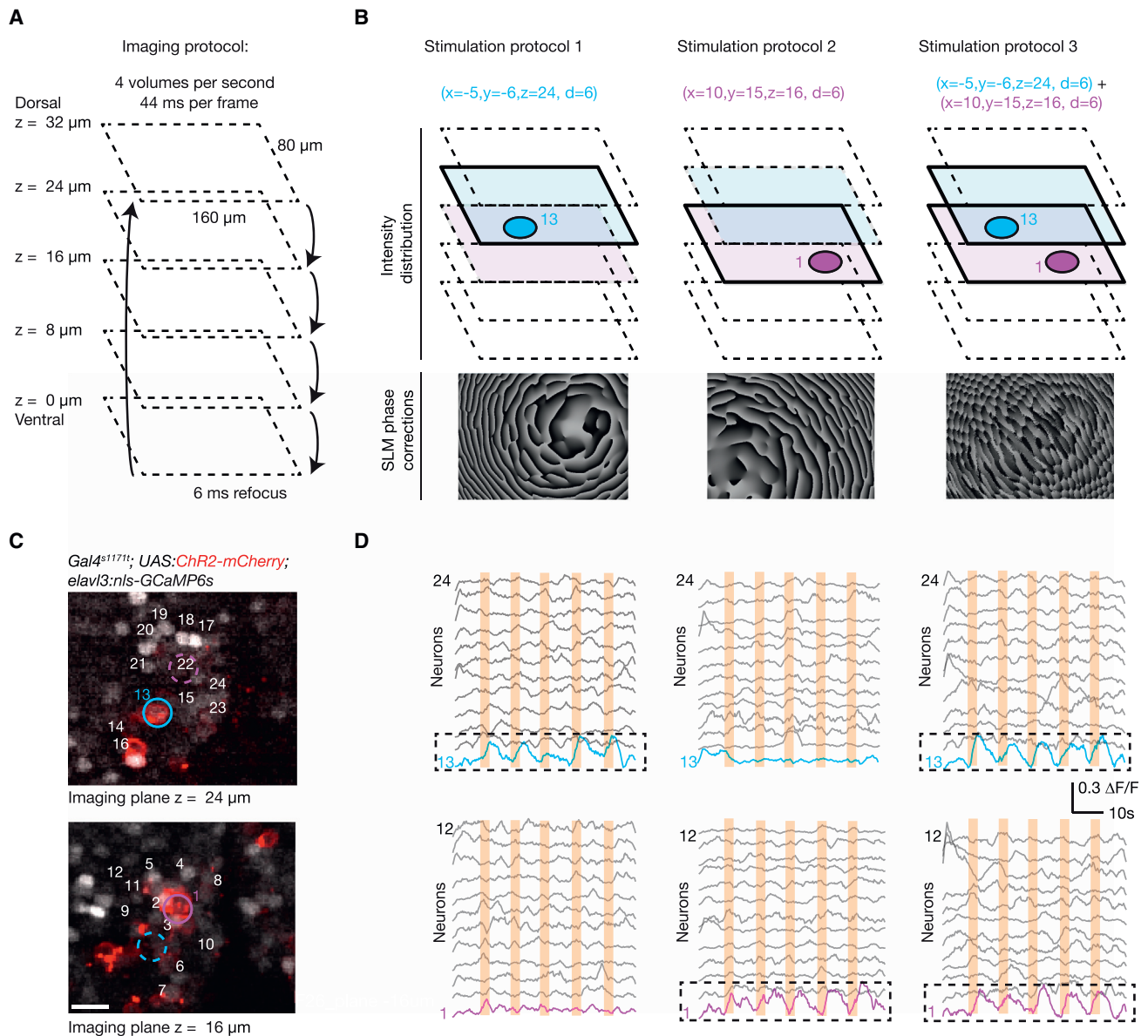
Figure 2. In Vivo 3D High-Resolution Photostimulation and Calcium Imaging

(A) Multiplane imaging protocol. An ETL is used to switch rapidly between five imaging planes separated by 8 μm and to record GCaMP6s signals across a volume of 160 × 80 × 32 μm^3 at 4 Hz.

(B) Design of 3D photostimulation protocols. Based on an acquired z stack, three different 3D photostimulation protocols are designed to target 6-μm stimulation spots either independently or simultaneously to two ChR2-expressing neurons localized in different planes (cell no. 1, purple, in the ventral plane at z = 16 μm; cell no. 13, blue, in the dorsal plane at z = 24 μm). The corresponding phase correction patterns are calculated based on the photostimulation targets and superimposed on the light wavefront by means of the spatial light modulator.

(C) A view of the two planes selected for photostimulation from a fish expressing pan-neuronal nuclear localized calcium indicator (nlsGCaMP6s) and ChR2-mCherry. Colored regions of interest (ROIs) indicate the cells selected for the stimulation. The scale bar represents 10 μm.

(D) The activity from a subset of cells in the imaged planes during photostimulation. The induced activity matches the spatio-temporal photostimulation protocol (five epochs; 2 s; cell no. 1 and/or cell no. 13), with the targeted cells showing an activity profile locked to the stimulus timing, with minimal cross-activation of the surrounding cells.

Combined Imaging and Computational Analysis of Behavior-Linked Circuit Dynamics

After functionally identifying a small subset of behaviorally relevant nMLF neurons, we recorded the activity induced in the circuit by multiplane imaging. We imaged a five-plane volume, including the nMLF, while photostimulating the identified neurons for 2 s and tracking the behavior (Figures 4A and 4B). This allowed the recording of hundreds of neurons (Figure 4C).
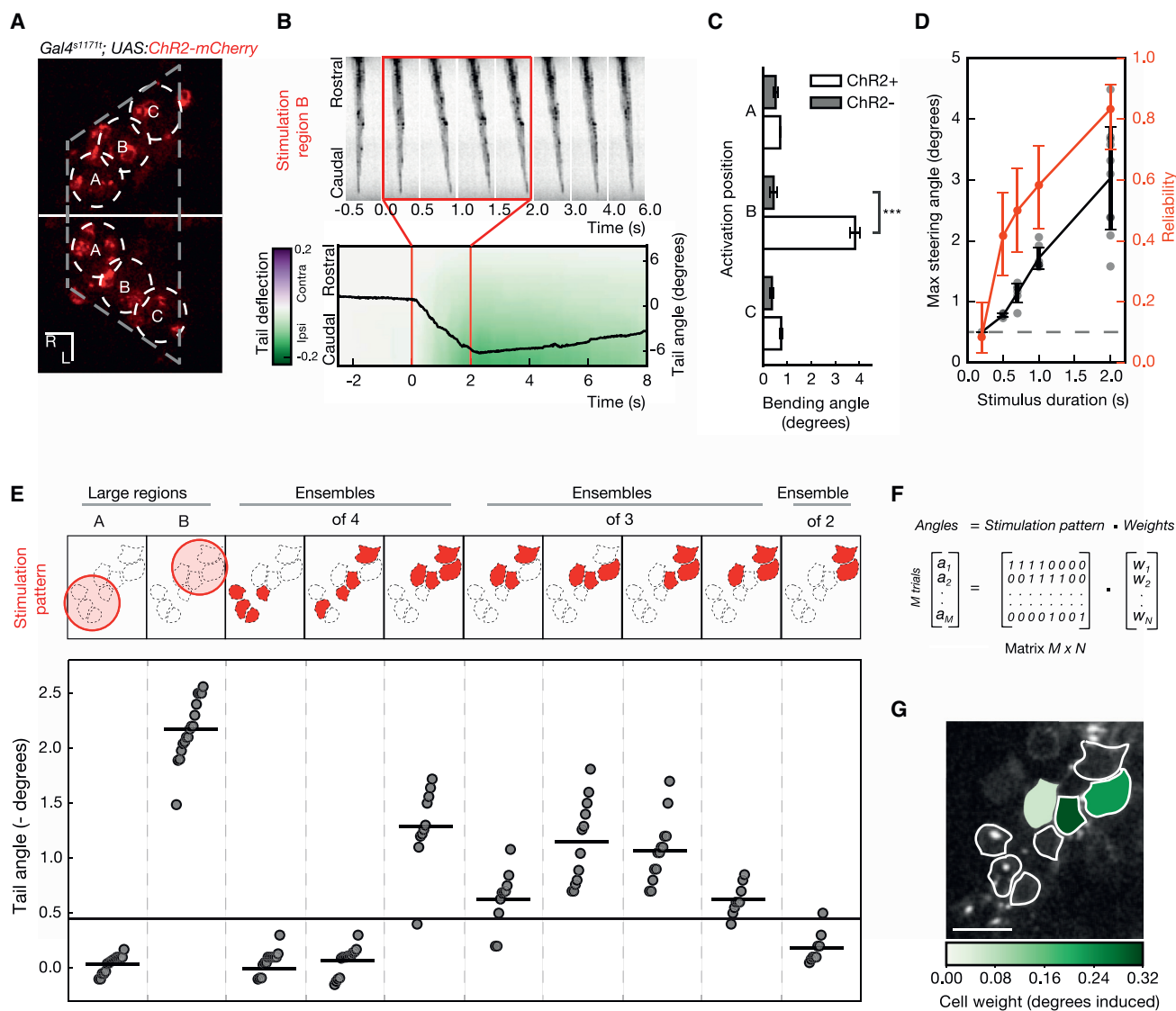
Figure 3. Functional Identification of Behaviorally Relevant Neurons

(A) Probing the neuronal substrates driving a motor outcome. Slightly overlapping photostimulation regions, 18 μm in diameter, were targeted in fish expressing ChR2-mCherry in the nMLF for an initial characterization of the circuit.

(B) Kinematics of the induced tail bending. When position B is targeted, a slow ipsilateral deflection of the tail is detected, followed by relaxation to the baseline level at the end of stimulation. The angle between the base and the caudal tip of the tail is shown as a black line, overlaid onto a heatmap, which shows the relative lateral deflection along the tail.

(C) Comparison of the maximum tail bending angle induced by 2P photostimulation of different regions. The difference in deflection angle is only significant for region B (p value < 0.001; Welsh's t test; Bonferroni corrected; n = 15 trials across six fish for ChR2+; n = 12 trials across four fish for ChR2−). Error bars indicate SEM.

(D) The influence of photostimulation duration on behavior. Stimulations longer than 200 ms lead to tail deflection (judged as a deflection angle greater than five SDs of the baseline). Increasing the duration of the photostimulations causes tail bending in a larger fraction of trials (red) and larger amplitude tail deflections (black). Error bars indicate the SD.

(E) Behavior-based identification of neurons driving tail bends. From the regions used for initial mapping, smaller subsets of neurons are iteratively selected for stimulation, based on the induced behavior magnitude (tail angle). This procedure, reducing trial after trial the number of units probed, converges to minimal selections of neurons that significantly drive behavior (at least five SDs above baseline—black horizontal line).

(F) Model for neuron contribution to behavior. The magnitude of the tail angle (angles) induced in every trial is expressed as linear combination of the neurons included in the pattern (0, excluded; 1, included) and the contribution/weight of each neuron (weights).

(G) Weight map of behavior. A regularized regression on the model in (F) is used to fit the behavior data. This returns a map with the contribution in degrees from each stimulated cell to the behavioral outcome. The scale bars represent 10 μm.

Gal4s1171t; UAS:ChR2-mCherry; elavl3:nlsGCaMP6s
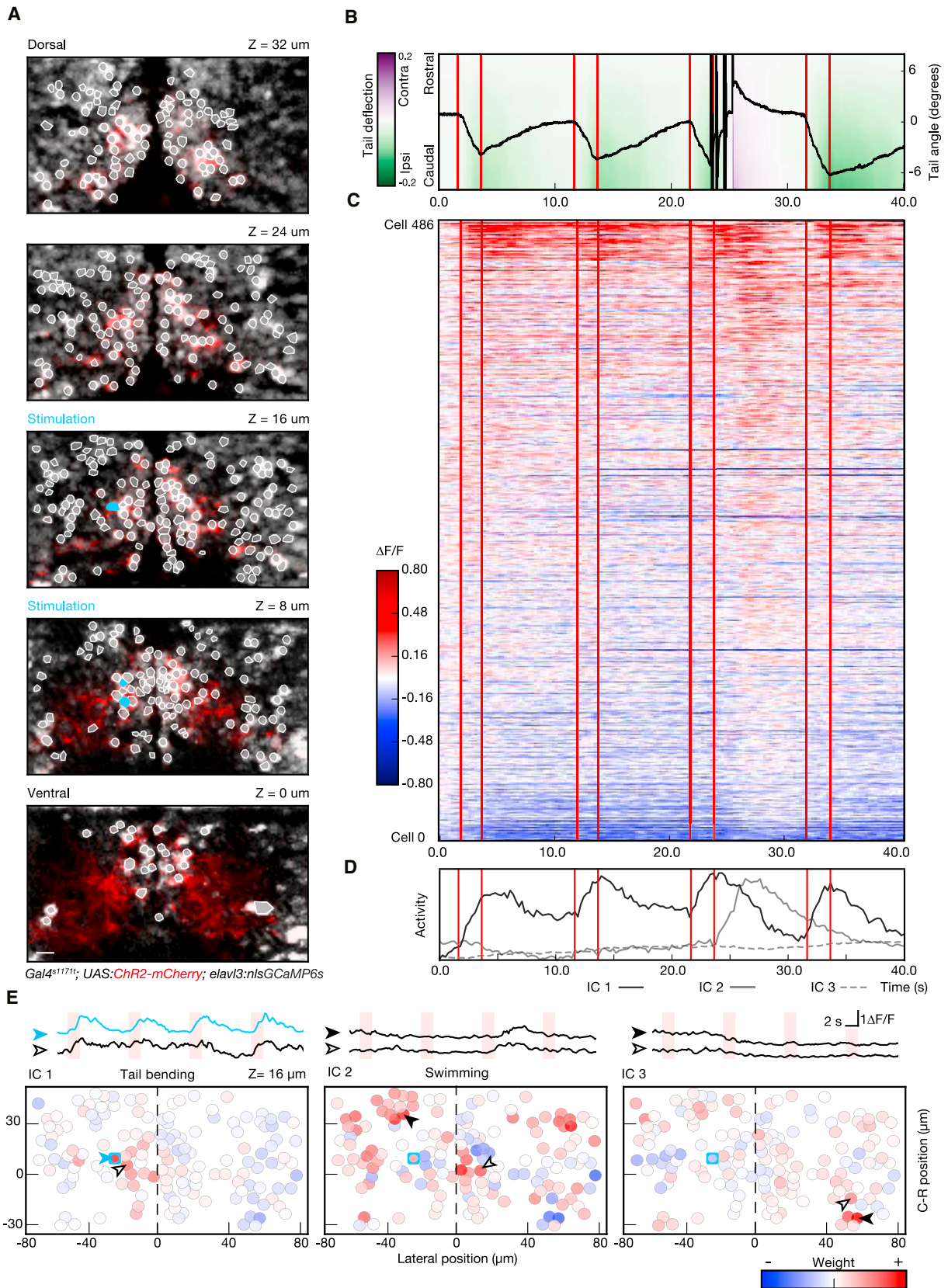
(legend on next page)

Consistently across different stimulation trials and fish, a subset of neurons showed activity profiles locked to the stimulation and to tail bending (113 trials; three fish; Figures 4B, 4C, and S7–S9). A different set of neurons showed activity in relation to large-amplitude tail oscillations (swimming), which occurred with low probability (in approximately 13% of stimulation trials; Figures 4B and 4C; trial 3).

To extract the relevant temporal components of circuit activity, we adopted an analytical framework based on dimensionality reduction through independent component analysis (ICA). This approach projects shared activity patterns across all recorded neurons in the circuit into a reduced number of activity components. In the representative trial shown in Figure 4, a 3D representation via ICA captured more than 40% of the variance in the network dynamics (Figure 4D). The first component (IC1) captured the phasic increase in activity induced by photostimulation and the onset of tail bending. The other two components were generally associated with swimming (IC2) or with slow, perhaps adaptive, changes in circuit state (IC3).

This compact description of the neuronal activity allowed us to reveal the spatial position of individual neurons contributing to each IC and to the behavior outcome (Figures 4E and S9). For IC1 ("tail bending"), the corresponding map showed that most neurons were localized on one side of the fish, ipsilateral to the stimulation. For IC2 ("swimming") and IC3 ("slow dynamics"), the patterns of activity were broader and extended to the contralateral side. A laterality index was computed for each IC, showing a significant lateralization only for IC1 (Figure 4E). This asymmetric activity increase for IC1 was consistent across multiple trials and several fish and was not present with different stimulation patterns that failed to induce ipsilateral tail bending (n = 30 trials in three fish; Figure S7B).

In addition to the ipsilateral activity increase, in some of the fish tested, we identified a small group of cells that showed a negative weight for IC1. Focusing on this aspect, we found that these cells were mostly contralateral and responded with a substantial delay of 1.6 ± 0.5 s (mean ± SD) after the onset of the stimulation. Whereas the cells on the photostimulated side of the nMLF took on average 1.7 ± 0.4 s to reach a positive ΔF/F maximum, this population of contralateral cells reached a negative peak in 2.2 ± 0.6 s, followed by a gradual return to baseline levels (Figures S9C–S9E). Previous imaging studies (Dunn et al., 2016; Thiele et al., 2014) have reported largely symmetric patterns of broad activation in the nMLF during spontaneous behavior. Our high-resolution approach revises this view by isolating partially lateralized activities that are associated with different motor components.

Linking Network Dynamics to Specific Behavior Outcomes

We next focused our analysis on the relation between neuronal activity and behavior. A clustering procedure applied to the tail kinematics, specifically the Fourier power spectrum of the tail angle (Figure 5A; see STAR Methods for details), revealed that the elicited behaviors fell into two distinct classes: one representing the trials in which a tail deflection of varying amplitude was observed (38/44 trials, red), the other in which large-amplitude swimming bouts were also engaged (6/44 trials, green). We adopted a logistic model to evaluate the relationship between network states and behavior. Each neuron was assigned a weight, which related its activity to a specific behavioral output. A regularization was included to generate a sparse representation of circuit activity (see STAR Methods). This analysis showed that a subset of neurons was not generally associated with every motor outcome but rather specifically tuned to particular behavioral parameters (Figure 5B).

Next, we examined the dominant behavioral cluster (tail bending events without swims) and employed a regularized linear regression with cross-validation to model the instantaneous tail angle based on the neuronal activity recorded (Figure 5C). The behavior map resulting from a training subset of trials highlighted a cluster of cells with increased activity when the tail was deflected toward the side of activation (in red) and a second population, mostly contralateral, with decreased signals during tail bending (in green). When we applied this simplified model in a testing dataset (excluded from training), the tail angle was effectively predicted (Figure 5D, cyan). Regressions using simplified representations of circuit activity with a small set of ICs achieved a reasonable level of prediction for the tail angle despite using far fewer components than a model using every

---

Figure 4. Combining Photostimulation with Functional Imaging and Behavior Recording

(A) Multiplane recording of the activity of 486 cells during optogenetically induced behavior. Planes imaged in the midbrain of fish expressing ChR2-mcherry (red) and nlsGCaMP6s (gray) are shown. ROIs, corresponding to the cell bodies selected for analysis, are highlighted in white, and units selected for photostimulation are shown in cyan.

(B) Kinematics of the tail in response to stimulation. This example shows the temporal evolution of the tail angle for four repetitions of 2-s photostimulation (red lines indicate stimulation onset and offset). Note that, at the third photostimulation episode, after an initial bending of the tail toward the side of the stimulation, the fish responded with a large-amplitude swim. Trials with this kind of transition bending-swimming were common in all the larvae tested (n = 3) and occurred in approximately 20% of the trials.

(C) Raster plot showing the activity for the recorded neuronal population, with the same timescale as the behavior shown in (B). A small subset of neurons shows a reliable activity pattern temporally locked to stimulation and tail bending. A larger number of neurons show an activity increase corresponding to the large-amplitude swim.

(D) Representation of temporal patterns in population activity by ICA. The first three components of the representation are shown: IC1 is associated to the activity during tail bending; IC2 represents the activity picked during the large-amplitude swimming bout; and IC3 represents a slow modulation in the activity not linked to a detectable behavior.

(E) Circuit activity maps for the plane at z = 16 μm, showing the spatial distribution across the population of the three activity components. Representative traces, corresponding to the different ICs, are shown for the cells indicated with arrowheads in the corresponding maps (blue trace represents a stimulated cell). For IC2 and IC3, the calculated laterality indices were −0.13 ± 0.11 and 0.06 ± 0.15 (mean ± SD; p value 0.12 and 0.22), indicating slight, if any, ipsilateral bias. IC1, on the other hand, is significantly lateralized (−0.36 ± 0.15; p value 0.01). The scale bars represent 10 μm.
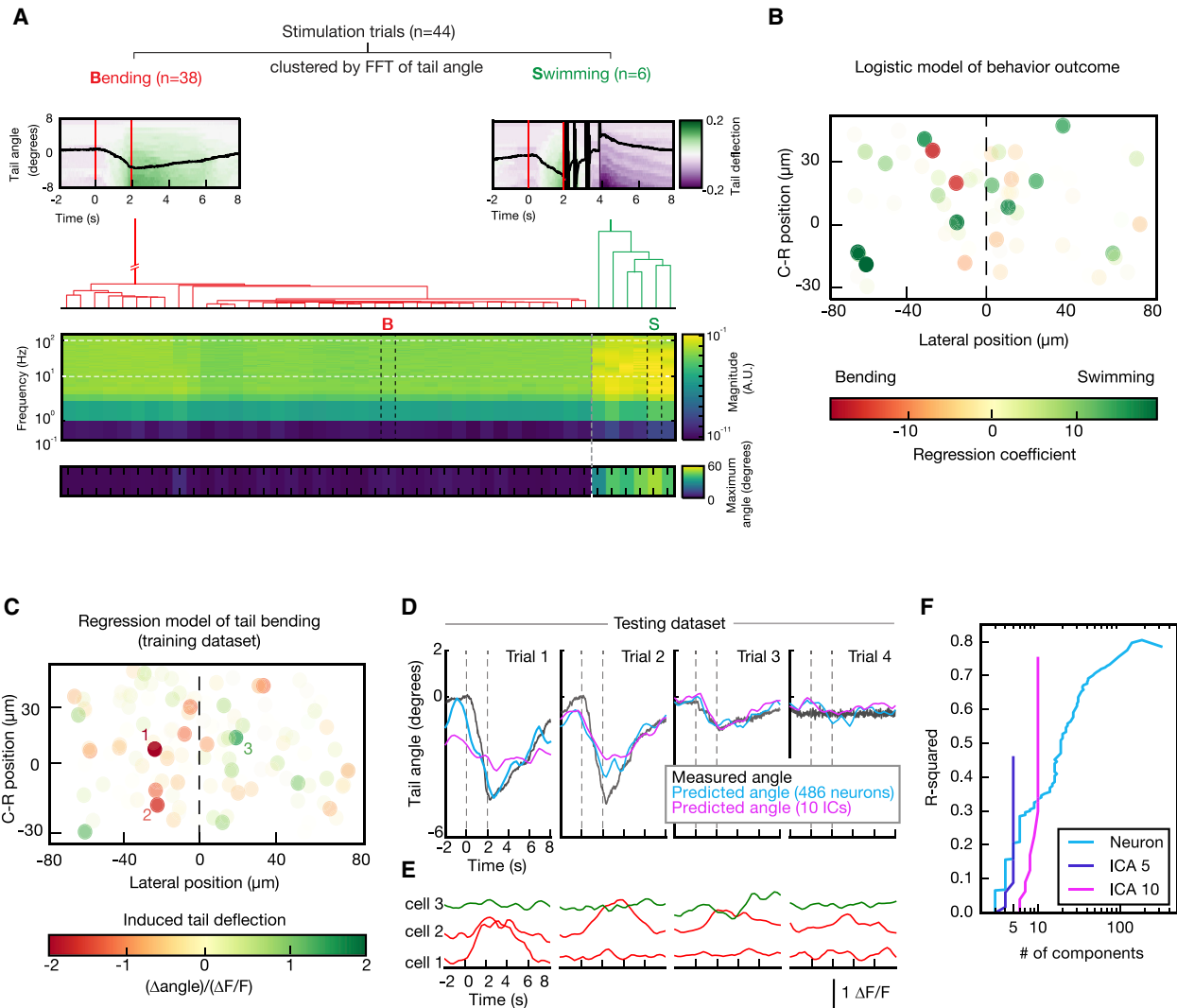
Figure 5. Analysis of Behavior by Means of Regression Models

(A) Classification of the induced behavioral outcome. For each stimulation trial, a 10-s window, including the stimulation, is examined and the behavioral outcome is hierarchically clustered based on the frequency content of the tail angle. Two distinct groups are found: one including trials characterized by large-amplitude tail angles and high-frequency content in their spectrum (S, swimming; green) and the other with low-amplitude or minimal tail deflection and reduced high-frequency content (B, bending; red). Two representative examples illustrate the typical tail dynamics. The frequency content and the corresponding maximum tail angle are plotted, aligned to each trial in the tree above.

(B) Modeling behavioral outcomes. To evaluate the relationship between neuronal activity and identified behavioral classes, a logistic regression is used. This model assigns a weight to neurons, based on how their activity correlates with the behavioral outcome elicited. A map shows the projection of the neurons from all five planes imaged, indicating cells preferentially tuned to large-amplitude swims (green) and those associated with tail bending (red).

(C) Modeling the neuronal contribution to tail bending. A subset of the tail bending trials (training dataset) is used to fit a regularized regression model for the tail angle based on the concurrent neuronal activity. In the circuit map, the color assigned to each neuron represents the contribution of its activity toward the total deflection angle. Negative values in this map correspond to increased activity relating to the typical behavior outcome—tail deflection toward the stimulated side, whereas positive values correspond to a reduction of activity.

(D) Testing the behavior model. The 162 non-null coefficients extracted are then applied to represent the behavior outcome in a separate set of trials (testing dataset). The prediction of the tail angle based on the recorded neuronal data is close to the measured angles ($R^2 = 0.85$; cyan and black, respectively—see F). Using a large number of neurons to fit a model can raise statistical issues, which can be circumvented by reducing the number of parameters in the model and reducing their correlations. A simplified model, based on a ten-component ICA representation of the circuit activity, still provides a good quality fit ($R^2 = 0.74$; magenta—see F).

(E) The activity of three example neurons in a subset of testing trials, with labels corresponding to the map in (C).

(F) Accuracy of the tail angle regression versus number of regression components. A model based on the set of recorded neurons (cyan) requires a large number of parameters to perform effectively. Models based on a reduced representation of circuit activity using ICA (purple, five ICs; magenta, ten ICs) perform well with a reduced number of parameters.

782 Neuron *94*, 774–789, May 17, 2017

46

neuron recorded (Figures 5D and 5F). This approach can be used to evaluate how individual neurons contribute to behavior (Figure 5E) and can serve as the starting point for further exploration of the circuit.

Imaging of Long-Range Neural Activity across Midbrain and Hindbrain

In addition to local effects, circuit activity can also influence neurons in distant downstream networks. Therefore, we took advantage of our configuration to detect the induced GCaMP6s signals across the brain. To record activity distant from the stimulation site, we imaged a 550-μm field of view at 4 Hz. Up to ten different planes, each separated by 12 μm, were sequentially acquired. This volume contained almost the entire midbrain and hindbrain of the larva. A pixelwise regression analysis (Miri et al., 2011) was used to identify cells active upon stimulation leading to behavior. This novel approach of focal stimulation and wide field-of-view imaging revealed behavior-linked activity at and near the stimulation sites (Figures 6A and 6B) but also other "hotspots" in the hindbrain localized 250–300 μm caudal and 60–70 μm dorsal to the nMLF.

Most responsive cells in this hindbrain cluster, not expressing ChR2, showed an activity pattern that was in phase with the photostimulation. However, some cells presented activity profiles out of phase, with a more prominent component near the end of stimulation, coinciding with the relaxation of the tail (Figure 6C, right panel). The optimal regression for these cells included a temporal shift for the fitting functions of 1.6–1.9 s after the onset of the photostimulation. The presented approach enables monitoring the activity, triggered by only a small subset of neurons, throughout a large portion of the brain to uncover the spatiotemporal dynamics underlying behavior.

Morphological Characterization of Functionally Identified Neurons

Developing a model of the circuit mechanisms requires not only accurate interpretation of functional recordings but also knowledge of the interconnectivity and anatomical organization of the circuit. We devised a method to label cells of interest and reconstruct their basic morphology following functional characterization. This approach, based on 2P photoactivation of paGFP, is compatible with ChR2 photostimulation and with GCaMP recordings in the same experiment (Figure 7A). In fish co-expressing nuclear localized GCaMP6s, ChR2, and paGFP, we show that selective photoactivation at 750 nm and the rapid diffusion of activated paGFP enables morphological tracing. This approach can be applied to neurons identified by our analysis, whose photostimulation strongly drives behavior (Figures 7A–7C and S10), or to hindbrain neurons activated in response to targeted stimulation of nMLF neurons (Figures 7D–7F). Tracings of several neurons in different fish can then be merged to find commonalities in their morphology and characteristic projection patterns (Figure S10).

DISCUSSION

Current approaches linking neural function to behavior typically employ either, or both, of two complementary experimental strategies. Functional imaging can be used to identify neuronal subpopulations whose activity is correlated with a behavioral outcome. Alternatively, or in addition, genetically labeled, functionally identified, or spatially confined groups of neurons are targeted by activity manipulations in order to probe their sufficiency or necessity for behavior. Several recent studies in zebrafish have successfully applied the two approaches (Del Bene et al., 2010; Dunn et al., 2016; Kubo et al., 2014; Miri et al., 2011; Thiele et al., 2014). However, all of them lack information about the actual activity patterns elicited by optogenetic stimulation, preventing a mechanistic understanding of the network dynamics causing, supporting, and shaping the behavior. Also, the identity of the neurons, i.e., their morphologies and connectivities, cannot be revealed by imaging or optogenetics alone.

To close these gaps, we have extended the state of the art in four directions: first, we designed a flexible protocol using ChR2 and GCaMP6s that combines 3D 2P high-resolution photostimulation and 3D functional imaging. Volumetric imaging allowed the detection of neuronal activity in planes and regions independent of the stimulation positions. Second, we devised an exploratory strategy to identify behavior-relevant neuronal subsets and to tackle the combinatorial complexity that accompanies multineuron activation experiments. Third, we outlined a flexible computational workflow to relate neuronal activity patterns to specific aspects of the induced behavior, which helps to generate testable hypotheses about circuit mechanisms. Fourth, we combined the expression of ChR2 and nuclear-targeted GCaMP6s with paGFP for the morphological reconstruction of functionally identified and behaviorally relevant neurons.

Many previous reports of 2P activation of ChR2 (Prakash et al., 2012; Rickgauer and Tank, 2009; Zhu et al., 2009) and C1V1 (Prakash et al., 2012) have used fast raster or spiral scanning of a single excitation point over the soma. These scanning approaches have been further extended using CGH to generate a set of beamlets, which are simultaneously scanned over multiple cells with a common trajectory to activate a population of neurons (Carrillo-Reid et al., 2016; Packer et al., 2012, 2015). In general, scanning-based schemes exploit a combination of temporal and spatial current integration from sequentially activated opsins and benefit from long tau-off opsins to sustain the photo-induced current (Chaigneau et al., 2016; Prakash et al., 2012). Here, we adopted a scanless approach to drive simultaneous and parallel activation of ChR2 molecules using spatially extended 2P-CGH profiles (Bègue et al., 2013; Chaigneau et al., 2016; Dal Maschio, 2014; Dal Maschio et al., 2012; Hernandez et al., 2016; Oron et al., 2012; Vaziri and Emiliani, 2012), thereby maximizing instantaneous membrane currents (Oron et al., 2012; Rickgauer and Tank, 2009). In this scheme, temporal integration is less crucial and spatial integration of the current is the principal mechanism of neuronal activation. Using a scanless, 2D extended stimulation approach presents two potential advantages. First, because currents can be effectively integrated using opsins with a relatively short decay time, like ChR2 (Papagiakoumou et al., 2010) and Chronos (Ronzitti et al., 2016), the temporal precision in driving the activity can be enhanced to a submillisecond level (Ronzitti et al., 2016). Second, by using opsins with shorter off kinetics, we are able to minimize the chance of inadvertent photostimulation during
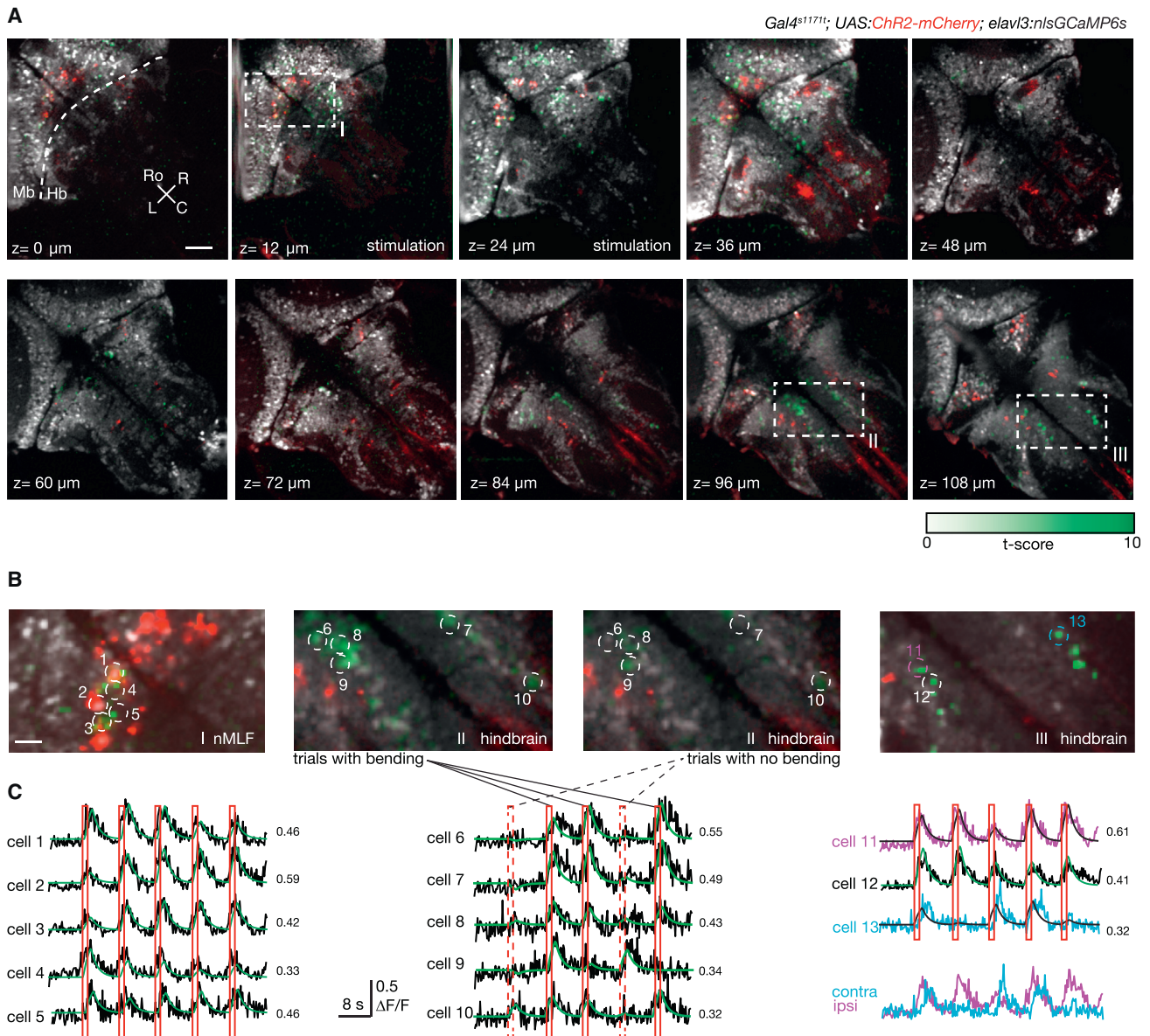
Figure 6. Imaging the Activity Associated with Behavior in Distant Brain Regions

(A) Brain activity induced by nMLF activation. Activity across a large volume of the brain is captured by sequentially imaging ten planes, each separated by 12 μm (at four frames per second). Remote focusing of the imaging plane is combined with the 3D control of the photostimulation pattern to acquire GCaMP signals at each plane while keeping the stimulation targeted on the behaviorally identified neurons in the nMLF. Pixelwise regression analysis of the temporal series is used to pinpoint brain regions with activity profiles matching the stimulation epochs. For stimulation trials resulting in tail bending, the corresponding t-statistic for each pixel is averaged to create a map showing hotspots with activity associated with the behavioral outcome induced (in green). Also shown: ChR2-mcherry expression (in red), and nlsGCaMP6s expression (in gray). The scale bar represents 50 μm.

(B) Higher-magnification view of the regions with dashed outlines in (A), focusing on areas with a high average t-statistic. In the plane at the level of the nMLF (z = 12 μm), where stimulation occurs, the activity is strongly lateralized. However, in the more dorsal layers, regions on both sides of the rostral and caudal hindbrain are active during tail bending. For the plane z = 96 μm, two maps are generated for the t-statistics: one considering trials with tail bending events and the other only trials with no behavior. The scale bar represents 10 μm.

(C) Single-cell profiles of the induced activity in the hindbrain. Example ΔF/F traces (black), from selected neurons in (B), are shown along with the fit (green) and the corresponding coefficient of determination (R^2) from the regression analysis. Red solid bars indicate trials that resulted in behavior, whereas trials without behavior outcome are indicated with dashed red bars. Two response profiles are shown (magenta and cyan; in detail on the right side), which have a noticeable difference in the timing of their responses.
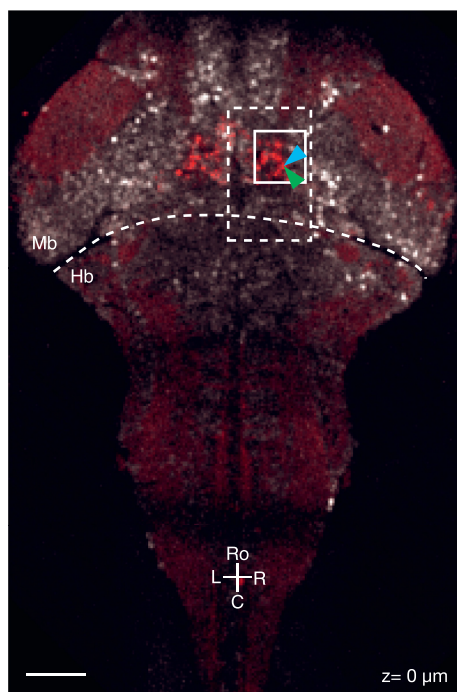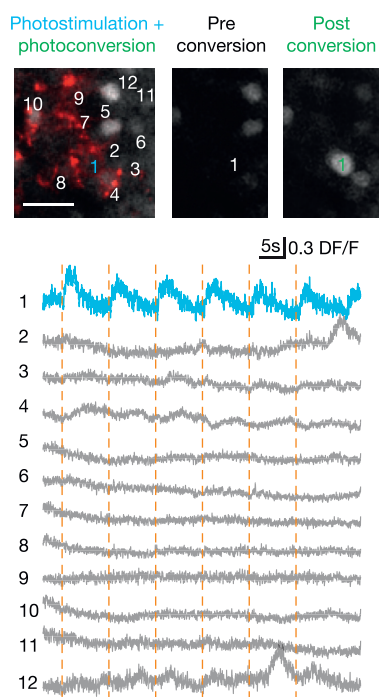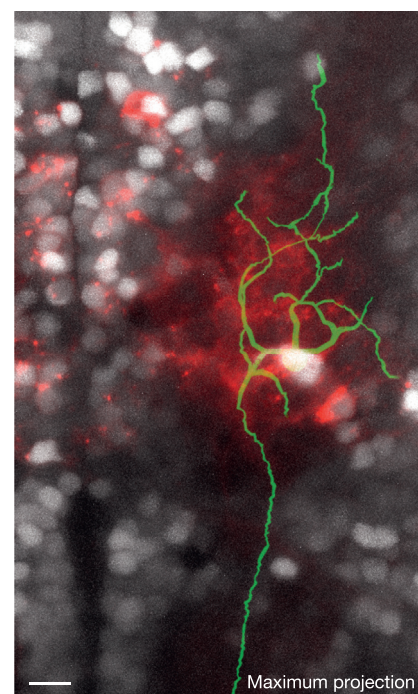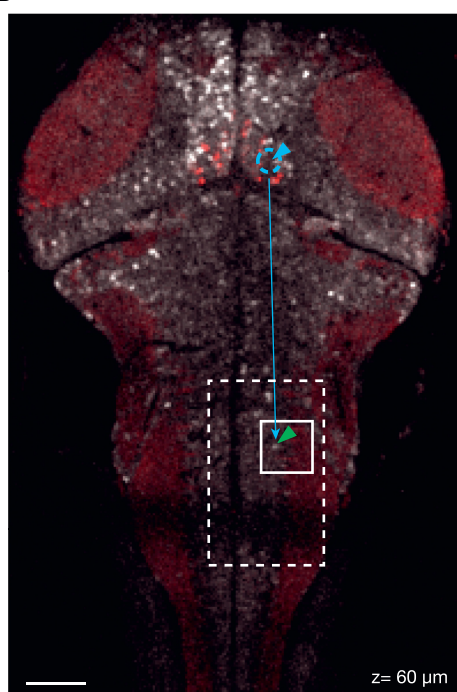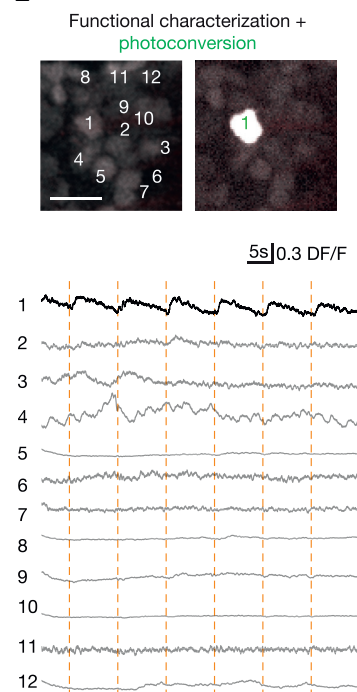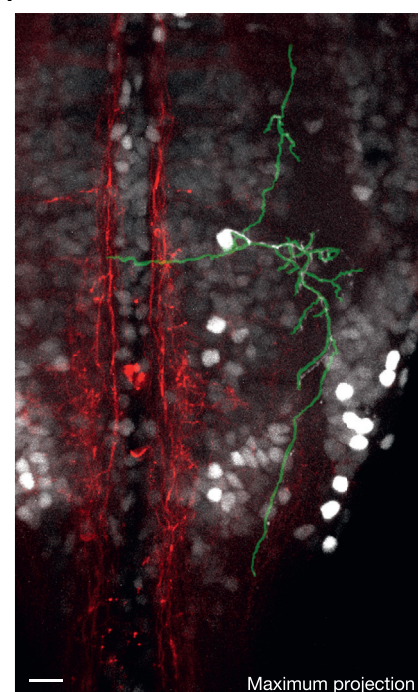
Figure 7. Morphological Reconstruction of Functionally Identified Neurons with Photoactivatable GFP

(A) Combined ChR2 photostimulation, GCaMP imaging, and paGFP photoconversion. A larval brain with pan-neuronal expression of nlsGCaMP6s (gray) and Lyn-TagRFP (light red), ubiquitous expression of paGFP, and cells in the nMLF expressing ChR2 (bright red) are shown. The scale bar represents 50 μm.

(B) Photostimulation + photoactivation protocol. First, a neuron is targeted for ChR2 photostimulation at 920 nm (cell 1; blue) while nlsGCaMP6s signals are imaged at 1,020 nm. The targeted neuron responds reliably to the stimulation. Such triggered activity is not detected in surrounding neurons. Afterward, the same

(legend continued on next page)

recording, since activation of the opsin by the GCaMP6 imaging light will decay more quickly. (Baker et al., 2016; Ronzitti et al., 2016). We note that scanless CGH can be used to generate extended excitation profiles, which can be tailored to the actual sizes and shapes of targeted neurons independently (Dal Maschio et al., 2010). We achieved parallel activation of up to eight neurons in densely packed regions of the zebrafish brain (typical cell body diameter is 6 or 7 μm; inter-cell membrane gaps are 1–3 μm). The current axial confinement of the patterns could potentially be further improved using a 3D temporal focusing approach coupled to the CGH (Hernandez et al., 2016).

We systematically considered actuator/sensor pairs and identified an effective scheme involving ChR2 and GCaMP6s. The current protocol could be straightforwardly adapted or expanded to include a red-shifted calcium sensor, e.g., to image two different neuronal populations or to reduce potential crosstalk. However, we note that the currently available red-emitting indicators produce substantially weaker signals than GCaMP6s (Dana et al., 2016; Shen et al., 2015). Additionally, these sensors have been reported to show a secondary absorption component in the band typically used for 2P ChR2 activation. This leads to a fluorescence emission in a rather broad range (520–600 nm; Dana et al., 2016), which potentially still requires a processing step for contamination subtraction from the functional signal. Even more crucially, there is no information regarding the stability of these sensors when exposed to the 2P light doses occurring in all-optical experimental protocols. GCaMP6s has been extensively evaluated (including in this study) for all these aspects.

Whereas independent technical proofs of principle for 3D photostimulation (Anselmi et al., 2011; Packer et al., 2012) or 3D functional imaging (Grewe et al., 2011; Ji et al., 2016; Lu et al., 2017; Sofroniew et al., 2016; Stirman et al., 2016; Yang et al., 2016) have been reported, we show how these two methods can be optimized and effectively integrated. Several approaches have been proposed for remotely controlled volumetric imaging (Botcherby et al., 2012; Dal Maschio et al., 2011; Duemani Reddy et al., 2008; Grewe et al., 2011). We adopted a configuration based on an ETL (Grewe et al., 2011), because it is relatively easy to implement in an existing optical path and offers a temporal resolution of a few milliseconds.

The combination of volumetric imaging and 3D optogenetics was employed here to investigate two conceptually different aspects. First, what is the response of a local circuit to the stimulation of only a few cells? Second, how do stimulated neurons interact with other circuits across the brain during the execution of a behavioral output? Our approach captured activity throughout the nMLF, identifying distinct sets of neurons tuned to bending or swimming. This result suggests the existence of modular sub-circuits for different behavioral components. In addition, we were able to record the induced activity of distant hindbrain neurons. Such circuit exploration, using cell-scale manipulation, opens up new possibilities to investigate brain circuits. This experimental approach can be used to reveal new intra- and inter-circuit connectivity maps and to functionally validate connectivities predicted by neuroanatomy.

Identifying a subset of neurons from a population, whose activation is sufficient to affect behavior, is a major challenge. Even ignoring differences in activation power and timing, selecting just five neurons from an ensemble of 50 produces over two million possible combinations. Therefore, we used behavior to guide a direct iterative search strategy. First, we identified a relatively large group of neurons in the nMLF that, when activated, evoked a bending of the tail. From this starter set of neurons, several new stimulation patterns were generated, each targeting one neuron less than the previous pattern. Each of these activation patterns was tested, and the group of neurons that induced the greatest tail deflection was selected as the starting point for the next round of refinement. Repetition of this procedure quickly converged on a small subset of neurons that were sufficient to drive the behavioral outcome. Such iterative searches are not feasible with traditional approaches (Aravanis et al., 2007; Fenno et al., 2011; Kubo et al., 2014; Schoonheim et al., 2010; Thiele et al., 2014). Efficiently selecting sets of neurons to activate is a critical step for circuit exploration, which will become especially important when technical solutions enable activating large numbers of cells (Chaigneau et al., 2016; Paluch-Siegler et al., 2015).

Our approach allowed us to identify neuronal ensembles associated with control of tail bending. To handle the complexity of this dataset, we used dimensionality reduction to extract simplified activity patterns from the network. Encouragingly, we found that a small number of independent components captured the most relevant features of network dynamics and behavioral output. This analysis was complemented by regularized regression models to quantify the contributions of individual neurons to behavioral outcome. Neurons within a local circuit may often be correlated, which poses a challenge for regression models; however, the combination of ICA and regularized regression effectively solved this problem. Modeling the behavioral parameters suggests that individual neurons in this network contribute differently to the induced tail deflection. These models, based on the

photostimulated neuron is targeted for 2P paGFP photoactivation with 1 s of 750-nm illumination, resulting in a strong increase in fluorescence. Image extents are outlined in (A) in white.

(C) Reconstruction of the targeted cell. After the diffusion of paGFP, the cell is imaged and its basic morphology can be traced. Image sizes are outlined in (A) with a dashed white box.

(D) Morphological characterization of downstream neurons in the fish hindbrain recruited during nMLF photostimulation. As shown in Figure 6, activation of nMLF neurons drives activity in hindbrain neurons located 250–300 μm caudally. The scale bar represents 50 μm.

(E) From a group of neurons in the hindbrain, imaged during nMLF stimulation, a secondary activated cell is identified and can be photolabeled with paGFP. Image sizes are outlined in (D) in white.

(F) After applying the paGFP photolabeling protocol, functionally identified downstream neurons can be traced to reveal their morphology. Image sizes are outlined in (D) in dashed white. The scale bars in (B), (C), (E), and (F) represent 10 μm. Hb, hindbrain; Mb, midbrain.

recorded activity and behavior, generate testable hypotheses relating the network state to behavioral outcome.

Although the circuit architecture of the zebrafish brain is highly stereotyped (Kubo et al., 2014; Portugues et al., 2014; Robles et al., 2011, 2014), the number and position of most neurons appear to be intrinsically variable among animals. Therefore, to merge and compare findings across different individuals (Randlett et al., 2015), it is useful to obtain additional information about the neurons identified. Our modular approach enabled visualizing the projection patterns of these cells by photoactivation of co-expressed paGFP (Patterson and Lippincott-Schwartz, 2002). The reconstructed neurons can then be compared and validated with a high-resolution annotated anatomical database (e.g., Costa et al., 2016). Combining such morphological information with functional characterizations allows the creation of sophisticated models of circuit function and wiring. Together, the suite of tools introduced here represents a key step for connecting neural circuit architecture to animal behavior at the scale of individual neurons.

STAR★METHODS

Detailed methods are provided in the online version of this paper and include the following:

- KEY RESOURCES TABLE
- CONTACT FOR REAGENT AND RESOURCE SHARING
- EXPERIMENTAL MODEL AND SUBJECT DETAILS
  - ○ Fish procedures
- METHOD DETAILS
  - ○ Imaging pathway
  - ○ 3D 2P-CGH photostimulation
  - ○ Module for behavioral recording
  - ○ Calibration procedures
  - ○ GCaMP6s data processing
  - ○ Resolution measurements
  - ○ Computational analysis
  - ○ Kinematic analysis of behavioral recordings
  - ○ Behavioral models
  - ○ Morphological reconstruction
- QUANTIFICATION AND STATISTICAL ANALYSIS
  - ○ Statistical details
- DATA AND SOFTWARE AVAILABILITY
  - ○ Software main interface
  - ○ Calculation of the phase patterns
  - ○ Pseudocode for phase computation

SUPPLEMENTAL INFORMATION

Supplemental Information includes ten figures and one data file and can be found with this article online at http://dx.doi.org/10.1016/j.neuron.2017.04.034.

AUTHOR CONTRIBUTIONS

M.d.M., J.C.D., and H.B. conceived the project. M.d.M. developed the holographic configuration. J.C.D. developed the software for 3D-2P-CGH, user interface, behavior tracking, and their integration. M.d.M. conducted the experiments, J.C.D. characterized the CGH algorithm performance, and T.O.H. developed the protocol for paGFP and the tracing pipeline. M.d.M., J.C.D.,

and T.O.H. worked on the formal data analysis. M.d.M. wrote the original draft. M.d.M., J.C.D., T.O.H., and H.B. reviewed and edited the final version. H.B. supervised the project.

ACKNOWLEDGMENTS

REFERENCES

Ahrens, M.B., Li, J.M., Orger, M.B., Robson, D.N., Schier, A.F., Engert, F., and Portugues, R. (2012). Brain-wide neuronal dynamics during motor adaptation in zebrafish. Nature 485, 471–477.

Akerboom, J., Chen, T.-W., Wardill, T.J., Tian, L., Marvin, J.S., Mutlu, S., Calderon, N.C., Esposti, F., Borghuis, B.G., Sun, X.R., et al. (2012). Optimization of a GCaMP calcium indicator for neural activity imaging. J. Neurosci. 32, 13819–13840.

Anselmi, F., Ventalon, C., Bègue, A., Ogden, D., and Emiliani, V. (2011). Three-dimensional imaging and photostimulation by remote-focusing and holographic light patterning. Proc. Natl. Acad. Sci. USA 108, 19504–19509.

Aravanis, A.M., Wang, L.P., Zhang, F., Meltzer, L.A., Mogri, M.Z., Schneider, M.B., and Deisseroth, K. (2007). An optical neural interface: in vivo control of rodent motor cortex with integrated fiberoptic and optogenetic technology. J. Neural Eng. 4, S143–S156.

Arrenberg, A.B., Del Bene, F., and Baier, H. (2009). Optical control of zebrafish behavior with halorhodopsin. Proc Natl Acad Sci USA 106, 17968–17973.

Baker, C.A., Elyada, Y.M., Parra, A., and Bolton, M.M. (2016). Cellular resolution circuit mapping with temporal-focused excitation of soma-targeted channelrhodopsin. Elife 5, e14193.

Bègue, A., Papagiakoumou, E., Leshem, B., Conti, R., Enke, L., Oron, D., and Emiliani, V. (2013). Two-photon excitation in scattering media by spatiotemporally shaped beams and their application in optogenetic stimulation. Biomed. Opt. Express 4, 2869–2879.

Bianco, I.H., Ma, L.H., Schoppik, D., Robson, D.N., Orger, M.B., Beck, J.C., Li, J.M., Schier, A.F., Engert, F., and Baker, R. (2012). The tangential nucleus controls a gravito-inertial vestibule-ocular reflex. Curr Biol. 22, 1285–1295.

Botcherby, E.J., Smith, C.W., Kohl, M.M., Débarre, D., Booth, M.J., Juškaitis, R., Paulsen, O., and Wilson, T. (2012). Aberration-free three-dimensional multi-photon imaging of neuronal activity at kHz rates. Proc. Natl. Acad. Sci. USA 109, 2919–2924.

Carrillo-Reid, L., Yang, W., Bando, Y., Peterka, D.S., and Yuste, R. (2016). Imprinting and recalling cortical ensembles. Science 353, 691–694.

Chaigneau, E., Ronzitti, E., Gajowa, M.A., Soler-Llavina, G.J., Tanese, D., Brureau, A.Y., Papagiakoumou, E., Zeng, H., and Emiliani, V. (2016). Two-photon holographic stimulation of ReaChR. Front. Cell. Neurosci. 10, 234.

Chicharro, D., and Ledberg, A. (2012). When two become one: the limits of causality analysis of brain dynamics. PLoS ONE 7, e32466.

Conti, R., Assayag, O., de Sars, V., Guillon, M., and Emiliani, V. (2016). Computer generated holography with intensity-graded patterns. Front. Cell. Neurosci. 10, 236.

Costa, M., Manton, J.D., Ostrovsky, A.D., Prohaska, S., and Jefferis, G.S. (2016). NBLAST: rapid, sensitive comparison of neuronal structure and construction of neuron family databases. Neuron 91, 293–311.

Dal Maschio, M. (2014). Computer-generated holographic beams for the investigation of the molecular and circuit function. In Novel Approaches for Single Molecule Activation and Detection, F. Benfenati, E.D. Fabrizio, and V. Torre, eds. (Springer Berlin Heidelberg), pp. 7–26.

Dal Maschio, M., Difato, F., Beltramo, R., Blau, A., Benfenati, F., and Fellin, T. (2010). Simultaneous two-photon imaging and photo-stimulation with structured light illumination. Opt. Express 18, 18720–18731.

Dal Maschio, M., De Stasi, A.M., Benfenati, F., and Fellin, T. (2011). Three-dimensional in vivo scanning microscopy with inertia-free focus control. Opt. Lett. 36, 3503.

Dal Maschio, M., Difato, F., Beltramo, R., De Stasi, A.M., Blau, A., and Fellin, T. (2012). Optical investigation of brain networks using structured illumination. In Cellular Imaging Techniques for Neuroscience and Beyond, F.G. Wouterlood, ed. (San Diego: Academic Press), pp. 101–120.

Dana, H., Chen, T.-W., Hu, A., Shields, B.C., Guo, C., Looger, L.L., Kim, D.S., and Svoboda, K. (2014). Thy1-GCaMP6 transgenic mice for neuronal population imaging in vivo. PLoS ONE 9, e108697.

Dana, H., Mohar, B., Sun, Y., Narayan, S., Gordus, A., Hasseman, J.P., Tsegaye, G., Holt, G.T., Hu, A., Walpita, D., et al. (2016). Sensitive red protein calcium indicators for imaging neural activity. eLife 5, e12727.

Del Bene, F., Wyart, C., Robles, E., Tran, A., Looger, L., Scott, E.K., Isacoff, E.Y., and Baier, H. (2010). Filtering of visual information in the tectum by an identified neural circuit. Science 330, 669–673.

Duemani Reddy, G., Kelleher, K., Fink, R., and Saggau, P. (2008). Three-dimensional random access multiphoton microscopy for functional imaging of neuronal activity. Nat. Neurosci. 11, 713–720.

Dunn, T.W., Mu, Y., Narayan, S., Randlett, O., Naumann, E.A., Yang, C.-T., Schier, A.F., Freeman, J., Engert, F., and Ahrens, M.B. (2016). Brain-wide mapping of neural activity controlling zebrafish exploratory locomotion. eLife 5, e12741.

Fenno, L., Yizhar, O., and Deisseroth, K. (2011). The development and application of optogenetics. Annu. Rev. Neurosci. 34, 389–412.

Gahtan, E., Tanger, P., and Baier, H. (2005). Visual prey capture in larval zebrafish is controlled by identified reticulospinal neurons downstream of the tectum. J. Neurosci. 25, 9294–9303.

Grewe, B.F., Voigt, F.F., van 't Hoff, M., and Helmchen, F. (2011). Fast two-layer two-photon imaging of neuronal cell populations using an electrically tunable lens. Biomed. Opt. Express 2, 2035–2046.

Haist, T., Schönleber, M., and Tiziani, H.J. (1997). Computer-generated holograms from 3D-objects written on twisted-nematic liquid crystal displays. Opt. Commun. 140, 299–308.

Hernandez, O., Guillon, M., Papagiakoumou, E., and Emiliani, V. (2014). Zero-order suppression for two-photon holographic excitation. Opt. Lett. 39, 5953–5956.

Hernandez, O., Papagiakoumou, E., Tanese, D., Fidelin, K., Wyart, C., and Emiliani, V. (2016). Three-dimensional spatiotemporal focusing of holographic patterns. Nat. Commun. 7, 11928.

Houweling, A.R., and Brecht, M. (2008). Behavioural report of single neuron stimulation in somatosensory cortex. Nature 451, 65–68.

Huber, D., Petreanu, L., Ghitani, N., Ranade, S., Hromádka, T., Mainen, Z., and Svoboda, K. (2008). Sparse optical microstimulation in barrel cortex drives learned behaviour in freely moving mice. Nature 451, 61–64.

Inagaki, H.K., Jung, Y., Hoopfer, E.D., Wong, A.M., Mishra, N., Lin, J.Y., Tsien, R.Y., and Anderson, D.J. (2014). Optogenetic control of Drosophila using a red-shifted channelrhodopsin reveals experience-dependent influences on courtship. Nat. Methods 11, 325–332.

Inoue, M., Takeuchi, A., Horigane, S., Ohkura, M., Gengyo-Ando, K., Fujii, H., Kamijo, S., Takemoto-Kimura, S., Kano, M., Nakai, J., et al. (2015). Rational design of a high-affinity, fast, red calcium indicator R-CaMP2. Nat. Methods 12, 64–70.

Ji, N., Freeman, J., and Smith, S.L. (2016). Technologies for imaging neural activity in large volumes. Nat. Neurosci. 19, 1154–1164.

Kiehn, O. (2016). Decoding the organization of spinal circuits that control locomotion. Nat. Rev. Neurosci. 17, 224–238.

Kim, C.K., Miri, A., Leung, L.C., Berndt, A., Mourrain, P., Tank, D.W., and Burdine, R.D. (2014). Prolonged, brain-wide expression of nuclear-localized GCaMP3 for functional circuit mapping. Front. Neural Circuits 8, 138.

Kim, S.S., Franconville, R., Turner-Evans, D., and Jayaraman, V. (2015). Optogenetics in Drosophila melanogaster. In New Techniques in Systems Neuroscience, A.D. Douglass, ed. (Springer International Publishing), pp. 147–176.

Kubo, F., Hablitzel, B., Dal Maschio, M., Driever, W., Baier, H., and Arrenberg, A.B. (2014). Functional architecture of an optic flow-responsive area that drives horizontal eye movements in zebrafish. Neuron 81, 1344–1359.

Lu, R., Sun, W., Liang, Y., Kerlin, A., Bierfeld, J., Seelig, J.D., Wilson, D.E., Scholl, B., Mohar, B., Tanimoto, M., et al. (2017). Video-rate volumetric functional imaging of the brain at synaptic resolution. Nat. Neurosci. 20, 620–628.

Miri, A., Daie, K., Burdine, R.D., Aksay, E., and Tank, D.W. (2011). Regression-based identification of behavior-encoding neurons during large-scale optical imaging of neural activity at cellular resolution. J. Neurophysiol. 105, 964–980.

Naumann, E.A., Fitzgerald, J.E., Dunn, T.W., Rihel, J., Sompolinsky, H., and Engert, F. (2016). From whole-brain data to functional circuit models: the zebrafish optomotor response. Cell 167, 947–960.e20.

Olsen, S.R., and Wilson, R.I. (2008). Cracking neural circuits in a tiny brain: new approaches for understanding the neural circuitry of Drosophila. Trends Neurosci. 31, 512–520.

Oron, D., Papagiakoumou, E., Anselmi, F., and Emiliani, V. (2012). Two-photon optogenetics. Prog. Brain Res. 196, 119–143.

Packer, A.M., Peterka, D.S., Hirtz, J.J., Prakash, R., Deisseroth, K., and Yuste, R. (2012). Two-photon optogenetics of dendritic spines and neural circuits. Nat. Methods 9, 1202–1205.

Packer, A.M., Russell, L.E., Dalgleish, H.W.P., and Häusser, M. (2015). Simultaneous all-optical manipulation and recording of neural circuit activity with cellular resolution in vivo. Nat. Methods 12, 140–146.

Paluch-Siegler, S., Mayblum, T., Dana, H., Brosh, I., Gefen, I., and Shoham, S. (2015). All-optical bidirectional neural interfacing using hybrid multiphoton holographic optogenetic stimulation. Neurophotonics 2, 031208.

Panzeri, S., Harvey, C.D., Piasini, E., Latham, P.E., and Fellin, T. (2017). Cracking the neural code for sensory perception by combining statistics, intervention, and behavior. Neuron 93, 491–507.

Papagiakoumou, E., Anselmi, F., Bègue, A., de Sars, V., Glückstad, J., Isacoff, E.Y., and Emiliani, V. (2010). Scanless two-photon excitation of channelrhodopsin-2. Nat. Methods 7, 848–854.

Patterson, G.H., and Lippincott-Schwartz, J. (2002). A photoactivatable GFP for selective photolabeling of proteins and cells. Science 297, 1873–1877.

Portugues, R., Feierstein, C.E., Engert, F., and Orger, M.B. (2014). Whole-brain activity maps reveal stereotyped, distributed networks for visuomotor behavior. Neuron 81, 1328–1343.

Prakash, R., Yizhar, O., Grewe, B., Ramakrishnan, C., Wang, N., Goshen, I., Packer, A.M., Peterka, D.S., Yuste, R., Schnitzer, M.J., et al. (2012). Two-photon optogenetic toolbox for fast inhibition, excitation and bistable modulation. Nat. Methods 9, 1171–1179.

Randlett, O., Wee, C.L., Naumann, E.A., Nnaemeka, O., Schoppik, D., Fitzgerald, J.E., Portugues, R., Lacoste, A.M.B., Riegler, C., Engert, F., et al. (2015). Whole-brain activity mapping onto a zebrafish brain atlas. Nat. Methods 12, 1039–1046.

Rickgauer, J.P., and Tank, D.W. (2009). Two-photon excitation of channelrhodopsin-2 at saturation. Proc. Natl. Acad. Sci. USA 106, 15025–15030.

Rickgauer, J.P., Deisseroth, K., and Tank, D.W. (2014). Simultaneous cellular-resolution optical perturbation and imaging of place cell firing fields. Nat. Neurosci. 17, 1816–1824.

Robles, E., Smith, S.J., and Baier, H. (2011). Characterization of genetically targeted neuron types in the zebrafish optic tectum. Front. Neural Circuits 5, 1.

Robles, E., Laurell, E., and Baier, H. (2014). The retinal projectome reveals brain-area-specific visual representations generated by ganglion cell diversity. Curr. Biol. 24, 2085–2096.

Ronzitti, E., Conti, R., Papagiakoumou, E., Tanese, D., Zampini, V., Chaigneau, E., Foust, A.J., Klapoetke, N., Boyden, E.S., and Emiliani, V. (2016). Sub-millisecond optogenetic control of neuronal firing with two-photon holographic photoactivation of Chronos. bioRxiv. http://dx.doi.org/10.1101/062182.

Schoonheim, P.J., Arrenberg, A.B., Bene, F.D., and Baier, H. (2010). Optogenetic localization and genetic perturbation of saccade-generating neurons in zebrafish. J. Neurosci. 30, 7111–7120.

Scott, E.K., and Baier, H. (2009). The cellular architecture of the larval zebrafish tectum, as revealed by gal4 enhancer trap lines. Front Neural Circuits 3, 13.

Semmelhack, J.L., Donovan, J.C., Thiele, T.R., Kuehn, E., Laurell, E., and Baier, H. (2014). A dedicated visual pathway for prey detection in larval zebrafish. Elife 3, e04878.

Severi, K.E., Portugues, R., Marques, J.C., O'Malley, D.M., Orger, M.B., and Engert, F. (2014). Neural control and modulation of swimming speed in the larval zebrafish. Neuron 83, 692–707.

Shen, Y., Lai, T., and Campbell, R.E. (2015). Red fluorescent proteins (RFPs) and RFP-based biosensors for neuronal imaging applications. Neurophotonics 2, 031203.

Smirnov, M.S., Evans, P.R., Garrett, T.R., Yan, L., and Yasuda, R. (2017). Automated remote focusing, drift correction, and photostimulation to evaluate structural plasticity in dendritic spines. PLoS ONE 12, e0170586.

Sofroniew, N.J., Flickinger, D., King, J., and Svoboda, K. (2016). A large field of view two-photon mesoscope with subcellular resolution for in vivo imaging. Elife 5, e14472.

Stirman, J.N., Smith, I.T., Kudenov, M.W., and Smith, S.L. (2016). Wide field-of-view, multi-region, two-photon imaging of neuronal activity in the mammalian brain. Nature Biotechnol. 34, 857–862.

Szabo, V., Ventalon, C., De Sars, V., Bradley, J., and Emiliani, V. (2014). Spatially selective holographic photoactivation and functional fluorescence imaging in freely behaving mice with a fiberscope. Neuron 84, 1157–1169.

Thiele, T.R., Donovan, J.C., and Baier, H. (2014). Descending control of swim posture by a midbrain nucleus in zebrafish. Neuron 83, 679–691.

Vaziri, A., and Emiliani, V. (2012). Reshaping the optical dimension in optogenetics. Curr. Opin. Neurobiol. 22, 128–137.

Weichwald, S., Meyer, T., Özdenizci, O., Schölkopf, B., Ball, T., and Grosse-Wentrup, M. (2015). Causal interpretation rules for encoding and decoding models in neuroimaging. Neuroimage 110, 48–59.

Yang, W., Miller, J.K., Carrillo-Reid, L., Pnevmatikakis, E., Paninski, L., Yuste, R., and Peterka, D.S. (2016). Simultaneous multi-plane imaging of neural circuits. Neuron 89, 269–284.

Yizhar, O., Fenno, L.E., Prigge, M., Schneider, F., Davidson, T.J., O'Shea, D.J., Sohal, V.S., Goshen, I., Finkelstein, J., Paz, J.T., et al. (2011). Neocortical excitation/inhibition balance in information processing and social dysfunction. Nature 477, 171–178.

Zhu, P., Narita, Y., Bundschuh, S.T., Fajardo, O., Schärer, Y.P., Chattopadhyaya, B., Bouldoires, E.A., Stepien, A.E., Deisseroth, K., Arber, S., et al. (2009). Optogenetic dissection of neuronal circuits in zebrafish using viral gene transfer and the Tet system. Front. Neural Circuits 3, 21.

STAR★METHODS

KEY RESOURCES TABLE

REAGENT or RESOURCE	SOURCE	IDENTIFIER
Experimental Models: Organisms/Strains		
Zebrafish: Et(−0.6hsp70l:Gal4-VP16)s1171t	Scott and Baier, 2009	ZFIN: ZDB-GENO-080327-167
Zebrafish: Tg(UAS:ChR2(H134R)-mCherry)mpn134	First reference here	N/A
Zebrafish: Tg(UAS:ChR2(H134R)-mCherry)s1985t	Arrenberg et al., 2009	ZFIN: ZDB-FISH-150901-20696
Zebrafish: Tg(UAS:GCaMP6s)mpn101	Thiele et al., 2014	ZFIN: ZDB-FISH-150901-22562
Zebrafish: Tg(Cau.Tuba1:c3paGFP)a7437	Bianco et al., 2012	ZFIN: ZDB-FISH-150901-16227
Zebrafish: Tg(elavl3:nlsGCaMP6s)mpn400	First reference here	N/A
Zebrafish: Tg(elavl3:lyn-tagRFP)mpn404	First reference here	N/A
Zebrafish: Tg(UAS:paGFP)mpn143	First reference here	N/A
Software and Algorithms		
Multiplane Adaptive Gerchberg-Saxton algorithm (Python)	Haist et al., 1997	https://github.com/joe311/holo_project
Custom image processing routines, ICA, Linear regression models	Python 2.7 (plus sklearn)	RRID: SCR_008394
Message passing library	Zeromq	http://zeromq.org/
Message serialization library	Google Protocol Buffers	https://developers.google.com/protocol-buffers/
Image analysis	Fiji	RRID:SCR_002285
Neuron morphology reconstruction	neuTube	http://www.neutracing.com/
Other		
2P Photostimulation source	Coherent	Chameleon Ultra II
Electro-optic modulator	Conoptics	Model 302RM
Beam expander upstream the SLM	Thorlabs	BE02-B (2x), AC254-30-B-ML and AC254-80-B-ML
Half-wave plates	Thorlabs	AQWP10M
Spatial light modulator	Hamamatsu	X10468-07
Telescopes downstream the SLM	Thorlabs	AC508-400-B-ML, AC508-200-B-ML and AC508-120-B-ML, Tube lens
Combining optics	Thorlabs	PBS102
Objectives for imaging and photostimulation	Olympus	Olympus 20x NA 1.0 wd 2.0mm (XLUMPLFLN)
Objectives for calibration and behavior tracking	Olympus	Olympus 60x NA 1.0 wd 2mm (LUMPLanFL N), Olympus 4x NA 0.1 wd 18.5mm (XLUMPLFLN)
Camera for calibration and behavior tracking	Thorlabs	DCC1545M (12801x1024, USB2.0,Monochrome)
Light source for behavior	Thorlabs	M850LP1 and ACL2520U

CONTACT FOR REAGENT AND RESOURCE SHARING

As Lead Contact, Herwig Baier is responsible for all reagent and resource requests. Please contact Herwig Baier at hbaier@neuro.mpg.de with requests and inquiries.

EXPERIMENTAL MODEL AND SUBJECT DETAILS

Fish procedures

Experiments were carried out in accordance with an animal protocol approved by the regional government (Regierung von Oberbayern). Fish were raised at 28°C on a 14h light/10h dark cycle using standard procedures. Zebrafish larvae 5-7 days post-fertilization (dpf) carrying *alpha-tubulin:paGFP* were used to test the system. *Gal4s1171t;UAS:ChR2(H134R)-mCherry* and *Gal4s1171t;UAS:ChR2(H134R)-mCherry;UAS:paGFP* fish were used for circuit mapping experiments. *Gal4s1171t;UAS:GCaMP6s* was used as a ChR2-negative control. *Gal4s1171t;UAS:ChR2(H134R)-mCherry;UAS:GCaMP6s* and *elavl3:GCaMP5G;Gal4s1171t/UAS:ChR2(H134R)-mCherry* as well as *elavl3:nlsGCaMP6s;Gal4s1171t;UAS:ChR2(H134R)-mCherry* fish were used in experiments

combining photostimulation and calcium imaging. For validation and testing of the approach, including morphological constructions, the following genotype was used: *elavl3:nlsGCaMP6s;Gal4s1171t;UAS:ChR2(H134R)-mCherry;elavl3:lyn-TagRFP;alpha-tubulin:paGFP.* Larvae aged 5-7 dpf were embedded in 1.5%–2% low-melting-point agarose and the agarose surrounding the tail was carefully removed using a scalpel blade to free the tail. Fish were allowed to recover for four hours before starting the experimental sessions. A full list of the fish lines used is provided in the Key Resource Table.

METHOD DETAILS

Imaging pathway

The imaging path is based on a galvo-galvo commercial 2P design (Femtonics 3DRC, Femtonics, Tuzlo, Hungary) driven by a Ti:Sapphire source (Chameleon Ultra II, Coherent). The fluorescence collection path includes a DM670HP dichroic mirror, an IR blocking filter, and a 563HP mirror splitting the fluorescence light toward two GaAsP detectors (Hamamatsu H10770PA-40) equipped with EM525/50 and EM590/60 emission filters, respectively. In addition to the original layout, an electrically tunable lens (ETL, Optotune, EL-10-30-Ci-IR-LD-MV) was inserted along the path upstream of the galvo scanner, to enable fast remote refocusing. In this position, the ETL achieved a 75 μm z-travel range at the sample, when coupled with a 20x LUMPLAN Olympus (NA 0.9, WD 2.2 mm) objective (used for most experiments), or 125 μm with a 16x CFI70 Nikon objective (NA 0.8, WD 3.0mm). As the combination of the imaging and photostimulation paths is achieved by combining beams with different polarization orientations, before the ETL, a half-wave plate (AQWP10M, Thorlabs) is inserted to rotate the polarization of the imaging beam and a polarizing beam splitter (PBS, PBS102, Thorlabs) is placed after the scan lens, allowing the vertically polarized imaging beam to pass through.

3D 2P-CGH photostimulation

The path for Computer Generated Holography (CGH) is driven by a dedicated Ti:Sapphire laser (Chameleon Ultra II, Coherent) whose intensity is modulated using a Pockel's cell (Model 302RM, Conoptics). The phase modulation is obtained using a nematic liquid-crystal spatial light modulator (SLM, Hamamatsu, X10468-07). Following intensity control but before the SLM, the path includes a beam expansion step (first stage: BE02M-B, Thorlabs; second stage f1 = 30mm, f2 = 80mm, about 4.2x in total), a diaphragm, and a half-wave plate (AQWP10M, Thorlabs). These components are required to condition the input beam and to match it to the window size and the polarization preference of the SLM. The resulting beam slightly under-fills the short side of the SLM window (12 × 15.8 mm^2). Downstream of the SLM, a lens (f3 = 400mm, AC508-400-B-ML, Thorlabs) conjugates the SLM plane, where the phase modulation is imposed, to the first Fourier plane where the amplitude modulation is rendered. At this plane, a mirror can be combined with a zero order block (constructed from aluminum foil on a glass slide) to suppress the residual light component not effectively modulated by the SLM. Alternatively (as in Hernandez et al., 2014), a cylindrical lens with long focal distance can be inserted in front of the SLM, with a digital lens applied to the first-order diffracted component to separate it from the zero-order. A lens (f4 = 200mm, AC508-200-B-ML, Thorlabs) is used as second element of a telescope, to relay the SLM plane to an intermediate plane where a replica of the SLM image is generated. This replica of the SLM is imaged at the backfocal plane of the objective by means of a second telescope (f5 = 120mm and the tube lens). This is achieved by rotating the polarization direction with a half-wave plate (AQWP10M, Thorlabs), so that the photostimulation beam is reflected at the level of the PBS combining the two paths. With this layout for the phase modulation path, a volume of 200 × 200 × 250 μm^3 could be effectively addressed using the 20x objective. A camera is included under the imaging/photostimulation objective for the alignment of the two optical paths. The combination of a 60x objective (Olympus LumPLanFl N W WD 2.0mm NA = 1) with a short focal length lens (f = 60 mm) is used for system calibration.

A detailed interactive drawing of the optical path is accessible as Data S1. This 3D pdf can be viewed in Adobe Acrobat PDF Reader to evaluate the optical path from different perspectives and to measure distances between optical elements.

Module for behavioral recording

To record the behavior, the larvae was illuminated with a high power IR LED (850 nm, M850LP1, Thorlabs) placed approximately 10 cm from the fish's position and collimated with an aspheric condenser (ACL2520U, Thorlabs). A high-speed IR-sensitive camera (Thorlabs DCC1545M CMOS) was used for acquisition at 300 frames per second. A lens (f6 = 100mm) and a 4x objective (4X Plan N NA = 0.1, Olympus) were used to conjugate the fish plane to the camera plane.

A complete list of parts is available in the Key Resource Table.

Calibration procedures

At the beginning of an experimental session, a calibration routine is run involving four sequential steps: 1. Mapping of the working range of the ETL to obtain a z-shift versus voltage relation; 2. Identification of the optimal look up table (LUT) for the SLM, to map a 2π phase stroke onto the SLM's 8-bit modulation values; 3. XY registration, to map the coordinate system of the imaging beam to the patterns generated by the phase modulation system; 4. Z registration, to precisely map how axial shifts by phase modulation relate to z-offsets (in μm) in the sample volume. To calibrate the ETL, ten command voltages, covering the full travel range, are sequentially applied. At each voltage, the corresponding offset along z of the imaging beam is measured with respect to the reference position by moving the objective to bring the shifted beam into focus. A fit is calculated on these data, to generate a function returning the voltage required for a desired offset of the focal plane.

In the second step, which calibrates the LUT for the SLM values by finding the optimal linear scaling factor, two routines are executed. In the first coarse routine, phase patterns using 8 different scaling factors for the LUT are projected. The pattern that minimizes zero and second order components is selected. The second routine, centered around the previous optimum, evaluates a finely-spaced set of 8 values and selects the best. Following this, XY spatial registration begins. The galvo mirrors are used to sequentially steer the imaging beam to a series of points. At each point, the calibration camera captures an image, and the beam center is automatically detected. Next, a series of phase modulation patterns corresponding to points are played, and the corresponding images are also automatically captured and quantified. Based on the points captured from the two different paths, the optimal affine transformation between the two coordinate systems is calculated. This transformation is applied to all following holographic patterns. The maximal spatial discrepancy accepted between the imaging and photostimulation beams is 1 μm. In the last step, for the registration along the axial (Z) dimension, a similar approach is used. The holographic system plays a series of patterns, with phase modulations that correspond to different axial offsets. For each pattern, the objective position required to optimally focus the holographic pattern is measured. A low-order polynomial is fit onto the measured values, to provide a transformation between a desired axial (Z) position, and the required 'lens' for the computation of the phase modulation pattern.

GCaMP6s data processing

For all acquisitions that included behavior tracking and photostimulation, standard raster scanning was used at 4 volumes, or frames, per second (for multiplane or single-plane recordings, respectively). For some timing-sensitive measurements, for instance to characterize the protocol, a quick random access line scan was used at 300-500 Hz with 15-25 pixels per cell. To correct for offsets in the image background/baseline in some recordings, a region outside of the expression pattern was selected, and the average intensity of this background region was subtracted.

With the adopted sensor-actuator pair the fluorescence imaging signal can be contaminated by photostimulation. However, this can be effectively subtracted by a post-processing algorithm. The contamination artifact equally affects all pixels, whether the pixels are 'silent' and only contain the artifact, or if there are also underlying changes in GCaMP fluorescence from neuronal activity. The algorithm automatically selects a subset of inactive pixels, across the different lines of the imaging field of view, and uses percentile filtering on these inactive pixels to detect the level of the stimulation artifact. This can then be subtracted, resulting in a nearly contamination-free signal at the scale of the normal GCaMP activity transients. These data were further processed with custom Python routines. First for volumetric imaging, the raw data series are de-interleaved into sub-streams, one for each plane imaged. This was followed by rigid-body image registration to correct for drift and motion. Next the dataset was temporally filtered, with a 0.65 s rolling average window, to reduce noise. As is usual for such data, $\Delta F/F$ was used for normalization, using a baseline measured toward the start of imaging.

Resolution measurements

For measuring the lateral resolution of ChR2 stimulation, circular regions of interest, 6 μm in diameter, were moved across a subset of neurons expressing ChR2 and GCaMP6s. The activity of all sampled cells was recorded at 300 Hz by line scan or with high-resolution acquisition protocols with stimulation epochs lasting for 200 ms. For the axial (Z) resolution, the relative displacement between the imaging and the photostimulation planes was achieved either by controlling the z level computed in the phase correction or by moving the objective in a different plane and refocusing with the ETL on the reference plane. To score the activity change, the maximum $\Delta F/F$ relative to the targeted cell was computed for each pixel. This was fit with an exponential model based on the distance from the target cell. For the data comparing spontaneous and ChR2 induced GCaMP responses, both GCaMP6s and nlsGCaMP6s were evaluated. The time-to-peak and halftime-decay of the signal were used as the basis for a comparison of the temporal dynamics.

Computational analysis

To extract relevant patterns in network activity, a dimensionality reduction approach was applied, using Independent Component Analysis (ICA) from the Python scikit-learn library. This analysis extracts common temporal patterns of activity, and returns for each neuron a set of weights, one for each component, representing the contribution of the neuron to the component. Circuit activity maps were generated showing the position and weights of neurons that contribute to each component. A laterality index was then calculated to represent the spatial degree of symmetry of the activity associated to the different maps. The laterality index, defined as ((sum of weights on the right) – (sum of weights on the left)) / (sum of all the weights)), produces a score that ranges from -1 to 1. Imaging data over large fields of view (about 500 × 500 μm^2) were analyzed using a pixel-wise regression-based identification of activity recorded. For every stimulation epoch in the protocol, a binary regressor was created and convolved with a single exponential kernel to model nlsGCaMP6s signals. The time constant for the sensor impulse response was set to $tau_{off} = 2.3$ s based on the optimization of the coefficient of determination (R^2) for a set of test recordings. Regressors were then fit to the data using a linear combination including a constant term. From the resulting set of coefficients, the t-statistic was calculated for each pixel and averaged across trials with consistent behavioral outcome.

Kinematic analysis of behavioral recordings

From the behavior data recorded at 300 fps, the tail dynamics were extracted using an automated Python-based algorithm, which maps ~30 points along the tail. A heat-map of the tail position was calculated to show the lateral deflection of each point along the tail,

relative to the overall tail length. To quantify the tail movement using a single parameter, the tail deflection angle was extracted, which is the angle between a line drawn from the base of the tail to the most caudal points of the tail and a reference direction corresponding to the fish midline. A median or Gaussian filter with a duration of a 50 ms was applied to smooth the recording and reduce high-frequency noise. A threshold for significant tail bending was set to an angle beyond 5 standard deviations from the baseline.

Behavioral models

A regularized regression was applied to assign a behavioral score to the photostimulated neurons based on the deflection angle (see Figure 3). The regression, from the Python scikit-learn library, took advantage of an elastic-net regularization to reduce the overfitting and to provide a sparse representation of the components involved. To discriminate between different behavior outcomes across different trials, a hierarchical clustering was used (Figure 5A). This takes as input vectors the Fourier spectra of the tail deflection angle measured in a 10 s window surrounding the stimulation event. A logistic model was applied to characterize the contribution of the individual neurons differentially associated with the two main classes of behavioral outcomes (bending and swimming). For each neuron, the coefficients of the resulting model were used to generate a map showing its impact toward each of the two observed main behaviors. To characterize the influence of the neural activity on tail deflection, we generated a regularized linear model on a subgroup (training subset) of the trials of tail bending events to express the contribution of each neuron to the tail deflection in terms of degree per $\Delta F/F$. This model was then tested on a non-overlapping subgroup of tail bending trials (testing subset) to reconstruct the tail deflection from the activity of all neurons. This cross-validation procedure used a random split in the dataset. The quality of the regression with respect to the number of components was evaluated in terms of the coefficient of determination (R^2).

Morphological reconstruction

paGFP photoactivation was carried out at 750 nm, typically with a one second long stimulation. For the reconstruction of the behaviorally relevant neurons, the imaging source was tuned to 750 nm and the beam scanned over a small ROI centered in the soma for about 1 s. A few minutes after the photoconversion protocol, a z stack was acquired at 1020 nm. The photoactivated neurons were traced using the software neuTube (Build1.0z). The corresponding traced 3D representation was then projected onto the original image to highlight the morphology of the photolabeled neuron.

QUANTIFICATION AND STATISTICAL ANALYSIS

Statistical details

All tests performed were two-sided. Data distributions were checked, when applicable, for normality with a quantile plot. For statistics involving multiple fish, the mean value for each fish was used for test comparisons, as pooling individual trials together from multiple fish violates the assumption of independent measurements. Fish with stronger and more complete expression patterns (covering as many cells as possible) were preferentially selected for experiments. Behavioral trials with two or more spontaneous swimming bouts in the 60 s preceding experimental trials were excluded. Imaging trials with a Z-drift greater than 2 μm were excluded. XY shifts before and after stimulation protocols were checked following registration, and trials with shifts exceeding 2 μm were discarded.

DATA AND SOFTWARE AVAILABILITY

Software main interface

A Python-based library was developed to control the SLM and to interface with the proprietary software controlling the imaging system (MES, Femtonics Ltd.). The core of the system is a server module (holobase.py – see diagram Figure S3A) which is in charge of all the procedures required for the generation of the calibrated light distribution including camera acquisition, calibration, SLM look up table (LUT) and flatness correction, Z control, and phase pattern computation. Different client applications can interface with the server. One client application is hooked into the MES software (using holoclient.py) and is used to launch the calibration procedure from MES. A simple client provides a script interface for quick control of multiplane patterns (holomultiZ.py). Another client is a graphical user interface (GUI – holoGUI.py), which is the primary point of interaction for the user. This interface allows the user to load TIF stacks acquired on the imaging system. Temporal and power parameters can be configured and a polygonal selection tool is used to select the desired illumination patterns at the different planes of the z stack. The patterns are compactly stored in a scalable vector graphics (SVG) based format, exchanged with the server, and are mapped onto the holographic system's coordinates obtained during the calibration. All the information about the stimulation pattern are sent to a routine for the calculation of the phase profile with an algorithm based on Discrete Fourier Transforms (maGS engine). The communication between the clients and server uses messages passed with the ZMQ library (http://zeromq.org). Google protocol buffers (https://developers.google.com/protocol-buffers/) are used to provide language-neutral data storage.

Calculation of the phase patterns

In order to engineer the desired light distribution at the sample, a multiplane adaptive Gerchberg-Saxton (maGS) algorithm (Haist et al., 1997) was implemented. With this iterative procedure based on Fast Fourier Transforms, the phase modulation required for

multiplane photostimulation patterns is computed from the mixing of multiple complex 2D fields, one for each different plane along the propagation direction z. Basically, for each loop through the algorithm execution, the phase of each 2D field computed at different planes is adjusted with a lens-type modulation corresponding to its axial offset. This adjustment is applied twice per loop, once with a negative profile before the forward propagation of the wavefront, and once with a positive profile after the backward propagation of the wavefront before the mixing step. The mixing of all the independently calculated fields is obtained by a summation of the electrical fields and the calculation of the argument to retrieve the unified phase profile. The basic GS algorithm can generate graded intensities when initialized with the proper target distribution within the same plane (Conti et al., 2016) or control the relative intensities between planes (Hernandez et al., 2016). We used the same approach to correct for the diffraction efficiency. However, to handle the relative power intensities between different planes/ROIs, our algorithm reweights the corresponding fields before mixing, using an adaptive procedure. Below is pseudocode corresponding to the core of the algorithm, where i refers to the imaginary unit, *abs* is the absolute value, *exp* is the exponential function, *arg* returns the argument of complex numbers, *FFT* is the fast Fourier transform, *iFFT* is the inverse FFT, and # denotes comment lines.

Pseudocode for phase computation

```
def GS_3D(target_amplitudes, target_Zs):
    # target_amplitudes is a list of desired amplitude patterns
    # target Zs is a corresponding list of axial offsets for each target amplitude

    target_ratios = compute the ideal normalized intensity across all planes
    ini_amplitudes = random initial fields
    unified_slm_field = random initial field

    for each iteration:
      slmfields= emply list of fields

      for each plane:
        slm_field = ini_amplitude at this plane * exp(i * (unified_slm_field - plane_lens))
        target_field = fft2((slm_field)
        target_field = abs(target_amplitude at this plane) * exp(i * np.angle(target_field))
        slm_field = ifft2(target_field)
        slm_field = angle(slm_field) + plane_lens
        slm_field = ini_amplitude at this plane * exp(i * slm_field)
        slmfields = append slmfield

      compute the normalized intensity across all planes
      reweight the slm_fields by half of the difference between the computed and ideal target_ratios
      unified_slm_field = angle(sum(slm_fields)) % (2 * pi)
    return unified_slm_field
```

We have released the core components of our code under a GPL open-source license. For more details about the software and the code, please see: https://github.com/joe311/holo_project.

Supplemental Information

Linking Neurons to Network Function

and Behavior by Two-Photon Holographic

Optogenetics and Volumetric Imaging

Marco dal Maschio, Joseph C. Donovan, Thomas O. Helmbrecht, and Herwig Baier

Figure S1   (related to Figure 1)

A

Fourier Lens f3 = 400mm

First Fourier Plane

Spatial Light Modulator (SLM)

Beam Expander (2.5x)
f1 = 30mm, f2 = 80mm

Telescope
f3 = 400mm, f4 = 200mm

Half-wave Plate

Half-wave Plate

Photostimulation
Source

Imaging Source

Half-wave Plate

First SLM replica

f5 = 120mm

Electrically Tunable Lens

Galvo Mirrors

Scan Lens

Polarizing Beam Splitter
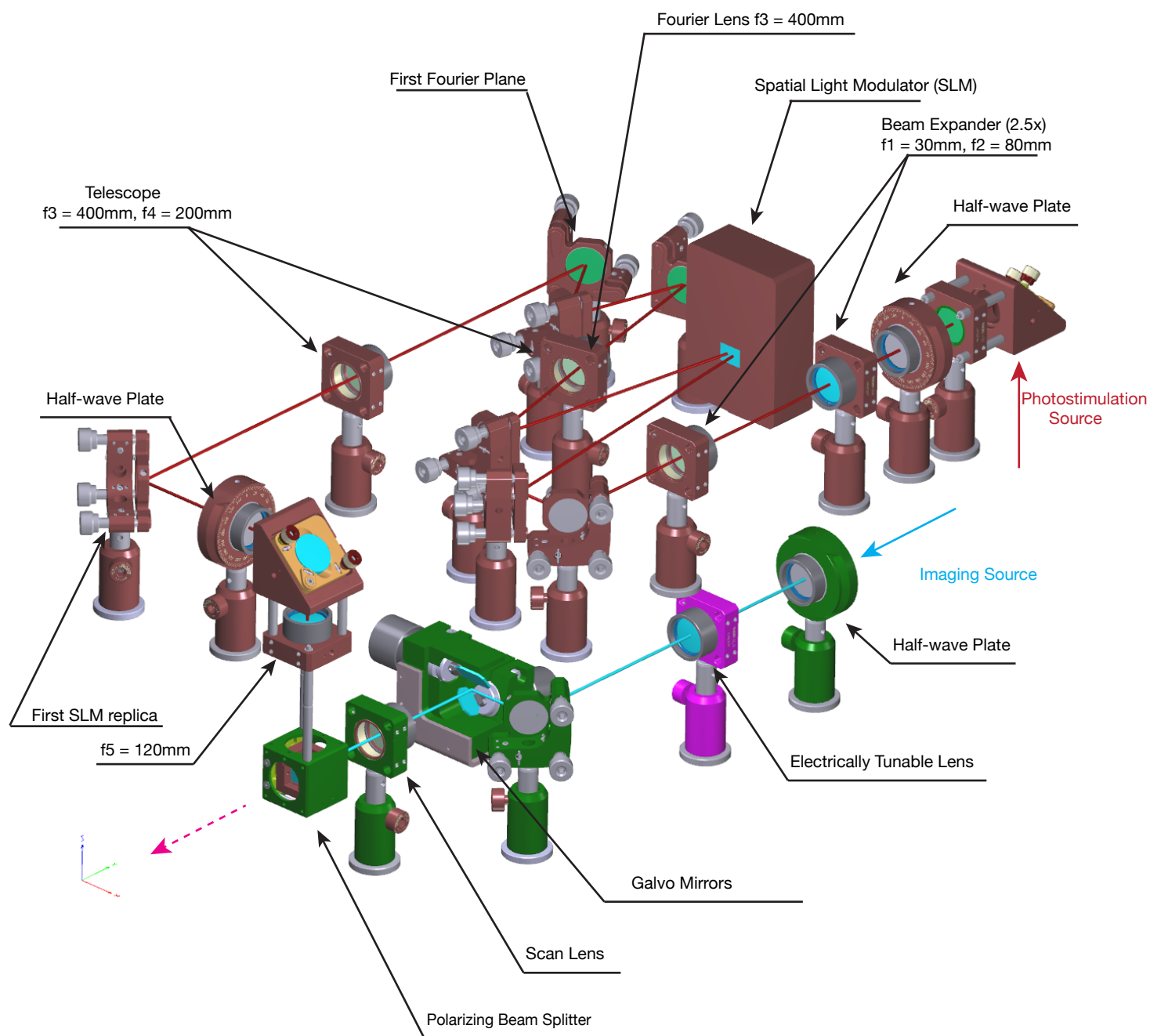
Legends for Supplementary Figures

Figure S1. Hardware configuration (related to Figure 1).

(A) Hardware integration. The module for 3D-2P-Computer Generated Holography (*brown*) is integrated in a commercial 2P imaging setup (*green*) equipped with a galvo-galvo scanhead, and an ETL (*magenta*) for the remote control of the imaging plane independently from the objective position. The two paths are combined before the tube lens by a polarizing beam splitter. In the photostimulation path, downstream of the half-wave plate required to match the SLM polarization preference, a 2.5x beam expansion stage is inserted (f1 = 30 mm and f2 = 80 mm). The overall expansion (2.5x and 2x upstream) results in a beam diameter of 12 mm at the SLM, slightly underfilling the short side of the LC matrix. A Fourier lens (f3 = 400 mm) transforms the phase pattern imposed on the SLM into an intensity distribution at the level of the first Fourier plane. Downstream from the first Fourier plane, a lens (f4 = 200 mm) renders a replica of the phase modulation imposed at the SLM at its focal plane. At this position, a second galvo scanner can be mounted, increasing the capability of this layout. Indeed, this kind of conjugation (Dal Maschio et al., 2010; Dal Maschio et al., 2011) can be used for spiral scanning of an ensemble of dots (Packer et al., 2015) or, in combination with a grating, to use the galvo mirrors to move a temporally focused beam across the sample field of view (Baker et al., 2016; Rickgauer et al., 2014). A second halfwave plate changes the polarization of the holographic beam before a polarizing beamsplitter combines it with the imaging beam through. A lens (f5 = 120 mm) conjugates the plane of the SLM replica to the focal plane of the tube lens of the imaging configuration.

Figure S2 (related to Figure 1) - interactive 3D content, please view in Adobe Acrobat
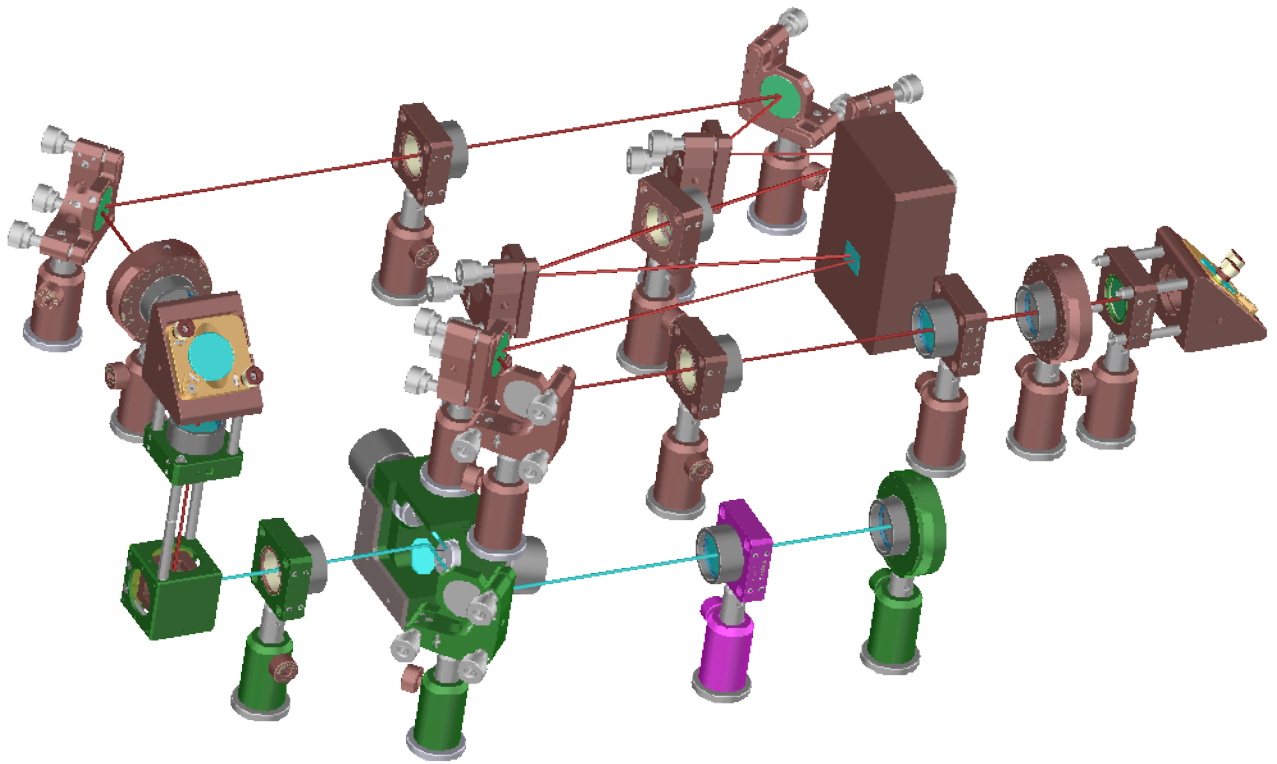
Figure S2. System hardware layout (related to Figure 1).

Interactive 3D rendering of the core optical path. Using Adobe Acrobat Reader, it is possible to navigate, explore and take measurements of t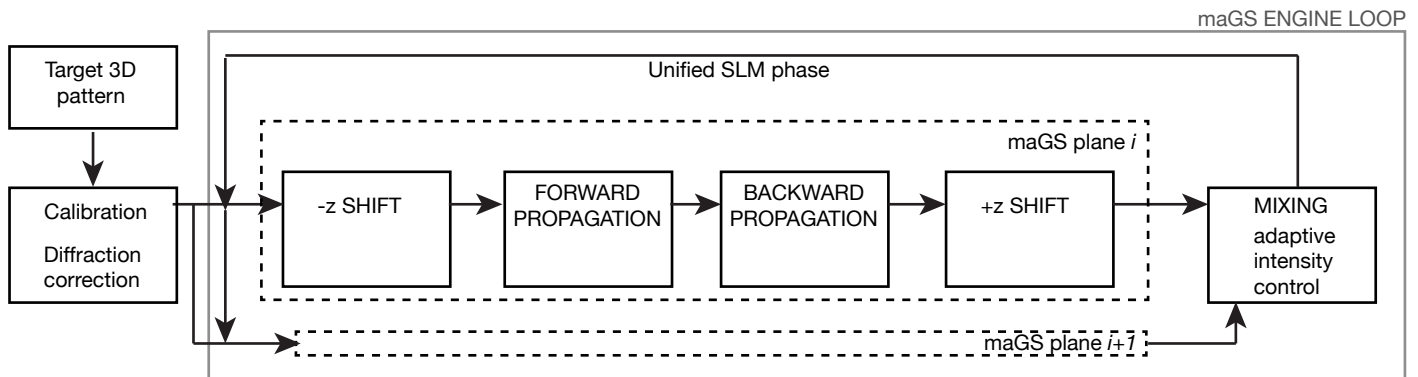he distances between different components. Based on the annotated diagram presented in Figure S1, the reader can explore all aspects of the optical path.
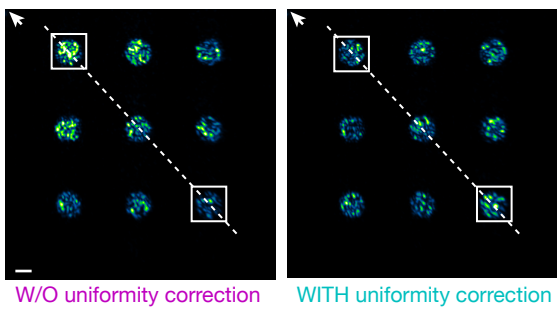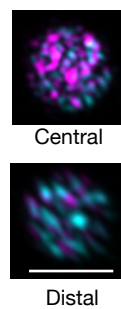
Figure S3 (related to Figure 1)
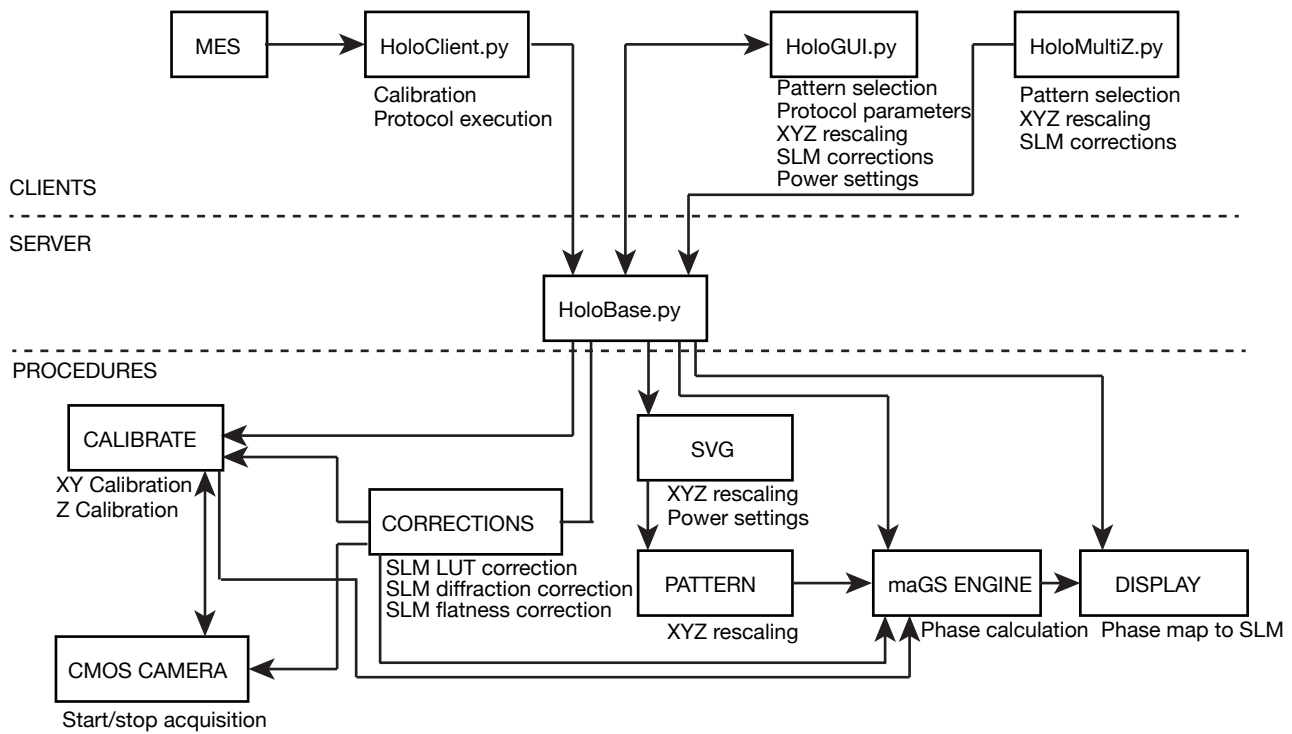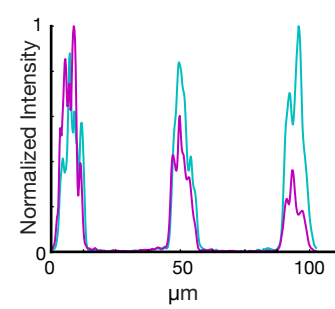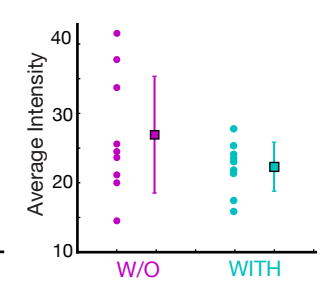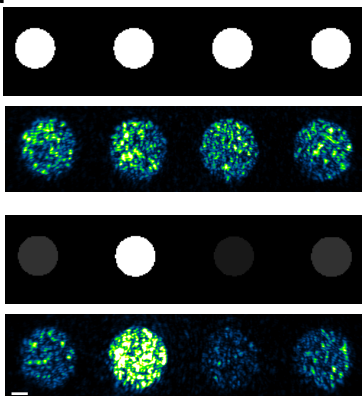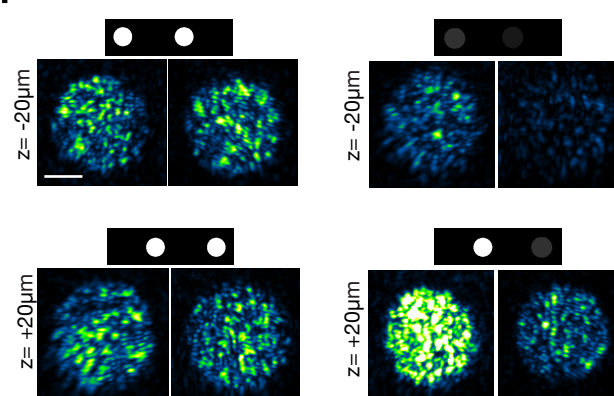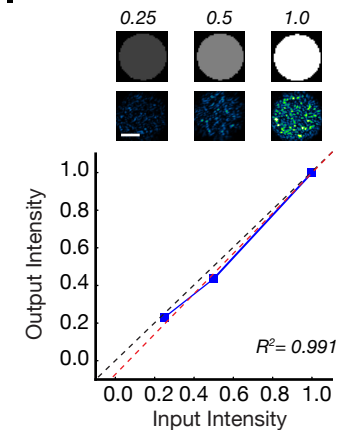
Figure S3. Software integration and maGS algorithm (related to Figure 1).

(A) Schematic of the software architecture. Requests from different client processes are sent to a server application (connected with the hardware), which calls the low-level functions required for execution and computation of the photostimulation protocol (see also STAR Methods). **(B)** Basic loop of the maGS algorithm. The designed phase calculation engine is a variant of the multiplane Gerchberg-Saxton algorithm (Haist et al., 1997). In every iteration of the algorithm (*maGS engine loop*), the propagation of the light from the source to the target plane is calculated for each plane (*maGS plane i loop*). The resulting fields are mixed together at the end of each iteration. During the mixing step (in detail in the STAR Methods), the target intensity at the different planes can be adjusted. **(C)** Uniformity correction. As a consequence of the non-homogeneous diffraction efficiency of the SLM, illumination regions towards the edge of the addressable field tend to have lower intensity. The algorithm includes the possibility to compensate for such distortion, correcting the target intensity distribution at the input of the algorithm, This is done with a correction based on the measured intensities. The panel on the left shows an array of 9 circles, 12 µm in diameter, covering a range of 100 µm, without the correction for uniformity. This field of view corresponds to about a quarter of the addressable field with the arrowhead indicating the center. The same illumination pattern but with the uniformity correction is shown on the right. **(D)** Relative intensities for two circles, are shown without (magenta) and with (cyan) uniformity correction. **(E)** The intensity profile along the dashed line from **C** clearly shows a decay in illumination from the center without uniformity correction (*magenta*). When uniformity correction is applied (*cyan*), the relative brightness is more consistent. **(F)** Effects of the uniformity correction. The standard deviation of intensity, measured across the field is halved (*26.9 ± 8.4* vs *22.3 ± 3.52, mean±sd*) when the uniformity is corrected. **(G)** 2D Intensity control. The algorithm designed provides the possibility to control the intensity of the shapes generated at the same plane, correcting the relative weight of the input patterns. In the first row the input and the corresponding acquired patterns for a series of identical circles, 25 µm in diameter, are shown. In the bottom

panel, the intensity of the circles is adjusted, which is reflected in the generated patterns. **(H)** 3D Intensity control. Four circles are generated, as in **G**, however here two circles are shifted +20 μm and the other two –20 μm. The input intensity of these patterns is equal for the panels on the left. On the right side, the weights were changed with the same unequal ratio used in **G**. **(I)** Input-output intensity relation. For three shapes with three different weights, the corresponding mean values are plotted (blue squares). The linear fit (dotted red line) returns a coefficient of determination (R^2) of 0.991 with 1.061 $\pm$ 0.102 for the slope and -0.075 $\pm$ 0.067 for the intercept respectively. Scale bars are 10 μm.

Figure S4 (related to Figure 1)

A 3D 2P CGH 750nm

B *alphaTubulin:paGFP*

C

D **E** **F**

G *alphaTubulin:paGFP*
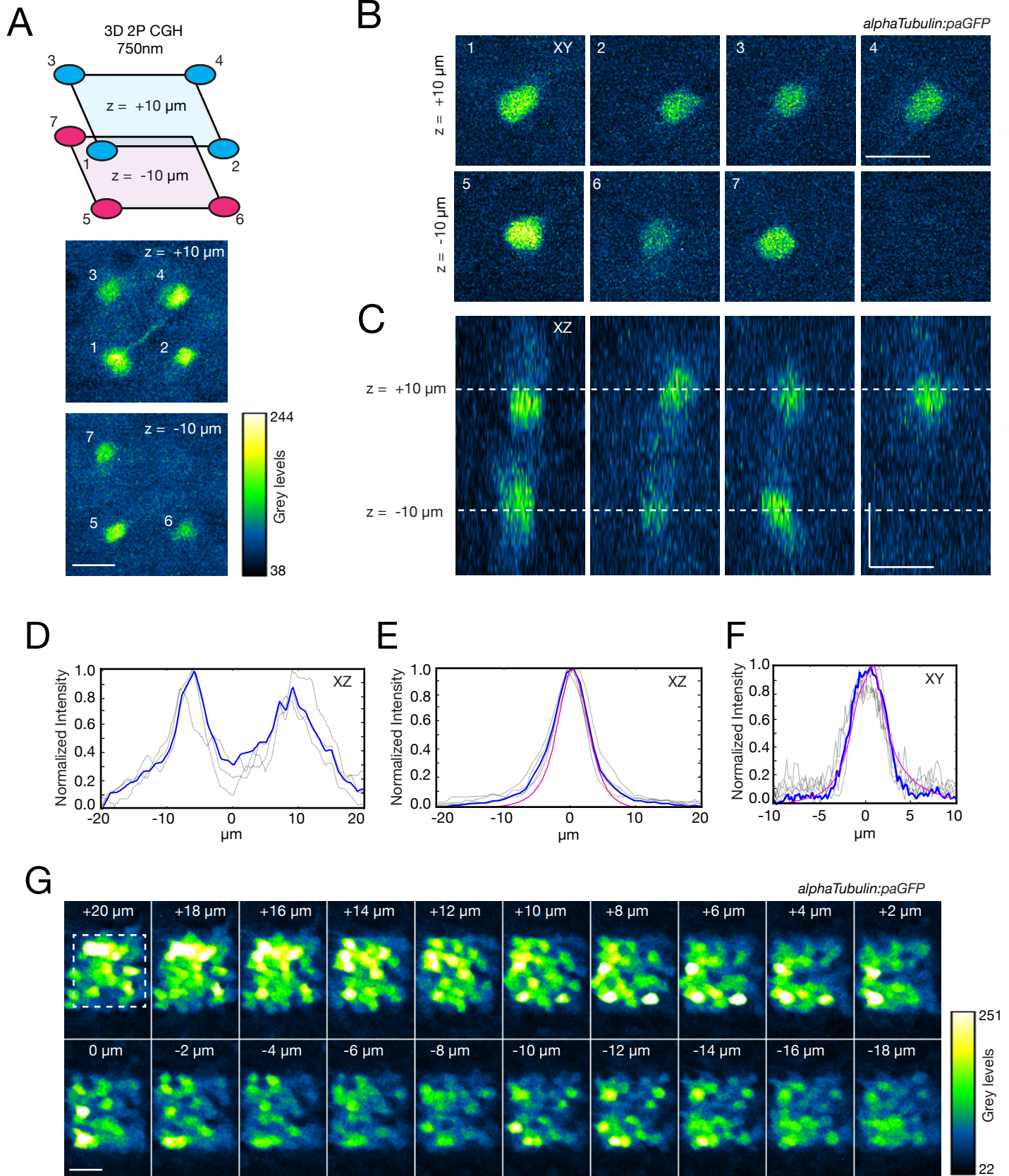
Figure S4. paGFP photoactivation (related to Figure 1).

(A) Fluorescence signal measured in a zebrafish larva with pan-neuronal expression of paGFP after photoactivation with the 3D pattern shown in Figure 1C. The pattern consists of 7 illumination circles, 6 μm in diameter, placed at the corners of a 20x20x20 μm^3 cube in the optic tectum. One corner was not illuminated to provide a comparison. **(B)** XY view of the fluorescent stack of the corresponding planes. Note that no fluorescence is detected from the plane at -10 μm in the region corresponding to the non-illuminated corner**. (C)** A side (XZ) view of the fluorescent signal. No fluorescence is detected in the region around -10 μm corresponding to the non-illuminated corner**.**
(D) Intensity profiles in the XZ view from **C**. The two photoconverted foci, although with some extended and overlapping tails, are clearly separated and distinguishable. In blue is the average (3 measurements). **(E)** For comparison, we photoconverted paGFP with a single circle, 6 μm in diameter. Individual intensity profiles in the XZ view are shown in grey. In blue is the average across 4 photoconverted spots. The resulting FWHM measured along the z-axis is 8.9 ± 0.9 μm. In magenta is the average of the profiles recorded from a thin fluorescein layer. The photoconversion tails in the paGFP Z profile measured *in vivo*, can be explained by light scattering in the tissue (as reported in Hernandez et al., 2016). **(F)** XY intensity profiles from dataset in **E** (average in blue, fluorescein reference in magenta). The FWHM is 5.79 ± 0.91 μm, **(G)** paGFP expression coverage. A 20x20x20 μm^3 cube is photoconverted by raster scanning the imaging beam at 750 nm. The stack acquired at 920 nm shows that, although with different expression levels, the majority of the cells are expressing paGFP. It is possible however to find cells without detectable paGFP photoconversion (<7.5% ± 2.2%, across different planes). This could be due to cells where the promoter is not active.

A
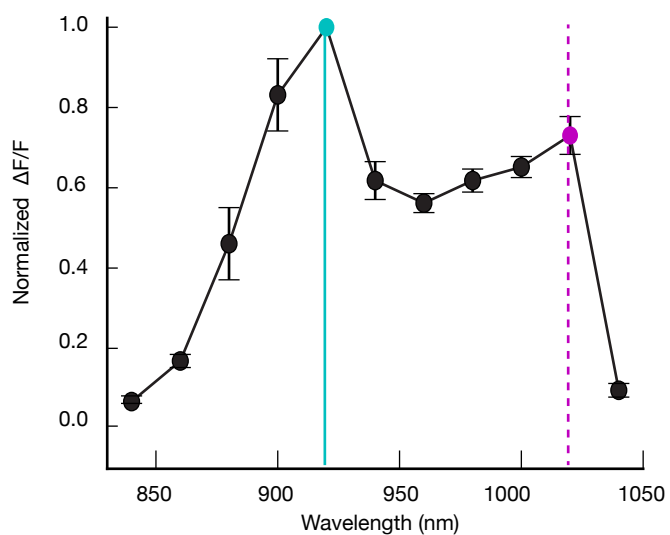
B

C
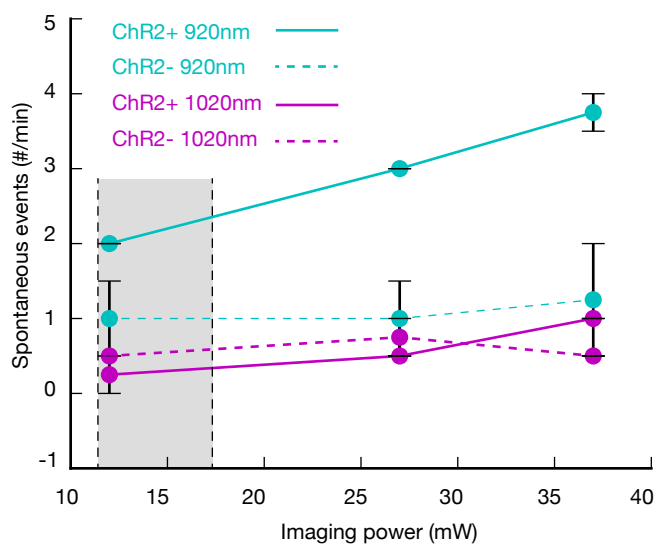
D
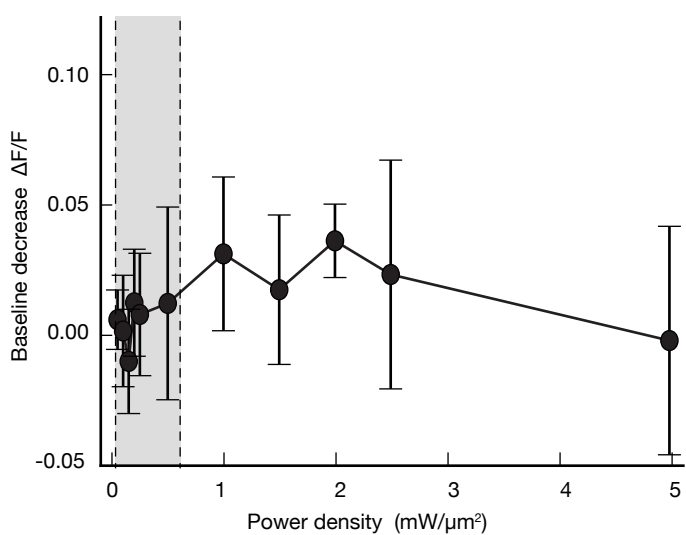
E
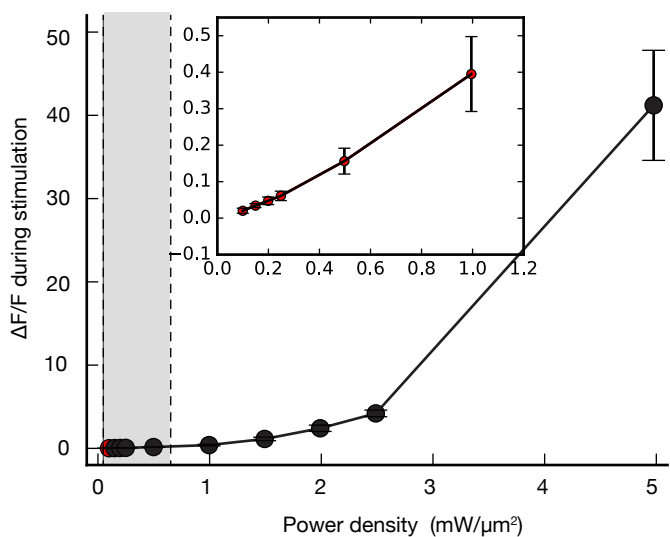
F
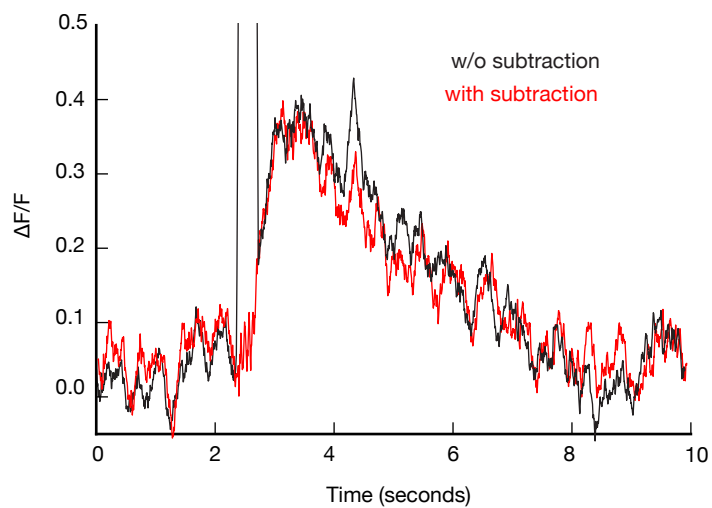
Figure S5. Characterization of the optogenetic actuator and sensor pair (related to Figure 1).

(A) ΔF/F characteristic for GCaMP6s at different wavelengths. Neuronal responses were measured in the zebrafish optic tectum during a repeated visual stimulation protocol consisting of light flashes, each 500 ms long. Signals were acquired at different excitation wavelengths with a constant excitation power at the sample of 9 mW, and were normalized with respect to the peak at 920 nm (cyan). The dashed line indicates the 1020 nm wavelength (magenta) used in this paper for imaging GCaMP. **(B)** Signal-to-noise ratio. Neuronal activity in response to a visual stimulation of 500 ms light flash, recorded at high spatiotemporal resolution at 4 different imaging powers. The S/N is quantified as the maximum increase in fluorescence with respect to the baseline (F_{max}-F_0) divided by the standard deviation of the baseline measured in a 5 second window before the response onset. Each point represents the maximum response over a set of 8 repetitions of the stimulation. The mean ratio of the ΔF/F recorded at 1020 nm with respect to 920 nm was 0.73 ± 0.7 (7 cells, 2 fish). **(C)** Excitability of neurons due to the imaging beam. The number of spontaneous events detected from individual cells were compared at two different imaging wavelengths, 920 and 1020 nm. The imaging power range typically used in this work is highlighted in grey. With respect to the control condition, no significant differences are detectable when imaging neurons expressing ChR2 at 1020 nm, while an increased number of transients are detected when imaging ChR2+ cells at 920 nm. (11 cells from 3 fish). **(D)** GCaMP6s baseline stability following photostimulation. The change in GCaMP fluorescence (excited at 1020 nm) is measured for different photostimulation power densities, before and after 2 s stimulation at 920 nm. There is no significant change with respect to the baseline acquired before the onset of the stimulation, confirming the photostability of the reporter under our protocol conditions. The typical photostimulation power used in this work is highlighted in grey. **(E)** Effect of the photostimulation light on the detected signal from GCaMP. Absorption of GCaMP6s at the wavelength used for ChR2 activation leads to a crosstalk contamination in the signal detected. The contribution of this

component, in terms of ΔF/F, increases non-linearly with the stimulation power. The inset shows a magnified view of the lower left corner of the graph. **(F)** Contamination subtraction procedure. To filter out the crosstalk component of the signal, a post-processing step is applied (details in STAR Methods). A comparison is shown between a GCaMP response with and without subtraction of the contamination component. The stimulation artifact is removed, with only minor perturbation to the signal. Error bars indicate the S.D.
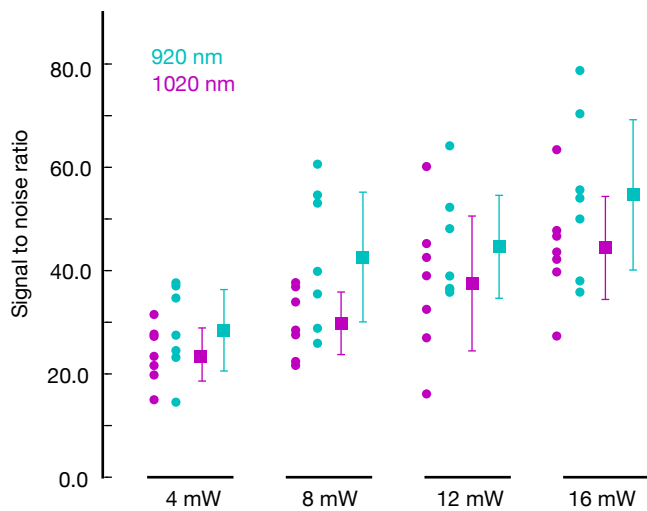
Figure S6 (related to Figure 1)

A — t_{peak}, stimulated events (s) vs t_{peak}, spontaneous events (s). nlsGCaMP6s, GCaMP6s

B — t_{decay}, stimulated events (s) vs t_{decay}, spontaneous events (s). nlsGCaMP6s, GCaMP6s

C — Maximum $\Delta F/F$ vs mCherry(ChR2)/ GCaMP6s baseline. **

D — Relative frequency vs Stimulation Reliability

E — GCaMP+, ChR2+ GCaMP+, Stimulated Region. 1 spot, 1 spot, 2 spots, 3 spots, 4 spots. $\Delta F/F$ vs Time (s)

F — Normalized $\Delta F/F$ vs ON 1 spot, OFF 1 spot, OFF 2 spots, OFF 3 spots, OFF 4 spots. 0.11 mW/µm², 0.16 mW/µm², 0.35 mW/µm², 0.09 mW/µm², 0.41 mW/µm², 0.22 mW/µm², 0.17 mW/µm², 0.15 mW/µm²

G — 0.4 $\Delta F/F$, 8 s. z = 0 µm, GLM, t-score 2.5 to -0.1

H — z = -8 µm, z = -4 µm, z = 4 µm, z = 8 µm

Gal4^s1171t; UAS:ChR2-mCherry; elavl3:nlsGCaMP6s

72

Figure S6. Characterization of induced GCaMP responses and photostimulation resolution (related to Figure 1).

(A) GCaMP onset temporal dynamics. Comparison of the time to the peak (0 to 100%) for GCaMP responses imaged at 1020 nm for events driven by ChR2 photostimulation at 920 nm (0.1 - 0.22 mW/μm^2) versus spontaneous events in the same cells. No significant difference was found between the stimulated and spontaneous conditions (p-value 0.35, t-test, saturated colors indicate means, with bars indicating s.e.m.) for GCaMP6s or nlsGCaMP6s. **(B)** Comparison of the decay time (to reach 50%) for the same molecules shown in **A**. No significant difference was found between the two conditions (p-value 0.16, t-test). **(C)** Dependency of the recorded ΔF/F on ChR2 expression level. Neurons expressing both nlsGCaMP6s and ChR2 were imaged at 1020 nm with 9 mW while being photo-stimulated at 920 nm with 0.11 mW/μm^2. The maximum recorded amplitudes are plotted as function of the ratio between the fluorescence level of ChR2-mcherry and GCaMP baseline. Data were grouped into three bins, black dots and error bars indicate averages and s.e.m respectively (p-value 0.021, t-test). **(D)** Histogram of stimulation reliability. Individual cells were repeatedly stimulated, with many cells responding reliably. (50 trials from 10 cells). **(E)** Induced ΔF/F in neurons with off-target stimulations. These experiments validate the spatial selectivity of stimulation, starting with a reference using the response to a stimulation spot targeted exactly to a neuron expressing ChR2 ("on-target", shown in red). This is compared to the response when one or more off-target spots are simultaneously stimulated, each 10 μm from the on-target cell. In all the trials, the power density per spot was constant and matched the power of the on-target spot. For each stimulation pattern (inset with blue icons), a 200 ms activation pulse was applied. The response of the on-target cell is shown in light grey for each trial, with the average in red (4 or more trials per stimulation pattern). **(F)** Response characteristics. With respect to the on-target stimulation, the normalized responses to off-target stimulations do not reach comparable levels of activity. The response characteristics for 8 cells (from 3 fish) are color

coded, and in black is the mean value (error bars show standard deviation). The corresponding photostimulation power density per spot is indicated on the right. **(G)** Example of stimulation precision. A neuron expressing ChR2 is targeted with a 6 μm photostimulation spot. Simultaneous multiplane imaging provides the activity of neurons in the same and nearby planes. On the left are ΔF/F traces for target cell (blue) and surrounding cells. The position of the recorded cells is shown in the upper right panel. The lower right panel shows the t-scores from a pixel-wise generalized linear model (GLM, details in STAR Methods). The targeted cell has the highest tscores for this model of activity based on the stimulation protocol. **(H)** Other neurons show only low t-scores, indicating they are not effectively activated by the stimulation. Scale bar is 10 μm.

Figure S7 (related to Figure 4)
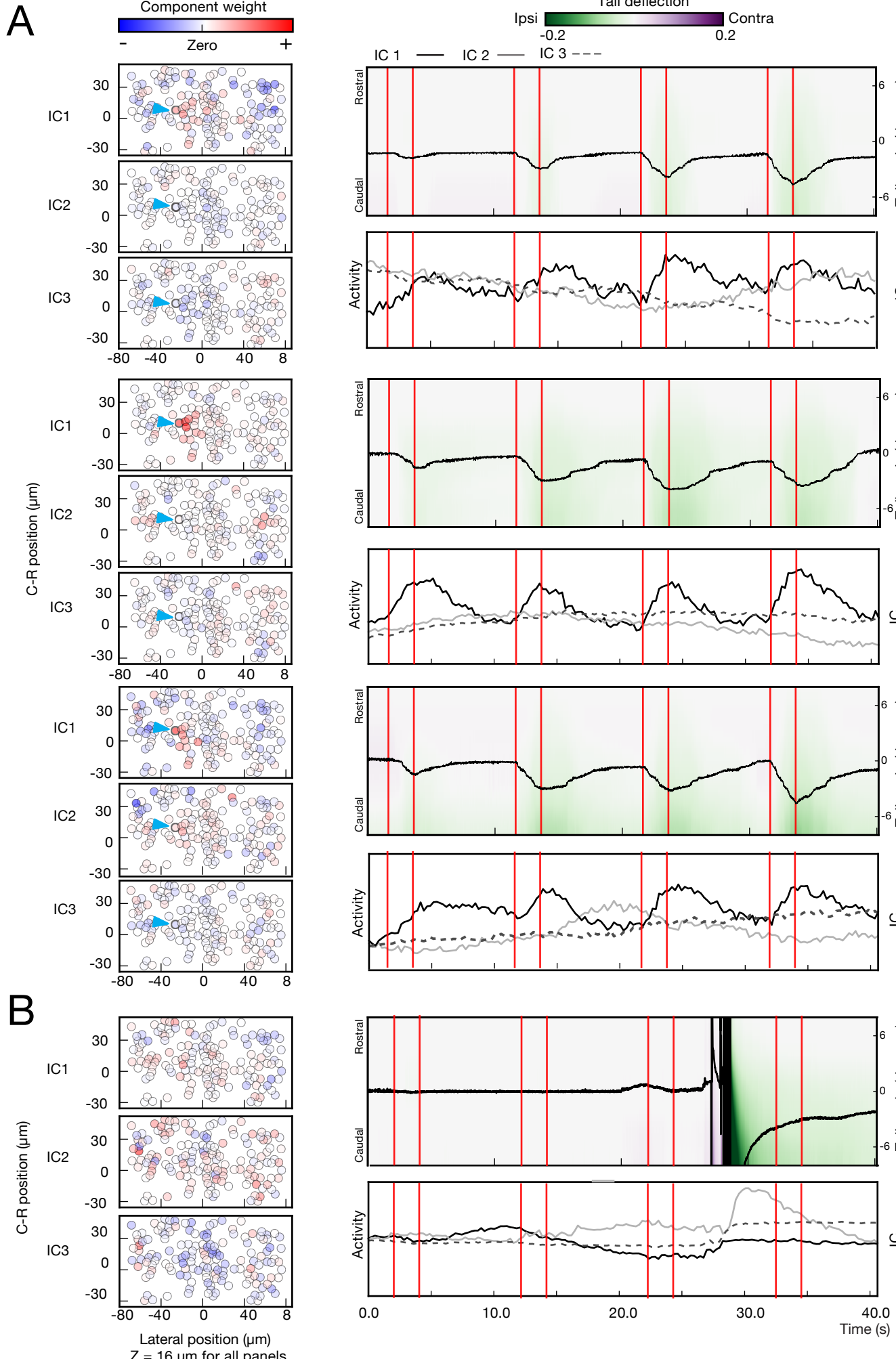
Figure S7. Reliability of the circuit outcome (related to Figure 4)

(A) Additional stimulation trials from the fish shown in Figure 4. The induced tail bending angle is shown, along with independent components representing network activity. For the same stimulation pattern used in Figure 4, tail bending of varying amplitudes is reliably detected. The weights of dimensional reduction components are shown to characterize the consistency between trials in the response of the recruited subnetwork, represented by a consistent focus of activity for IC1. **(B)** A photostimulation pattern with the same geometric profile as in **A**, but shifted 20 µm in the dorsal direction failed to induce the characteristic activity pattern and tail bending. The only activity component identified is associated with a spontaneous swimming bout not temporally synchronized to stimulation.

Figure S8 (related to Figure 4)

A

Dorsal   Z = 32 μm

Z = 24 μm

Stimulation   Z = 16 μm

Stimulation   Z = 8 μm

Ventral   Z = 0 μm

Gal4^s1171t; UAS:ChR2-mCherry;
elavl3:nlsGCaMP6s

B

C

Cell 246

Cell 0

D

IC1   IC2   IC3

E

FastICA

PCA

MDS
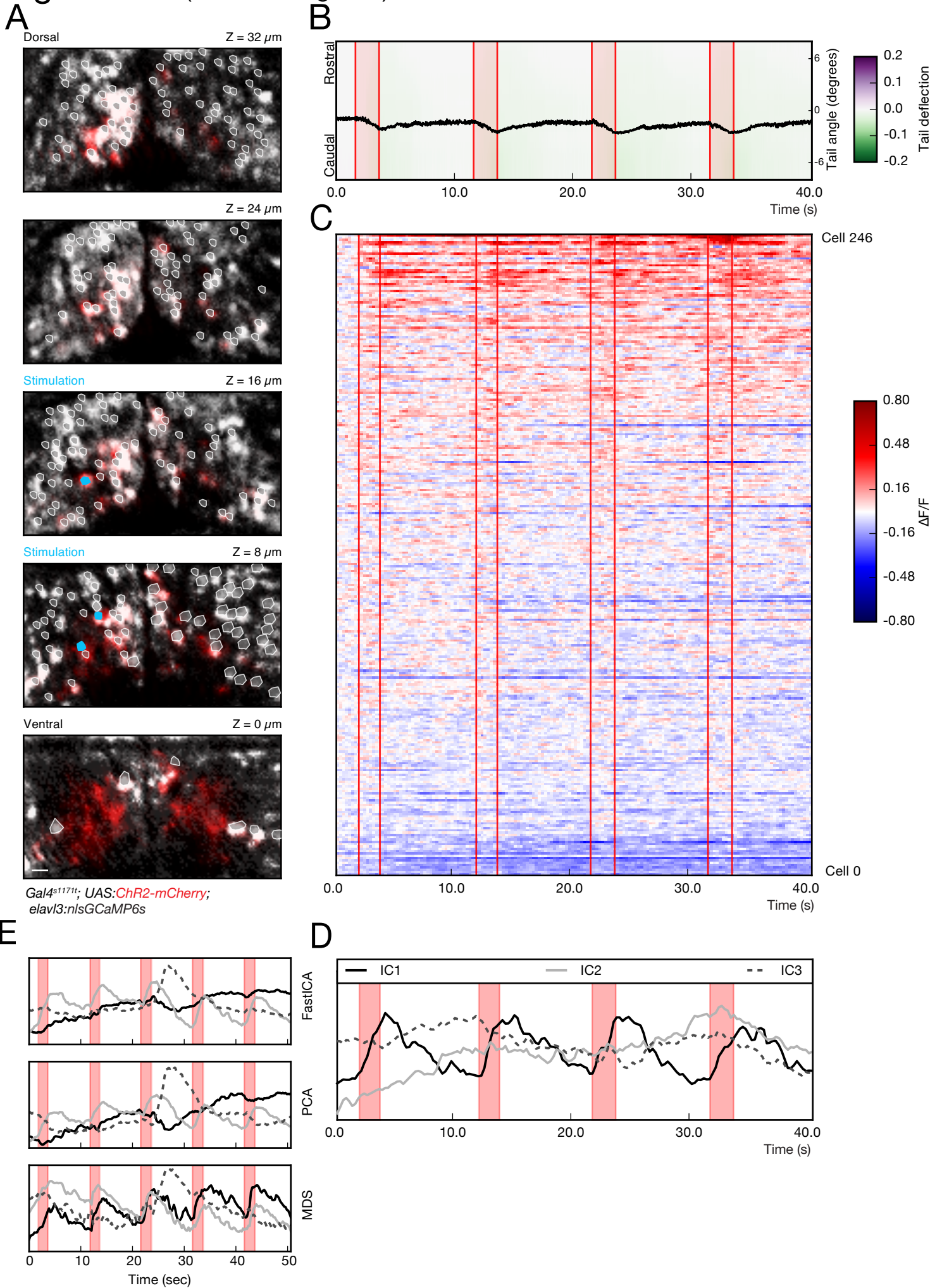
Figure S8. Investigation protocol demonstrated in an additional larva (related to Figure 4).

(A) Volumetric recording of the activity of hundreds of neurons during stimulation-induced behavior. 5 planes are imaged in the midbrain of a fish expressing ChR2-mcherry (red) and nlsGCaMP6s (grey). ROIs corresponding to the cell bodies selected for the analysis are highlighted in white, and neurons selected for the photostimulation are shown in cyan. **(B)** The kinematics of the tail show a reliable tail deflection upon stimulation (red lines indicate stimulation onset and offset). **(C)** Raster plot showing the activity for the recorded population of 246 neurons, temporally aligned with the behavior recording shown in **B**. Similar to the example in Figure 4, a small subset of neurons shows a reliable activity pattern temporally locked to the stimulation and tail deflection. **(D)** Representation of common patterns in population activity by independent component analysis. The first component captures the stimulation induced network activity that corresponds to the tail bending behavior. (**E**) Comparison of dimensionality reduction methods on the same data shown in Figure 4. The different methods tested, Independent Component Analysis (fastICA), Principal Component Analysis (PCA), and Multi-Dimensional Scaling (MDS), all capture a rather similar representation of the network. One component captures the consistent activity induced by photostimulation, and a different component picks the activity associated with the large swim. The ICA and PCA representations are almost identical, while for MDS, which is a non-linear a manifold learning technique, the activity induced by stimulation is partially distributed into two components. Scale bar is 10 µm.

A

IC1

IC3

Time (s)
0 10 20 30 40 50

IC1

Swim event

IC2

B

Bending   Swimming

IC1   Z= 0 µm   IC2   IC3

IC1   Z= 8 µm   IC2   IC3

IC1   Z= 16 µm   IC2   IC3

IC1   Z= 24 µm   IC2   IC3

IC1   Z= 32 µm   IC2   IC3

C-R position (µm)

Lateral position (µm)

-        Zero   +
Component weight

C

Gal4^s1171t; UAS:ChR2-mCherry; elavl3:nlsGCaMP6s

D

Ipsilateral   Contrateral

ΔF/F

Time (s)

E

Tail deflection
Contra
Ipsi

Rostral
Caudal

ΔF/F

Tail angle (degrees)

Time (s)

79
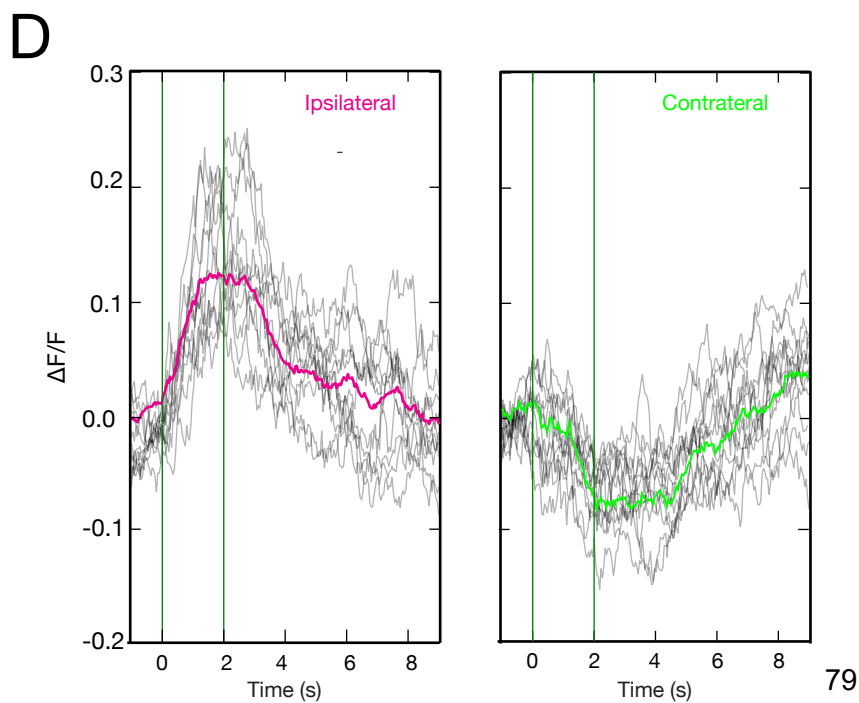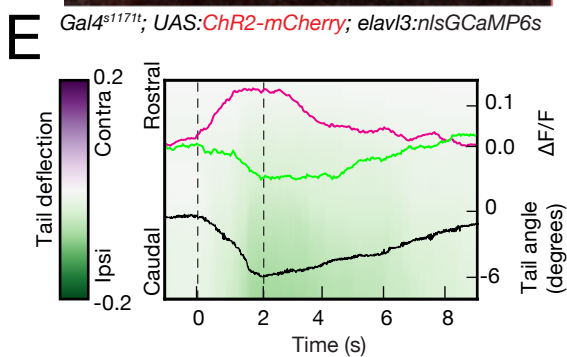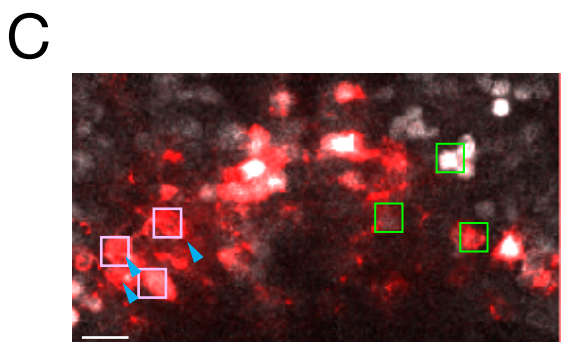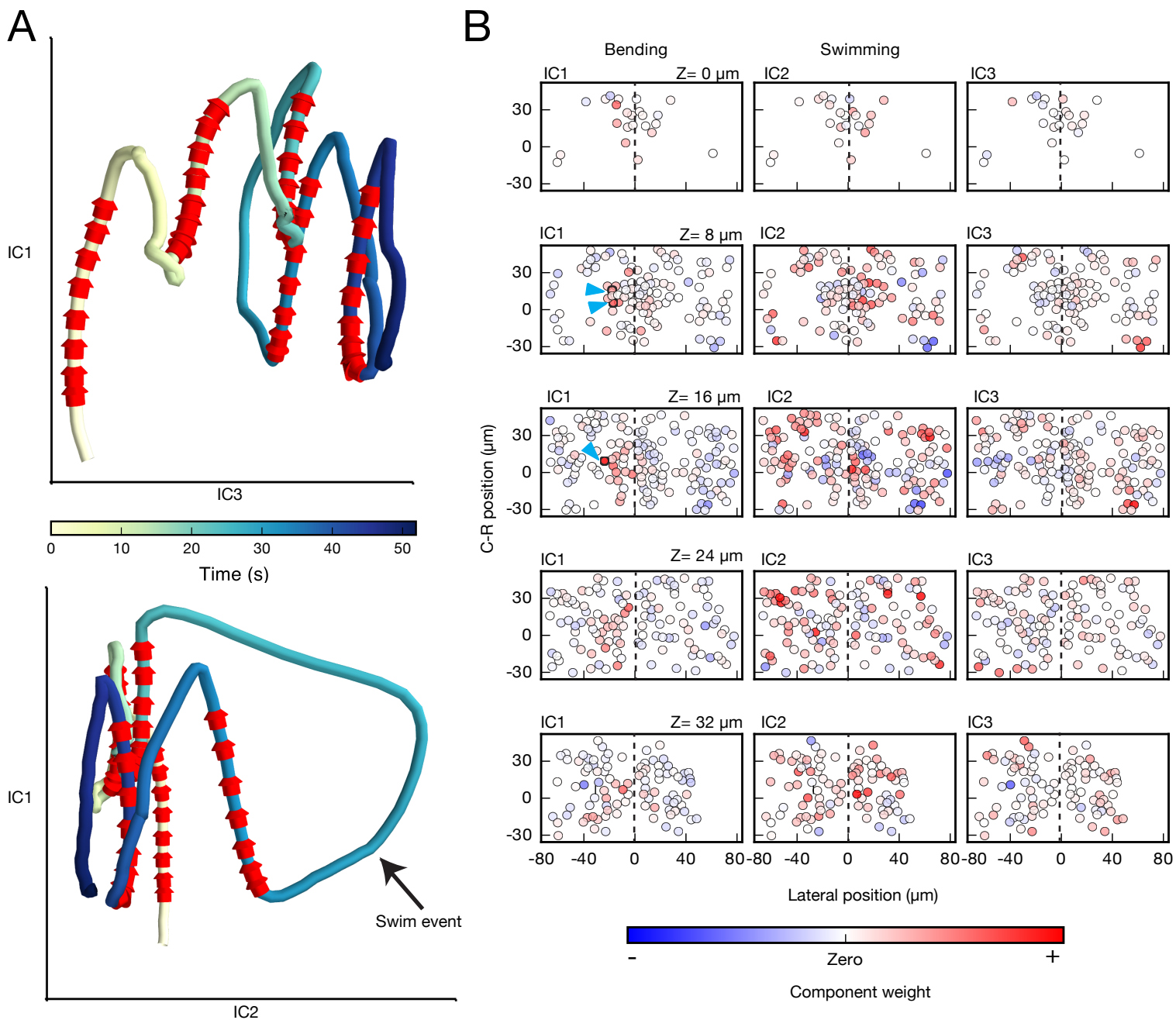
Figure S9. Dimensionality reduction representation of circuit dynamics (related to Figure 4)

(**A**) The network activity of 486 neurons is projected into a simplified three dimensional space obtained by independent component analysis. The color encodes the temporal evolution of the network state, with stimulation phases indicated by red arrows. Each stimulation epoch shifts the circuit into a different state, with a return towards baseline following the end of stimulation. In this compact representation, the trajectory of the network activities associated with tail bending are well separated from the large swim bout. (**B**) Spatial patterns of the independent components at each imaged plane. The relative weights of neurons in the independent component representation are used to visualize the spatial organization of these common activity modes across the circuit. IC1, capturing the dynamics temporally locked to tail bending, shows a focused and lateralized pattern near the stimulation site. IC2 (swimming) and IC3 (slow circuit dynamics), have a broader and more symmetric distribution of activity across the midline. (**C**) Induced network activity resulting from nMLF stimulation driving behavior. Stimulated neurons are marked with a blue arrow. Scale bar is 10 µm. (**D**) Two different activity patterns in the circuit associated with the tail deflection can be detected, when comparing the neuronal responses ipsilateral versus contralateral to the stimulation side (light pink and green squares in **C** respectively). While in cells ipsilateral to the stimulation an increase in activity is detected (grey lines for single trials, pink trace for mean), a signal decrease in some of the contralateral neurons is noticeable (green trace for mean). (**E**) The activity profile recorded on the contralateral side (green trace), although temporally synchronized to the stimulation and tail deflection, shows a distinct temporal shift (see main text for quantification).

A
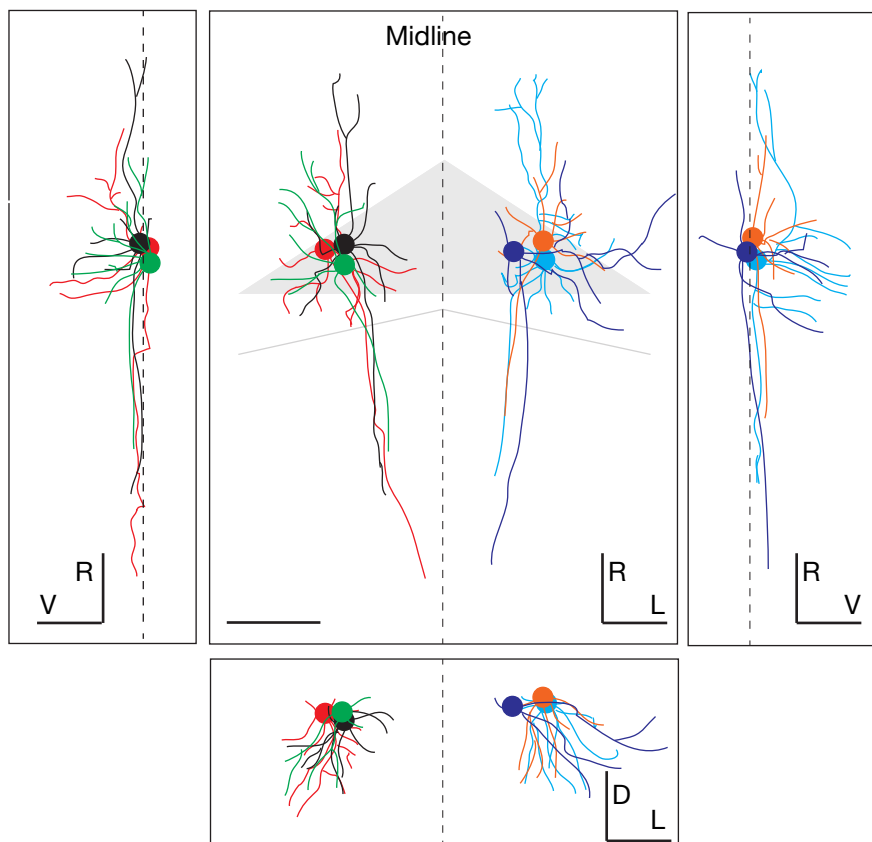
Figure S10. Reconstruction and registration of behavior driving neurons (related to Figure 7)

(A) Morphological reconstruction by paGFP photoactivation. Identified cells with the highest behavioral scores were photoconverted, and diffusion of photoactivated paGFP allowed visualization and tracing of their morphologies. The neurons shown here are registered from five fish (one fish has two neurons – one on each side) based on the distance from the midline, the dorsal extent of the nMLF (grey triangle) and the distance from the midbrain-hindbrain boundary. Rostral-caudal axis aligned according to the average axonal direction. Scale bars are 10 µm.

Paper III: Topography of a visuomotor transformation

Thomas O. Helmbrecht, Marco dal Maschio, Joseph C. Donovan, Styliani Koutsouli, Herwig Baier

This manuscript is currently under review. The version presented here was submitted as a Research Article to *Neuron* on 30.04.2018.

Topography of a visuomotor transformation

Thomas O. Helmbrecht, Marco Dal Maschio, Joseph C. Donovan, Styliani Koutsouli, Herwig Baier[*]

Max Planck Institute of Neurobiology

Department Genes – Circuits – Behavior

Am Klopferspitz 18, 82152 Martinsried, Germany

*Author of correspondence at hbaier@neuro.mpg.de

Summary

The brain converts perceptual information into appropriate patterns of muscle activity. This task requires both categorization and localization of sensory cues. This information might either be encoded by distributed network activity, or "labeled lines" connecting sensory channels to dedicated approach or avoidance pathways. Here we investigate, in the context of natural behavior, how the tectum of larval zebrafish projects to hindbrain premotor areas. Using an optogenetic mapping strategy, we first showed that the tectum is capable of inducing either approach or escape maneuvers. Based on single-cell reconstructions, we were able to assign approach and escape commands to two spatially segregated, uncrossed, descending pathways. Moreover, we found that tectofugal axons dedicated to approach are retinotopically ordered to convey information about target position to specific premotor ensembles. Importantly, this tectum-generated space code is sufficient to steer orienting movements. We conclude that topographically organized labeled lines control object-directed behavior in this vertebrate brain.

Introduction

One of the most fundamental decisions animals are faced with is whether to approach an attractive stimulus, such as a prey item, or to escape from an aversive stimulus, such as a predator or an object on a collision course. In addition to this valence decision the behavior needs to be finely tuned in spatial coordinates in order to attain the animal's goal, such as catching prey or swimming to safety. Thus, two processes take place. One, the stimulus is categorized, and this categorical information is mapped onto a specific motor ensemble, driving behavior toward, or away from, the object. Two, the stimulus is localized, and this spatial information is converted into graded motor output to steer the direction of movements. We show here that these two processes are carried out in parallel via distinct tectofugal pathways and we describe a topographic principle underlying this sensorimotor map.

Previous work identified the teleost optic tectum, the homologue of the mammalian superior colliculus, as a central hub executing visuomotor transformations. Tectal motor functions in orienting movements have been studied in several vertebrates, including mammals (Bergeron et al., 2003; DeSouza et al., 2011; Freedman et al., 1996), birds (du Lac and Knudsen, 1990), amphibians (Ingle, 1983; Masino and Grobstein, 1989) and adult goldfish (Herrero et al., 1998). In the superficial layers of the tectum, projections from retinal ganglion cells form a map of the visual space in retinotopic coordinates. Deeper layers appear to contain a motor map; focal stimulation is able to generate coordinated head, body and eye movements toward the corresponding position in visual space. Most studies postulate that the output signal of the motor map is a 'space code' whereby the focus of tectal activity defines the required movement to reach a target (Klier et al., 2001; van Opstal et al., 1991; Sadeh et al., 2015; Sparks and Gandhi, 2003). However, how this space code is conveyed to hindbrain premotor structures to modulate orienting movements has not yet been elucidated. We show here that the organization of the tectal motor map is maintained in the topographic arrangement of tectofugal fibers that carry behaviorally relevant signals to the hindbrain reticular formation.

During hunting behavior, zebrafish larvae engage in finely tuned turning maneuvers to orient towards prey (Patterson et al., 2013), and this task requires an intact tectum (Gahtan et al., 2005; Roeser and Baier, 2003; Semmelhack et al., 2014). In zebrafish and rats, the tectum is also involved in the sensorimotor decision to approach or to avoid a novel visual object (Barker and Baier, 2015; Bianco and Engert, 2015; Felsen and Mainen, 2012; Shang et al., 2015; Temizer et al., 2015). Different descending pathways from the tectum have been proposed to route this

behavior selection to the hindbrain. Although the evidence is thin, the contralateral (crossed) tectobulbar tract has been implicated in approach behavior (i.e. pursuit of prey) and the uncrossed tectobulbar tract in aversive behavior (i.e. escape from a predator) (Huerta and Harting, 1984; Ingle, 1983; Pérez-Pérez et al., 2003; Sooksawate et al., 2013). Consistent with this notion, lesions of the uncrossed tract impaired escapes (Ellard and Goodale, 1988). Lesions of the crossed tract, however, only mildly affected orienting movements (Dean et al., 1986; Ellard and Goodale, 1988), and the corresponding neurons are not visually responsive in rodents (Westby et al., 1990). Therefore, it is still debated which tectofugal pathway underlies visual orienting movements (Dean et al., 1989; Kostyk and Grobstein, 1987). We show here that escape and approach signals are carried by adjacent, spatially segregated fiber bundles within the ipsilateral tectobulbar tract.

While there is common agreement about the central function of the tectum in all aspects of the sensorimotor transformation, the anatomical and functional implementation at the scale of individual neurons remains unclear (Basso and May, 2017). For the larval zebrafish tectum, we fill this gap and show that "labeled lines", consisting of functionally and morphologically distinct classes of tectal projection neurons, are involved in the control of goal-directed behavior.

Results

Focal optogenetic activation of tectal neurons triggers either of two distinct motor outcomes

To establish that the zebrafish larval tectum contains a motor map, similar to that of adult goldfish (Herrero et al., 1998; Saitoh et al., 2007), we employed an optogenetic mapping strategy (Arrenberg et al., 2009; Kubo et al., 2014; Schoonheim et al., 2010; Thiele et al., 2014) (Figure 1A). Optic-fiber stimulation of tectal regions in 5-7 dpf larvae expressing ChR2 in most tectal neurons *(Gal4s1013t X UAS:ChR2-mCherry*; Scott and Baier, 2009) triggered swim bouts that resembled either approach swims or escapes (Figure 1B). Stimulating a different population of tectal neurons, by moving the optic fiber to a different position, often resulted in a different behavior, demonstrating that the same tectum was able to control both escapes and approaches (Suppl. Video S1).

Consistent with our qualitative interpretation of the behavior, cluster analysis on the maximum tail amplitude and mean bout angle (a proxy for the directionality of bouts) from all the induced swims

(n = 484 from 28 fish) revealed that the two classes of bouts were clearly segregated in the component space (Figure 1C, Suppl. Figure S1A). Escapes showed tail deflections with amplitudes greater than 50 degrees and directed ipsilateral to the stimulation side, as indicated by negative mean bout angles (i.e. turning left when the left tectum is stimulated) (Figure 1C, D). Approaches, on the other hand, were characterized by smaller oscillations, displaying a broader distribution along the ipsi-contralateral axis, but skewed to the side that was contralateral to the stimulated tectum (Figure 1C, D). Cluster analysis further showed that approach bouts appeared with a shorter delay and lower tail-beat frequency compared to escapes (Suppl. Figure S1B). Importantly, while ChR2+ fish responded more than four out of five times during the stimulation (85.9 ± 2.5 %), ChR2- fish responded only rarely (3.9 ± 1.2 %), most likely due to spontaneous bouts that coincided with the laser stimulation (Figure 1E, **$p = 1.3 \times 10^{-6}$).

Retinotopic coordinates are integrated with viewing direction to elicit graded orientation turns

Having established that tectum activation is sufficient to trigger escapes and approaches, we first asked whether behavior outcomes depended on the anterior-posterior position of the stimulated population. To label the stimulation site, we co-expressed photo-activatable GFP (paGFP) along with ChR2. This allowed us to photoactivate cells around the stimulation spot after each of our experiments (Figure 1F). We used the center of mass of the activated paGFP to estimate the photostimulation site within the tectum. First, we noted that escapes were triggered only in more posterior regions (Suppl. Figure S1D), whereas approaches could be induced in all areas of the tectum (Figure 1G). Furthermore, for approach swims, we found that the directionality of bouts was correlated with the location of the stimulated cell population along the anterior-posterior axis of the tectum (**$p = 3.4 \times 10^{-4}$). In animals in which we stimulated the anterior-most part of the tectum, the triggered approaches were symmetric (i.e. forward swims) or sometimes even slightly ipsiversive. Stimulating increasingly more posterior regions resulted in increasingly larger turning angles of the bouts to the contralateral side (Figure 1G, Suppl. Figure S1C). This correlation suggests that retinotopic coordinates of the visual stimulus are transformed into a directed motor command within a continuous motor map for approaches.

Studies in primates have shown that viewing direction (i.e., initial eye position) affects head movements initiated by the tectum (Freedman et al., 1996; Klier et al., 2001). We wondered if the same is true for the direction of tail movements in zebrafish larvae. To address this, we carried out optogenetic stimulations of the tectum in animals in which the eyes were free to move. Here the fish repeatedly changed their gaze following spontaneous saccades. We discovered that

stimulating the exact same population of tectal cells resulted in a change in the direction of the induced swim bout depending on the initial position of the contralateral eye (average position over 200 ms before stimulation onset) (Figure 1H,I; n = 8 fish, **p = 7.4e^{-4}). For most eye positions, the mean tail deflection was directed away from the stimulated tectum (as indicated by positive mean bout angles). A more nasal orientation of the eye, however, combined with an optogenetic stimulation of the anterior tectum, often resulted in ipsiversive tail beats (negative mean bout angles). For example, when the fish was looking left, photostimulation of the anterior part of the right tectum resulted in a swim to the left. When the fish was looking right, stimulation of the same position evoked a swim slightly to the right. Together, these findings suggest that the zebrafish motor map uses eye-centered coordinates to adjust tail movements, and is not just computing the retinotopic location of the visual object, but also integrating the animal's viewing direction.

<u>Specific neurons in the caudal hindbrain receive tectal orientation commands</u>

During an approach, the fish turns and swims toward the position of the stimulus. Such swim and turn maneuvers might be mediated by V2a neurons in the caudal hindbrain (Kimura et al., 2013). Moreover, the eye position integrator neurons, which influence turning direction, are also situated in this part of the hindbrain (Lee et al., 2015). We therefore predicted that the downstream neurons activated by tectal orientation commands would largely reside in the contralateral caudal hindbrain. To test this prediction, we combined simultaneous 2-photon whole-brain GCaMP6s imaging, optogenetic ChR2 activation of tectal neurons and behavior tracking (Figure 2A). With this approach, we could consistently evoke approach-like behavior (Figure 2B, C). The acquisition protocol consisted of 90 seconds of behavioral and functional recordings of an individual plane, and every plane was imaged at least three times. During each sweep, short phases of optogenetic stimulation were started manually and turned off automatically as soon as the fish responded (Figure 2C – cyan shading). To remove spontaneous bouts coinciding with stimulations, we applied kernel density estimation on all induced bouts (Figure 2B – background shadings), and only used bouts placed in a density of more than 95%.

With this behavioral segmentation, we analyzed our functional imaging data using linear regression models. We first defined individual regions of interest (ROIs) as clusters of co-active pixels, using time series correlations of each pixel with its neighboring pixels (Portugues et al., 2014). We created regressors for individual bouts and one regressor for the stimulation and calculated corresponding scores (coefficient * R^2) for each ROI (Suppl. Figure S2A). Using these scores, we classified the response of each ROI as either stimulation-correlated or behavior-

correlated by calculating a "stimulation vs. behavior" index (SB index; Figure 2D, E - green cells, correlated with stimulation; Suppl. Fig S2A, C, D). By inspection of the raw imaging data, most of these ROIs correspond to single cell bodies and behavior-correlated ROIs were located predominantly in the reticular formation of the caudal hindbrain (Fig. 2D, Suppl. Fig S2D). To find cells that were involved in the initiation of the induced behavior, we calculated an "induced vs. spontaneous" index (IS index; Suppl. Figure S2A, C, D; Figure 2D, E – magenta cells, correlated with induction of behavior). Applying this classification to several imaging planes (Suppl. Figure S2D) from a total of three fish, revealed a slightly lateralized distribution (62.9%, *p = 4.0×10^{-2}) of the cells involved in the initiation of contralateral turns in a circumscribed region of the contralateral reticular formation (Figure 2F – right panel, E – magenta cells; Suppl. Figure S2D). From these findings, we conclude that stimulated tectal neurons are functionally connected to hindbrain premotor circuits primarily in the contralateral caudal reticular formation, which in turn initiate the appropriate behavior.

The tectal projectome reveals the anatomical substrate of sensorimotor transformations

We hypothesized that escape and approach commands are relayed to premotor areas via direct axonal projections from the tectum to the reticular formation. To identify such pathways anatomically, we generated a single-cell atlas of tectofugal neurons. We used an established method for genetic single-cell labelling, BGUG (Scott et al., 2007), which results in stochastic labeling of single, or few, *Gal4s1013t* cells with membrane-tethered GFP, in a *Tg(elavl3:lyn-tagRFP)* background. The *lyn-tagRFP* reporter highlights primarily the neuropil and can be used as a reference channel for registration of individual GFP-labeled cells to a standard brain across different fish (Figure 3A, B). Tracing the neurons and mirroring them to one hemisphere, we generated an atlas containing 133 single projection neurons aligned in a common coordinate system (Figure 3C, E; Suppl. Figure S3C). When viewed summarily, the axons reproduce the complete, anatomically discernible projection pattern of fish larvae from the *Gal4s1013t X UAS:ChR2-mCherry* cross, which we used for our optogenetic experiments (Suppl. Figure S3A, B). This suggests that most, or all, tectofugal patterns are represented in this dataset.

We detected individual tectofugal axons in the following output pathways: postoptic commissure, intertectal commissure, ipsilateral tectobulbar tract (iTB), contralateral tectobulbar tract (cTB), tecto-pretectal tract, tecto-tegmental tract and optic tract. Tectofugal axons projected to seventeen major brain areas, which received collaterals from individual cells in various combinations. Among the tectorecipient regions are areas situated in the pretectum (ipsilateral

retinal arborization fields AF7 and AF9), thalamus (including ipsilateral and contralateral AF2, AF4 and AF6; Burrill and Easter, 1994), the contralateral tectum, the ipsilateral tegmentum (including oculomotor nucleus and nucleus of the medial longitudinal fascicle), medulla oblongata (ipsilateral and contralateral nucleus of the isthmi) and ipsilateral and contralateral reticular formation. For each of the annotated 17 tectorecipient regions, we evaluated every neuron's arborization as either present or absent. We then applied hierarchical clustering and identified seven distinct classes of tectofugal collateralization patterns (projection classes I through VII – Suppl. Figure S4, Suppl. Video S2). We decided to further split class VI to distinguish cells that project to the hindbrain (class VI-b) from those that do not (class VI-a). When considering each cell's dendritic stratification in the tectum, these seven projection classes are further refined into 29 subclasses (Figure 3D; Suppl. Figure S5). Twenty-seven of the 29 types were found more than once. This suggests that our sample size is not exhaustive and that more types could be discovered through continued labeling efforts. We show here, that tectal projection neurons assume highly diverse shapes and connectivity patterns.

Tectofugal fibers with diverse morphologies are topographically organized within the ipsilateral tectobulbar tract

To visualize the brain regions innervated by each of our tectal projection classes, we quantified the density of neurite branching (as a proxy for areas containing synaptic partners) using Strahler numbers (Vormberg et al., 2017) along each of the 133 traced neurons (see Figure 3C). In short, terminal branches of a neurite ("leaves") have Strahler numbers of 1 and the Strahler number increases towards the cell body ("root") (Suppl. Figure S4). Using spatial information of the arbor terminals outside the tectum, we generated color density maps for each class (Figure 3F, Suppl. Figure S4). This enabled us to draw a mesoscale wiring diagram of tectal outputs (Suppl. Figure S5), revealing how morphologically distinct projection neurons of the tectum contact different downstream circuits.

The most caudal areas in the reticular formation coincide with the foci of activity following tectum stimulation and are likely recipients of tectal premotor commands. We therefore investigated, in greater detail, the positioning of the axons that project to the caudal hindbrain within the tectobulbar tracts (ipsilateral and contralateral tectobulbar tract - iTB and cTB; classes III, IV, V and VI-b). All Class IV axons cross the midline and all but one project to the hindbrain within the cTB. Interestingly, only 8 of the 78 tectobulbar axons in our sample belong to this class (light blue in Figure 3E, F). Without exception, these axons form collaterals in the region of the nucleus of

the medial longitudinal fascicle and the oculomotor nucleus, suggesting that they carry a specific behavioral function related to eye movements, tail posture or swimming speed (Severi et al., 2014; Thiele et al., 2014). Of the remaining 69 ipsilaterally projecting axons, class VI-b axons take the most medial positions in the iTB and send collaterals to the non-retinorecipient thalamus and the tegmentum (magenta in Fig. 3E, F). Class V axons (dark blue in Figure 3E, F) assume lateral positions in the iTB; these axons send collaterals to the tegmentum and the pretectum near the optic tract (dark blue in Figure 3E, F). Class III axons are the most numerous and are probably a heterogeneous group (n=56; cyan in Fig. 3E, F); they are also positioned laterally in the iTB, intermingled with class V axons. Unlike the other two iTB-projecting classes V and VI, whose dendrites are restricted to deep layers of the tectum, class III neurons stratify, as a population, in all layers of the tectum. The distinct morphologies, connectivities and axon trajectories of tectal projection neurons suggest fundamental differences in their function.

<u>Behavioral functions can be assigned to morphological classes of tectal projection neurons</u>

To test if the different tracts within the iTB encode different functional information, we combined visual stimulation and calcium imaging to record responses to prey-like, dimming, brightening and looming stimuli (Figure 4A). We imaged *Gal4s1013t* X *UAS:GCaMP6s* fish at different planes within and below the tectum, paying particular attention to the level of the iTB (200-250 µm from the dorsal surface). While we observed soma-level GCaMP6s signals scattered across the tectum for each of the stimuli employed (Figure 4B, left panel), the tectofugal projections showed spatially segregated response profiles. Axons running in the medial iTB responded maximally to dimming and looming stimuli, whereas the lateral portion of the iTB was tuned preferentially to prey-like stimuli (Figure 4B, right panel). This organization was consistent throughout many planes and during multiple repetitions of the stimuli (Figure 4C) and was significant in all fish tested (medial iTB: **$p = 1.7 \times 10^{-6}$, lateral iTB: **$p = 4.7 \times 10^{-7}$ by *t*-test for paired samples; Figure 4D).

To link this functional observation to our anatomical dataset, we registered our single-cell reference atlas to the z-stack of the GCaMP6s-imaged fish (Figure 4E). We found that iTB-projecting neurons of class VII spatially overlap with those conveying looming/dimming information. Class III and V neurons, on the other hand, match those that relay information about prey-like stimuli to the hindbrain (Figure 4F; only the more numerous class III axons were visualized in this overlay). This result confirms our hypothesis that different morphological types of tectofugal neurons, taking different routes within the iTB, convey distinct behaviorally relevant signals underlying escape or approach to the reticular formation.

The lateral iTB relays a space code to the hindbrain via retinotopic ordering of its axons

We showed above that orientation movements are finely graded depending on target location and viewing direction (Figure 1). To investigate the topographic principles of class III axons (the candidate prey-response "channel") in the iTB, we designed a stimulus protocol to investigate retinotopic mapping with a small dark dot (8 degrees), which moved on a circular trajectory (radius 5 degrees, 3 rotations/sec) at different positions along the horizontal (anterior-posterior) axis of the visual field (Figure 5A). Recordings of tectal activity confirmed the expected retinotopic organization (Figure 5B, upper panel). Remarkably, recording functional responses in tectofugal axons of the lateral iTB revealed that retinotopic information is conserved in the tract (Figure 5B, lower panel). Pixel-by-pixel analysis of the responses showed that the retinotopic space along the anterior-posterior axis of the tectum is mapped onto the medial-lateral axis of the lateral iTB (Figure 5E, solid lines).

This topographic principle encouraged us to examine the underlying anatomical organization of the lateral iTB. We again took advantage of our single-cell atlas, color-coding individual class III neurons with respect to their cell-body position along the tectal anterior-posterior axis (Figure 5C; cf. Figure 5B, upper panel). We found that axons originating from cells in the anterior tectum projected preferentially along the medial portion of the lateral iTB, while axons from more posterior regions of the tectum projected more laterally (Figure 5D, E). In fact, functional responses to the spatial location of prey-like targets within the lateral iTB can be explained by the origin of the tectofugal projections of the 56 class III axons (Figure 5E, Suppl. Figure S7). This was especially true for the class III projections from the medial (n = 31 neurons) and posterior (n = 20 neurons; Pearson's correlation 0.857 and 0.956 respectively). Class III tectal projection neurons in the anterior third of the tectum were too sparse in our sample (n = 5) to contribute measurably to this effect. This space code of prey-like targets in the lateral iTB could thus be read out by the reticulospinal cells that control turn angle.

The topography of the lateral iTB dictates behavioral directionality

To test whether topographic activity in the lateral iTB controls the directionality of orienting movements, we optogenetically stimulated the axons within the tract. We expressed ChR2 in the *Gal4s1013t* tectal line and stimulated a small target area (roughly 16 x 16 μm^2) in the lateral iTB using two-photon raster scanning (920 nm; Figure 6A, B). We stimulated five times for three seconds (32.7 Hz, 35.2 ± 8.3 mW) starting every 20 seconds and repeated this protocol 30 times

(Figure 6C). As a control, we stimulated near the midline (Figure 6B), where ChR2 is not expressed. We found that photostimulation of the lateral iTB reliably induced swims (53.2%) whereas the control stimulation rarely coincided with behavior (13.9 %) for all fish tested (*p = 3.8×10^{-2}; Figure 6C, D). The mean bout angles of the induced swims were similar to the previously observed approaches induced by optic fiber activation of the tectum (n = 5 fish, Figure 6E). This suggests that axons of the lateral uncrossed tectobulbar tract carry the information necessary to drive approach swims.

We finally tested if the topographical organization of lateral iTB controls the directionality of swim bouts. Correlating the medial-lateral position of the photostimulation with the mean bout angle of the swims, we could indeed show that the angle increased linearly as we moved the target area more laterally, with a highly significant correlation of 0.98 (p-value=1.3×10^{-3}, Figure 6F). This observed relationship between functional topography and behavior directionality suggests that this tectofugal projection not only relays the spatial location of an attractive stimulus to hindbrain premotor areas, but is also sufficient to finely direct tail movements orienting the animal toward the presumptive prey object.

Discussion

Through a combined functional and anatomical characterization of tectal projection neurons (Lerner et al., 2016; Zeng, 2018), we show here that the zebrafish larval tectum transforms visual inputs into directed behavior by sending categorical and spatial information down to hindbrain premotor areas through dedicated labeled lines. To our knowledge, our study is the first to provide a cellular-resolution map of the information transfer that underlies a visuomotor transformation.

Three principles have emerged from our analysis, which are summarized in Figure 7. First, morphologically distinct populations of tectal projection neurons are forming at least seven output pathways to distribute information throughout the brain and to generate complex behavior. Second, categorical information is channeled along anatomically separable, uncrossed output pathways, the medial iTB and the lateral iTB, which likely target different ensembles of neurons in the reticular formation (see Figure 7). Third, focal activity in neurons projecting within the lateral portion of the iTB encode the position of an attractive object and are sufficient to direct tail movements to orient the animal toward the stimulus. Such a space code forms the output of the

tectal motor map and can be matched to the anatomical wiring of this projection (see Figure 7 – right panel). Thus, graded positional information about the stimulus in visual space is carried forward through the tectal processing layers to generate the graded motor outputs of the reticular formation.

Activation of the zebrafish tectum is sufficient to drive either approach or escape maneuvers, as has been observed in other vertebrates, using electrical stimulation protocols (Dean et al., 1986; Herrero et al., 1998; du Lac and Knudsen, 1990). We observed that escapes are more frequently evoked when the stimulation area is in the posterior region of the tectum, similar to what has been reported in goldfish (Herrero et al., 1998). Approaches, on the other hand, are not associated with any spatial preference; the turning angle of the tail is linearly increasing when the activation focus is moved along the anterior-posterior axis of the tectum. This topographic relationship, described previously as a "motor map" (Freedman et al., 1996; du Lac and Knudsen, 1990), is the result of transforming the retinotopic position of the target into a space code of movements necessary to reach it. Finally, we show that swim direction is computed by integrating the position of the target (in retinotopic coordinates) with the position of the eye, thus adjusting the final motor command to the animal's viewing direction.

By combining optogenetic stimulation with volumetric calcium imaging and behavioral tracking, we could identify neurons across the brain that were activated during the induced approach behavior. Active neuronal subpopulations were most prominent in, although not exclusive to, the caudal hindbrain. Previous studies have shown that this area harbors glutamatergic reticulospinal neurons of the V2a lineage, whose activity is sufficient and necessary for swimming (Kimura et al., 2013). Interestingly, a different population of V2a neurons in close proximity to the reticulospinal set are part of the velocity-to-position neural integrator (VPNI), a circuit that encodes information about eye position in zebrafish (Lee et al., 2015; Miri et al., 2011) and primates (Dale and Cullen, 2015; Robinson, 1989). Indeed, in primates, neuronal integrator neurons have been implicated in adjusting head movements according to eye position (Crawford et al., 2011; Sparks, 2002), and it has recently been discussed that this circuit may be homologous to that in zebrafish (Joshua and Lisberger, 2015). In monkeys, the tectum targets different hindbrain centers for eye and head coordination (Freedman et al., 1996; Klier et al., 2003; Lee and Groh, 2012), which keep the total gaze displacement constant (DeSouza et al., 2011). We hypothesize that V2a neurons in the caudal hindbrain play a similar role in larval zebrafish.

To systematically identify the neural pathways that originate in the tectum and potentially drive behavior, we created a comprehensive cellular-resolution atlas of tectal projection neurons, similar to related approaches in zebrafish and *Drosophila* for other brain areas (Costa et al., 2016; Miyasaka et al., 2014; Robles et al., 2014). The resulting projectome, generated by co-registering tracings of 133 individual neurons, revealed the tectofugal pathways described in adult goldfish (Ebbesson and Vanegas, 1976; Meek, 1983) and mammals (Huerta and Harting, 1984). Tectorecipient areas were tentatively identified, based on arborization densities, and annotated according to the neuroanatomical literature. Our approach of manual annotation and hierarchical clustering of the extratectal arborization patterns led to the identification of seven main projection classes, covering at least 29 types. Definitive proof of direct connectivity will come from stainings with synaptic markers or electron microscopic reconstructions. While the frequency of morphological cell types we reconstructed suggests that our survey is likely incomplete, we consider this atlas as the first and, at the moment, the most complete classification of tectal projection neurons in any vertebrate.

We demonstrated the power of this anatomical characterization as a reference framework to register and interpret the functional data associated with visuomotor transformations. Imaging calcium responses in axon bundles in the iTB revealed a topographic arrangement: Axons in the medial portion of the iTB, belonging to class VI-b projection neurons, were mostly tuned to threatening (looming or dimming) stimuli. Axons in the lateral iTB, belonging to class III or V, responded most strongly to prey-like stimuli. Our class III neurons resemble projection type XII neurons in adult goldfish (Meek, 1983) and are likely those that express the transcription factor Brn3a in zebrafish (Sato et al., 2007). Class VI-b neurons resemble tectal cells projecting to the area pretectalis pars dorsalis and the tectobulbar tract characterized in the trout and PV+ lateral posterior thalamic nucleus (LPTN) projecting neurons in mice (Kinoshita et al., 2006; Shang et al., 2018). This anatomical segregation of different functional responses provides a readout for the sensorimotor decision making that is taking place in the tectum (Barker and Baier, 2015; Filosa et al., 2016; Kardamakis et al., 2015).

In order to approach or orient towards an object of interest it is essential to know the location of the target in the visual field. So how is the space code – as the output of the motor map – encoded and relayed to brainstem locomotor centers? We found that axons of the lateral iTB functionally encode the position of the target in retinal space through their topographic wiring. Furthermore, we could show using optogenetics that activating the axons induces approach swims directed to the target in space. From these functional and optogenetic experiments, we conclude that the

visual responses in the axons resemble a space code of targets (Hafed and Krauzlis, 2008), which is sent via topographically arranged class III axons to dedicated premotor areas to induce directed behavior.

Contrary to our results, the iTB has been implicated in escape and the cTB in approach behavior in gerbils, toads and rodents (Dean et al., 1986; Ellard and Goodale, 1988; Ingle, 1983). However, in these studies, sectioning the tegmental area at the level of the tectobulbar decussation only partially abolished approaches. Consequently, it has already been proposed that orientation movements might be mediated by different pathways, including the uncrossed tectobulbar tract (Ellard and Goodale, 1988). At least for larval zebrafish, we show here that the lateral uncrossed tectobulbar tract, iTB, is sufficient to induce goal-directed approaches.

Interestingly, contraversive approach swims are controlled by ipsilaterally descending projections from the tectum, and similar to observations in rats (Westby et al., 1990), we detected no visual responses in contralateral descending projections. This raises the question as to how this ipsilateral stream crosses the midline to activate reticulospinal neurons on the other side of the brain. Many neurons in the hindbrain of zebrafish larvae are known to have contralaterally projecting axons, including T-reticular interneurons, which contact descending reticulospinal populations (Kimmel et al., 1985; Koyama et al., 2011), and the V2a neurons of the neural integrator (Lee et al., 2015). Some of these commissural neurons are candidates for transmitting tectum-generated motor commands.

Little is known about how tectal cell types are wired up to route behavior selection and to generate orienting movements. We show here, that labeled lines of tectal projection neurons are used to send behavior-coding information to hindbrain premotor areas. In the future, it will be interesting to dissect how this space code is translated by reticulospinal neurons into motor activity that steers behavior (dal Maschio et al., 2017; Vanwalleghem et al., 2018).

Main Figures and Legends

Figure 1 Optogenetic mapping of the tectum reveals a motor map
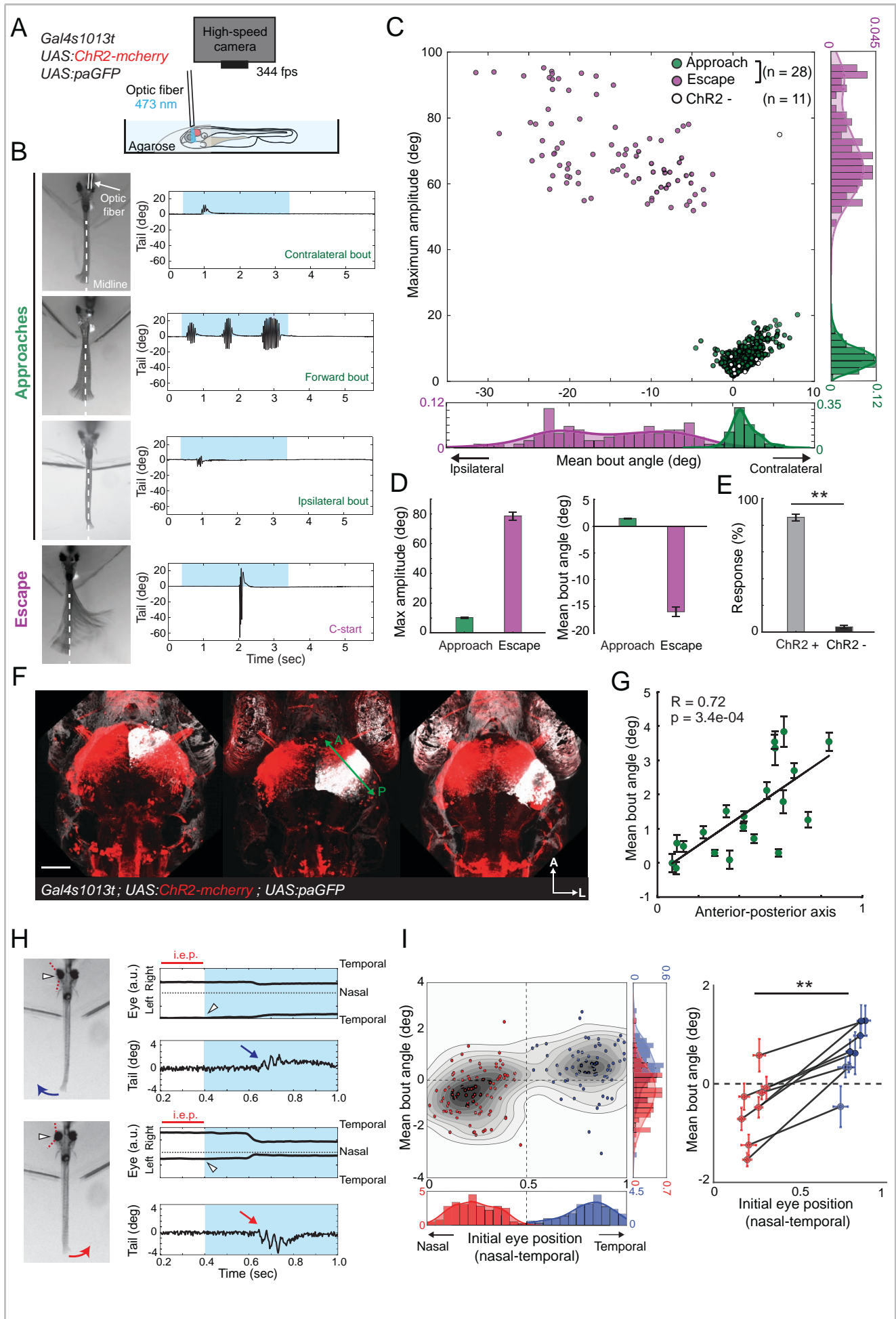
Figure 1

Optogenetic mapping of the tectum reveals a motor map. **(A)** Schematic drawing of the optogenetic setup. Zebrafish larvae (5-7dpf; *Gal4s1013t; UAS:ChR2-mCherry; UAS:paGFP*) are head-embedded in agarose, while the tail is free to move. A 50 μm optic fiber is used to stimulate ChR2 expressing tectal neurons at 473 nm, while the behavior is recorded at 344 fps. **(B)** Optogenetic activation of tectal neurons triggers behavior. Different elicited behavioral outcomes are shown as time projections along with the corresponding tail kinematics. Fish were stimulated for 3 seconds (blue background). **(C)** Characterization of the behavior. DBSCAN clustering of the mean bout angle and maximum amplitude of the first bouts triggered in each stimulation reveal two kinematically distinct behavioral outcomes: approaches and escapes. On each axis, the probability density functions displayed for the two behaviors. **(D)** Average of maximum amplitudes and mean bout angles for the different clusters of behavior. **(E)** Response probabilities for ChR2 expressing and non-expressing fish. **(F)** Fish co-expressing ChR2 (red) and paGFP were used to mark the stimulated region by photoconverted paGFP (white) after photostimulation with ChR2. **(G)** Mean bout angle increases with stimulations along the anterior-posterior axis (n=20 fish) estimated by the center of gravity of photoactivated neurons. **(H)** Influence of the initial eye position (i.e.p.) on the induced behavior. Time projection of the optogenetically induced behavior in fish with the eyes freed. The colored arrows indicate the left or right movements of the tail depending on the initial eye position (white arrowheads). Right panels show traces of eye and tail angles for the time projections, highlighting the stimulation (blue) and the initial position of the contralateral eye (dashed red line). **(I)** Quantification of the mean bout angle in relation to the initial eye position. For all induced bouts (n=8 fish), red points indicate nasal and blue points temporal eye positions. The probability density histograms show a bimodal distribution for the eye position resulting in a shift in the distribution of tail angles. The right panel depicts the shift in mean bout angle depending on the eye position for eight fish. Scale bar represents 50 μm.

Figure 2 Hindbrain neurons associated with induced approach behavior

A 20x
473 nm
Optic fiber   Prism
High-speed camera
Intensity
106 µm
0   µm   700

B
Maximum amplitude (deg)
Induced beh.
Spont. beh.
Mean bout angle (deg)
Ipsilateral   Contralateral

C Induced beh.   Spont. beh.
Tail (deg)
Time (sec)

D
Cell #
401
206
189
Stimulation
Induced beh.
Spont. beh.
ΔF/F
Time (sec)

E *Gal4s1013t ; UAS:ChR2-mcherry ; elavl3:H2B-GCaMP6s*
Stimulated tectum
Caudal hindbrain
z = 60 µm
Induced behavior   Stimulation

F
ROIs (%)
Induced beh.   Spont. beh.
*   n.s
Contra   Ipsi   Contra   Ipsi
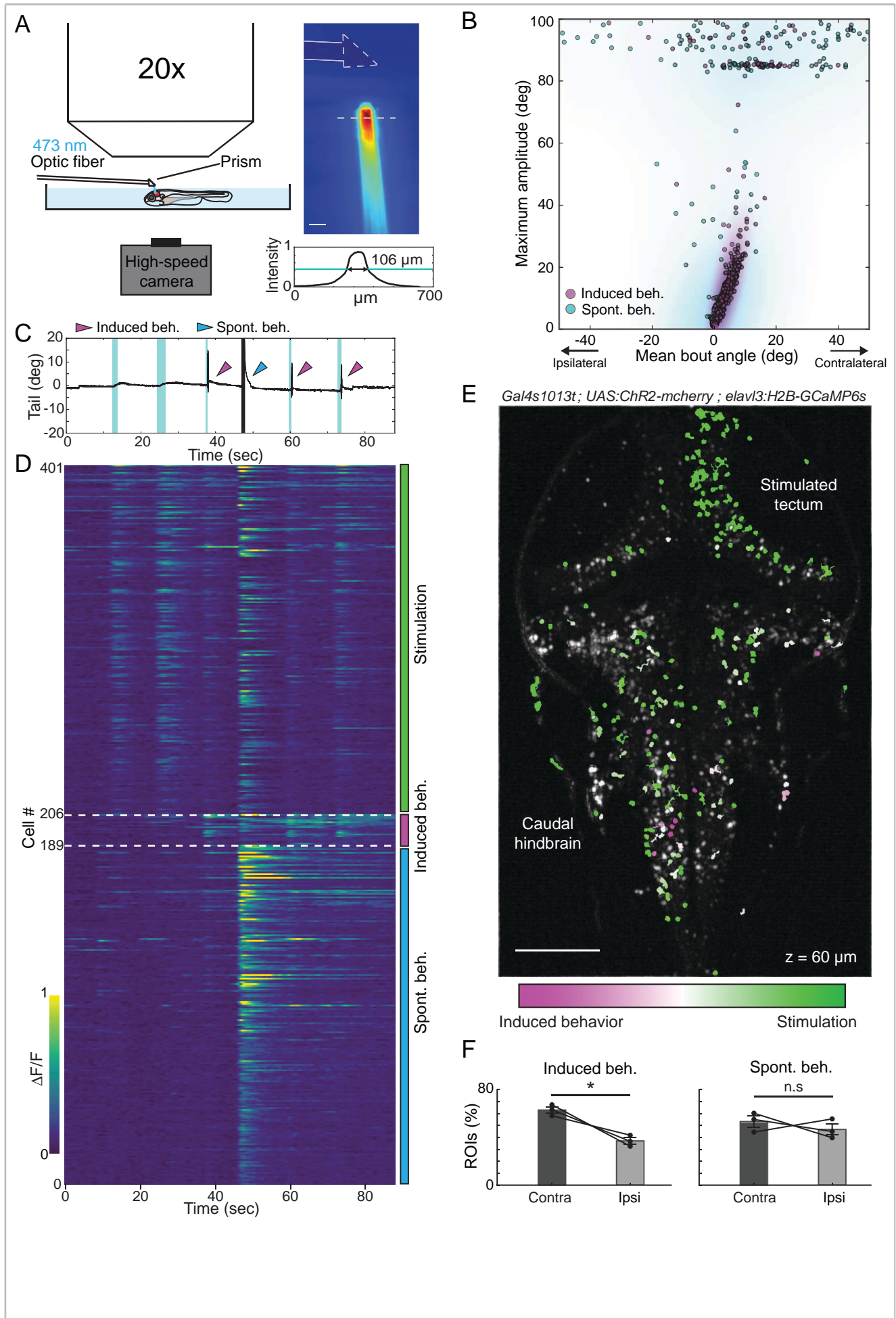
Figure 2

Hindbrain neurons associated with induced approach behavior. (A) Schematic drawing of the setup. A micro-prism (200 μm edge length) is attached to a 25 μm optic fiber, for combined 2P imaging, 1P optogenetics and behavior tracking. The right panel shows the excitation profile of the blue light (473 nm) in a fluorescein solution, yielding a diameter of 106 μm at FWHM. **(B)** Behavioral space of induced (magenta) and spontaneous (cyan) bouts. The mean and maximum bout angles are overlaid on a kernel density estimation for the two behaviors. **(C)** Tail kinematics (black trace) during the imaging protocol of 90 sec with stimulation epochs highlighted in cyan. The arrows indicate the observed behavior. **(D)** Calcium responses of 401 segmented ROIs for a plane at 60 μm below the surface of the fish. The traces are ordered according to their best correlation as depicted in (E). **(E)** ROIs correlated to the stimulation and the induced behavior. ROI responses were analyzed by calculating two indexes (detailed description of the analysis in Figure S2A, S2B, S2D). The color map indicates ROIs that are best correlated to the stimulation (green) vs. the induced behavior (magenta). **(F)** Proportion of ROIs found in the ipsilateral or contralateral hemisphere in relation to the stimulated tectum. ROIs correlated with induced behaviors were found significantly more (*p*-value 0.04) in the contralateral hemisphere, while spontaneous behaviors showed equally good correlations with ROIs in both hemispheres. Scale bars represent 100 μm.

Figure 3 The tectal projectome reveals at least seven different classes of projection neurons
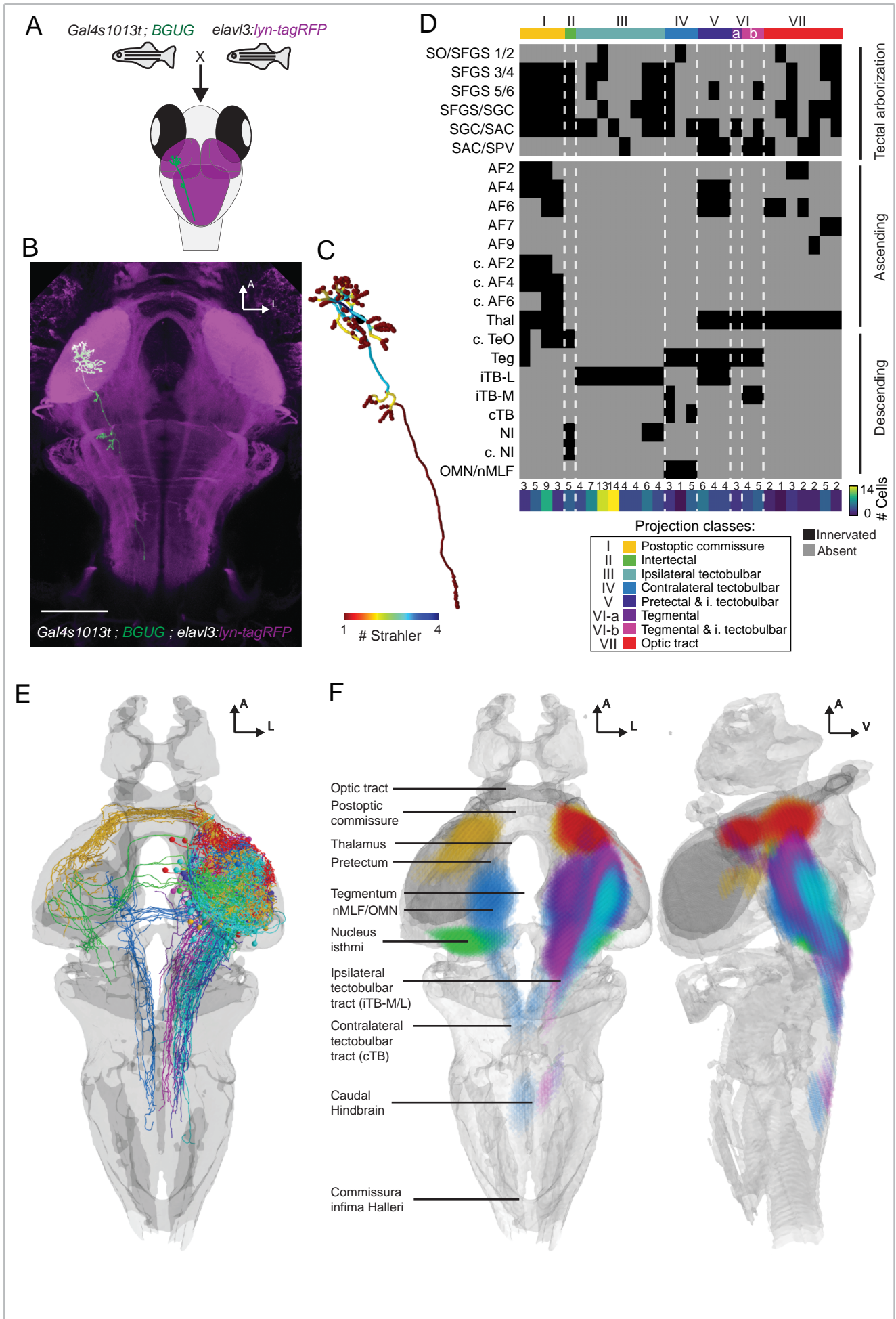
Figure 3

The tectal projectome reveals at least seven different classes of projection neurons. (A)
Single cell reconstruction strategy. Crossing BGUG (*Brn3c:Gal4;UAS:GFP*) fish to *Gal4s1013t; elavl3:lyn-tagRFP* fish results in a stochastic labeling of individual tectal neurons expressing GFP (green), while pan-neuronally expressed lyn-tagRFP (magenta) serves as a registration reference channel across different fish **(B)** Example z-projection of a single tectal projection neuron labeled with GFP in a fish expressing pan-neuronally lyn-tagRFP. **(C)** Tracing of the labeled neuron, color-coded with the Strahler number of each point highlighting arbor terminals. **(D)** Summary of all neuronal types found (133 projection neurons). Connectivity matrix revealed by manual annotation of innervated tectal and extra-tectal targets of every neuron subclass (black: innervated; grey: absent). The ordering was determined by hierarchical clustering of the extra-tectal targets. Seven main projection classes can be distinguished (I-VII, the dendrogram is shown in Suppl. Figure S4A), determined by their main projection targets, with 29 subclasses differing in final target structures (compare the wiring diagram in Suppl. Figure S5). The number of cells for each subclass is indicated below the table. **(E)** Cellular atlas of tectal projection neurons, visualized by color-coding every cell by its projection class. **(F)** Main arborization targets for every main projection class, determined by kernel density estimation of the last 10 points of neurons' skeletons with Strahler numbers of 1 (leaves) for points outside the tectum (more detailed information in Suppl. Figure S4). Scale bar represents 100 μm.

Figure 4 The lateral and medial iTB are differentially tuned to prey-like and dimming/looming stimuli
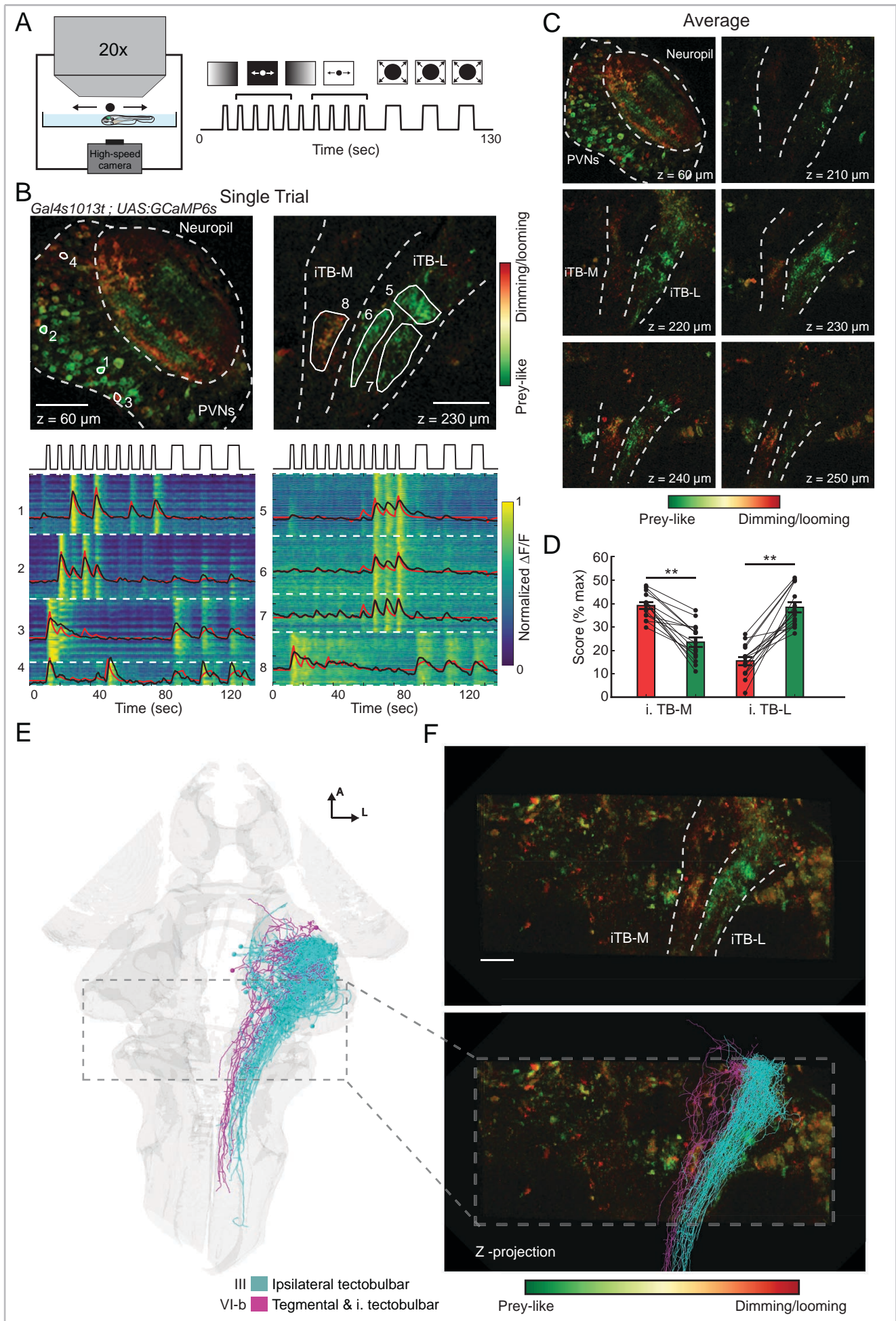
Figure 4

The lateral and medial iTB are differentially tuned to prey-like and dimming/looming stimuli. (A) Schematic drawing of the 2p imaging experiment, together with the panel of different visual stimuli used for calcium imaging (see details in Star Methods). **(B)** Single trial responses to the stimuli recorded in the tectum and the projections ventral to the tectum in a monocularly enucleated fish; Suppl. Figure S6). Top: Single planes recorded in the tectum (left) and projections (right) with pixels color-coded by preference for prey-like or dimming/looming stimuli. Note the different responses in the medial and lateral iTB. Bottom: Single pixel responses organized by ROIs (white dashed line). Black: Average calcium response for each ROI. Red: Regression model. **(C)** Average responses of a minimum of three repetitions of the protocol for the different planes imaged, highlighting the spatial separation of prey-like and dimming/looming responses in the lateral and medial iTB. **(D)** Differential responses to prey-like and dimming/looming stimuli in the medial and lateral iTB (iTB-M: **$p = 1.7 \times 10^{-6}$, iTB-L: **$p = 4.7 \times 10^{-7}$ by t-test for paired samples). **(E)** Single-cell reconstructions of class III (cyan) and VI-b (magenta) projection neurons that descend in the lateral and medial iTB, respectively. **(F)** Registration of single-cell reconstructions in (E) to a z-projection of functional imaging data. Scale bars represent 50 μm.

Figure 5   Retinotopic target information is maintained in iTB-L axons.
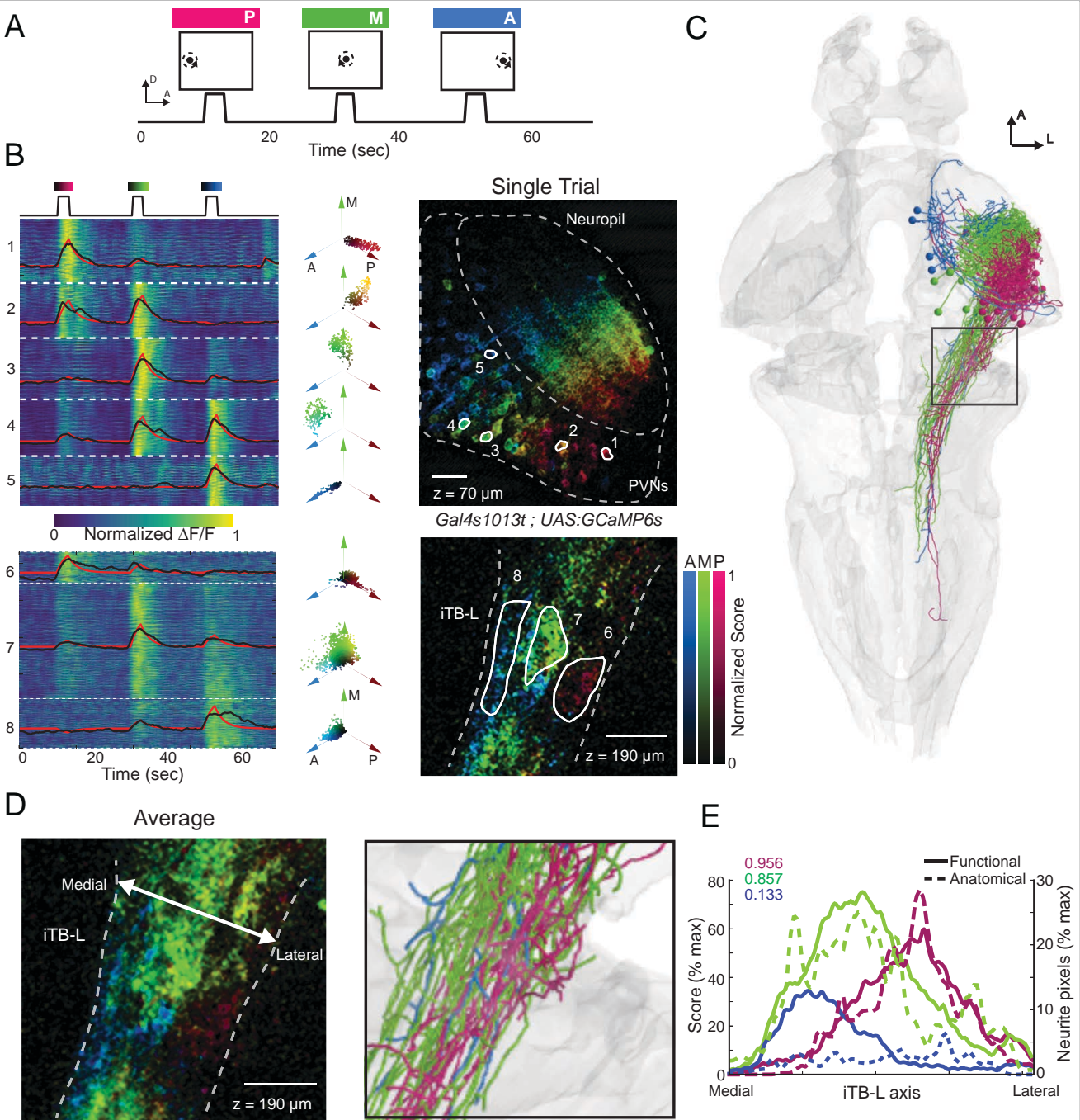
Figure 5

Retinotopic target information is maintained in iTB-L axons. (A) Stimulus protocol displaying a black dot (8 deg) circling around a center point for three seconds in three different positions of the visual field (posterior, medial and anterior). **(B)** Single trial representation of responses to the three stimulus positions. The left panel represents a raster plot of the $\Delta F/F$ traces for every pixel together with an average (black) and fitted (red) response for each ROI (right panel). The right panel shows the scores from a linear regression to the three stimuli color-coded in a HSV image that was hue-shifted to increase the contrast. Dashed lines represent the tectal neuropil, PVNs and the lateral portion of the iTB, whereas solid lines show the outline of manually drawn ROIs. The middle panel displays a polar plot of pixel responses in each ROI as its two dimensional HSV representation. The hue (angle) represents the tuning to the stimulus position, while the saturation (radius) shows the normalized score of each pixel. **(C)** Anatomical substrate of the conserved retinotopic output. Neurons in the reference brain of the projection class III, targeting solely the iTB-L, are color-coded with respect to their cell-body position along the anterior-posterior axis of the tectum. **(D)** Comparing the average functional responses of the iTB-L (three trials) with the anatomical wiring (zoom in of black box in C) illustrates a similar representation of information flow. **(E)** Overlap of functional (solid lines – n=3 fish) and anatomical (dashed lines) distributions in the iTB-L. Pearson correlation coefficients of the functional and corresponding anatomical distributions are shown in the upper left corner. Scale bars represent 10 µm.

Figure 6   Activating iTB-L projection neurons is sufficient to evoke directed approach behavior.

A

2p optogenetics 920 nm

cTB   iTB-M   iTB-L

B

Ctrl   Target

iTB-L

A
L

Gal4s1013t ; UAS:ChR2-mcherry

C

Target

Trial

Ctrl

Trial

90° L
3 sec

D

Response (%)

Target   Ctrl

E

Mean bout angle (deg)

Induced   Spont

F

Medial   Lateral

iTB-L

A
L

Gal4s1013t ; UAS:ChR2-mcherry

R = 0.98
p = 1.3e-03

Mean bout angle (deg)

medial   iTB-L axis   lateral
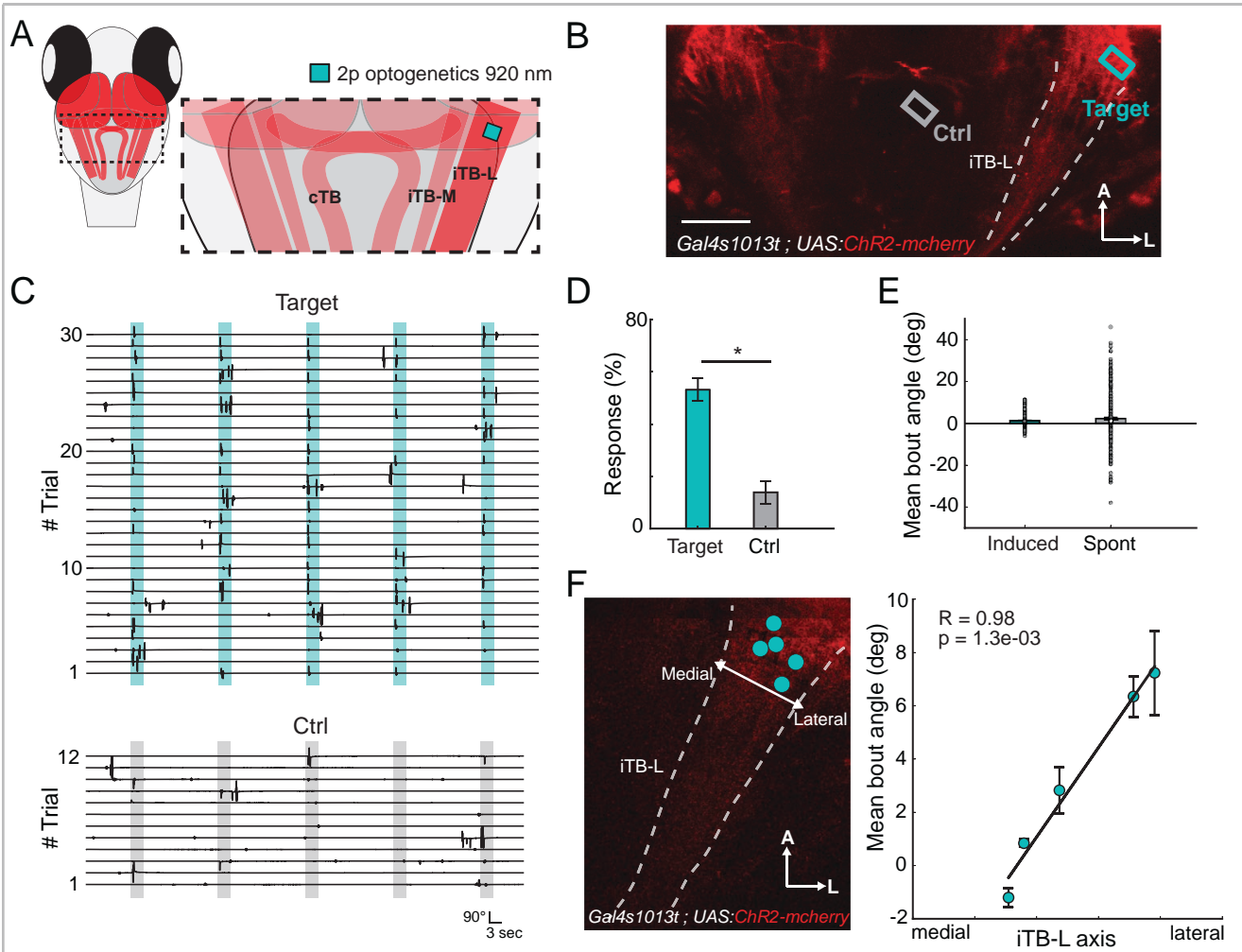
Figure 6

Activating iTB-L projection neurons is sufficient to evoke directed approach behavior. (A)
2P optogenetic stimulation of the lateral iTB. ChR2 expressing fish in the tectum were mounted
under a 2P microscope to stimulate regions of the iTB-L. **(B)** Example of stimulated zones in a
Gal4:s1013t x UAS:ChR2-mcherry fish. The cyan outline represents the targeted area (10.5 x
16.7 µm^2) to induce swims, while the grey box indicates the control stimulation where no ChR2 is
expressed. **(C)** Stimulation protocol and behavioral outcome. The laser was repeatedly scanned
(32.7 Hz) for 3 seconds with 920 nm over the target area. The target stimulation (cyan boxes)
consistently induced ipsilateral turns, whereas behavior only rarely coincides with stimulation of
the control region (grey box). **(D)** Quantification of average stimulation efficiency for target (cyan)
and control (grey) stimulations in three fish. **(E)** Mean bout angle distributions for the most
common bout types (kernel density estimation > 95%) for five fish. **(F)** Correlation between
stimulation site and tail directionality. Comparing the registered stimulation areas for five fish
indicates a bias in bout directionality that increases with medial to lateral position in the iTB-L.
Scale bar represents 50 µm.

Figure 7

Schematic summary of tectofugal visuomotor topography
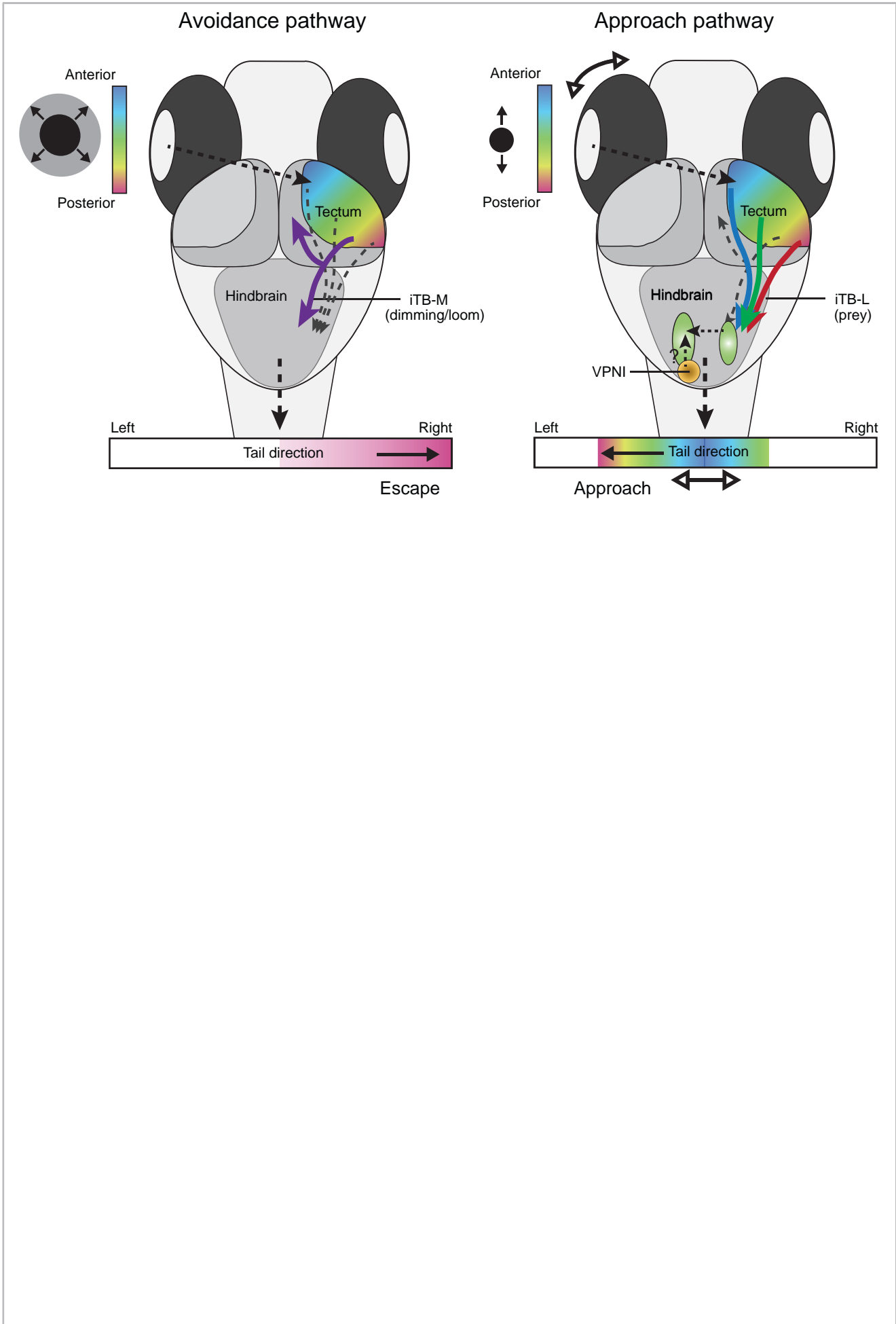
Figure 7

Schematic summary of tectofugal visuomotor topography. A sensorimotor decision regarding looming or prey-like objects is made by differentially recruiting either of two uncrossed output channels to the hindbrain. The lateral uncrossed tectobulbar tract (iTB-L) carries spatial information about prey-like targets to hindbrain premotor pools. This space code of target location contains a graded motor command necessary to reach it. The tectofugal pathway is ipsilateral so motor commands cross the midline within the hindbrain to induce orienting movements. The involved premotor areas (green), together with the eye velocity and position neural integrator (VPNI - yellow), coordinate the tail movements taking into account on the animal's viewing direction.

Figure S1 - related to Fig. 1

A

Silhouette coefficient

0.88
0.78

5   6.1   10
Inter-point-distance (e)

0   2   5
Clusters

B

Tailbeat frequency (Hz)

40
30
20
10
0

Approach   Escape

Delay (sec)

2

1

0

Approach   Escape

C

A
L

D
L

0   Mean bout angle (deg)   3

D

R = 0.36
p = 3.8e-01

Mean bout angle (deg)

0
-5
-10
-15
-20
-25
-30

0   Anterior-posterior axis   1
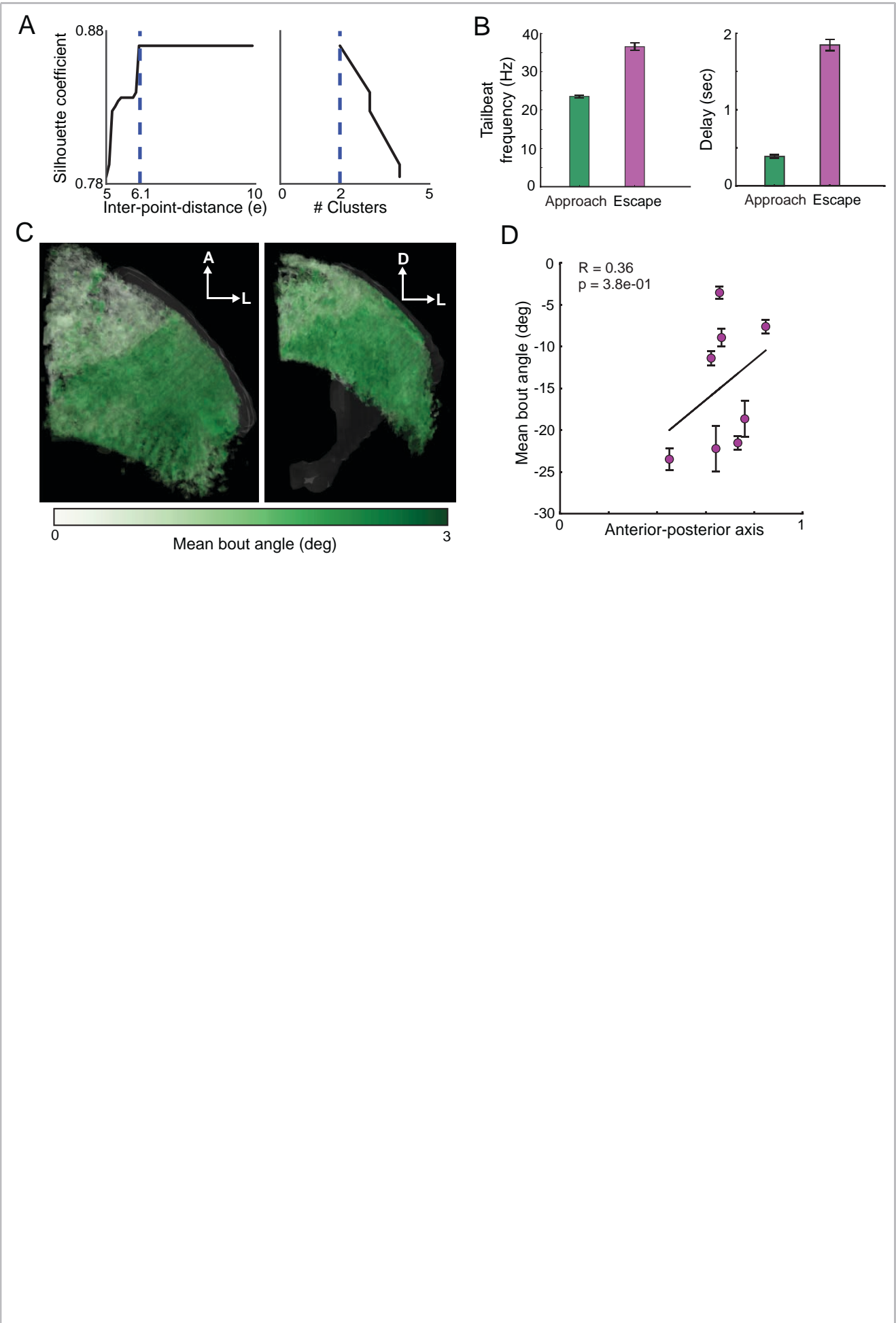
Suppl. Figure S1 – related to Figure 1

(A) Behavioral clustering. Silhouette coefficients found for different inter-point distances and the resulting best estimation of two clusters (DBSCAN). **(B)** Two additional parameters, tail beat frequency and delay of behavioral onset to stimulation start, extracted for approaches and escapes. **(C)** Registration of the paGFP signal of all 20 fish color-coding the mean bout angle. **(D)** Induced escapes show low correlation with the stimulation side and were triggered only in more posterior regions of the tectum.

Figure S2 - related to Fig. 2

A

Regressors | Linear regression | Scores (R² * coefficients) | Classification

Stimulation

Behavior (n): Induced, Spontaneous, Induced, Induced

Response 1 — Induced

Response 2 — Spontaneous

Response 3 — Stimulation

Scores axis: 1.2 / -0.5

Ind Spont Ind Ind Stim
Behavior

B

Max amplitude (deg): Induced, Spont.

Mean bout angle (deg): Induced, Spont.

C

Average ≥ 3 Trials:

$$\text{SB-Index} = \frac{\text{median(Behavior)} - \text{median(Stimulation)}}{\text{median(Behavior)} + \text{median(Stimulation)}}$$

$$\text{IS-Index} = \frac{\text{median(Spontaneous)} - \text{median(Induced)}}{\text{median(Spontaneous)} + \text{median(Induced)}}$$

D

Stimulation / Behavior / Induced / Spontaneous

z = 0 µm, z = 40 µm, z = 80 µm, z = 120 µm
z = 10 µm, z = 50 µm, z = 90 µm, z = 130 µm
z = 20 µm, z = 60 µm, z = 100 µm, z = 140 µm
z = 30 µm, z = 70 µm, z = 110 µm, z = 150 µm

Average ≥ 3 Trials

-1 Stimulation — Behavior 1

-1 Induced beh. — Spont. beh. 1

median (R²) > 0.6

116

Suppl. Figure S2 – related to Figure 2

(A) Linear regression analysis of functional traces for reconstructed ROIs. One regressor is created for optogenetic stimulations and one for every behavioral bout detected (spontaneous or optogenetically induced). These regressors are convolved with a kernel according to the time constants of H2B-GCaMP6s. A linear regression model is constructed for the ΔF/F response of every ROI and the corresponding coefficients and the coefficient of determination (R^2) are calculated, to obtain a score (coefficients*R^2). **(B)** Max amplitude and mean bout angle for induced and spontaneous bouts. **(C)** SB and IS indices. Every plane was imaged at least 3 times. The SB-Index (Stimulation vs Behavior) was calculated for every ROI as the difference between the median of all behavioral scores and the median of all stimulation scores and normalized to the sum of both, thus ranging from -1 to 1. Similarly, an IS-index (Induced behavior vs Spontaneous behavior) was calculated for all ROIs that had an SB-Index > 0 (i.e. better correlated to behavior) **(D)** Summary of all planes imaged (0-150 µm) color-coding the ROIs for each plane according to the SB (left, green-orange) and IS-Index (right, magenta-cyan). ROIs were only counted if the median R^2 over the trials was larger than 0.6. Scale bar represents 100 µm.

Figure S3 - related to Fig. 3

A *Gal4s1013t ; UAS:ChR2-mCherry*

B All neurons   Mirrored

C

Optic tract	Postoptic commisure	Intertectal
Ipsilateral tectobulbar	Contralateral tectobulbar	SPN
Pretectal & i. tectobulbar	Tegmental	Tegmental & i. tectobulbar
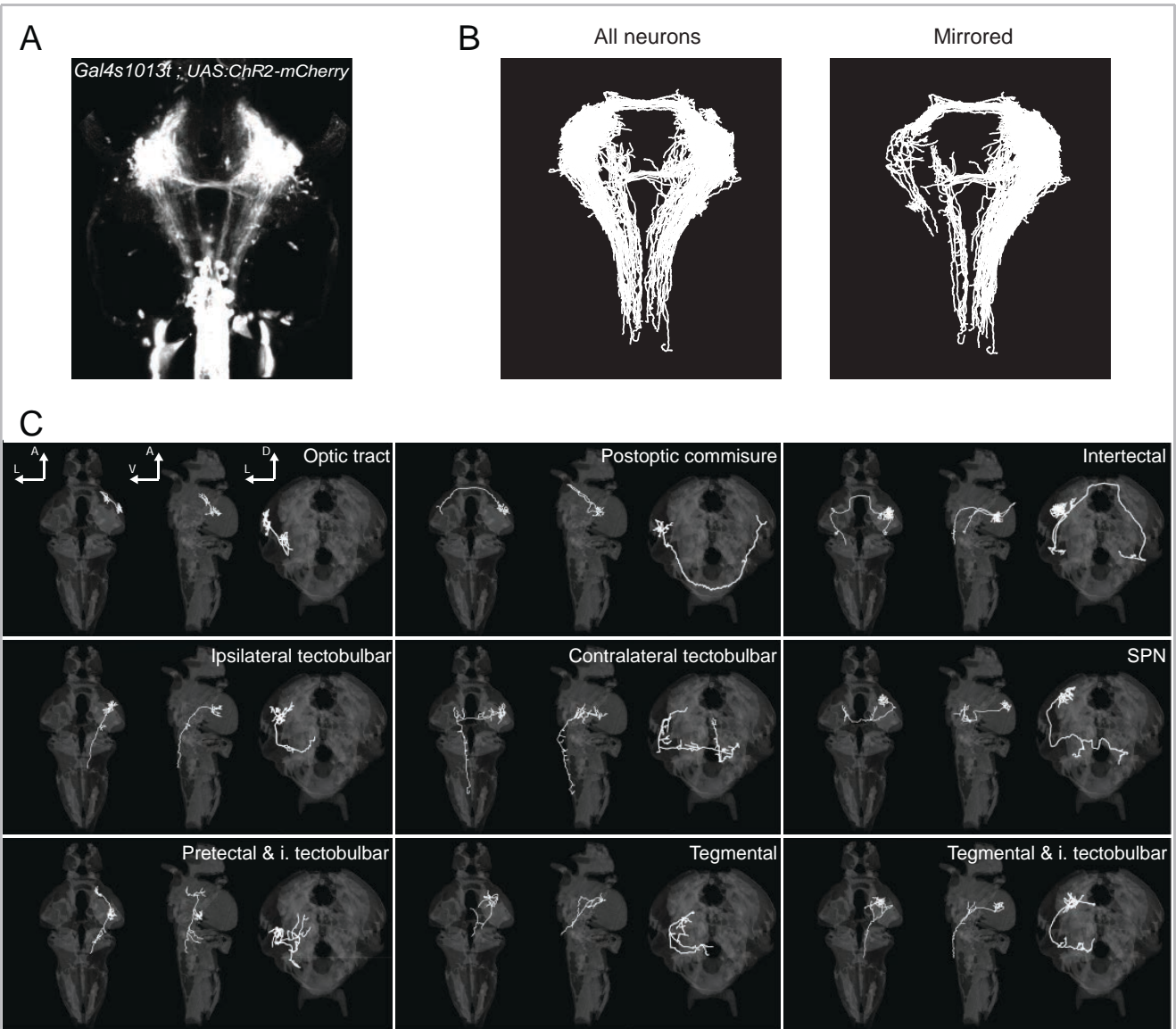
Suppl. Figure S3 – related to Figure 3

(A) Maximum intensity z-projection of tectal tracts from ChR2-mcherry expressing neurons in the Gal4s1013t line illustrating the projections to tegmental, thalamic and hindbrain regions. **(B)** Z-projection of all traced neurons below the tectum and for neurons mirrored to one hemisphere. **(C)** Exemplars of different classes of projection neurons in xy, xz and yz projections targeting different brain structures. SPN: superficial projection neuron.

Figure S4 - related to Fig. 3

Projection classes:
- I — Postoptic commissure
- II — Intertectal
- III — Ipsilateral tectobulbar
- IV — Contralateral tectobulbar
- V — Pretectal & i. tectobulbar
- VI-a — Tegmental
- VI-b — Tegmental & i. tectobulbar
- VII — Optic tract

Strahler 1 — 4

Class I: Postoptic commisure

Class II: Intertectal

Class III: Ipsilateral tectobulbar

Class IV: Contralateral tectobulbar

Class V: Pretectal & i. tectobulbar

Class VI-a: Tegmental

Class VI-b: Tegmental & i. tectobulbar

Class VII: Optic tract

Suppl. Figure S4 – related to Figure 3

(A) Dendrogram of the hierarchical clustering used to generate the connectivity matrix shown in Figure 3D. **(B)** Schematic representation of the Strahler number ordering. The Strahler number represents the number of children of every node. Leaves (neurites that have no children) have Strahler numbers of 1. **(C)** Strahler numbers calculated for every point in the tracing of a tectal interneuron. **(D)** Calculation of arborization densities for traced points inside the tectum of the last 10 points in leaves. Color-coding is according to the projection class of the neurons. **(E)** Detailed representation of arborization densities for all projection classes, together with the single tracings of the corresponding neurons.

Figure S5 - related to Fig. 3

Suppl. Figure S5 – related to Figure 3

Wiring diagram of all seven main classes of projection neurons, including the 29 subclasses. Solid lines represent the neurite trajectory and solid nodes indicate branching. The table at the bottom lists the abbreviations used in the diagram.

Figure S6 - related to Fig. 4

A

Enucleated - Average

z = 230 µm

iTB-M

iTB-L

Untreated - Average

iTB-M

iTB-M

iTB-L

z = 215 µm
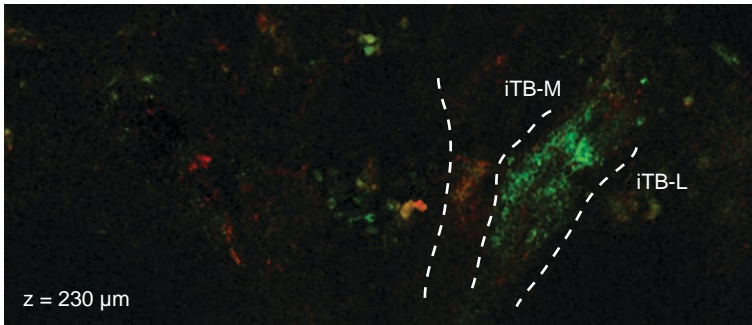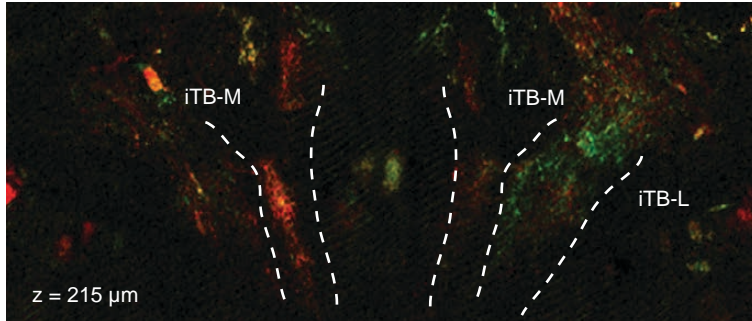
Dimming/looming

Prey-like

B
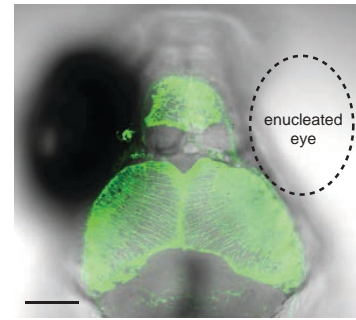
Gal4s1013t ; UAS:GCaMP6s
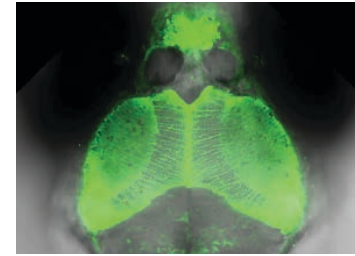
enucleated
eye

Suppl. Figure S6 – related to Figure 4

(**A**) Comparison of response profiles in the different tracts in monocular enucleated (upper panel) and untreated (lower panel) fish in similar planes. (**B**) Expression of GCaMP6s reporter in the Gal4:s1013t pattern in fish where one eye was surgically removed and control fish without any manipulation. The enucleated side is depicted in the upper panel. Scale bar represents 100 µm.

Figure S7 - related to Fig. 5

A

Medial   Lateral

A
M
P

0   Normalized Score   1

Functional

B

Medial Lateral

Anatomical

126
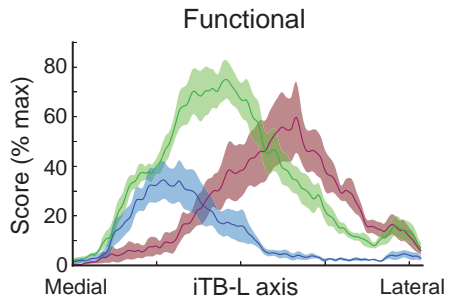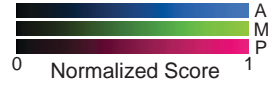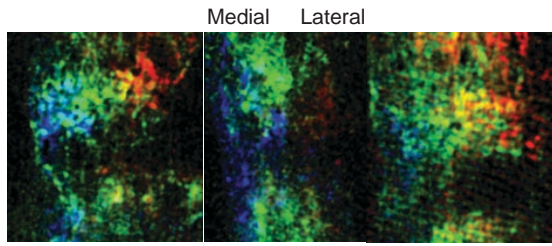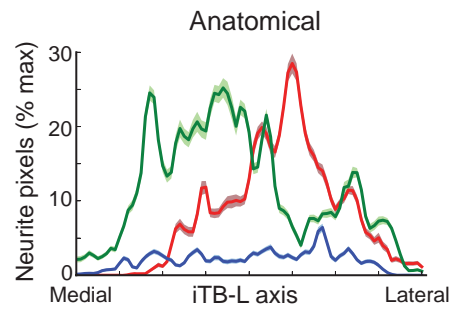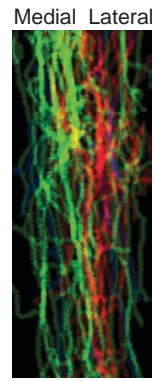
Suppl. Figure S7 – related to Figure 5

(**A**) Analysis of the spatial distributions of response profiles in the iTB-L for three different fish, after rotation to the perpendicular axis of the iTB-L. The pixel values for every channel in the RGB image were averaged along the vertical axis in a total of 7 planes and normalized to calculate the distributions for every channel. The average traces are plotted in the corresponding color (anterior, medial, posterior stimulus – blue, green, red) and the shading represents the s.e.m. for each channel. (**B**) Similar analysis was performed on the traced neurons, by creating an RGB image color-coding the cell-body location along the anterior-posterior axis of the tectum.

Supplemental Movies

Movie S1 – related to Figure 1

Optic fiber optogenetic stimulation of tectal neurons in the line *Gal4:s1013t x UAS:ChR2-mCherry*. Stimulating different regions of the tectum in the same fish, demonstrates that the same tectum is capable to induce both approach and escape maneuvers. The behavior is recorded at 344 fps, while the movie playback is 35 fps.

Movie S2 – related to Figure 3

The tectal projectome. Tracings of 133 tectal projection neurons (randomly colored) were registered to a standard brain (gray) and mirrored to one hemisphere. Clustering the neurons based on their extratectal stratifications revealed at least seven morphological distinct classes. The neurons are recolored in the middle of the video according to their classes as shown in Figure 3.

REFERENCES

Arrenberg, A.B., Del Bene, F., and Baier, H. (2009). Optical control of zebrafish behavior with halorhodopsin. Proc. Natl. Acad. Sci. U. S. A. *106*, 17968–17973.

Barker, A.J., and Baier, H. (2015). Sensorimotor decision making in the Zebrafish tectum. Curr. Biol. *25*, 2804–2814.

Basso, M.A., and May, P.J. (2017). Circuits for Action and Cognition: A View from the Superior Colliculus. Annu. Rev. Vis. Sci. *3*, annurev-vision-102016-061234.

Bergeron, A., Matsuo, S., and Guitton, D. (2003). Superior colliculus encodes distance to target, not saccade amplitude, in multi-step gaze shifts. Nat. Neurosci. *6*, 404–413.

Bianco, I.H., and Engert, F. (2015). Visuomotor Transformations Underlying Hunting Behavior in Zebrafish. Curr. Biol. *25*, 831–846.

Burrill, J.D., and Easter, S.S. (1994). Development of the retinofugal projections in the embryonic and larval zebrafish (Brachydanio rerio). J. Comp. Neurol. *346*, 583–600.

Costa, M., Manton, J.D., Ostrovsky, A.D., Prohaska, S., Jefferis, G.S.X.E., Costa, M., Manton, J.D., Ostrovsky, A.D., Prohaska, S., and Jefferis, G.S.X.E. (2016). NBLAST: Rapid, Sensitive Comparison of Neuronal Structure and Construction of Neuron Family Databases. Neuron *91*, 293–311.

Crawford, J.D., Henriques, D.Y.P., and Medendorp, W.P. (2011). Three-Dimensional Transformations for Goal-Directed Action. Annu. Rev. Neurosci. *34*, 309–331.

dal Maschio, M., Donovan, J.C., Helmbrecht, T.O., and Baier, H. (2017). Linking Neurons to Network Function and Behavior by Two-Photon Holographic Optogenetics and Volumetric Imaging. Neuron *94*, 774–789.e5.

Dale, A., and Cullen, K.E. (2015). Local Population Synchrony and the Encoding of Eye Position in the Primate Neural Integrator. J. Neurosci. *35*, 4287–4295.

Dean, P., Redgrave, P., and Sahibzada, N. (1986). Head and body movements produced by electrical stimulation of SC in rats_effects of interruption of crossed tectoreticulospinal

parhway.pdf. *19*, 367–380.

Dean, P., Redgrave, P., and Westby, G.W.M. (1989). Event or emergency? Two response systems in the mammalian superior colliculus. Trends Neurosci. *12*, 137–147.

DeSouza, J.F.X., Keith, G.P., Yan, X., Blohm, G., Wang, H., and Crawford, J.D. (2011). Intrinsic Reference Frames of Superior Colliculus Visuomotor Receptive Fields during Head-Unrestrained Gaze Shifts. J. Neurosci. *31*, 18313–18326.

Ebbesson, S.O., and Vanegas, H. (1976). Projections of the optic tectum in two teleost species. J. Comp. Neurol. *165*, 161–180.

Ellard, C.G., and Goodale, M.A. (1988). A functional analysis of the collicular output pathways: a dissociation of deficits following lesions of the dorsal tegmental decussation and the ipsilateral collicular efferent bundle in the Mongolian gerbil. Exp. Brain Res. *71*, 307–319.

Felsen, G., and Mainen, Z.F. (2012). Midbrain contributions to sensorimotor decision making. J. Neurophysiol. *108*, 135–147.

Filosa, A., Barker, A.J., Dal Maschio, M., and Baier, H. (2016). Feeding State Modulates Behavioral Choice and Processing of Prey Stimuli in the Zebrafish Tectum. Neuron *90*, 596–608.

Freedman, E.G., Stanford, T.R., and Sparks, D.L. (1996). Combined eye-head gaze shifts produced by electrical stimulation of the superior colliculus in rhesus monkeys. J. Neurophysiol. *76*, 927–952.

Gahtan, E., Tanger, P., and Baier, H. (2005). Visual Prey Capture in Larval Zebrafish Is Controlled by Identified Reticulospinal Neurons Downstream of the Tectum. J. Neurosci. *25*, 9294–9303.

Giovannucci, A., Friedrich, J., Deverett, B., Staneva, V., Chklovskii, D., and Pnevmatikakis, E. (2017). Caiman: An open source toolbox for large scale calcium imaging data analysis on standalone machines. Cosyne Abstr.

Hafed, Z.M., and Krauzlis, R.J. (2008). Goal Representations Dominate Superior Colliculus Activity during Extrafoveal Tracking. J. Neurosci. *28,* 9426–9439.

Herrero, L., Rodríguez, F., Salas, C., and Torres, B. (1998). Tail and eye movements evoked by electrical microstimulation of the optic tectum in goldfish. Exp. Brain Res. *120*, 291–305.

Huerta, M.F., and Harting, J.K. (1984). Connectional Organization of the superior colliculus.

Ingle, D.J. (1983). BRAIN MECHANISMS OF VISUAL LOCALIZATION BY FROGS AND TOADS Department of Psychology Brandeis University Classical ethology provides two fundamental themes which remain at the heart of current research in neuroethology . First , is the assumption that even. Adv. Vertebr. Neuroethol. 177–226.

Jefferis, G.S.X.E., and Manton, J.D. (2014). NeuroAnatomy Toolbox v1.5.2. Zenodo.

Joshua, M., and Lisberger, S.G. (2015). A tale of two species: Neural integration in zebrafish and monkeys. Neuroscience *296*, 80–91.

Kardamakis, A.A., Saitoh, K., and Grillner, S. (2015). Tectal microcircuit generating visual selection commands on gaze-controlling neurons.

Kimmel, C.B., Metcalfe, W.K., and Schabtach, E. (1985). T reticular interneurons: A class of serially repeating cells in the zebrafish hindbrain. J. Comp. Neurol. *233*, 365–376.

Kimura, Y., Satou, C., Fujioka, S., Shoji, W., Umeda, K., Ishizuka, T., Yawo, H., and Higashijima, S. (2013). Hindbrain V2a neurons in the excitation of spinal locomotor circuits during zebrafish swimming. Curr. Biol. *23*, 843–849.

Kinoshita, M., Ito, E., Urano, A., Ito, H., and Yamamoto, N. (2006). Periventricular efferent neurons in the optic tectum of rainbow trout. J. Comp. Neurol. *499*, 546–564.

Klier, E.M., Wang, H., and Crawford, J.D. (2001). The superior colliculus encodes gaze commands in retinal coordinates. Nat. Neurosci. *4*, 627–632.

Klier, E.M., Wang, H., and Crawford, J.D. (2003). Three-Dimensional Eye-Head Coordination Is Implemented Downstream From the Superior Colliculus. J. Neurophysiol. *89*, 2839–2853.

Kostyk, S.K., and Grobstein, P. (1987). Neuronal organization underlying visually elicited prey orienting in the frog-I. Effects of various unilateral lesions. Neuroscience *21*, 41–55.

Koyama, M., Kinkhabwala, A., Satou, C., Higashijima, S., and Fetcho, J. (2011). Mapping a sensory-motor network onto a structural and functional ground plan in the hindbrain. Proc. Natl. Acad. Sci. U. S. A. *108*, 1170–1175.

Kubo, F., Hablitzel, B., Dal Maschio, M., Driever, W., Baier, H., and Arrenberg, A.B. (2014). Functional Architecture of an Optic Flow-Responsive Area that Drives Horizontal Eye Movements in Zebrafish. Neuron *81*, 1344–1359.

du Lac, S., and Knudsen, E.I. (1990). Neural maps of head movement vector and speed in the optic tectum of the barn owl. J. Neurophysiol. *63*, 131–146.

Lee, J., and Groh, J.M. (2012). Auditory signals evolve from hybrid- to eye-centered coordinates in the primate superior colliculus. J. Neurophysiol. *108*, 227–242.

Lee, M.M., Arrenberg, A.B., and Aksay, E.R.F. (2015). A Structural and Genotypic Scaffold Underlying Temporal Integration. J. Neurosci. *35*, 7903–7920.

Lerner, T.N., Ye, L., and Deisseroth, K. (2016). Communication in Neural Circuits: Tools, Opportunities, and Challenges. Cell *164*, 1136–1150.

Masino, T., and Grobstein, P. (1989). The organization of descending tectofugal pathways underlying orienting in the frog, Rana pipiens. Exp. Brain Res. *75*, 227–244.

Meek, J. (1983). Functional anatomy of the tectum mesencephali of the goldfish. An explorative analysis of the functional implications of the laminar structural organization of the tectum. Brain Res. Rev. *6*, 247–297.

Miri, A., Daie, K., Burdine, R.D., Aksay, E., and Tank, D.W. (2011). Regression-Based Identification of Behavior-Encoding Neurons During Large-Scale Optical Imaging of Neural Activity at Cellular Resolution. J. Neurophysiol. *105*, 964–980.

Miyasaka, N., Arganda-Carreras, I., Wakisaka, N., Masuda, M., Sümbül, U., Seung, H.S., and Yoshihara, Y. (2014). Olfactory projectome in the zebrafish forebrain revealed by genetic single-neuron labelling. Nat. Commun. *5*, 3639.

Murayama, M., Pérez-Garci, E., Lüscher, H.-R., and Larkum, M.E. (2007). Fiberoptic system for recording dendritic calcium signals in layer 5 neocortical pyramidal cells in freely moving rats. J.

Neurophysiol. *98*, 1791–1805.

van Opstal, a J., Hepp, K., Hess, B.J., Straumann, D., and Henn, V. (1991). Two- rather than three-dimensional representation of saccades in monkey superior colliculus. Science *252*, 1313–1315.

Patterson, B.W., Abraham, A.O., MacIver, M.A., and McLean, D.L. (2013). Visually guided gradation of prey capture movements in larval zebrafish. J. Exp. Biol. *216*, 3071–3083.

Peirce, J.W. (2007). PsychoPy-Psychophysics software in Python. J. Neurosci. Methods *162*, 8–13.

Pérez-Pérez, M.P., Luque, M. a., Herrero, L., Nunez-Abades, P. a., and Torres, B. (2003). Connectivity of the goldfish optic tectum with the mesencephalic and rhombencephalic reticular formation. Exp. Brain Res. *151*, 123–135.

Pnevmatikakis, E.A., and Giovannucci, A. (2017). NoRMCorre : An online algorithm for piecewise rigid motion correction of calcium imaging data. BioRxiv 1–12.

Portugues, R., Feierstein, C.E., Engert, F., and Orger, M.B. (2014). Whole-Brain Activity Maps Reveal Stereotyped, Distributed Networks for Visuomotor Behavior. Neuron *81*, 1328–1343.

R Core Team (2016). R: A language and environment for statistical computing. R Found. Stat. Comput. Vienna, Austria.

Robinson, D.A. (1989). Integrating with Neurons. Annu. Rev. Neurosci. *12*, 33–45.

Robles, E., Laurell, E., and Baier, H. (2014). The retinal projectome reveals brain-area-specific visual representations generated by ganglion cell diversity. Curr. Biol. *24*, 2085–2096.

Roeser, T., and Baier, H. (2003). Visuomotor behaviors in larval zebrafish after GFP-guided laser ablation of the optic tectum. J. Neurosci. *23*, 3726–3734.

Rohlfing, T., and Maurer, C.R. (2003). Nonrigid image registration in shared-memory multiprocessor environments with application to brains, breasts, and bees. IEEE Trans. Inf. Technol. Biomed. *7*, 16–25.

Sadeh, M., Sajad, A., Wang, H., Yan, X., and Crawford, J.D. (2015). Spatial transformations between superior colliculus visual and motor response fields during head-unrestrained gaze shifts. Eur. J. Neurosci. *42*, 2934–2951.

Saitoh, K., Ménard, A., and Grillner, S. (2007). Tectal control of locomotion, steering, and eye movements in lamprey. J. Neurophysiol. *97*, 3093–3108.

Sato, T., Hamaoka, T., Aizawa, H., Hosoya, T., and Okamoto, H. (2007). Genetic single-cell mosaic analysis implicates ephrinB2 reverse signaling in projections from the posterior tectum to the hindbrain in zebrafish. J. Neurosci. *27*, 5271–5279.

Schoonheim, P.J., Arrenberg, A.B., Del Bene, F., and Baier, H. (2010). Optogenetic localization and genetic perturbation of saccade-generating neurons in zebrafish. J. Neurosci. *30*, 7111–7120.

Scott, E.K., and Baier, H. (2009). The cellular architecture of the larval zebrafish tectum, as revealed by gal4 enhancer trap lines. Front. Neural Circuits *3*, 13.

Scott, E.K., Mason, L., Arrenberg, A.B., Ziv, L., Gosse, N.J., Xiao, T., Chi, N.C., Asakawa, K., Kawakami, K., and Baier, H. (2007). Targeting neural circuitry in zebrafish using GAL4 enhancer trapping. Nat. Methods *4*, 323–326.

Semmelhack, J.L., Donovan, J.C., Thiele, T.R., Kuehn, E., Laurell, E., and Baier, H. (2014). A dedicated visual pathway for prey detection in larval zebrafish. Elife *4*, 1–19.

Severi, K.E., Portugues, R., Marques, J.C., O'Malley, D.M., Orger, M.B., and Engert, F. (2014). Neural Control and Modulation of Swimming Speed in the Larval Zebrafish. Neuron *83*, 692–707.

Shang, A.C., Chen, Z., Liu, A., Li, Y., Zhang, J., and Yan, F. (2018). Divergent midbrain circuits orchestrate escape and freezing responses to looming stimuli in mice. Nat. Commun. 1–17.

Shang, C., Liu, Z., Chen, Z., Shi, Y., Wang, Q., Liu, S., Li, D., and Cao, P. (2015). A parvalbumin-positive excitatory visual pathway to trigger fear responses in mice. Science (80-.). *348*, 1472–1477.

Sooksawate, T., Isa, K., Matsui, R., Kato, S., Kinoshita, M., Kobayashi, K., Watanabe, D.,

Kobayashi, K., and Isa, T. (2013). Viral vector-mediated selective and reversible blockade of the pathway for visual orienting in mice. Front. Neural Circuits *7*, 162.

Sparks, D.L. (2002). The brainstem control of saccadic eye movements. Nat. Rev. Neurosci. *3*, 952–964.

Sparks, D.L., and Gandhi, N.J. (2003). Single cell signals: An oculomotor perspective. Prog. Brain Res. *142*, 35–53.

Temizer, I., Donovan, J.C., Baier, H., and Semmelhack, J.L. (2015). A Visual Pathway for Looming-Evoked Escape in Larval Zebrafish. Curr. Biol. *25*, 1823–1834.

Thiele, T.R., Donovan, J.C., and Baier, H. (2014). Descending Control of Swim Posture by a Midbrain Nucleus in Zebrafish. Neuron *83*, 679–691.

Vanwalleghem, G.C., Ahrens, M.B., and Scott, E.K. (2018). Integrative whole-brain neuroscience in larval zebrafish. Curr. Opin. Neurobiol. *50*, 136–145.

Vladimirov, N., Mu, Y., Kawashima, T., Bennett, D. V, Yang, C.-T., Looger, L.L., Keller, P.J., Freeman, J., and Ahrens, M.B. (2014). Light-sheet functional imaging in fictively behaving zebrafish. Nat. Methods *11*, 883–884.

Vormberg, A., Effenberger, F., Muellerleile, J., and Cuntz, H. (2017). Universal features of dendrites through centripetal branch ordering. PLoS Comput. Biol. *13*, 1–25.

Westby, G.W.M., Keay, K., Redgrave, P., Dean, P., and Bannister, M. (1990). Output pathways from the rat superior colliculus mediating approach and avoidance have different sensory properties. Exp. Brain Res. *81*, 626–638.

Zeng, H. (2018). Mesoscale connectomics. Curr. Opin. Neurobiol. *50*, 154–162.

STAR METHODS

KEY RESOURCES TABLE

REAGENT or RESOURCE	SOURCE	IDENTIFIER
Experimental Models: Organisms/Strains		
Et(-1.5hsp70l:Gal4-VP16)s1013t	Scott et al., 2007	ZFIN: ZDB-FISH-150901-5417
Tg(brn3c:GAL4, UAS: gap43-GFP)s318t - BGUG	Scott et al., 2007	ZFIN: ZDB-FISH-150901-25363
Tg(UAS:ChR2(H134R)-mCherry)s1985t	Arrenberg et al., 2009	ZFIN: ZDB-FISH-150901-20696
Tg(UAS:GCaMP6s)mpn101	Thiele et al., 2014	ZFIN: ZDB-FISH-150901-22562
Tg(elavl3:lyn-tagRFP)mpn404	dal Maschio et al., 2017	N/A
Tg(UAS:paGFP)mpn143	dal Maschio et al., 2017	N/A
Tg(elavl3:H2B-GCaMP6s)	Vladimirov et al., 2014	jf5
Software and Algorithms		
Neuron morphology reconstruction	neuTube	http://www.neutracing.com/
Image analysis	Fiji	http://fiji.sc/Fiji
CMTK	Rohlfing and Maurer, 2003	https://www.nitrc.org/projects/cmtk/
Python 2.7.12	Anaconda2	https://www.anaconda.com/
Python 3.4.3	Anaconda3	https://www.anaconda.com/
Psychopy2	Peirce, 2007	http://www.psychopy.org/
R 3.3.1	R Core Team, 2016	https://www.R-project.org/
NeuroAnatomy Toolbox – nat 1.8.6	Jefferis and Manton, 2014	https://github.com/jefferis/nat

CONTACT FOR REAGENT AND RESOURCE SHARING

Further information and requests for resources and reagents should be directed to and will be fulfilled by the Lead Contact, Herwig Baier (hbaier@neuro.mpg.de).

136

EXPERIMENTAL MODEL AND SUBJECT DETAILS

All animal procedures conformed to the institutional guidelines set by the Max Planck Society, and with an animal protocol approved by the regional government (Regierung von Oberbayern).

Transgenic zebrafish lines

For all experiments in this study we used 5-7 days post fertilization (d.p.f.) larvae carrying mutations in the *mitfa* allele (nacre), which were raised on a 14h light/ 10h dark cycle at 28 °C. For optic fiber optpogenetic studies we used *Gal4s:1013t;UAS:ChR2-mCherry;UAS;paGFP* fish and as a control *Gal4s:1013t;UAS:paGFP* fish. 2-Photon optogenetic stimulation of axons was performed in fish of the genotype *Gal4s:1013t;UAS:ChR2-mCherry*. For experiments where we combined optogenetics and whole brain functional recordings we used *elavl3:H2B-GCaMP6s; Gal4s:1013t;UAS:ChR2-mCherry* fish. *Gal4s:1013t;UAS:GCaMP6s* fish were employed to record functional responses to visual stimuli in tectal neurons and their projections. To generate single-cell reconstructions we used fish of the genotype *elavl3:lyn-tagRPF;Gal4s:1013t;BGUG(brn3c:Gal4,UAS:gap43-GFP)*.

METHOD DETAILS

Zebrafish preparation

Zebrafish larvae were embedded in 2% low melting point agarose (Invitrogen), which was removed from the tail and, for some experiments, around the eyes (Figure 1H) to allow behavior tracking. Fish were allowed to recover for several hours (minimum of 3 hours, mainly overnight) before the experiment. For some functional imaging experiments, we anesthetized fish (0.02% tricaine – MS-222, Sigma-Aldrich) and surgically removed one eye (Figure 4) with two sterile 25G needles the day before the embedding to avoid detection of luminance changes via the contralateral eye (Suppl. Figure S6). Before acquiring confocal stacks, fish were anesthetized with 0.02% tricaine.

Single-cell reconstructions and generation of the brain atlas

After a first embedding, larvae were initially screened using a Carl Zeiss LSM-700 confocal microscope for single GFP labeled projection neurons and positive larvae were re-embedded and properly oriented to record a confocal stack (640.17 x 640.17 μm^2 mostly captured at 1024 x 1024

pixels, 1 µm in z, GFP at 488 nm, RFP at 543 nm) of the entire brain (Figure 3). The collected neurons were then traced using the software neuTube (Build1.0z) and confirmed by a second trained tracer. All registrations were performed with the Computational Morphometry toolkit (CMTK - https://www.nitrc.org/projects/cmtk/) using the following code: -awr 01 -T30 -X52 -C8 -G120 -R3 -A'--accuracy 0.8' -W'--accuracy 0.8'. To generate the standard brain (*elavl3:lyn-tagRFP*), we averaged the RFP channel of 30 registered fish brains. All stacks were registered to this standard brain and the warp-and-affine registration was applied to the traced neurons using the reformatx command of the R package nat (Jefferis and Manton, 2014). Custom-written Python code was used to mirror neurons along a manually defined plane along the midline of the fish and to visualize single neurons or the complete atlas (Python Mayavi library). To determine arborization densities of neurons, we calculated Strahler numbers of each neuron and applied a kernel density estimation to all neurite points that were labeled as endpoints of "leaves" (last 10 points within a segment of Strahler number 1 - red points in the axon of Figure 3C) within one projection class.

Single-photon light fiber optogenetic experiments and behavior classification

Optogenetic experiments (Figure 1) were performed as described before (Thiele et al., 2014). Briefly, a 50 µm light fiber (M42L05, Thorlabs) was positioned via a microcontroller (MC1000e, Siskiyou) and connected to a laser beam combiner (Lighthub, Omicron) to either stimulate (473 nm, LuxX 80 mW, Omicron) or photoconvert (405 nm, LuxX 60 mW, Omicron) neurons in the tectum. The protocol consisted of a stimulation phase of three seconds with blue light (473 nm, 30-40 mW/mm^2), while a camera (Pike F032B, Allied Vision Technologies) recorded the induced tail and eye movements for six seconds at 344 fps. For every fish, a minimum of 20 trials were recorded within intervals of 1 minute between stimulations. Afterwards the light source was switched to UV (405 nm) for 5 minutes to photoactivate paGFP in the cells of the stimulated region. It is important to note that the extent of the paGFP label does not match the photostimulated volume due to the different scattering properties of blue (for ChR2) and ultraviolet light (for paGFP) in the tissue (Arrenberg et al., 2009), as well as different activation thresholds of the two types of actuators. After the experiments, confocal stacks were acquired for every fish. To analyze the photoactivated area, the stacks were first registered to one exemplar fish using the *s1013t:Gal4 x UAS:ChR2-mCherry* pattern (CMTK, -awr 0102 -T30 -X52 -C8 -G120 -R3 -A'--accuracy 0.8' -W'--accuracy 0.8' -s), and all registered stacks were then averaged. In a second round, we affine-registered the original stacks to this average brain (CMTK, -ar 0102 -I af -v -T30 -X52 -C8 -G120 -R3 -A'--accuracy 0.8'). Using the aligned paGFP channel, we calculated the

center of mass of the photoactivated paGFP cell bodies (Python scipy.ndimage library), which was normalized along the anterior-posterior axis of the tectum. For the behavioral classification, a custom written tail-tracking algorithm was used to map approximately 30-40 points along the tail. Tail curvature was extracted as the angle between the base and the tip of the tail (Semmelhack et al., 2014). To extract bout features, we calculated the maximum tail angle and the mean bout angle, which was defined as the integral of the first three tail oscillations. A DBSCAN algorithm was used to cluster the first triggered bouts after the stimulation onset using these two parameters (Python scikit-learn library). To extract the eye angles, we calculated the image moments inside a rectangle drawn around each individual eye (OpenCV). This angle was then normalized to the minimum and maximum angle detected throughout all recordings of each individual fish.

Combined optogenetics and calcium imaging

To combine 1-photon optogenetics with 2-photon calcium imaging (Figure 2) (Femtonics 3DRC microscope, Femtonics, Tuzlo, Hungary), we glued a micro prism (90° 0.2 x 0.2 x 0.2 mm, Zünd Precision Optics AG) to a 25 µm light fiber (M67L02, Thorlabs) placed below the objective (20x LUMPLAN Olympus, NA 0.9, WD 2.2 mm). This enabled stimulation (488 nm) of tectal neurons perpendicular to the axis of the optic fiber (compare Murayama et al., 2007). To combine stimulation with blue light and functional recordings, the light was pulsed during the galvo turnaround period between lines of bidirectional scanning (10 µs). During the 90 seconds of functional recordings, the tail was tracked online at approximately 300 fps (MQ003MG-CM, XIMEA GmbH) by finding maximum pixel values of 10 arcs spaced along the tail (Severi et al., 2014). The optogenetic stimulation was turned on manually and off automatically when the tail started to move, via a custom-written Python software. After the experiment, bouts were detected from the tail traces and classified as "during stimulation" (only the first bout) or "spontaneous". To clean the data from outliers, we applied a kernel density estimation (Python scipy.stats library) on a 2D representation of maximum amplitude and mean bout angle of all bouts during the stimulation. All bouts within a density higher than 95% where then assigned as induced bouts. Imaging data were motion-corrected twice using the CaImAn package (Giovannucci et al., 2017; Pnevmatikakis and Giovannucci, 2017), by first correcting each single trial and second all concatenated trials of each plane. To analyze neuronal activity across the brain, we wrote a custom Python script that segments single ROIs via correlations of pixel fluorescent time series with neighboring pixels inspired by Portugues et al., 2014. Briefly, as a first step we calculated for the whole image local correlations of a pixel's time series with its surrounding pixels (correlation

map). This correlation map was used to start a seeding algorithm, beginning at the pixel with the largest correlation value defined as the seeding pixel. The segmentation algorithm correlated the time series of the four neighboring pixels to the seeding pixel and if the correlation value passes a threshold the neighbor pixel was incorporated in the ROI. Iteratively, the ROI grows by correlating new neighboring pixels to the added pixels in the ROI, and the correlation threshold is adaptively increased or decreased until the number of pixels lies in between a lower and upper pre-defined size threshold of a typical cell. If the correlation threshold decreases below a defined value (0.2) the segmentation of this ROI was stopped and all pixels were considered as noise. As soon as one ROI is completed, the segmentation algorithm starts with the next seeding pixel (the next maximum in the correlation map). The time series of each ROI was analyzed using linear regression (from the Python scikit-learn library) and is explained in detail in Suppl. Figure S2.

Two-photon optogenetics

For local stimulation of tectofugal axon populations, we used two-photon laser scanning over a small rectangular ROI (920 nm). The stimulation area (264.13 ± 60.95 µm^2) was manually defined, and different stimulation sites were probed to induce behavior. To this end, the tail was tracked online to evaluate the stimulation efficiency. The protocol consisted of 100 seconds of recording, while every 20 seconds the shutter opened and the target ROI was stimulated for 3 seconds (33.9 ± 2.8 Hz, 35.2 ± 8.3 mW). A minimum of 30 trials of 100 sec were recorded for each fish. After the experiment, we analyzed the behavior as before and grouped the bouts into induced and spontaneous behavior, and an average mean bout angle for the induced behavior was calculated for each fish. The stimulation area was quantified by aligning the ChR2-mCherry expression in the stimulated plane of individual fish via landmark registration (Fiji, align image by line ROI plugin). We then calculated the center of mass of each stimulation ROI and normalized the position to the medial-lateral axis of the lateral iTB.

Functional recordings of responses to visual stimuli

Visual stimuli were projected onto a white diffusive screen using the red channel of a LED projector (LG, Model No. PA72G). Stimuli were generated using PsychoPy2 (http://www.psychopy.org/) and consisted either of a dimming (red to black, 1 sec), brightening (black to red, 1 sec), prey-like (8 deg, 56.3 deg/sec, black on red or red on black) or a black looming stimulus (expanding 30 deg/s). In some experiments, we used solely a prey-like stimulus turning in a circular trajectory (8 deg, radius of circular motion 2 deg, 3 rotations/sec) in three

different positions (-45, 0, 45 deg) of the anterior to posterior visual field. Imaging data were motion-corrected twice using the CaImAn package as described before. Detected calcium responses were analyzed pixel-wise, and regressors were created for each stimulus and the recorded behavior. The regressors were convolved with a GCaMP6s kernel, and linear regression (Python scikit-learn) was used to calculate a score (coefficient * R^2) of all regressors to the functional responses of each pixel. In experiments, using prey-like or looming/dimming stimuli (Figure 4), the maximum coefficient of either looming or dimming and the maximum of the two prey-like stimuli was considered for the score. The scores were then normalized to the overall maximum of the image, and an RGB image was created (Red = looming/dimming, Green = prey-like score – Figure 4, Red = posterior, Green = medial, Blue = anterior position score – Figure 6). For measurements of the topography (Figure 5), we hue-shifted the RGB image (30 deg) for better visualization. To calculate average responses per plane (minimum of 3 trials), we averaged the different trials and weighted every pixel by its R^2.

Registration of projection neurons to calcium imaging data

Average projections of functional imaging planes were registered to a confocal stack of the same fish using a custom Python script. Briefly, the average GCaMP6s projection was scaled and rotated to match the confocal stack and the best corresponding plane of the confocal stack was found using template matching (Python scikit-image library). Next, the average projection was registered to the confocal plane using affine registration provided by SimpleElastix (http://simpleelastix.github.io/). The transformations were then applied to the calculated scores (RGB images) of the functional responses, leading to a confocal stack that carries functional information of the imaged planes. In a second round of registration, the average expression pattern of four *Gal4s1013t* X *UAS:GCaMP6s* fish (already registered to the standard brain) were registered to the confocal stack of the functionally imaged fish using CMTK (-awr 0102 -T30 -X52 -C8 -G120 -R3 -A'--accuracy 0.8' -W'--accuracy 0.8'), and the transformation was applied to all projection neurons. As a result, projection neurons were registered in the same space as the functional data.

QUANTIFICATION AND STATISTICAL ANALYSIS

For statistical tests we used the Python SciPy library. Statistical significance across fish was tested by either two-sided paired t-tests (Figures 1I, 4D, 6D), two-sided one-sample t-test (Figure 2F), Wilcoxon signed-rank test (Figures 1E) or linear regression (Figure 1G, 6F). When data from

multiple fish were compared, we used average values to assure independent measurements. Fish with strong expression were preferentially selected for the experiments. All error bars represent SEM.

DATA AND SOFTWARE AVAILABILITY

All custom software will be made available upon request. The atlas of the 133 tectal projection neurons will be made publically available via a web browser.

Discussion and Outlook

The evolutionary drive of developing such a complex and expensive organ as the brain is its necessity for an animal to interact with the surrounding world. To serve this process, animals employ their nervous system to perceive sensory cues, extract the most important features and react to the environment by the control of behavior. However, many principles regarding how the vast number of individual neurons work together to process information and to create appropriate behavior still need to be solved. During my PhD thesis, we asked several questions to address these principles: How are neuronal circuits wired to extract and send sensory information to downstream premotor regions? How is the location of a stimulus encoded? How do individual neurons contribute to circuit activity within larger ensembles?

As a first step to explore these questions, we sought to improve and develop strategies to investigate neuronal circuits at cellular resolution with the overall goal to link the brain's anatomical and functional wiring with behavior. Two conceptually different strategies can be applied to refine the current experimental approaches. 1) The expression specificity of genetic markers, actuators or sensors can be increased by the use of more specific driver lines or the use of intersectional approaches. 2) The neurons of interest can be more precisely targeted using technological advances such as two-photon optogenetics to modulate individual circuit elements and volumetric calcium imaging to increase the readout of circuit activity. The first two publications addressed the improvement of these strategies and we demonstrated their applications.

Genetic access to specific neuronal subpopulations

In the first publication (Förster et al., 2017b), we aimed to generate gene-specific transgenic lines. Therefore, we used BAC recombineering (Bussmann and Schulte-Merker, 2011; Suster et al., 2011) to insert either Gal4VP16, Gal4VP16-BH or Cre-CH directly downstream of the start codon of the genes of interest. Genomic integration of the BAC constructs is finally mediated by Tol2 recombination. The advantage of linking Gal4 or Cre with the bleeding (BH) or cold heart (CH) cassette, respectively, was to improve the screening process of potential founders and to generally facilitate identification of transgene carriers. These reporters express mCherry (BH) or Cerulean (CH) under control of the cmlc2 promotor, via labelling of heart muscle cells. So far,

most transgenic driver lines have been generated using stochastic insertions of the driver (Gal4/Cre) via enhancer/gene trap screens or by fusing the driver to minimal promotors or enhancers of a specific gene. BAC recombination is superior to these methods, because Gal4 or Cre is inserted at the position of the target gene, which is flanked on the BAC by large regulatory regions between 50 to 300kb both up- and downstream of the gene. In this way, the likelihood to recapitulate the endogenous gene expression is highly increased. Although we did not find any correlation of the BAC size to the probability of successful genomic insertion, using these large BAC plasmids could affect the germline transformation. We could generate 22 stable transgenic lines out of 58 BAC constructs, however, and similar to other BAC studies (Bussmann and Schulte-Merker, 2011) the average founder rate of 6.3% was relatively low. Recently, new methods like CRISPR/Cas9 (Cong et al., 2013; Jinek et al., 2012) have emerged, which allow precise knock-ins for genome editing. While this method opens new doors for the generation of transgenic zebrafish lines (Albadri et al., 2017), one has to consider that through the knock-in of a driver/reporter a potential knock-out of the targeted gene is created and the germline efficiency remains low as well.

The candidate genes for BAC recombineering were primarily chosen to target RGCs, tectal neurons, neurotransmitters and neuropeptides, and mainly evaluated via available RNA *in situ* hybridizations. With my selection of BACs, I aimed to find genetic markers for tectal subpopulations, and more specifically tectal projection neurons. For instance, the genes *pcp4a* (purkinje cell protein 4a) and *rorb* (RAR-related orphan receptor B) have been recently discussed to be markers in the neocortex of either descending projection neurons (*pcp4a*) or target neurons of ascending projections (*rorb*) (Dugas-Ford et al., 2012; Karten, 2013). A role for the same genes has also been proposed in the optic tectum (Karten, 2013), and expression patterns of these genes in output regions of the optic tectum of zebrafish seemed promising (Flores et al., 2007; Mione et al., 2006; Molyneaux et al., 2007).

While we could not generate stable transgenic lines for markers of tectal projection neurons, as for other target genes, new technologies will enable better evaluation of candidate genes and will give insights into the genes regulating circuit formation and function. For instance single-cell RNA sequencing methods, such as Drop-seq (Macosko et al., 2015) or the 10x Genomics system (Zheng et al., 2016) have recently been developed to efficiently barcode thousands of single cells. These methods employ nanoliter droplets to encapsulate individual cells and to sequence the mRNA transcripts in parallel. As a result, thousands of transcription profiles can be clustered to reveal molecular markers of the different cell-types in the population.

Applying this strategy together with CRISPR/Cas9 knock-ins of binary expression systems like Gal4/UAS or Cre/Lox will allow unprecedented precision in the generation of cell-type specific transgenic lines. These specific zebrafish lines can then be employed to dissect circuit functions on the cell-type level and allow functional investigations in head unrestrained preparations. Up to now, most calcium imaging or optogenetic studies in zebrafish are performed in head embedded larvae (Dunn et al., 2016b; Semmelhack et al., 2014; Thiele et al., 2014). However, new microscopes that allow calcium imaging in free-swimming larvae are evolving (Cong et al., 2017; Kim et al., 2017; Symvoulidis et al., 2017) and while these strategies claim near-cellular resolution, a more specific expression of functional indicators (GCaMP or others) might improve the signal especially in periods when the fish is accelerating (Naumann et al., 2010). Furthermore, this approach would allow a combination with optogenetics without targeting the light to single neurons but rather by expressing the ChR2 only in a specific neuronal population (Barker and Baier, 2015).

Dissecting neuronal circuits with light

In the second publication of this thesis (dal Maschio et al., 2017), we sought to combine whole brain imaging with cellular-resolution optogenetic stimulation. This method is especially useful when cell-type specific transgenic lines are not available, a problem most studies have to face. To resolve this issue, several strategies to combine cellular resolution optogenetics and calcium imaging have emerged in the recent years (Chen et al., 2018; Packer et al., 2015; Yang et al., 2018). This combination offers the ability to dissect neuronal circuits, by reading and writing neuronal activity (Yang and Yuste, 2018).

We designed a two-photon holography approach to stimulate individual cells expressing ChR2 and simultaneously recorded the activity of hundreds of GCaMP6s expressing neurons and the induced behavior. While the principal concept of two-photon holography using a spatial light modulator (SLM) has been described in details before (Dal Maschio, 2014; Dal Maschio et al., 2010, 2012; Vaziri and Emiliani, 2012), we demonstrated in this study an optimized approach by combining 3D optogenetics with volumetric calcium imaging. Using dimensionality reduction and linear regression models, we could dissect the role of individual neurons within the nMLF for a specific behavioral outcome, the steering of the tail (Thiele et al., 2014), while reconstructing the activity patterns across the brain that are supporting such behavior outcome. Knowledge about

the behavioral contribution or functional properties of a single neuron within a larger ensemble can be only partially satisfying, if no information about the cells identity is available. Therefore, we developed a strategy to anatomically visualize the photostimulated cells and/or functionally connected neurons, by restricting the expression of GCaMP to the nucleus of the cell (nls-GCaMP6s) and co-expressing paGFP. This allowed us to photoactivate paGFP in the cells of interest at the end of an experiment, to reconstruct their morphology and to register and compare stimulated cells between different fish.
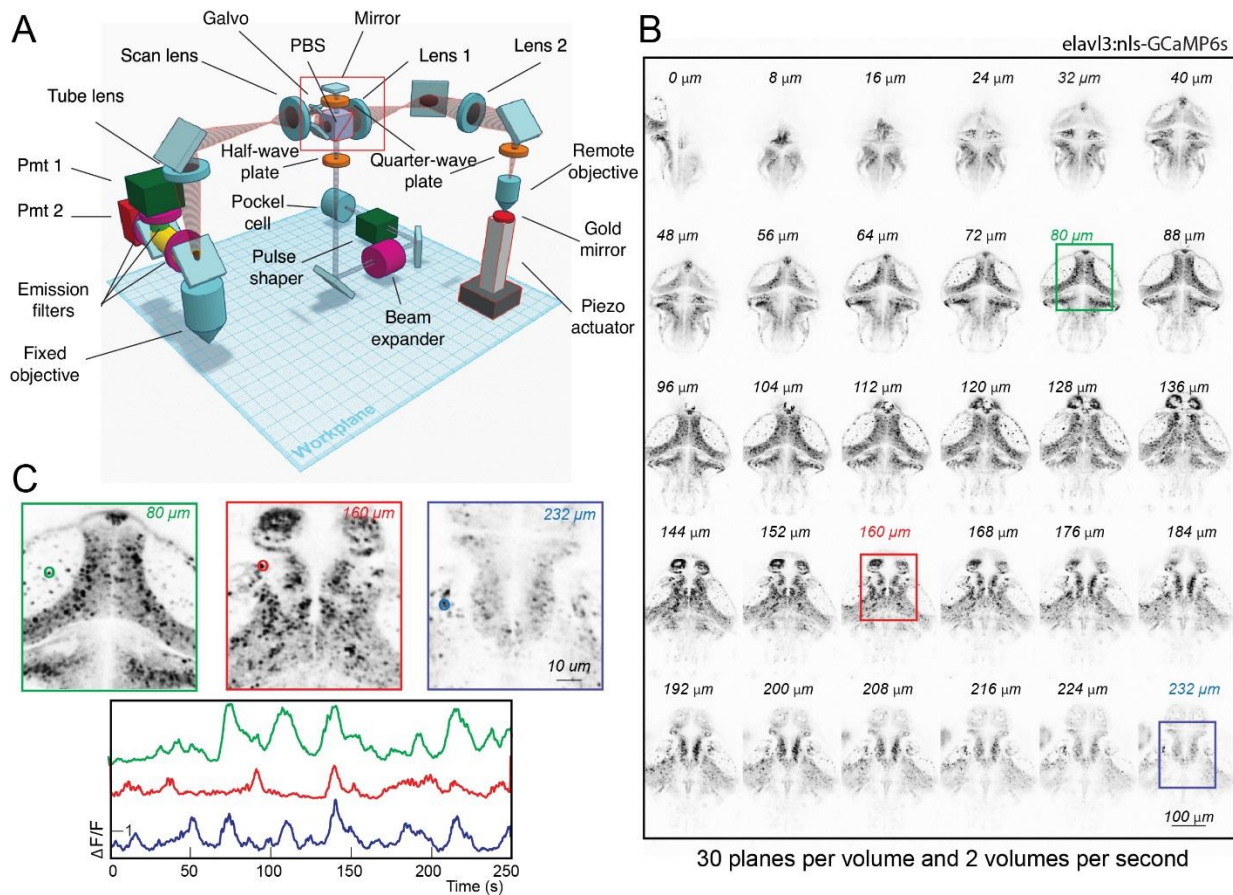
Figure 8: Two-photon volumetric line scan imaging. (**A**) Optical design of the microscope. A conventional two-photon microscope was upgraded with a second arm for volumetric imaging. Therefore, the beam passes through a half-wave plate and a PBS directs the light towards the remote objective. The light gets reflected at the moveable mirror and passes on its way twice through a quarter-wave plate to allow the light to pass straight through the PBS towards the imaging objective. (**B**) Average projection of 30 volumetrically (2 volumes/second) imaged planes in pan-neuronal expressing GCaMP6s fish. (**C**) Magnification of three imaged planes, demonstrating the cellular-resolution and functional traces of individual cells.

To gain access to multiple planes for calcium imaging, we employed an electrically tunable lens (ETL) to remotely focus the imaging beam (Grewe et al., 2011). However, with the used configuration, the time needed to refocus a plane in a distance of 75 μm is at 6 ms rather long and we could only achieve a z-travel range of 75 to 125 μm using a 20x or 16x objective, respectively. Other methods of shifting the focus of the excitation light (Ji et al., 2016) have been demonstrated to be either faster or to cover a larger traveling range (Botcherby et al., 2012; Yang et al., 2016). These methods employ either a SLM to quickly change the wavefront of the imaging beam (Dal Maschio et al., 2011, 2012) or a second objective that focuses on a moveable mirror (Figure 8), whereby the axial movements of the mirror change the focus of the imaging objective (Botcherby et al., 2012; Rupprecht et al., 2016). During my PhD project I have built such a system, by coupling a second objective (remote objective) to mirror, which can be moved through a piezo (Figure 8 A). This allowed us to record volumes greater than 200 μm spanning 30 planes at a rate of 2 volumes per second at cellular resolution (Figure 8 B, C).

As we have demonstrated, CGH allows precise targeting of individual neurons with light in a 3D volume. Similar to Hernandez et al., 2016, we employed an multiplane Gerchberg-Saxton (GS) algorithm (Gerchberg and Saxton, 1972), which was improved by an adaptive reweighting of the ROIs across z-positions, to achieve uniform intensity distributions within the different stimulation patterns and to minimize spherical aberrations. A further improvement of the 3D-CGH resolution could be achieved by temporal focusing (TF) to minimize the z-extension of the photostimulation patterns. TF can be realized by inserting a reflective grating after the SLM to compress the light pulse and to temporally disperse out of focus light. This reduces the out of plane two-photon efficiency and sharpens the axial resolution at the imaging plane (Dal Maschio et al., 2012; Oron et al., 2012; Papagiakoumou et al., 2013). However, because TF works on 2D patterns, in general a second SLM after the grating has to be employed to shift the temporal focused pattern in 3D (Hernandez et al., 2016; Ronzitti et al., 2017; Yang and Yuste, 2018).

Another strategy to improve the resolution of optogenetic approaches is to reduce the non-specific activation of surrounding cells. Recently, soma-targeted opsins have been engineered by fusing opsins either to a Kv2.1-motif (potassium channel, Wu et al., 2013), such as ChR2-Kv2.1 (Baker et al., 2016; Forli et al., 2018), ST-ChroME (Mardinly et al., 2018) and GtACRs (inhibition, Govorunova et al., 2015; Mahn et al., 2017) or KA2, a kainate receptor subunit, such as soCoChR (Shemesh et al., 2017). Although the restriction of the opsin to the soma is leaky and needs to be further improved, these approaches are promising as they effectively reduce activation of neighboring cells.

Functional anatomy of a visuomotor transformation

The main project during my PhD was to functionally and anatomically dissect visuomotor circuits in the tectum of zebrafish larvae. More specifically, I wanted to characterize how the tectum processes visual features such as the position and the valence of a stimulus to convert this visual map representation into a motor map of behavioral outcomes. To investigate this question, we have chosen a parallel approach of functional manipulations, recordings and anatomical quantifications.

First, using light-fiber optogenetics, we aimed to characterize tectum-induced motor outcomes. Optogenetic stimulation was sufficient to drive approach and escape behavior and we found that behavior directionality directly depends on the stimulation site within the tectum and is influenced by the animals viewing direction. This space code of swimming direction is determined by the position of focal activity along the anterior-posterior axis of the tectum as described in other models (Freedman et al., 1996; Herrero et al., 1998a; du Lac and Knudsen, 1990). Having established a method to trigger behavior, we wanted to gather information about the downstream premotor neurons involved in the initiation of this behavior. Therefore, we combined optogenetics with calcium imaging. Two-photon holography was not suitable to address this problem, because genetic markers of output neurons in the tectum were not available and thus larger ensembles of cells needed to be stimulated. However, CGH would require high laser power to simultaneously stimulate larger groups of neurons (two-photon efficiency is proportional to the square of the peak power), which increases tissue heating and cell damage (Ronzitti et al., 2017; Yang and Yuste, 2018). To resolve this issue and to enable perpendicular one-photon optogenetics of tectal neurons with functional recordings we glued a micro prism (edge length 200 µm) to an optic fiber (Murayama et al., 2007). Correlating calcium responses throughout the brain to repeated stimulation trails of tectal neurons and the behavior, we could show that a small subset of neurons in the contralateral caudal hindbrain was specifically active during the induced behavior. V2a neurons reside in this area of the caudal hindbrain and have been shown to be sufficient to drive swims in zebrafish (Kimura et al., 2013). However, how tectal projection neurons are wired to target these premotor areas is mostly unknown.

Therefore, and in parallel, we started to investigate the anatomical output pathways of the tectum. Using a single-cell labeling strategy (BGUG), we reconstructed 133 tectal projection neurons and annotated them according to their intra- and extratectal stratifications. Hierarchical clustering

revealed 8 main classes of projection neurons, targeting pretectal or thalamic areas, the contralateral tectum, the nucleus isthmi and the hindbrain via crossed (cTB) and uncrossed (iTB) projections through the tectobulbar tract.
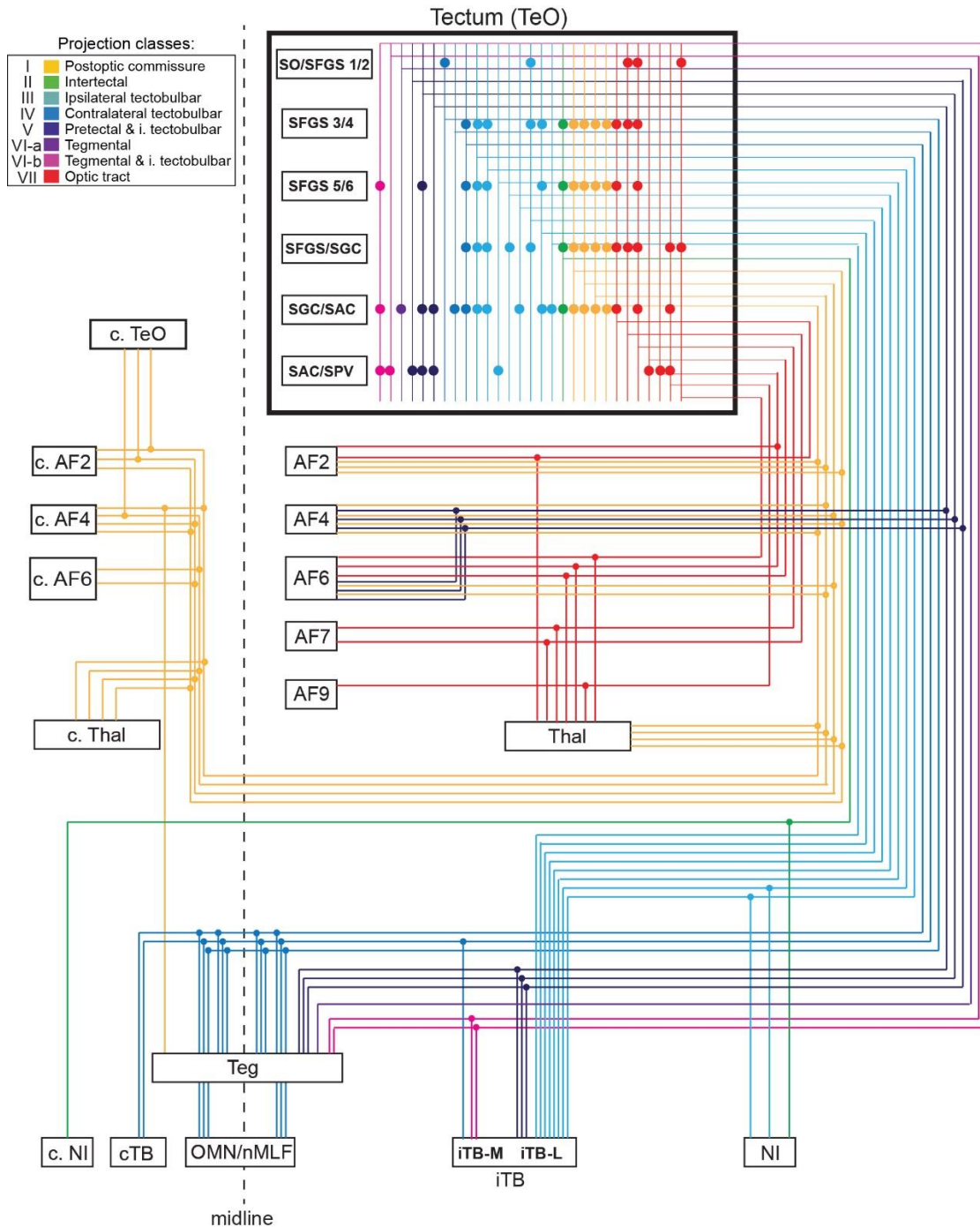

Figure 9: Wiring diagram of tectal projection neurons. Projection trajectories with in- and output relationships of the 29 subclasses described by the collection of 133 reconstructed neurons. The pathways are colored according to the main projection classes.

These pathways closely resemble the described tectofugal projections of goldfish (Ebbesson and Vanegas, 1976; Meek, 1983) and seem to be even conserved in mammals (Huerta and Harting, 1984b). Importantly, we registered the traced neurons into one reference brain, which allowed us to generate an atlas of tectal projection neurons with unprecedented resolution (Figure 9). This anatomical database together with the optogenetic observations inspired and enabled us to ask more specific questions about the functional roles of the different cell-types.

What pathways encode the valence of a novel object and contribute to the decision of whether to approach it or to escape from it? How is the visual location of this object relayed to the hindbrain circuits? What is the difference between the known retinotopic representation of stimulus location and the space code of the tectal motor map steering the behavior? To address these questions, we designed different sets of visual stimuli, consisting of small prey-like dots, looming and luminance changes. Imaging in the tectobulbar tract revealed that the medial iTB (iTB-M) is most sensitive to looming/dimming, whereas the lateral iTB (iTB-L) being most sensitive to prey-like objects. Registration of the anatomical dataset to the imaging space revealed distinct neuronal cell-classes explaining this functional observation. Class VI-b neurons closely resembled the iTB-M, whereas class III and V neurons overlapped with the iTB-L. Moreover, we found that tectofugal axons running through the iTB-L (class III neurons) are retinotopically ordered within their fiber bundle. This arrangement conveys the space code of target position to the hindbrain circuits that control the required movements, which we prove by two-photon activation of axon subpopulations. A summary of our findings is presented in Figure 10 A.

The optic tectum and the superior colliculus have been intensely studied over the last decades. Starting with studies about eye and head movements, a more complete picture about this structure has been established and the tectum/SC is now a well-established center for controlling attention and behavioral decisions (Basso and May, 2017). Several interpretations of the functional role of the tectum have been proposed, including the 'the goal location hypothesis' formulated by Hafed and Krauzlis, 2008. They proposed the SC/tectum to be placed at an intermediate level of pure sensory representation or motor control. The tectum rather represents a map of behaviorally relevant goal locations, whereby focal activity defines the locus of visuospatial attention (Lai et al., 2011) and the target of upcoming movements. Our findings support this interpretation, as we could show that the projection neurons of the iTB-L not only encode the location of an attractive visual stimulus but also control the corresponding movements to reach this goal. Most importantly, we found a sophisticated biological principle of how this two-sided functionality can be implemented: a topographic tectal projection that sends potential goal

locations towards the reticular formation, which in turn generates the graded motor outcomes (Figure 10 A – right panel).
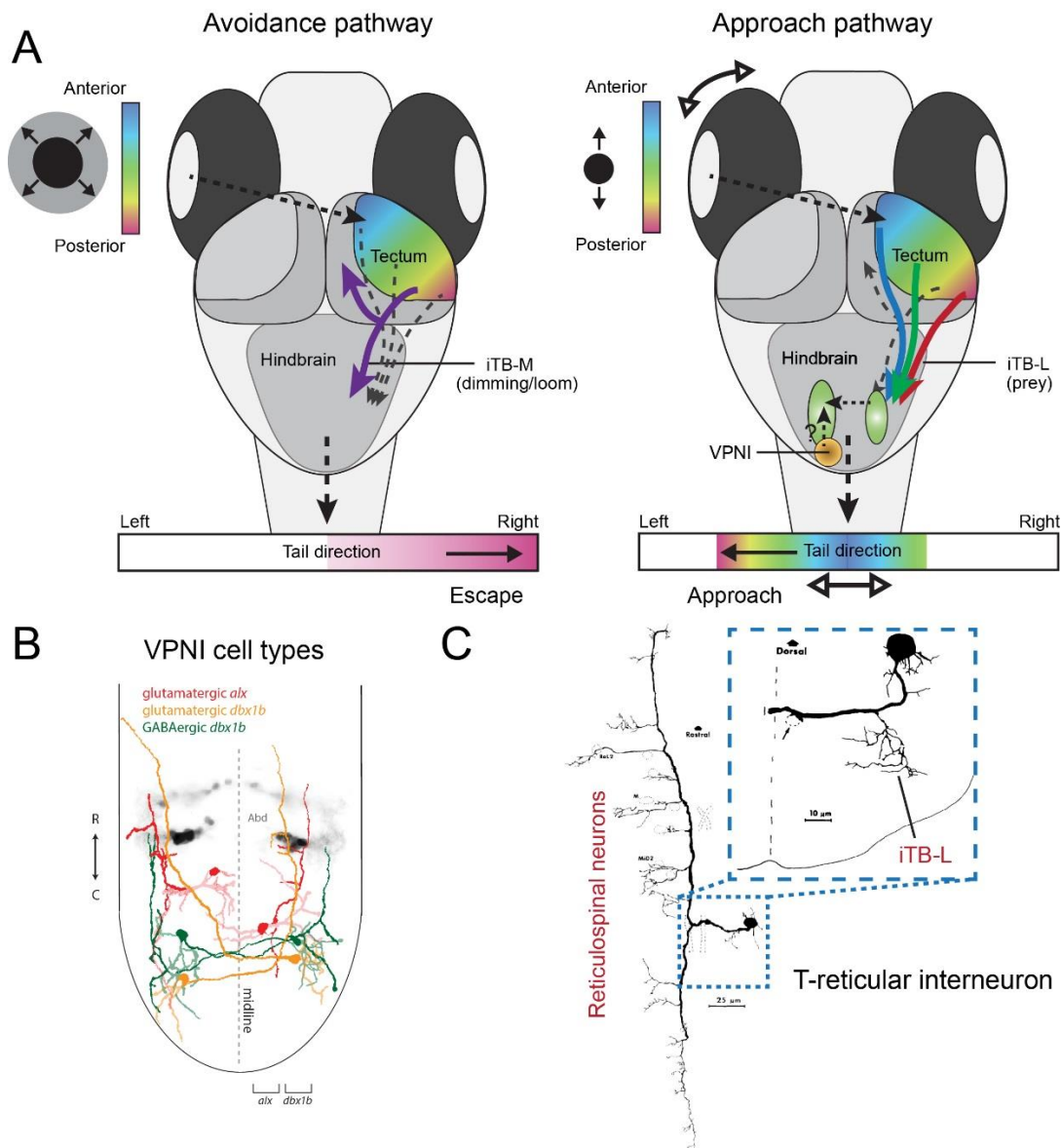
Figure 10: Proposed circuit models and candidate premotor target neurons. (**A**) Summary of the findings proposed in the main study of my PhD project (Helmbrecht et al.). (**B**) Identified VPNI neurons in the caudal hindbrain of zebrafish larvae. V2a neurons are referenced here as glutamatergic *alx* neurons (figure adapted from Lee et al., 2015). (**C**) Reconstructed T-reticular interneurons, labeled by HRP application near the soma in 5 d.p.f. larvae (figure adapted from Kimmel et al., 1985).

However, our findings also raise many new questions that remain to be resolved: What is the role of the class IV neurons, which cross the midline and run along the contralateral tectobulbar tract? Are they required for prey-capture (Dean et al., 1986)? How and where are signals of turning

direction integrated with the position of the eyes? What are the target neurons of looming/dimming encoding class VI-b neurons in the iTB-M? How is the space code of goal locations in the iTB-L translated at the level of the reticular formation to steer the tail movements? Where and how does the activity cross the midline? To address these questions, the set of tools we developed during my PhD may prove particularly useful. By combining volumetric calcium imaging of premotor hindbrain areas with two-photon holographic excitation of individual fiber segments within the iTB-L, we might gain deeper insights about the relationship of topographically organized iTB-L axons and the targeted populations of hindbrain neurons. Is there a hindbrain motor map? If so, how is it organized? In addition, targeted photoactivation and reconstruction of functionally responsive ipsilateral hindbrain neurons might reveal the neuronal population that conveys information to the contralateral hemisphere. Will we label the proposed V2a positive velocity to positon neural integrator neurons (VPNI, Lee et al., 2015) or T-reticular interneurons (Kimmel et al., 1985; Koyama et al., 2011) (Figure 10 B and C)?

The work described so far on visuomotor transformations mainly focused on tectal output neurons. However, the majority of tectal neurons are interneurons and their role in information processing remains largely unknown. To investigate the inner-tectal circuitry, we started to use the genetic tool 'FuGIMA' (Function-guided inducible morphological analysis, UAS-Janus:nlsGCamP6f,paGFP, Kramer et al. - in preparation, Förster et al. - in preparation). Using sparse expression of FuGIMA, functional responses can be recorded using nuclear localized GCaMP6s (nls-GCaMP6s) and co-expressed paGFP can be photoactivated to reconstruct the neuronal morphology. We expressed FuGIMA in tectal neurons and recorded neuronal responses to a variety of stimuli, including: looming, darkening, brightening and prey-like stimuli. Hierarchical clustering of functional scores to each of the stimuli revealed a minimum of 16 distinct response types and we found that neurons responding selectively to either prey-like or looming stimuli are mainly mutually exclusive (Figure 11 A). Anatomical reconstruction and registration of 68 functionally characterized cells revealed that prey-selective neurons arborize significantly more in the intermediate superficial layers of the tectum (SFGS 1-4) compared to looming-selective neurons, which arborize significantly more in deeper layers (SGC, SAC) (Figure 11 B). This finding is consistent with the information flow from RGCs (Semmelhack et al., 2014; Temizer et al., 2015), where we could find similar response profiles for the prey-like and looming stimuli. In addition, we reconstructed more than 250 interneurons labeled using the BGUG approach. Comparing the morphology of functionally characterized neurons with the entire catalogue of tectal neurons will help to categorize the functional structure of tectal microcircuits and will allow constructing sophisticated models of tectal information processing (Figure 11 C).
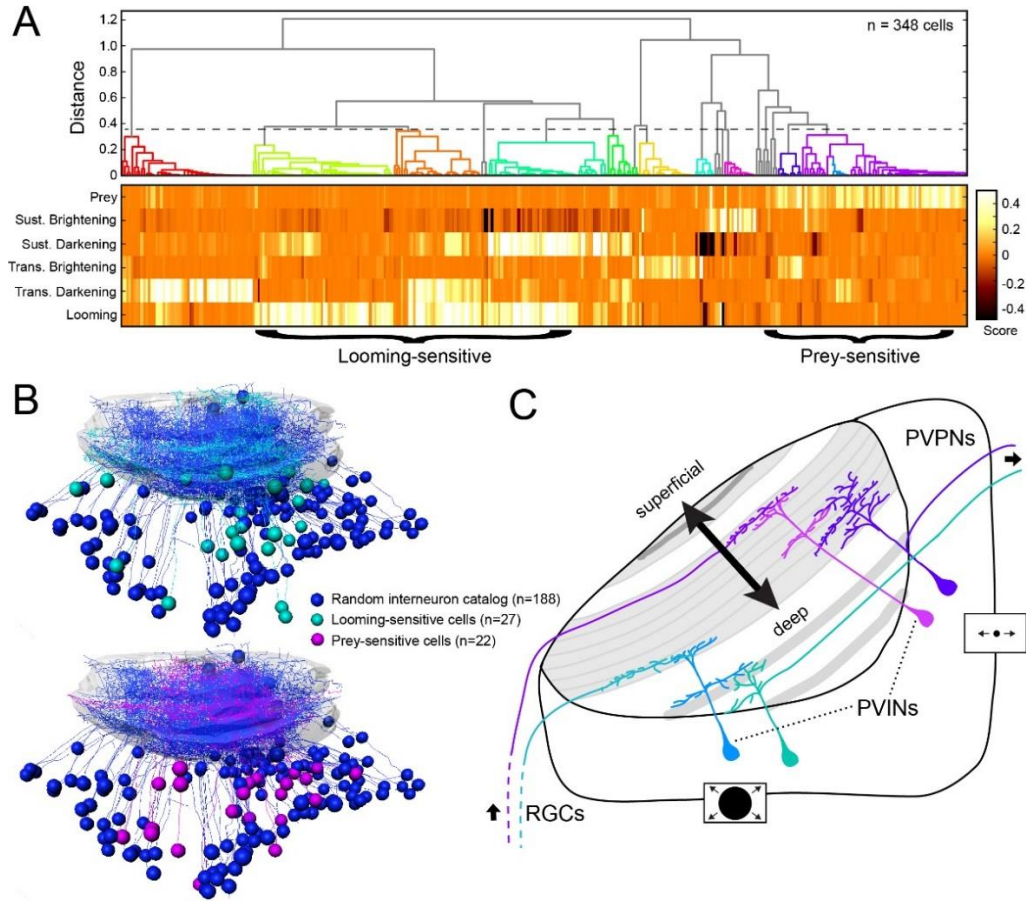
Figure 11: Tectal microcircuits. (**A**) Hierarchical clustering of functional response types of 348 functionally recorded tectal neurons. (**B**) Distribution and arborization of prey- (magenta) and looming-sensitive (cyan) neurons. The collection of stochastically labeled interneurons is marked in blue. (**C**) Model of information processing in tectal microcircuits. Förster et al., in preparation.

The tools to study neuronal circuits are becoming more refined every day and the generation of more specific genetic lines, like those available in Drosophila, will help to dissect neuronal networks with increased precision. EM reconstructions have been initiated to evaluate the complete connectome of larval zebrafish (Hildebrand et al., 2017) at a resolution down to single synapses (Svara et al., in preparation). With the growing community of neuroscientists working with the zebrafish model, we will soon be able to dissect the pathways underlying visuomotor transformations with unprecedented resolution in this scientifically attractive and accessible vertebrate brain.

154

References

Ahrens, M.B., Li, J.M., Orger, M.B., Robson, D.N., Schier, A.F., Engert, F., and Portugues, R. (2012). Brain-wide neuronal dynamics during motor adaptation in zebrafish. Nature *485*, 471–477.

Akerboom, J., Chen, T.-W., Wardill, T.J., Tian, L., Marvin, J.S., Mutlu, S., Calderón, N.C., Esposti, F., Borghuis, B.G., Sun, X.R., et al. (2012). Optimization of a GCaMP calcium indicator for neural activity imaging. J. Neurosci. *32*, 13819–13840.

Albadri, S., Del Bene, F., and Revenu, C. (2017). Genome editing using CRISPR/Cas9-based knock-in approaches in zebrafish. Methods *121–122*, 77–85.

Ando, R., Hama, H., Yamamoto-Hino, M., Mizuno, H., and Miyawaki, A. (2002). An optical marker based on the UV-induced green-to-red photoconversion of a fluorescent protein. Proc. Natl. Acad. Sci. *99*, 12651–12656.

Arrenberg, A.B. (2016). Fiber Optic-Based Photostimulation of Larval Zebrafish. In Kawakami K., Patton E., Orger M. (Eds) Zebrafish. Methods in Molecular Biology, Vol 1451. Humana Press, New York, NY, pp. 343–354.

Arrenberg, A.B., Del Bene, F., and Baier, H. (2009). Optical control of zebrafish behavior with halorhodopsin. Proc. Natl. Acad. Sci. U. S. A. *106*, 17968–17973.

Asakawa, K., and Kawakami, K. (2009). The Tol2-mediated Gal4-UAS method for gene and enhancer trapping in zebrafish. Methods *49*, 275–281.

Avants, B.B., Tustison, N.J., Song, G., Cook, P.A., Klein, A., and Gee, J.C. (2011). A reproducible evaluation of ANTs similarity metric performance in brain image registration. Neuroimage *54*, 2033–2044.

Baier, H. (2013). Synaptic Laminae in the Visual System: Molecular Mechanisms Forming Layers of Perception. Annu. Rev. Cell Dev. Biol. *29*, 385–416.

Baier, H., and Scott, E.K. (2009). Genetic and optical targeting of neural circuits and behavior--zebrafish in the spotlight. Curr. Opin. Neurobiol. *19*, 553–560.

Baker, C.A., Elyada, Y.M., Parra, A., and Bolton, M.M.L. (2016). Cellular resolution circuit mapping with temporal-focused excitation of soma-targeted channelrhodopsin. Elife *5*, 1–15.

Barker, A.J., and Baier, H. (2015). Sensorimotor decision making in the Zebrafish tectum. Curr. Biol. *25*, 2804–2814.

Barker, A.J., Helmbrecht, T.O., Grob, A.A., and Baier, H. (2017). Detection of whole-field luminance changes by superficial interneurons in the zebrafish tectum. BioRxiv.

Basso, M.A., and May, P.J. (2017). Circuits for Action and Cognition: A View from the Superior Colliculus. Annu. Rev. Vis. Sci. *3*, annurev-vision-102016-061234.

Del Bene, F., Wyart, C., Robles, E., Tran, A., Looger, L., Scott, E.K., Isacoff, E.Y., and Baier, H. (2010). Filtering of Visual Information in the Tectum by an Identified Neural Circuit. Science (80-.). *330*, 669–673.

Bergeron, A., Matsuo, S., and Guitton, D. (2003). Superior colliculus encodes distance to target,

not saccade amplitude, in multi-step gaze shifts. Nat. Neurosci. *6*, 404–413.

Bianco, I.H., Kampff, A.R., and Engert, F. (2011). Prey capture behavior evoked by simple visual stimuli in larval zebrafish. Front. Syst. Neurosci. *5*, 101.

Botcherby, E.J., Smith, C.W., Kohl, M.M., Débarre, D., Booth, M.J., Juškaitis, R., Paulsen, O., and Wilson, T. (2012). Aberration-free three-dimensional multiphoton imaging of neuronal activity at kHz rates. Proc. Natl. Acad. Sci. U. S. A. *109*, 2919–2924.

Burrill, J.D., and Easter, S.S. (1994). Development of the retinofugal projections in the embryonic and larval zebrafish (Brachydanio rerio). J. Comp. Neurol. *346*, 583–600.

Bussmann, J., and Schulte-Merker, S. (2011). Rapid BAC selection for tol2-mediated transgenesis in zebrafish. Development *138*, 4327–4332.

Chen, I.-W., Ronzitti, E., Lee, B.R., Daigle, T.L., Zeng, H., Papagiakoumou, E., and Emiliani, V. (2018). Parallel holographic illumination enables sub-millisecond two-photon optogenetic activation in mouse visual cortex in vivo. bioRxiv 250795.

Chen, T.W., Wardill, T.J., Sun, Y., Pulver, S.R., Renninger, S.L., Baohan, A., Schreiter, E.R., Kerr, R.A., Orger, M.B., Jayaraman, V., et al. (2013). Ultrasensitive fluorescent proteins for imaging neuronal activity. Nature *499*, 295–300.

Cong, L., Ran, F.A., Cox, D., Lin, S., Barretto, R., Habib, N., Hsu, P.D., Wu, X., Jiang, W., Marraffini, L.A., et al. (2013). Multiplex Genome Engineering Using CRISPR/Cas Systems. Science (80-.). *339*, 819–823.

Cong, L., Wang, Z., Chai, Y., Hang, W., Shang, C., Yang, W., Bai, L., Du, J., Wang, K., and Wen, Q. (2017). Rapid whole brain imaging of neural activity in freely behaving larval zebrafish (Danio rerio). Elife *6*, 1–20.

Costa, M., Manton, J.D., Ostrovsky, A.D., Prohaska, S., Jefferis, G.S.X.E., Costa, M., Manton, J.D., Ostrovsky, A.D., Prohaska, S., and Jefferis, G.S.X.E. (2016). NBLAST: Rapid, Sensitive Comparison of Neuronal Structure and Construction of Neuron Family Databases. Neuron *91*, 293–311.

Dal Maschio, M. (2014). Novel Approaches for Single Molecule Activation and Detection. 7–27.

Dal Maschio, M., Difato, F., Beltramo, R., Blau, A., Benfenati, F., and Fellin, T. (2010). Simultaneous two-photon imaging and photo-stimulation with structured light illumination. Opt. Express *18*, 18720.

Dal Maschio, M., De Stasi, A.M., Benfenati, F., and Fellin, T. (2011). Three-dimensional *in vivo* scanning microscopy with inertia-free focus control. Opt. Lett. *36*, 3503–3505.

Dal Maschio, M., Difato, F., Beltramo, R., De Stasi, A.M., Blau, A., and Fellin, T. (2012). Optical Investigation of Brain Networks Using Structured Illumination (Elsevier Inc.).

dal Maschio, M., Donovan, J.C., Helmbrecht, T.O., and Baier, H. (2017). Linking Neurons to Network Function and Behavior by Two-Photon Holographic Optogenetics and Volumetric Imaging. Neuron *94*, 774–789.e5.

Dean, P., Redgrave, P., and Sahibzada, N. (1986). Head and body movements produced by electrical stimulation of SC in rats_effects of interruption of crossed tectoreticulospinal parhway.pdf. *19*, 367–380.

Dean, P., Redgrave, P., and Westby, G.W.M. (1989). Event or emergency? Two response

systems in the mammalian superior colliculus. Trends Neurosci. *12*, 137–147.

Denk, W., Stricker, J., and Webb, W.W. (1990). Two-Photon Laser Scanning Fluorescence Microscopy. Science (80-.). *248*, 73–76.

DeSouza, J.F.X., Keith, G.P., Yan, X., Blohm, G., Wang, H., and Crawford, J.D. (2011). Intrinsic Reference Frames of Superior Colliculus Visuomotor Receptive Fields during Head-Unrestrained Gaze Shifts. J. Neurosci. *31*, 18313–18326.

Dugas-Ford, J., Rowell, J.J., and Ragsdale, C.W. (2012). Cell-type homologies and the origins of the neocortex. Proc. Natl. Acad. Sci. U. S. A. *109*, 16974–16979.

Dunn, T.W., Gebhardt, C., Naumann, E.A., Riegler, C., Ahrens, M.B., Engert, F., and Del Bene, F. (2016a). Neural Circuits Underlying Visually Evoked Escapes in Larval Zebrafish. Neuron 1–16.

Dunn, T.W., Mu, Y., Narayan, S., Randlett, O., Naumann, E.A., Yang, C.T., Schier, A.F., Freeman, J., Engert, F., and Ahrens, M.B. (2016b). Brain-wide mapping of neural activity controlling zebrafish exploratory locomotion. Elife *5*, 1–29.

Ebbesson, S.O., and Vanegas, H. (1976). Projections of the optic tectum in two teleost species. J. Comp. Neurol. *165*, 161–180.

Ellard, C.G., and Goodale, M.A. (1988). A functional analysis of the collicular output pathways: a dissociation of deficits following lesions of the dorsal tegmental decussation and the ipsilateral collicular efferent bundle in the Mongolian gerbil. Exp. Brain Res. *71*, 307–319.

Emiliani, V., Cohen, A.E., Deisseroth, K., and Hausser, M. (2015). All-Optical Interrogation of Neural Circuits. J. Neurosci. *35*, 13917–13926.

Ewert, J.-P. (1970). Neural Mechanisms of Prey-catching and Avoidance Behavior in the Toad *(Bufo bufo* L.). Brain. Behav. Evol. *3*, 36–56.

Felsen, G., and Mainen, Z.F. (2012). Midbrain contributions to sensorimotor decision making. J. Neurophysiol. *108*, 135–147.

Flores, M.V., Hall, C., Jury, A., Crosier, K., and Crosier, P. (2007). The zebrafish retinoid-related orphan receptor (ror) gene family. Gene Expr. Patterns *7*, 535–543.

Forli, A., Vecchia, D., Binini, N., Succol, F., Bovetti, S., Moretti, C., Nespoli, F., Mahn, M., Baker, C.A., Bolton, M.M., et al. (2018). Two-Photon Bidirectional Control and Imaging of Neuronal Excitability with High Spatial Resolution In Vivo. Cell Rep. *22*, 2809–2817.

Förster, D., Dal Maschio, M., Laurell, E., and Baier, H. (2017a). An optogenetic toolbox for unbiased discovery of functionally connected cells in neural circuits. Nat. Commun. *8*.

Förster, D., Arnold-Ammer, I., Laurell, E., Barker, A.J., Fernandes, A.M., Finger-Baier, K., Filosa, A., Helmbrecht, T.O., Kölsch, Y., Kühn, E., et al. (2017b). Genetic targeting and anatomical registration of neuronal populations in the zebrafish brain with a new set of BAC transgenic tools. Sci. Rep. *7*, 1–11.

Freedman, E.G., Stanford, T.R., and Sparks, D.L. (1996). Combined eye-head gaze shifts produced by electrical stimulation of the superior colliculus in rhesus monkeys. J. Neurophysiol. *76*, 927–952.

Gahtan, E., Tanger, P., and Baier, H. (2005). Visual Prey Capture in Larval Zebrafish Is Controlled by Identified Reticulospinal Neurons Downstream of the Tectum. J. Neurosci. *25*,

9294–9303.

Gerchberg, R.W., and Saxton, W.O. (1972). A Practical Algorithm for the Determination of Phase from Image and Diffraction Plane Pictures. Optik (Stuttg). *35*, 237–246.

Govorunova, E.G., Sineshchekov, O.A., Janz, R., Liu, X., and Spudich, J.L. (2015). Natural light-gated anion channels: A family of microbial rhodopsins for advanced optogenetics. Science (80-.). *349*, 647–650.

Grewe, B.F., Voigt, F.F., van 't Hoff, M., and Helmchen, F. (2011). Fast two-layer two-photon imaging of neuronal cell populations using an electrically tunable lens. Biomed. Opt. Express *2*, 2035–2046.

Gurskaya, N.G., Verkhusha, V. V, Shcheglov, A.S., Staroverov, D.B., Chepurnykh, T. V, Fradkov, A.F., Lukyanov, S., and Lukyanov, K. a (2006). Engineering of a monomeric green-to-red photoactivatable fluorescent protein induced by blue light. Nat. Biotechnol. *24*, 461–465.

Hafed, Z.M., and Krauzlis, R.J. (2008). Goal Representations Dominate Superior Colliculus Activity during Extrafoveal Tracking. J. Neurosci. *28*, 9426–9439.

Hellmann, B., Güntürkün, O., and Manns, M. (2004). Tectal mosaic: organization of the descending tectal projections in comparison to the ascending tectofugal pathway in the pigeon. J. Comp. Neurol. *472*, 395–410.

Hernandez, O., Papagiakoumou, E., Tanese, D., Fidelin, K., Wyart, C., and Emiliani, V. (2016). Three-dimensional spatiotemporal focusing of holographic patterns. Nat. Commun. *7*, 1–10.

Herrero, L., Rodríguez, F., Salas, C., and Torres, B. (1998a). Tail and eye movements evoked by electrical microstimulation of the optic tectum in goldfish. Exp. Brain Res. *120*, 291–305.

Herrero, L., Corvisier, J., Hardy, O., and Torres, B. (1998b). Influence of the tectal zone on the distribution of synaptic boutons in the brainstem of goldfish. J. Comp. Neurol. *401*, 411–428.

Hildebrand, D.G.C., Cicconet, M., Torres, R.M., Choi, W., Quan, T.M., Moon, J., Wetzel, A.W., Scott Champion, A., Graham, B.J., Randlett, O., et al. (2017). Whole-brain serial-section electron microscopy in larval zebrafish. Nature *545*, 345–349.

Huerta, M.F., and Harting, J.K. (1984a). Connectional Organization of the superior colliculus.

Huerta, M.F., and Harting, J.K. (1984b). Connectional Organization of the superior colliculus.

Ingle, D.J. (1983). Brain Mechanisms of visual localization by frogs and toads. Adv. Vertebr. Neuroethol. 177–226.

Jefferis, G.S.X.E., Potter, C.J., Chan, A.M., Marin, E.C., Rohlfing, T., Maurer, C.R., and Luo, L. (2007). Comprehensive Maps of Drosophila Higher Olfactory Centers: Spatially Segregated Fruit and Pheromone Representation. Cell *128*, 1187–1203.

Ji, N., Freeman, J., and Smith, S.L. (2016). Technologies for imaging neural activity in large volumes. *19*.

Jinek, M., Chylinski, K., Fonfara, I., Hauer, M., Doudna, J.A., and Charpentier, E. (2012). A Programmable Dual-RNA–Guided DNA Endonuclease in Adaptive Bacterial Immunity. Science (80-.). *337*, 816–822.

Kardamakis, A.A., Saitoh, K., and Grillner, S. (2015). Tectal microcircuit generating visual selection commands on gaze-controlling neurons.

Karlstrom, R.O., Trowe, T., Klostermann, S., Baier, H., Brand, M., Crawford, a D., Grunewald, B., Haffter, P., Hoffmann, H., Meyer, S.U., et al. (1996). Zebrafish mutations affecting retinotectal axon pathfinding. Development *123*, 427–438.

Karten, H.J. (2013). Neocortical evolution: neuronal circuits arise independently of lamination. Curr. Biol. *23*, R12-5.

Kawashima, T., Zwart, M.F., Yang, C.-T., Mensh, B.D., and Ahrens, M.B. (2016). The Serotonergic System Tracks the Outcomes of Actions to Mediate Short-Term Motor Learning. Cell 1–14.

Kim, D.H., Kim, J., Marques, J.C., Grama, A., Hildebrand, D.G.C., Gu, W., Li, J.M., and Robson, D.N. (2017). Pan-neuronal calcium imaging with cellular resolution in freely swimming zebrafish. Nat. Methods *14*, 1107–1114.

Kimmel, C.B., Metcalfe, W.K., and Schabtach, E. (1985). T reticular interneurons: A class of serially repeating cells in the zebrafish hindbrain. J. Comp. Neurol. *233*, 365–376.

Kimura, Y., Satou, C., Fujioka, S., Shoji, W., Umeda, K., Ishizuka, T., Yawo, H., and Higashijima, S. (2013). Hindbrain V2a neurons in the excitation of spinal locomotor circuits during zebrafish swimming. Curr. Biol. *23*, 843–849.

Kinoshita, M., Ito, E., Urano, A., Ito, H., and Yamamoto, N. (2006). Periventricular efferent neurons in the optic tectum of rainbow trout. J. Comp. Neurol. *499*, 546–564.

Klein, S., Staring, M., Murphy, K., Viergever, M.A., and Pluim, J.P.W. (2010). Elastix: A toolbox for intensity-based medical image registration. IEEE Trans. Med. Imaging *29*, 196–205.

Klier, E.M., Wang, H., and Crawford, J.D. (2001). The superior colliculus encodes gaze commands in retinal coordinates. Nat. Neurosci. *4*, 627–632.

Koyama, M., Kinkhabwala, A., Satou, C., Higashijima, S., and Fetcho, J. (2011). Mapping a sensory-motor network onto a structural and functional ground plan in the hindbrain. Proc. Natl. Acad. Sci. U. S. A. *108*, 1170–1175.

Kubo, F., Hablitzel, B., Dal Maschio, M., Driever, W., Baier, H., and Arrenberg, A.B. (2014). Functional Architecture of an Optic Flow-Responsive Area that Drives Horizontal Eye Movements in Zebrafish. Neuron *81*, 1344–1359.

du Lac, S., and Knudsen, E.I. (1990). Neural maps of head movement vector and speed in the optic tectum of the barn owl. J. Neurophysiol. *63*, 131–146.

Lai, D., Brandt, S., Luksch, H., and Wessel, R. (2011). Recurrent Antitopographic Inhibition Mediates Competitive Stimulus Selection in an Attention Network. J. Neurophysiol. *105*, 793–805.

Lee, M.M., Arrenberg, A.B., and Aksay, E.R.F. (2015). A Structural and Genotypic Scaffold Underlying Temporal Integration. J. Neurosci. *35*, 7903–7920.

Lister, J., Robertson, C., Lepage, T., Johnson, S., and Raible, D. (1999). Nacre Encodes a Zebrafish Microphthalmia-Related Protein That Regulates Neural-Crest-Derived Pigment Cell Fate. Development *126*, 3757–3767.

Luksch, H. (2003). Cytoarchitecture of the avian optic tectum: neuronal substrate for cellular computation. Rev. Neurosci. *14*, 85–106.

Luque, M. a, Pérez-Pérez, M.P., Herrero, L., and Torres, B. (2008). Afferent and efferent

connections of the mesencephalic reticular formation in goldfish. Brain Res. Bull. *75*, 480–484.

Macosko, E.Z., Basu, A., Satija, R., Nemesh, J., Shekhar, K., Goldman, M., Tirosh, I., Bialas, A.R., Kamitaki, N., Martersteck, E.M., et al. (2015). Highly parallel genome-wide expression profiling of individual cells using nanoliter droplets. Cell *161*, 1202–1214.

Mahn, M., Gibor, L., Malina, K.C.-K., Patil, P., Printz, Y., Oring, S., Levy, R., Lampl, I., and Yizhar, O. (2017). High-efficiency optogenetic silencing with soma-targeted anion-conducting channelrhodopsins. bioRxiv 225847.

Mardinly, A.R., Oldenburg, I.A., Pégard, N.C., Sridharan, S., Lyall, E.H., Chesnov, K., Brohawn, S.G., Waller, L., and Adesnik, H. (2018). Precise multimodal optical control of neural ensemble activity. Nat. Neurosci.

Marquart, G.D., Tabor, K.M., Brown, M., Strykowski, J.L., Varshney, G.K., LaFave, M.C., Mueller, T., Burgess, S.M., Higashijima, S., and Burgess, H.A. (2015). A 3D Searchable Database of Transgenic Zebrafish Gal4 and Cre Lines for Functional Neuroanatomy Studies. Front. Neural Circuits *9*, 1–17.

Marquart, G.D., Tabor, K.M., Horstick, E.J., Brown, M., Geoca, A.K., Polys, N.F., Nogare, D.D., and Burgess, H.A. (2017). High-precision registration between zebrafish brain atlases using symmetric diffeomorphic normalization. Gigascience *6*, 1–15.

Mattis, J., Tye, K.M., Ferenczi, E. a, Ramakrishnan, C., O'Shea, D.J., Prakash, R., Gunaydin, L. a, Hyun, M., Fenno, L.E., Gradinaru, V., et al. (2011). Principles for applying optogenetic tools derived from direct comparative analysis of microbial opsins. Nat. Methods *9*, 159–172.

Meek, J. (1983). Functional anatomy of the tectum mesencephali of the goldfish. An explorative analysis of the functional implications of the laminar structural organization of the tectum. Brain Res. Rev. *6*, 247–297.

Meek, J., and Schellart, N. a (1978). A Golgi study of goldfish optic tectum. J. Comp. Neurol. *182*, 89–122.

Mey, J., and Thanos, S. (2000). Development of the visual system of the chick. I. Cell differentiation and histogenesis. Brain Res. Brain Res. Rev. *32*, 343–379.

Mione, M., Lele, Z., Kwong, C.T., Concha, M.L., and Clarke, J.D. (2006). Expression of pcp4a in subpopulations of CNS neurons in zebrafish. J. Comp. Neurol. *495*, 769–787.

Molyneaux, B.J., Arlotta, P., Menezes, J.R.L., and Macklis, J.D. (2007). Neuronal subtype specification in the cerebral cortex. Nat. Rev. Neurosci. *8*, 427–437.

Murayama, M., Pérez-Garci, E., Lüscher, H.-R., and Larkum, M.E. (2007). Fiberoptic system for recording dendritic calcium signals in layer 5 neocortical pyramidal cells in freely moving rats. J. Neurophysiol. *98*, 1791–1805.

Nakai, J., Ohkura, M., and Imoto, K. (2001). A high signal-to-noise ca2+ probe composed of a single green fluorescent protein. Nat. Biotechnol. *19*, 137–141.

Naumann, E. a, Kampff, A.R., Prober, D. a, Schier, A.F., and Engert, F. (2010). Monitoring neural activity with bioluminescence during natural behavior. Nat. Neurosci. *13*, 513–520.

Neuhauss, S.C., Biehlmaier, O., Seeliger, M.W., Das, T., Kohler, K., Harris, W.A., and Baier, H. (1999). Genetic disorders of vision revealed by a behavioral screen of 400 essential loci in zebrafish. J. Neurosci. *19*, 8603–8615.

Nevin, L.M., Robles, E., Baier, H., and Scott, E.K. (2010). Focusing on optic tectum circuitry through the lens of genetics. BMC Biol. *8*, 126.

Nikolaou, N., Lowe, A.S., Walker, A.S., Abbas, F., Hunter, P.R., Thompson, I.D., and Meyer, M.P. (2012). Parametric Functional Maps of Visual Inputs to the Tectum. Neuron *76*, 317–324.

van Opstal, a J., Hepp, K., Hess, B.J., Straumann, D., and Henn, V. (1991). Two- rather than three-dimensional representation of saccades in monkey superior colliculus. Science *252*, 1313–1315.

Orger, M.B., Smear, M.C., Anstis, S.M., and Baier, H. (2000). Perception of Fourier and non-Fourier motion by larval zebrafish. Nat. Neurosci. *3*, 1128–1133.

Oron, D., Papagiakoumou, E., Anselmi, F., and Emiliani, V. (2012). Two-photon optogenetics. Prog. Brain Res. *196*, 119–143.

Packer, A.M., Russell, L.E., Dalgleish, H.W.P., and Häusser, M. (2015). Simultaneous all-optical manipulation and recording of neural circuit activity with cellular resolution in vivo. Nat. Methods *12*, 140–146.

Panser, K., Tirian, L., Schulze, F., Villalba, S., Jefferis, G.S.X.E., Bühler, K., and Straw, A.D. (2016). Automatic Segmentation of Drosophila Neural Compartments Using GAL4 Expression Data Reveals Novel Visual Pathways. Curr. Biol. *26*, 1943–1954.

Papagiakoumou, E., Bradley, J., Oron, D., Emiliani, V., Bègue, A., Leshem, B., Schwartz, O., Stell, B.M., Bradley, J., Oron, D., et al. (2013). Functional patterned multiphoton excitation deep inside scattering tissue. Nat. Photonics *7*, 274–278.

Patterson, G.H., Lippincott-Schwartz, J., Momethylase, C.-, Patterson, G.H., Lippincott-Schwartz, J., and Momethylase, C.- (2002). A photoactivatable GFP for selective photolabeling of proteins and cells. Science (80-.). *297*, 1873–1877.

Pérez-Pérez, M.P., Luque, M. a., Herrero, L., Nunez-Abades, P. a., and Torres, B. (2003). Connectivity of the goldfish optic tectum with the mesencephalic and rhombencephalic reticular formation. Exp. Brain Res. *151*, 123–135.

Podor, B., Hu, Y., Ohkura, M., Nakai, J., Croll, R., and Fine, A. (2015). Comparison of genetically encoded calcium indicators for monitoring action potentials in mammalian brain by two-photon excitation fluorescence microscopy. Neurophotonics *2*, 21014.

Portugues, R., Feierstein, C.E., Engert, F., and Orger, M.B. (2014). Whole-Brain Activity Maps Reveal Stereotyped, Distributed Networks for Visuomotor Behavior. Neuron *81*, 1328–1343.

Preuss, S.J., Trivedi, C.A., Vom Berg-Maurer, C.M., Ryu, S., and Bollmann, J.H. (2014). Classification of object size in retinotectal microcircuits. Curr. Biol. *24*, 2376–2385.

Randlett, O., Wee, C.L., Naumann, E. a, Nnaemeka, O., Schoppik, D., Fitzgerald, J.E., Portugues, R., Lacoste, A.M.B., Riegler, C., Engert, F., et al. (2015). Whole-brain activity mapping onto a zebrafish brain atlas. Nat. Methods 1–12.

Rein, M.L., and Deussing, J.M. (2012). The optogenetic (r)evolution. Mol. Genet. Genomics *287*, 95–109.

Renninger, S.L., and Orger, M.B. (2013). Two-photon imaging of neural population activity in zebrafish. Methods *62*, 255–267.

Rickgauer, J.P., and Tank, D.W. (2009). Two-photon excitation of channelrhodopsin-2 at

saturation. Proc. Natl. Acad. Sci. U. S. A. *106*, 15025–15030.

Rickgauer, J.P., Deisseroth, K., and Tank, D.W. (2014). Simultaneous cellular-resolution optical perturbation and imaging of place cell firing fields. Nat. Neurosci. *17*, 1816–1824.

Robles, E., Filosa, A., and Baier, H. (2013). Precise lamination of retinal axons generates multiple parallel input pathways in the tectum. J. Neurosci. *33*, 5027–5039.

Robles, E., Laurell, E., and Baier, H. (2014). The retinal projectome reveals brain-area-specific visual representations generated by ganglion cell diversity. Curr. Biol. *24*, 2085–2096.

Rohlfing, T., and Maurer, C.R. (2003). Nonrigid image registration in shared-memory multiprocessor environments with application to brains, breasts, and bees. IEEE Trans. Inf. Technol. Biomed. *7*, 16–25.

Ronzitti, E., Ventalon, C., Canepari, M., Forget, B.C., Papagiakoumou, E., and Emiliani, V. (2017). Recent advances in patterned photostimulation for optogenetics. J. Opt. (United Kingdom) *19*.

Rupprecht, P., Prendergast, A., Wyart, C., and Friedrich, R.W. (2016). Remote z-scanning with a macroscopic voice coil motor for fast 3D multiphoton laser scanning microscopy. Biomed. Opt. Express *7*, 1656.

Sadeh, M., Sajad, A., Wang, H., Yan, X., and Crawford, J.D. (2015). Spatial transformations between superior colliculus visual and motor response fields during head-unrestrained gaze shifts. Eur. J. Neurosci. *42*, 2934–2951.

Saitoh, K., Ménard, A., and Grillner, S. (2007). Tectal control of locomotion, steering, and eye movements in lamprey. J. Neurophysiol. *97*, 3093–3108.

Salas, C., Herrero, L., Rodriguez, F., and Torres, B. (1997). Tectal codification of eye movements in goldfish studied by electrical microstimulation. Neuroscience *78*, 271–288.

Sanes, J.R., and Zipursky, S.L. (2010). Design principles of insect and vertebrate visual systems. Neuron *66*, 15–36.

Sato, T., Hamaoka, T., Aizawa, H., Hosoya, T., and Okamoto, H. (2007). Genetic single-cell mosaic analysis implicates ephrinB2 reverse signaling in projections from the posterior tectum to the hindbrain in zebrafish. J. Neurosci. *27*, 5271–5279.

Scheer, N., and Campos-Ortega, J. a (1999). Use of the Gal4-UAS technique for targeted gene expression in the zebrafish. Mech. Dev. *80*, 153–158.

Schmitt, E. a, and Dowling, J.E. (1999). Early retinal development in the zebrafish, Danio rerio: light and electron microscopic analyses. J. Comp. Neurol. *404*, 515–536.

Schoonheim, P.J., Arrenberg, A.B., Del Bene, F., and Baier, H. (2010). Optogenetic localization and genetic perturbation of saccade-generating neurons in zebrafish. J. Neurosci. *30*, 7111–7120.

Scott, E.K., and Baier, H. (2009). The cellular architecture of the larval zebrafish tectum, as revealed by gal4 enhancer trap lines. Front. Neural Circuits *3*, 13.

Scott, E.K., Mason, L., Arrenberg, A.B., Ziv, L., Gosse, N.J., Xiao, T., Chi, N.C., Asakawa, K., Kawakami, K., and Baier, H. (2007). Targeting neural circuitry in zebrafish using GAL4 enhancer trapping. Nat. Methods *4*, 323–326.

Semmelhack, J.L., Donovan, J.C., Thiele, T.R., Kuehn, E., Laurell, E., and Baier, H. (2014). A dedicated visual pathway for prey detection in larval zebrafish. Elife *4*, 1–19.

Shang, A.C., Chen, Z., Liu, A., Li, Y., Zhang, J., and Yan, F. (2018). Divergent midbrain circuits orchestrate escape and freezing responses to looming stimuli in mice. Nat. Commun. 1–17.

Shang, C., Liu, Z., Chen, Z., Shi, Y., Wang, Q., Liu, S., Li, D., and Cao, P. (2015). A parvalbumin-positive excitatory visual pathway to trigger fear responses in mice. Science (80-.). *348*, 1472–1477.

Shcherbakova, D.M., Sengupta, P., Lippincott-Schwartz, J., and Verkhusha, V. V. (2014). Photocontrollable Fluorescent Proteins for Superresolution Imaging. Annu. Rev. Biophys. *43*, 303–329.

Shemesh, O.A., Tanese, D., Zampini, V., Linghu, C., Piatkevich, K., Ronzitti, E., Papagiakoumou, E., Boyden, E.S., and Emiliani, V. (2017). Temporally precise single-cell-resolution optogenetics. Nat. Neurosci. *20*, 1796–1806.

Sooksawate, T., Isa, K., Matsui, R., Kato, S., Kinoshita, M., Kobayashi, K., Watanabe, D., Kobayashi, K., and Isa, T. (2013). Viral vector-mediated selective and reversible blockade of the pathway for visual orienting in mice. Front. Neural Circuits *7*, 162.

Sparks, D.L. (2002). The brainstem control of saccadic eye movements. Nat. Rev. Neurosci. *3*, 952–964.

Sparks, D.L., and Gandhi, N.J. (2003). Single cell signals: An oculomotor perspective. Prog. Brain Res. *142*, 35–53.

Sugano, Y., and Neuhauss, S.C.F. (2012). Reverse genetics tools in zebrafish: A forward dive into endocrinology. Gen. Comp. Endocrinol. *188*, 303–308.

Suster, M.L., Abe, G., Schouw, A., and Kawakami, K. (2011). Transposon-mediated BAC transgenesis in zebrafish. Nat. Protoc. *6*, 1998–2021.

Symvoulidis, P., Lauri, A., Stefanoiu, A., Cappetta, M., Schneider, S., Jia, H., Stelzl, A., Koch, M., Perez, C.C., Myklatun, A., et al. (2017). NeuBtracker - Imaging neurobehavioral dynamics in freely behaving fish. Nat. Methods *14*, 1079–1082.

Temizer, I., Donovan, J.C., Baier, H., and Semmelhack, J.L. (2015). A Visual Pathway for Looming-Evoked Escape in Larval Zebrafish. Curr. Biol. *25*, 1823–1834.

Thiele, T.R., Donovan, J.C., and Baier, H. (2014). Descending Control of Swim Posture by a Midbrain Nucleus in Zebrafish. Neuron *83*, 679–691.

Vanegas, H., and Ito, H. (1983). Morphological aspects of the teleostean visual system: A review. Brain Res. Rev. *6*, 117–137.

Vaziri, A., and Emiliani, V. (2012). Reshaping the optical dimension in optogenetics. Curr. Opin. Neurobiol. *22*, 128–137.

Wu, C., Ivanova, E., Zhang, Y., and Pan, Z.H. (2013). rAAV-Mediated Subcellular Targeting of Optogenetic Tools in Retinal Ganglion Cells In Vivo. PLoS One *8*, 1–10.

Yang, W., and Yuste, R. (2018). Holographic imaging and photostimulation of neural activity. Curr. Opin. Neurobiol. *50*, 211–221.

Yang, W., Miller, J. eun K., Carrillo-Reid, L., Pnevmatikakis, E., Paninski, L., Yuste, R., and

Peterka, D.S. (2016). Simultaneous Multi-plane Imaging of Neural Circuits. Neuron *89*, 284.

Yang, W., Carrillo-Reid, L., Bando, Y., Peterka, D.S., and Yuste, R. (2018). Simultaneous two-photon imaging and two-photon optogenetics of cortical circuits in three dimensions. Elife *7*, 1–21.

Zheng, G.X.Y., Lau, B.T., Schnall-Levin, M., Jarosz, M., Bell, J.M., Hindson, C.M., Kyriazopoulou-Panagiotopoulou, S., Masquelier, D.A., Merrill, L., Terry, J.M., et al. (2016). Haplotyping germline and cancer genomes with high-throughput linked-read sequencing. Nat. Biotechnol. *34*, 303–311.